Modelling and Design of Permanent-magnet Machines for Electric Vehicle Traction

by

Xiao Chen

A thesis submitted in fulfilment of the requirements for the degree of Doctor of Philosophy

Department of Electronic and Electrical Engineering
Faulty of Engineering
The University of Sheffield

December 2015

ABSTRACT

Electrical machines with rare-earth permanent-magnets (PMs) exhibit high torque density and good efficiency over a wide operation range. However, the high cost and limited reserves of the rare-earth material makes it less sustainable to develop this machine technology for electric vehicle (EV) traction. To improve machine performance and reduce PM usage, this thesis investigates a number of issues pertinent to modelling and design of PM machines for EV traction applications. A four-wheel vehicle dynamic model is established to quantify the influence of tyre slip on machine sizing, and thus an optimum control for torque split ratio of distributed front-rear drives is realised by minimising the loss resulting from tyre slip. PM-assisted synchronous reluctance machines with fractional-slot windings are proposed to reduce PM usage whilst exploiting advantages of fractional-slot windings. To more accurately evaluate reluctance torque and thus maximise torque production of an interior PM (IPM) machine in design stage, a torque model allowing for torque component separation via frozen permeability is presented. A generic approach to magneto-motive force harmonics reduction using multiple 3-phase windings is proposed to reduce rotor iron loss and torque ripple whilst improve reluctance torque and machine efficiency. A 9-phase 18-slot 14-pole IPM machine is subsequently designed based on the proposed multiple 3-phase windings and its performance validated on a 10kW prototype. In order to accurately assess the performance of an IPM machine drive, a high-fidelity and computationally efficient machine model is proposed by considering magnetic saturation, spatial harmonics, iron loss and temperature effects. Furthermore, an electro-thermally coupled model is established by integrating the temperature-dependent electromagnetic model with a state-space lumped parameter thermal model. Both models are experimentally validated. An analytical mechanical stress model is proposed to incorporate mechanical strength constraints into machine global optimisation process. Thus, unfeasible designs whose mechanical strength cannot meet the requirement can be avoided.

ACKNOWLEDGEMENTS

4 years ago, I came to UK to pursue my Ph.D study which is an exciting journey but at that time I also felt anxious and uneasy due to lack of a clear goal. Luckily, I joined Electrical Machines and Drives (EMD) research group at The University of Sheffield and also made many new friends, offering me great opportunities to communicate, learn and obtain my research objectives. After 4 years' efforts, this thesis is on the point of completion. On this occasion, I would like to give my sincere gratitude to all the people who accompany me in this exciting journey.

The most I would like to thank is my supervisor, Prof. Jiabin Wang, who has offered me loads of favours and encouragements when I got confused and lost in my research. He spent plenty of time on our 4 years' weekly meetings and also my project reports and publications. I learned not only knowledge but also the way of thinking from him who is a knowledgeable, creative, conscientious and more than qualified supervisor.

I also would like to express my great thanks to my colleagues (also friends) who contribute to this thesis, including Dr. Vipulkumar I. Patel for his help on the winding of my machine prototype, Panagiotis Lazari for his help on the magnet magnetisation and assembly, Liang Chen for his global optimisation script which is very effective and useful, Mrs. Weiya Wang for her help to make the drawings of my machine prototype, Bhaskar Sen and Tianfu Sun for their help on my experiments, Bo Wang for his help on FEA computation, Qian Wang for his contribution to my lamination manufacture, and Dr. Antonio Griffo for his lumped parameter thermal model.

My acknowledgements are also given to the dedicated technicians in EMD group, particularly John A. Wilkinson for his help on my machine prototype and Richard Garraway for the power bank he made for my experimental test.

My friends, particularly my housemates Wei Li, Chaohui Liu, Hanlin Zhan, Haichen Shi and Yang Liu, also deserve my big thanks. They award me a joyful and wonderful Ph.D life which will never be forgotten.

I am also grateful to my second supervisor Prof. Z. Q. Zhu and my former supervisor Prof. Jibin Zou (in my M.Eng study) for their recommendations in my Ph.D application at the very beginning.

Last but not the least, I would like to say thank you to my parents who are always concerned about me, encourage me and feel pride of me. I love you.

TABLE OF CONTENTS

CHAPTER 1 Comparative Studies of Machine Topologies and Technologies for Electric Vehicle Traction Applications

1.1 Introduction

In the human urbanisation process, vehicles are essential and increasingly important due to their transport functions serving both human beings and commodities. The majority of vehicles (particularly personal cars) available in today's markets are still powered by the fossil fuel. Although the fossil fuel-powered vehicles are cost-effective and mature in manufacture, they consume non-renewable resources and meanwhile produce serious air pollution. Therefore, their use is hardly sustainable.

To address the foregoing problems of fossil fuel-powered vehicles, both academia and industries are performing researches on electric vehicles (EVs) which are powered by electrical machines rather than internal combustion engines (ICEs). Stored in the on-board battery, the electricity EVs consume can be generated from a wide variety of renewable resources such as solar power, wind power, tidal power, geothermal power, hydropower and/or any their combination. Apart from the renewable energy utilisation and zero carbon dioxide emissions, EVs also exhibit the advantages of less components and lower dependencies between systems, more flexible packaging and high energy efficiency due to both the high efficiency of electrical machines over a whole driving cycle and the regenerative braking by the bi-directional energy flow in the powertrain system.

As a key enabling technology for EVs, electrical machines need to satisfy the following requirements [1-3]:

(1) High power density and torque density;
(2) Wide speed range with constant-power operation approximately 3-4 times the base speed;

(3) High starting torque, sufficient hill climbing capability, and high power at cruising speed;

(4) Good efficiency over wide torque and speed ranges;

(5) High reliability and fault tolerance;

(6) Intermittent overload ability;

(7) Low acoustic noise and low torque ripple;

(8) Affordable cost.

The ideal torque-speed and power-speed curves for a traction machine are shown in Fig. 1-1. Region I is the constant-torque region where the peak torque can be reached with the maximum current supplied by an inverter. The peak torque requirement is determined by the acceleration and/or hill climbing demands. Region II is the constant-power region where output power is limited by the inverter and thus the maximum torque decreases with the increase of speed. Region III is the reducing power region where the output power cannot maintain at peak power owing to both the increase of back-electromotive force (EMF) and also inverter current and voltage limits [4].

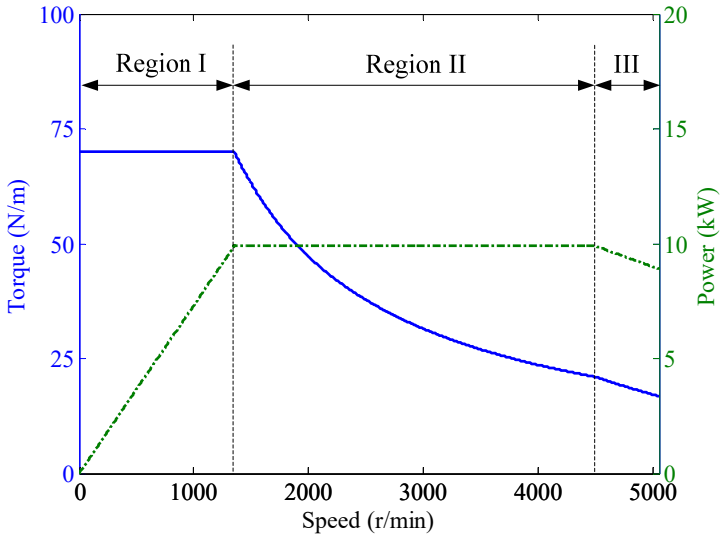

Fig. 1-1. Ideal torque and power versus speed curves for EV traction machines.

With respect to the foregoing machine design requirements and torque-speed characteristics of electrical machines for EV traction applications,

comparative studies of various machine topologies and technologies will be performed in this chapter. The candidate machine topologies for EV traction, their current state-of-the-art technologies and the qualitative comparison among alternative machine topologies are undertaken respectively in the following sections, before the most appropriate ones are selected for the EV traction with particular emphasis on high efficiency over wide torque and speed operating ranges. Subsequently, the overview of this thesis and the list of publications are presented.

1.2 Candidate Machine Technologies for EV Traction

The electromagnetic torque in an electrical machine is produced by interaction of magnetic field with electrical current. Thus, depending on how the magnetic field is generated and electrical current is supplied (as shown in Table 1-1), electrical machines can be classified, in Fig. 1-2, as Brushed DC Machine (BDCM), Induction Machine (IM), Synchronous Machine (SM), Switched Reluctance Machine (SRM), Synchronous Reluctance Machine (SynRM) and Permanent-magnet Machine (PMM). For each machine technology, there are different machine topologies but only those for PMM are shown in Fig. 1-2. The schematics for typical machines are illustrated in Fig. 1-3.

It should be noted that all the above machine topologies are of radial flux air-gap. There are also established axial flux machines in EV traction applications, such as the electrical machines developed by YASA Motors [5, 6] and GKN-EVO [7, 8]. However, considering the manufacturing and assembly difficulties and also the needs of special iron material to form a three-dimensional (3-D) flux path, this thesis will be focused on the radial flux machines.

Table 1-1. Operation Principles of Basic Machine Technologies

Item	Air-gap Field	Field excitation	Power supply
BDCM	Static	Field winding or PM	DC
IM	Rotating	Stator winding	AC Sine wave
SM	Rotating	Field winding	AC Sine wave
SRM	Rotating	Stator winding	Pulsed sequence
SynRM	Rotating	Stator winding	AC Sine wave
PMM	Rotating	PM	Sine/trapezoidal wave

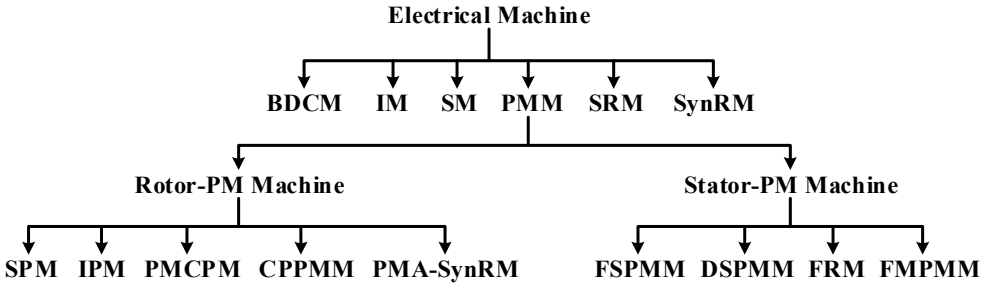

Fig. 1-2. Classification of electrical machines for EV traction.

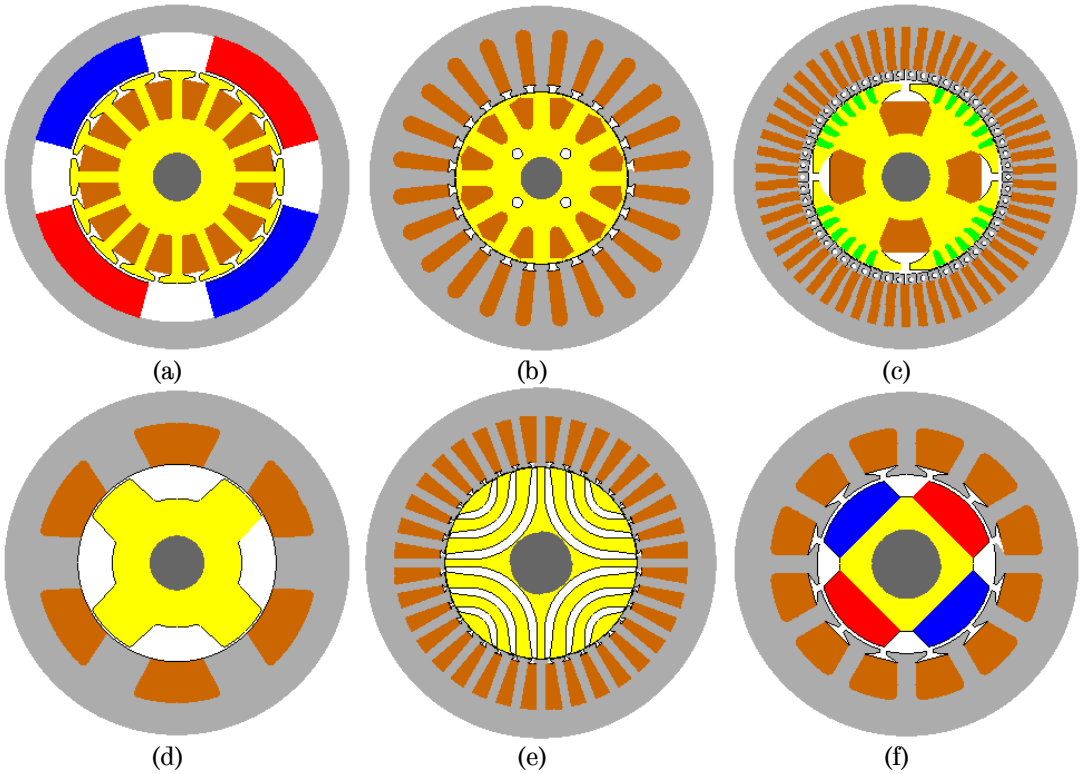

Fig. 1-3. Schematics of candidate electrical machines. (a) BDCM. (b) IM. (c) SM. (d) SRM. (e) SynRM. (f) PMM.

Broadly speaking, all electrical machine technologies can be employed for EV traction. However, due to the inherent merits of permanent-magnet

machines, such as high power density and high efficiency, a variety of PMM topologies has been developed. Depending on the location of magnets and windings, the PMM can be divided into Rotor-PM machine which includes Surface-mounted PM Machine (SPM), Interior PM Machine (IPM), PM Claw Pole Machine (PMCPM), Consequent Pole PM Machine (CPPMM), PM Assisted Synchronous Reluctance Machine (PMA-SynRM) and etc., and Stator-PM machine which includes Doubly Salient PM Machine (DSPMM), Flux Reversal Machine (FRM), Flux Switching PM Machine (FSPMM), Flux Mnemonic PM Machine (FMPMM) etc., as listed in Fig. 1-2.

All the above machine topologies are seen as candidate machines at the first stage, and will be evaluated regarding their relative merits and compared on the basis of the defined criteria in the following sections.

1.3 Current State-of-the-art of Electrical Machine Technologies

1.3.1 Brushed Direct Current Machine

As illustrated in Fig. 1-4, Brushed DC Machine (BDCM) consists of a stator with a DC field winding or PM and a soft magnetic core (iron), and a rotor with the armature winding and commutators mounted on the shaft. DC current is supplied to the rotor armature via brushes and commutators. The torque is produced from the interaction of the stator magnetic field with the armature current.

Although BDCM has various merits in terms of technological maturity, control simplicity and low initial cost, and has already been widely used in industry, its low life-span and high maintenance due to indispensable commutators and brushes make it less attractive to EV applications and will not be further considered in the subsequent sections.

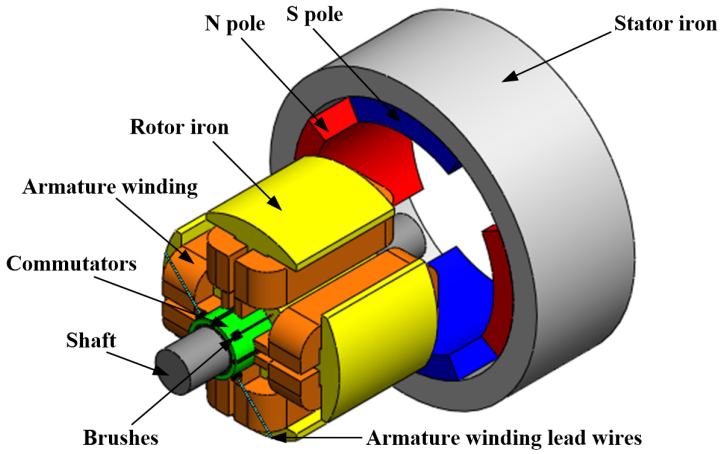

Fig. 1-4. Schematic of a brushed DC machine.

1.3.2 Induction Machine

Induction Machine (IM), as shown in Fig. 1-5, is driven by AC current supplied to its stator winding and generates torque from the interaction between the rotating magnetic field in the air-gap and the induced current in the rotor winding or squirrel cage. Since the rotor current can only be induced when the rotor speed is different to that of the rotating magnetic field in the air-gap, induction machine is also referred to as asynchronous machine.

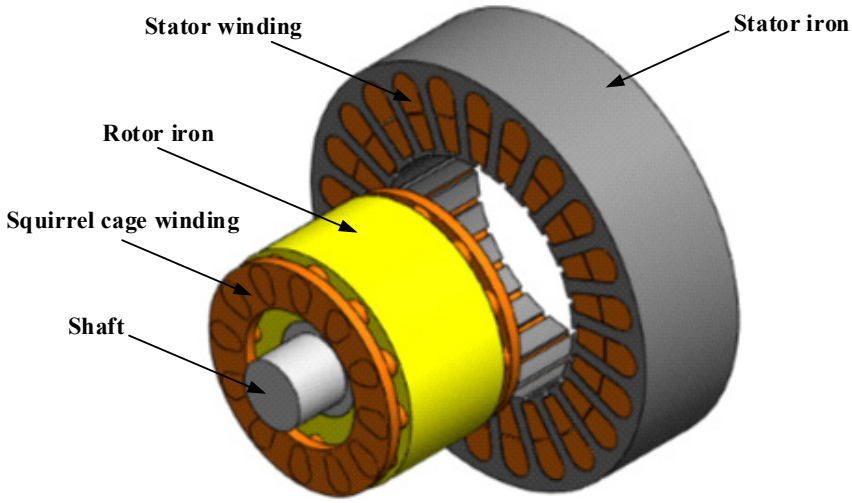

Fig. 1-5. Schematic of an induction machine.

Owing to a number of advantages such as a robust rotor structure particularly with a cage rotor, low cost and well established manufacturing techniques, induction machines are widely employed in industrial drives.

However, due to the presence of the copper loss in the rotor and a portion of stator current is needed for producing the magnetic field in the air-gap, induction machines have relatively low efficiency and low power factor which is disadvantageous for EV traction.

Therefore, a great many of researchers have been continuously striving to improve the efficiency of induction machines. S. Lie *et al* [9] substituted a cast aluminium rotor with a copper die-cast rotor in a squirrel cage induction machine to achieve higher efficiency since the electrical conductivity of copper is 60% higher than that of aluminium. J. Malinowski *et al* [10] summarised the advances in construction technologies of induction motors and showed that die-cast copper rotors could enable efficiency to be increased by 1%–2% compared with the aluminium one. These increases in efficiency are supposed to be more on smaller machines, reducing to 0.5% on bigger machines. However, considering copper is more costly than aluminium, the benefits obtained from copper cage utilisation in rotor is compromised [11].

Besides attempts from the perspective of design improvements, numerous researches have been undertaken in the control of IM to minimise the loss for traction application. R. E. Araújo *et al* [12] did experimental evaluation of a loss-minimisation control scheme based on FOC (Field-Oriented Control) and realised a reduction in energy consumption for 5.7%, 2% and 0.7% at 13km/h, 18km/h and 22km/h respectively. A. Haddoun *et al* [13] proposed a direct flux and torque control scheme to minimise the losses in the drive of an induction machine for EV traction. To achieve the efficiency-optimised drive performance, their control scheme treats stator flux as a control variable, and the flux level is determined by the torque demand from EV. Furthermore, they developed a DTC-SVM (Direct Torque Control using Space Vector Modulation) control scheme to reduce the loss further and proved that it outperformed the previous DTC and conventional FOC schemes [14]. E. Hussein *et al* [15] utilised an IFOC (Indirect Field-Oriented

Control) controller to adjust the flux level according to the load variation and improved the efficiency by 4.5% with optimal flux at half rated load. E. S. Sergaki [16] employed a real time optimum flux adjustment fuzzy controller cooperated with DTC adjustable speed drive for IM to achieve the motor drive loss minimisation while meeting the load and speed demands. The experiment result showed that the power losses had been reduced by 32% at no-load operation. A. Scarmin *et al* [17] proposed a new optimisation technique for energy saving in induction motor drives defined a Hybrid Adaptive Efficiency Controller (HAEC), which uses main characteristics of SC (Search Controller) and LMC (Loss Model Based Controller), and demonstrated that the energy consumption with HAEC approach was 1.77% smaller than that of LMC considering 5% variation of motor parameters. R. E. Janzen *et al* [18] presented an augmented proportion-integration (PI) control scheme with signal paths additively related with the reference speed and the slip ratio, improving the efficiency by 2.8% in average and 4.6% at specific speed range, evaluated in transient simulation with a magnetic saturation motor model.

Other than the relatively low efficiency problem, the relatively narrow constant-power range can also be an obstacle for IM to be applied in EV traction, which usually requires an expansion of 3-4 times the base speed, more than the typical range of 2-3 times that can be achieved by IMs, resulting in a complicated design to satisfy the field weakening requirement, high cost and low power density design. Besides, due to motor parameter variations, the control schemes for IM are complex as well.

1.3.3 Synchronous Machine

With field winding on rotor and armature winding on stator, as depicted in Fig. 1-6, Synchronous Machine (SM) produces torque via the interaction of stator current with the magnetic fields of the field winding which is energised through slip rings and brushes. Therefore, SM can reach a wide range constant-power operation in EV traction, whilst is more flexible in

controlling the current in the field winding to adjust the magnetic field of excitation and thus reach high efficiency operation over wide torque and speed ranges.

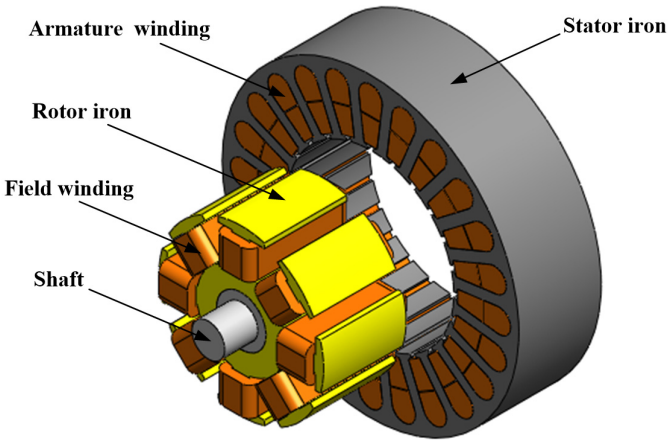

Fig. 1-6. Schematic of a synchronous machine.

However, SMs also exhibit obvious drawbacks for EV traction applications. First, the currents fed into the field winding result in extra copper losses and thus reduce operation efficiency. Besides, the indispensable slip rings and brushes also leads to high maintenance cost and low reliability of SMs. Moreover, given that the desirable power of an EV traction motor is usually in the range from 10kW to 100kW, the space for field windings on rotor is very limited.

1.3.4 Switched Reluctance Machine

Switched Reluctance Machine (SRM) consists of a salient stator with wound-armature coils and a salient rotor, as illustrated in Fig. 1-7. The operation principle of an SRM is based on the difference in magnetic reluctance between the aligned and unaligned rotor positions with respect to the stator winding. When a stator phase winding is energised, the rotor experiences a force which will pull it to the aligned position where the stored magnetic energy is at minimum. The rotor pole number is typically less than the stator pole number, to prevent the poles from all aligning simultaneously at a position where no torque is generated.

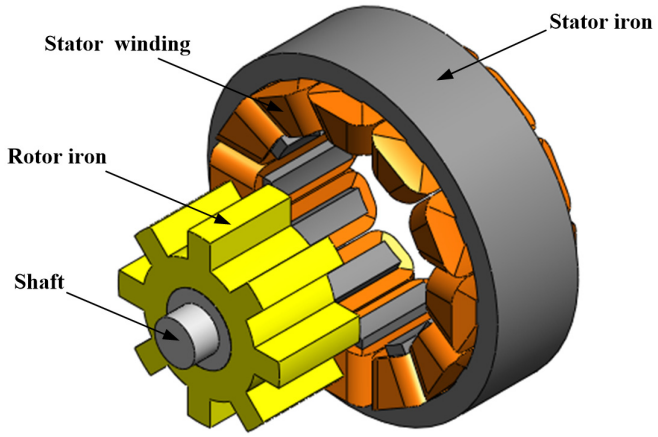

Fig. 1-7. Schematic of a switched reluctance machine.

SRM has advantages such as a simple rotor structure with no winding or magnets, as shown in Fig. 1-7, fail safe because a failure in one phase will not seriously affect operations of other phases, low cost, and ability to operate in high temperature environment. A. Chiba *et al* [19-21] developed a set of SRMs which can achieve comparable or even better efficiency, torque density, and speed operating range with respect to the rare-earth permanent-magnet machine used in the second-generation Toyota Prius hybrid electric vehicle. However, the high cost high-silicon steel with 0.1mm thickness lamination needs to be employed. The continuous-current mode needs to be applied at high speeds to ensure the high performance.

However, the torque ripple is an inherent drawback of switched reluctance motor drives, due to the sequential commutation of coils, doubly salient geometric structure, necessity of magnetic saturation in order to maximise the torque per mass ratio, and the pulsating magnetic field resulting from feeding successively the different stator phase windings.

Therefore, various approaches have been investigated by researchers to reduce the torque ripple of SRM in recent years. Y. Ozoglu *et al* [22] optimised stator and rotor pole tip shape to improve the inductance profile and reduced the torque ripple by 24.1% and 22.6% in short and full pitched SRMs respectively. Nevertheless, their proposed technique only works for unidirectional operation. T. Higuchi *et al* [23] presented a segment-type SRM

with 2-step slides or skewed rotor which reduced torque ripple by 19% at the expense of average torque being reduced by 10%. F. Sahin *et al* [24] proposed a method to obtain optimal magnetic-circuit parameters to minimise torque ripple of SRM at low speed and the minimum torque ripple of ~10% is reportedly achieved with the optimal geometric parameters.

Torque ripple can also be mitigated with the appropriate control. M. Divandari *et al* [25] employed fuzzy logic rules in current control and thus decreased torque ripple to 38% from 57% with piece-wise linear torque characteristic approach. Z. Zhang *et al* [26] investigated the Direct Torque Control (DTC) for SRM and reported that DTC can not only suppress the ripple caused by current chopping control but also significantly reduce the torque ripple during phase commutation. As a result, the torque ripple has been reduced dramatically to 10% from 71.4%. H. Ishikawa *et al* [27] introduced boost capacitors paralleling with stator windings in SRM drive system to obtain desirable current waveforms. Thus, the torque ripple of SRM with this proposed technique is 14% less than that of conventional drive with voltage control while 34.6% less than that of conventional drive with current control.

However, even with the foregoing new techniques on both machine design and control aspects, the torque ripple of SRM is still much higher than the typical maximum permissible limit for EV traction (5%). Furthermore, SRM also exhibits high pulsating radial force which will excites low modes of stator vibration and thus make NVH design of traction system more challenging [28, 29].

1.3.5 Synchronous Reluctance Machine

The schematic of a Synchronous Reluctance Machine (SynRM) is illustrated in Fig. 1-8. The conventional distributed winding is employed in the stator. With the multi-layer flux barriers in either transversally or axially laminated rotor iron, the main magnetic flux is guided through the

rotor iron which is between these flux barriers. Therefore, the electromagnetic torque mechanism of SynRM is the reluctance torque produced from the high rotor saliency, which is similarly with SRM.

Nevertheless, compared to SRM, SynRM has an equal number of stator and rotor poles, and only the rotor has salient poles while the stator structure is the same as that of conventional IM. Moreover, the supplied currents and voltages to SynRM are more sinusoidal than those to SRM. Thus, SynRM has less torque ripple and noise than SRM. Compared to IM, SynRM does not have windings in the rotor and operates at synchronous speed. Thereby, the rotor loss in SynRM is relatively low, which is conducive to satisfy the thermal constraints in that the rotor is more difficult to be cooled than the stator. Considering neither windings nor magnets exists in the rotor, SynRM is mechanically robust and has neither demagnetisation nor excessive back-EMF issues at fault conditions. G. Brown [30] reported that the power density of SynRMs made by ABB Ltd. can be 20-40% higher than that of IMs.

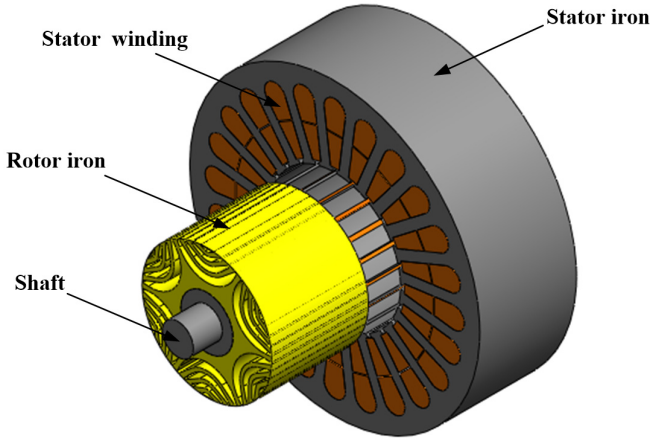

Fig. 1-8. Schematic of a synchronous reluctance machine.

Although the torque ripple of SynRM is lower than that of SRM, it is still relatively higher compared to the torque ripple requirement (≤5%) for electrical machines in EV traction application. This is because the reluctance torque is fundamentally produced by the reluctance variation which also causes a considerable torque ripple. It is well known that the torque ripple

can be reduced by appropriate skew techniques on the rotor, whereas the rotor geometry becomes complex and the average torque will also be reduced. Moreover, the residual torque ripple might be still high even after the skew technique is utilised [31]. Therefore, in literature, other approaches were proposed to reduce the torque ripple of SynRM. A. Vagati [32, 33] proposed a generic approach to minimisation of torque ripple of SynRM in the design stage, by selecting appropriate number of rotor equivalent slots which are suggested to be 4 slots difference against the stator slot number per pole pair. However, this torque ripple reduction technique cannot take the magnetic saturation effects of the stator and rotor irons into account. This might affect the torque ripple reduction effects at heavy load condition. M. Sanada *et al* [34] employed asymmetric flux barriers on the rotor to shift the relative positions of the flux barrier outer edges with respect to the stator teeth. With these asymmetric flux barriers, the torque ripple can be reduced from 50% to 10%. N. Bianchi *et al* [35] combined two rotor stacks where the flux barrier of each is designed differently to cancel out a given order torque harmonic. They also presented a design in which these two rotor stacks are combined and only the flux barrier shapes are optimised to eliminate certain order torque harmonics in [36]. They reported both of these two techniques can reduce the torque ripple to be less than 5%. T. Lange *et al* [37] employed asymmetric flux barrier angles and a flipped rotor structure to reduce certain torque harmonics by superposition. It was shown that the torque ripple was reduced to only 1.5% at rated torque operation in a 36-slot 4-pole SynRM machine.

The other drawback of SynRM is the poor power factor, resulting in the high VA rating of the inverter. T. A. Lipo [38] compared the performances of the SynRM and conventional IM using analytical analysis, and showed that the torque density of SynRM with a saliency ratio no less than 6 can be higher than that of IM at the same loss condition whereas the required VA rating of SynRM is approximately 1.4 times of that of IM. R. R. Moghaddam *et*

al [39] introduced a new operation diagram to analyse the SynRM electromagnetic behaviour and revealed that the poor power factor of SynRM is also dependent on the presence of the *q*-axis flux and cross-coupling between the *d*- and *q*-axis fluxes. T. Matsuo *et al* [40] found that the torque production of SynRM is subject to the ratio of the rotor void width, also known as "insulation" width, to the rotor iron width and showed that the power factor of 0.8 can be reached for the optimised rotor design with a 10.6 saliency ratio.

Therefore, SynRM can be considered as a machine candidate in EV traction applications considering its simple and robust rotor structure, high fault tolerance capability, relatively low cost, and wide speed operation. However, compared to the permanent-magnet synchronous machines which will be discussed in the following sections, the lower torque density, lower machine efficiency, lower power factor, and higher torque ripple make SynRM less attractive unless further improvements are made.

1.3.6 Permanent-magnet Machine

Without field windings on the rotor frame, conventional PM machine utilises permanent-magnets to generate the magnetic field against which the armature current interacts to produce torque. To minimise overall weight and size, high energy-product magnets made with neodymium or cobalt can be employed, whereas to balance the cost and performance, ferrite magnets can be considered as well.

Since the magnetic field which is essential for torque production is generated by permanent-magnets without incurring loss in a relatively small volume, in general, PM machines exhibit higher efficiency, higher torque and power density, lighter weight and more compact than other types of electrical machines. These attributes are particularly attractive for EV traction despite of some disadvantages, such as relatively high cost due to

PMs and the conflicts between field weakening capability and the risk of demagnetisation.

Therefore, this chapter will consider PMMs as a key candidate and perform a detailed literature review, which will be presented in the following sections where various machine topologies, PMs on the rotor vs. PMs on the stator will be discussed further.

1.3.6.1 Rotor-PM machine

Rotor-PM machine has magnets on the rotor and armature windings on the stator. They include Surface-mounted Permanent-magnet Machine (SPM), Interior Permanent-magnet Machine (IPM), PM Assisted Synchronous Reluctance Machine (PMA-SynRM), PM Claw Pole Machine (PMCPM), Consequent Pole PM Machine (CPPMM), and etc., each of which will be investigated below.

1.3.6.1.1 Surface-mounted Permanent-magnet Machine

With permanent-magnets mounted on the rotor surface, as illustrated in Fig. 1-9, SPMs produce torque by the interaction of the magnetic field contributed by permanent-magnets with the armature reaction field produced by the stator magnetic-motive force (MMF). This torque component is also named by the alignment torque. To balance the centrifugal force in rotation, the magnets are protected by a retaining sleeve (carbon fibre or stainless steel). From Fig. 1-9, it can be observed that the rotor saliency can be neglected and thereby practically no reluctance torque is generated in an SPM. In other words, the electromagnetic torque in an SPM is purely contributed by the alignment torque component which only depends on the permanent-magnet flux-linkage and q-axis current. Therefore, SPMs exhibit a relatively linear torque-current characteristic, good controllability, and low torque ripple.

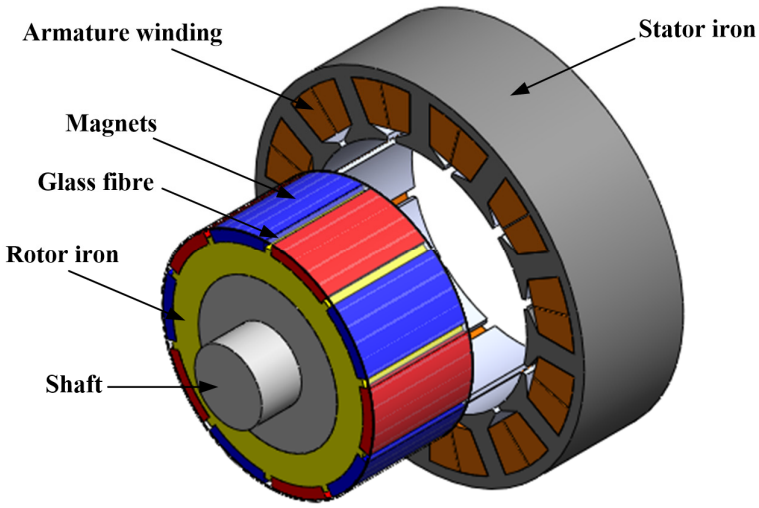

Fig. 1-9. Schematic of SPM.

Nevertheless, the surface-mounted magnets result in a large equivalent air-gap because their relative permeability approaches to 1. Hence, the inductances of the stator windings are low, leading to a high characteristic current and thereby low field weakening capability. However, F. Magnussen *et al* [41] demonstrated that the fractional-slot non-overlapping (concentrated) winding configuration can be utilised to increase the *d*-axis inductance and thus improve the field weakening capability of SPMs. A. M. EL-Refaie *et al* [42] also employed concentrated windings on SPMs and hence developed a 6kW SPM which can deliver constant-power over a 10:1 speed range by increasing the *d*-axis inductance and meeting the optimum field weakening conditions. These authors also investigated the scalability of the concentrated winding configuration for achieving optimal field weakening in SPMs in [43], and showed that the optimal field weakening can be reached over a wide range of machine power ratings from 1 to 60 kW. J. Cros *et al* [44] performed a synthesis of SPMs with concentrated windings and subsequently compared their performances with those of SPMs using conventional distributed windings. It is shown that by using the concentrated winding configuration, the copper loss can be reduced dramatically owing to both the short end-winding length and the high copper packing factor (if the modular stator structure is employed).

Moreover, the cogging torque can also be significantly reduced in that the least common multiple of the slot number and the pole number increases. Therefore, SPMs with concentrated windings exhibit advantages in EV traction applications, including high torque density, low copper loss, good field weakening capability, and low cogging torque.

However, by introducing concentrated winding configurations into SPMs, on the other hand, the rotor magnets adjacent to the air-gap are subjected to a large amount of stator MMF harmonics which are asynchronous with the rotor speed, and thereby a high eddy current loss is induced in rotor magnets [45]. This can further result in a high rotor temperature particularly at high speeds, and hence the rotor magnets will suffer from a high risk of irreversible demagnetisation. Therefore, it is necessary to accurately model and reduce the magnet eddy current losses.

K. Atallah *et al* [46] presented an analytical model to predict the magnet eddy current losses induced by low order stator MMF harmonics and demonstrated that circumferentially segmenting the magnets can effectively reduce the eddy current loss when the rotor pole number is greater than fundamental stator MMF pole number. J. Wang *et al* [47] improved the analytical model to calculate eddy current losses on magnets, and revealed that special attention should be paid on the non-uniform distribution of the magnet eddy current loss when more than two circumferential segments per magnet pole are utilised. K. Yamazaki *et al* [48] investigated the effect of reduction in eddy current losses by segmentation in magnets for SPMs with concentrated winding configurations, using both analytical method and three-dimensional (3-D) FEA. It was shown that the loss reduction effect increases with the wavelength of the eddy current loops along the segment surface whereas decreases with the frequency because of the skin effect. They also reported that the axial magnet segmentation is superior to the circumferential one in SPMs. J. D. Ede *et al* [49] proposed a computationally efficient method to predict the 3-D resistance-limited eddy current

distribution and the associated loss in the magnets. They also demonstrated that axial magnet segmentation is a very effective way to reduce the eddy current loss in magnets.

Apart from the foregoing magnet circumferential and/or axial segment techniques, the magnet eddy current loss can also be reduced by the reduction in MMF harmonics. G. Dajaku *et al* [50] proposed a 24-slot 10-pole SPM to cancel the unwanted sub- and high order MMF harmonics in a conventional 12-slot 10-pole winding configuration. Their proposed technique doubled the number of stator slots and thus utilised two sets of winding systems connected in series whereas shifted to each other by a specific angle. The uneven tooth width and asymmetric number of turns per coil for the neighbouring phase coils were also employed to enhance the MMF harmonic cancellation effects. Compared to the conventional 12-slot 10-pole SPM, the proposed 24-slot 10-pole SPM in [50] was reported to exhibit a clearly better performance due to the reduction in MMF harmonics and magnet eddy current losses. J. Wang *et al* [51] proposed a generic approach to developing fractional-slot permanent-magnet synchronous machines with low space harmonic contents, by doubling the slot number in stator and using two sets of winding systems. Both space and time shift angles of these two sets of winding systems can be selected, providing more freedom and thus more effective in cancelling MMF harmonics.

In summary, with the foregoing magnet eddy current loss reduction techniques, SPMs with fractional-slot winding configurations (including both non-overlapping ones and overlapping ones) can be considered as candidate machine topologies for EV traction applications, owing to their high torque density, short end-winging length, high copper packing factor, linear torque-current characteristic, good field weakening capability and thus high efficiency over wide torque and speed ranges. However, it should be noted that the conflicting requirements for high torque at low speeds and for low back-EMF at high speeds to guarantee safety in the event of inverter failure

cannot be reconciled in SPMs without increase in VA rating. This will result in the increase in inverter cost and losses.

1.3.6.1.2 Interior Permanent-magnet Machine

Compared with SPM, Interior PM machine (IPM) has magnets buried in the rotor iron [52], as shown in Fig. 1-10, where the retaining sleeve may no longer be needed, which simplifies the manufacture procedure and reduces the cost. Another benefit from the absence of the retaining sleeve is the reduction of the effective air-gap length, resulting in high inductance and high field weakening capability of IPM. Moreover, the difference in the *d*- and *q*-axis reluctances contributes to the variation of the reluctance in various rotor positions seen by the stator winding, thereby resulting in reluctance torque which is conducive to the reduction of PM volume in the IPM [53, 54].

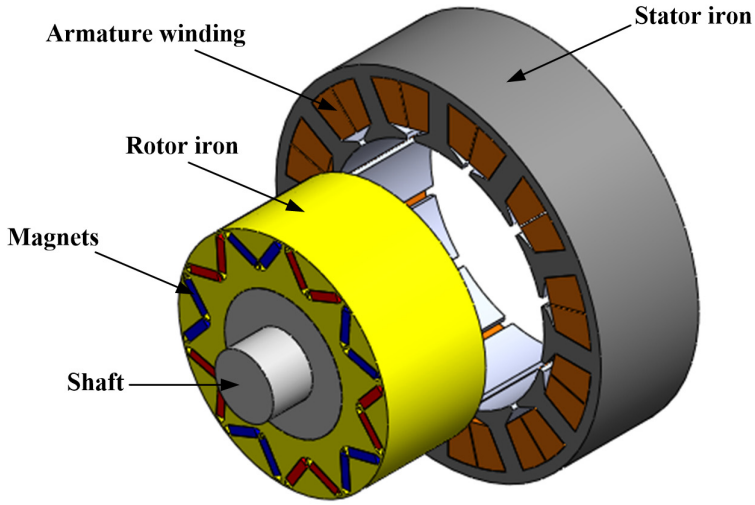

Fig. 1-10. Schematic of IPM.

However, it has been recognised that an IPM suffers from relatively high iron loss, particularly when operating at high speed region [55], due to plenty of harmonics in stator and rotor MMF, which can be further attributed to the reluctance fluctuation of the salient rotor geometry, strong armature reaction together with localised saturation in iron, and the increased low-order spatial harmonics if the fractional-slot concentrated winding is employed [56, 57].

Therefore, in recent years, many researchers have focused on reduction of iron loss in IPM, including the research on improved modelling of iron loss, understanding the influence of the rotor and stator geometry, system-level design approach, and the trade-off between torque ripple reduction and iron loss reduction, etc.

Regarding the modelling of iron loss, J.K. Tangudu *et al* [58] proposed a lumped parameter magnetic circuit model considering nonlinearities in magnetic saturation, cross-coupling effects between the *d*- and *q*-axes, stator slotting effects, and localised effects of rotor bridges. P.H. Mellor *et al* [59] presented a simple and computationally efficient iron loss model which can cater for both rated flux and field weakening operation, based on two discrete time-stepped two-dimensional (2-D) magneto-static finite element field solutions under open-circuit and short-circuit operations. Thereby, the iron loss map across the entire machine working envelope can be generated by the interpolation among the previous analysis results according to the *d-q* voltage model.

In terms of the influence of the rotor and stator geometry, M. Barcaro *et al* [60] illustrated the effect of the rotor flux barrier geometry of an IPM motor on the stator iron losses and reduced the stator iron loss with an improved design of the rotor flux barrier angle. K. Yamazaki *et al* [61] introduced a slit into the rotor geometry, optimised the shape of magnets, slit and flux barrier to minimise the harmonics in the form of spatial derivatives of the air-gap flux density distribution in field weakening region, and finally obtained the minimum iron loss which is close to 50% of that of the conventional design, without dramatic reduction in peak torque. V. Zivotic-Kukolj *et al* [62] utilised flat stator teeth with opening slots to reduce the zigzag leakage flux which occurs when stator flux crosses the air-gap to the rotor and then returns to the stator without passing through the rotor flux barriers, and thereby decreased the iron loss by 21% with experimental verification.

With respect to the system-level design approach, S.H. Han *et al* [63] presented a "minimum-THD" method which minimises the THD of the spatial waveform of rotor MMF in order to reduce undesirable high order MMF harmonics for IPMs with distributed windings. Furthermore, they developed an analytical index for eddy current losses associated with harmonics for IPMs, designed the rotor MMF function to minimise the proposed analytical index, and synthesised the rotor geometry to realise the desirable rotor MMF function without comprising machine performance [64]. It has been shown that the eddy current loss in stator teeth of IPM with double magnet layers is much less than that of IPM with single magnet layer, since two-layer rotors concentrate the rotor MMF source energy in a narrow range of harmonics far better than one-layer rotors.

Furthermore, S.H. Han *et al* [65] found that the conditions to reduce iron loss in stator (dominated by eddy current losses associated with harmonics in stator teeth) at field weakening region conflicts with those to reduce torque ripple of IPMs. The IPM designs which exhibit better trade-off between these two aspects are found out. G. Pellegrino *et al* [66] also performed a trade-off between them when designing an IPM, and presented the criteria for selecting the best design compromise.

As has been noted, a large amount of research achievement concerning the reduction of iron loss in IPM has been made with great efforts of researchers via various methods. This has improved the operating performance at high speed and will continuously promote the application of IPM in EV traction.

1.3.6.1.3 PM Assisted Synchronous Reluctance Machine

As discussed in Section 1.3.5, the drawbacks of SynRM include poor power factor and low torque density. However, these drawbacks can be overcome by inserting permanent-magnets into the flux barriers to produce the alignment torque to "assist" the reluctance torque. Therefore, this machine topology is called Permanent-magnet Assisted Synchronous Reluctance Machine (PMA-

SynRM) [38], whose schematic of PMA-SynRM is shown in Fig. 1-11. The torque mechanism of PMA-SynRM includes both the alignment torque and reluctance torque. This mechanism is similar with conventional IPM, whereas the main difference is that the reluctance torque is dominated in PMA-SynRM while the alignment torque is the major torque component in IPM. The magnets inserted in the flux barriers are usually of low remanence, such as ferrites with B_r=~0.4T or bonded NdFeB with B_r=~0.56T.

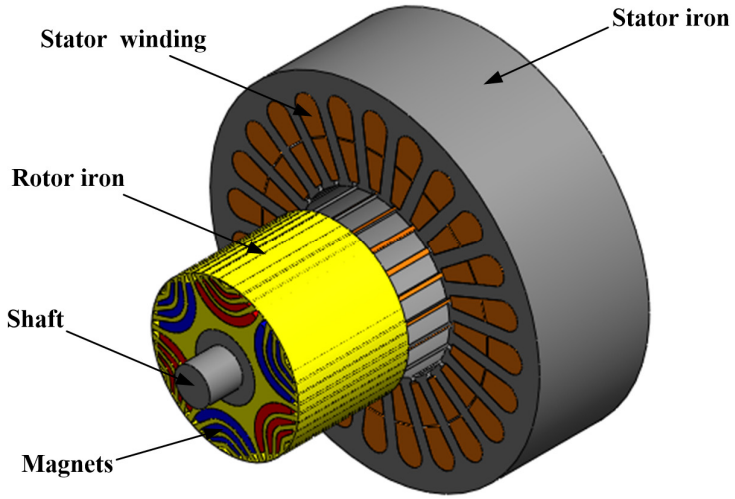

Fig. 1-11. Schematic of PM assisted synchronous reluctance machine.

To compensate the reduction in torque production contributed from permanent-magnets with low remanence, the saliency ratio of PMA-SynRM needs to be designed higher than that of IPM. Therefore, the rotor geometry design is vital for PMA-SynRM. S. Morimoto *et al* [67] designed a 100W PMA-SynRM with double layer U-shaped flux barriers and the ferrite magnets inserted in the middle of all the U shape layers. They demonstrated that this machine has a wider constant-power speed range, higher efficiency and higher power factor operation compared to SynRM. The constant-power speed range of the proposed PMA-SynRM can reach 1:5. H. Murakami *et al* [68] presented a 750W PMA-SynRM with four-layer arc-shaped flux barriers and the ferrite magnets embedded in the bottom layer. The rated efficiency of the developed PMA-SynRM achieves 94.4% which is almost the same as that of IPM, but the magnet usage is only 25% compared to IPM. S. Ooi *et al* [69]

proposed a 35kW PMA-SynRM with triple layer arc-shaped flux barriers and the ferrite magnets embedded in all the three layers. They achieved almost the same power density and the same constant-power range as those of the rare-earth IPM used in 2nd generation Toyota Prius 2003. The torque density at 20A/mm^2 is about 73% compared to that of IPM. The efficiency is more than 90% over a wide operating range and the maximum efficiency can be up to 97.2%.

Although the machine performances of PMA-SynRM can compete with conventional IPM, the low cost permanent-magnets used in PMA-SynRM are more vulnerable to the irreversible demagnetisation risks. This is because, on one hand the required current loading of this machine topology is high due to the low magnetic loading, and on the other hand the H-field at the knee point is low. Therefore, the demagnetisation risk needs to be carefully checked and overcome when designing a PMA-SynRM. H. Murakami *et al* [68] inserted the ferrite magnets into the deepest flux barrier layer of the rotor so as to avoid potential demagnetisation. The demagnetisation field is effectively obstructed by the multi-layer flux barriers, and thus the demagnetisation risks of ferrite magnets are dramatically reduced. It was shown that they can obtain the same demagnetisation characteristics as a conventional IPM. T. Tokuda *et al* [70] indicated that the anti-demagnetisation capability of PMA-SynRM can be improved by increasing the thickness of the magnets near the rotor surface. Moreover, they designed tapered flux barrier for the first layer to increase the localised permeability of rotor iron near magnet corners. Therefore, the magnetic field is guided to flow more in the rotor iron, and hence the irreversible demagnetisation risk of magnets is reduced. M. Paradkar *et al* [71] also reduced the width of flux barriers which do not contain magnets to address the irreversible demagnetisation problem. The principle is the same as tapering the flux barriers in [70]. They also revealed that the anti-demagnetisation capability of PMA-SynRM can be effectively improved by increasing the pole pair number in that the flux per pole will be reduced while the magnet thickness

can be kept constant. A. Vagati *et al* [72] formalised a set of design options which can improve the robustness against irreversible demagnetisation of PMA-SynRM. They concluded that the larger machines exhibit more demagnetisation risks than smaller ones. It was also shown that the short-circuit scenario is as serious as the maximum load conditions regarding the demagnetisation risk.

Given that the reluctance torque is the dominated torque component for a PMA-SynRM, the torque ripple will be relatively high. However, the approaches to reducing the torque ripple of SynRM can also be applied to PMA-SyRM. Hence, the literature review of this issue is not repeated here, and this part can refer to the torque ripple reduction methods of SynRM in section 1.3.5.

Compared to SynRM, PMA-SynRM improves the power factor and torque density, with slightly increases in the material cost, assembly cost and irreversible demagnetisation risk. Compared to IPM, the torque density and power factor of PMA-SynRM are not as high as those of IPM, whereas PMA-SynRM gains advantages on the material cost, fault tolerance capability (due to reduction in the back-EMF and short-circuit current), and the field weakening capability (since the permanent-magnet field of PMA-SynRM is weaker than that of IPM). Therefore, PMA-SynRM can be treated as a good candidate for the electrical machines in EV traction applications.

1.3.6.1.4 PM Claw Pole Machine

Conventional Claw Pole Machine (CCPM) is made up of an outer stator with silicon-steel laminations and three-phase windings, and an inner rotor with an iron-cored cylindrical exciting coil sandwiched between two claw pole halves as shown in Fig. 1-12 (a). The claw poles modulate the axially excited field into radial alternating field which interacts with the MMF of stator currents [73, 74] to produce torque.

Due to the low cost of the single field winding embraced by claw poles, CCPM has been employed in industrial applications for several decades, particularly for automobile alternators in a few kW power range. Besides, the power density of CCPM can be up to 3 times more than that of a conventional DC machine due to the fact that the 3-D transverse field in CCPM allows the machine pole pair number to be designed higher without compromising MMF per pole if leakage flux can be minimised.

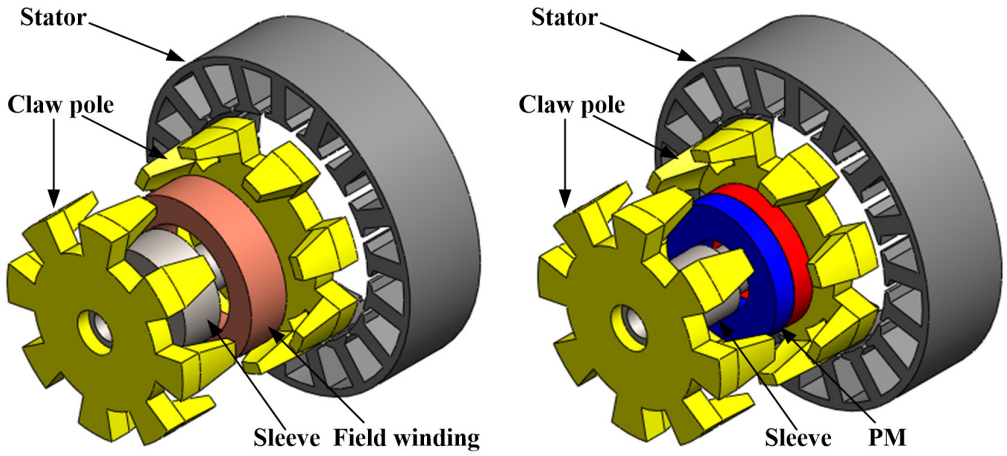

(a) (b)

Fig. 1-12. Schematic of claw pole machine. (a). Conventional claw pole machine, (b). PM claw pole machine.

However, brushes are indispensable in CCPMs for excitation of the field coil in the rotor, resulting in a low reliability and a high maintenance. Replacing the field windings with permanent-magnets can make CPM brushless, as illustrated in Fig. 1-12 (b), whereas the excessive eddy currents in solid steel claw poles limit the Permanent-magnet Claw Pole Machine (PMCPM) to very small size since it is considerably difficult to manufacture the claw poles with silicon-steel laminations due to their complex structures.

Fortunately, the Soft Magnetic Composite (SMC) material can provide a solution to this issue owing to their isotropic magnetic property (low conductivity in all 3 dimensions) which allows 3-D flux path design. Y.G. Guo *et al* [75] presented a PMCPM with SMC stator and outer PM rotor. Its stator consists of 3 stacks and each of them has 2 SMC claw poles, while the rotor is

of 3 sets of magnets, 2 end-plates and 1 steel case. The 3 claw pole stacks in stator are shifted by 120° in electrical degrees so as to form a balanced 3-phase system. However, no phase shift exists in the 3 sets of magnets. Furthermore, the modelling of the core loss, the modelling of thermal characteristics and the effect of armature reaction in PMCPM has been investigated in [76-79] taking into account the material characteristics of the SMC. F.G. Zhang *et al* [80] improved the claw pole shape of PMCPM to reduce back-EMF harmonics.

Another issue in the design of CPM is that long finite element analysis (FEA) computing time is required for the optimisation process of EV traction machines. S. Schulte *et al* [81] presented an analytical method for pre-determination of appropriate design parameters for a 6-phase CPM, followed by detailed numerical methods for the magnetic design. This method provides a time-saving alternative to solely FE calculation for both electrical and magnetic design and optimisation of electrical machines. Besides acceleration of computation, the combination of analytical and numerical methods allows for cross-verification of electromagnetic design results. Y.G. Guo *et al* [82] proposed an approach for accurate determination of major parameters of a 3-phase 3-stack PMCPM with a SMC stator core by FEA. Furthermore, they improved its phase variable model where a mathematical approach is applied to obtain the voltages of both energised and non-energised phases in [83].

1.3.6.1.5 Consequent Pole PM Machine

As shown in Fig. 1-13, Consequent Pole PM Machine (CPPMM) is of complex stator and rotor structures. The stator part includes two laminated stator iron stacks, a solid stator back-iron, armature windings, and a field winding located in between the two stator iron stacks. The rotor consists of radially magnetised PM poles, laminated iron poles, a laminated rotor iron which physically connects these two sets of poles, a solid rotor back-iron, and a shaft [84]. The solid stator and rotor back-irons are introduced to offer

flux paths in axial direction. The PM poles generate a magnetic field circulating from one N pole to the neighbouring S pole through laminated stator iron, solid stator back-iron, air-gap, laminated rotor iron and solid rotor back-iron. Meanwhile, the field winding fed by DC current produces another magnetic field circulating from one iron pole to its neighbouring one across the same flux path as that of PM magnetic field. These two magnetic fields are influenced by each other, and the net flux-linkage of the stator winding either add or subtract depending on the field current polarity [85].

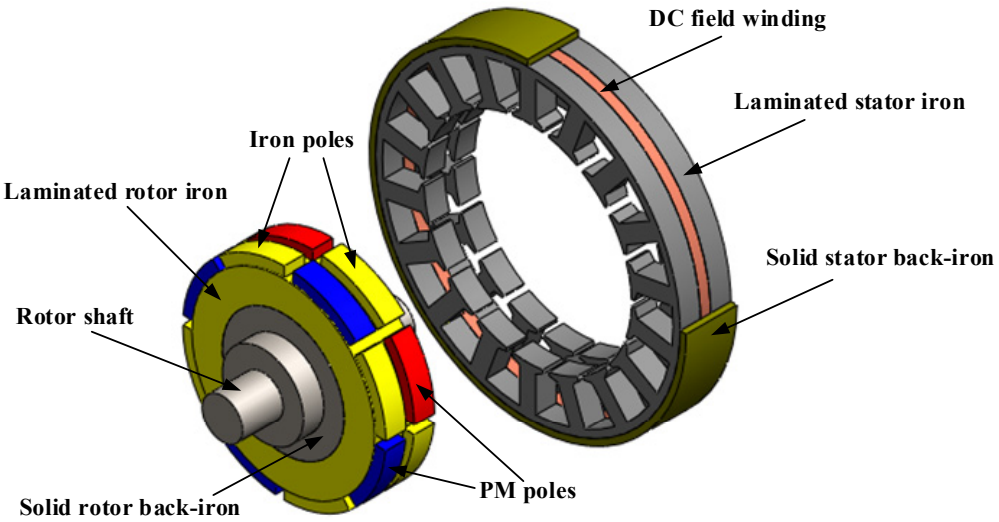

Fig. 1-13. Schematic of consequent pole PM machine.

Due to the independent control of the stator current and the excitation current, the constant-power operation can be maintained in a very wide speed range due to its flexibility in field control. Besides, no brushes or slip rings are required to implement this field control. Moreover, the demagnetisation risk is relatively low since the field control (either field weakening or field enhancing) is performed via iron poles [85].

However, the introduced field winding compromises the power density and volumetric efficiency. This is because the field winding competes the available space with the 3-phase stator winding and the air-gap surface associated with the field winding is not involved in the electro-mechanical

energy conversion. Furthermore, 3-D flux path design incurs additional losses and increases material usage since both the stator and rotor cores need radial, circumferential and axial flux conduction capability. Moreover, manufacturing cost also increases due to the complex structure.

1.3.6.2 Stator-PM Machine

Stator-PM machine has both magnets and armature windings on the stator, including Doubly Salient PM Machine (DSPMM), Flux Reversal Machine (FRM), Flux Switching PM Machine (FSPMM), and Flux Mnemonic PM Machine (FMPMM). It should be noted that the operation principle and electromagnetic performance of these machines are distinctly different, although they are all classified as stator-PM machines. The following sections will review the current state-of-the-art of these machine topologies.

1.3.6.2.1 Doubly Salient PM Machine

As illustrated in Fig. 1-14, Doubly Salient PM Machine (DSPMM) has a similar salient rotor with SRM but magnets in the stator which also exhibits a salient structure. The magnets are magnetised circumferentially in alternating polarity. The PM flux-linkage varies with rotor position linearly in a DSPMM, and thereby the induced back-EMF waveform is trapezoidal at no-load condition. Electromagnetic torque is produced by feeding a positive current when the PM flux-linkage increases whereas a negative current when the PM flux-linkage decreases. The generated torque is dominated by the permanent-magnet excited torque, and the resultant reluctance torque as well as cogging torque are negligible [86].

As most armature flux paths through the adjacent stator poles, not through PMs, the DSPMM is less sensitive to demagnetisation than conventional PM brushless machines. Besides, the corresponding rotor is similar to that of an SRM, hence, leading to a simple configuration and robust mechanical structure [87].

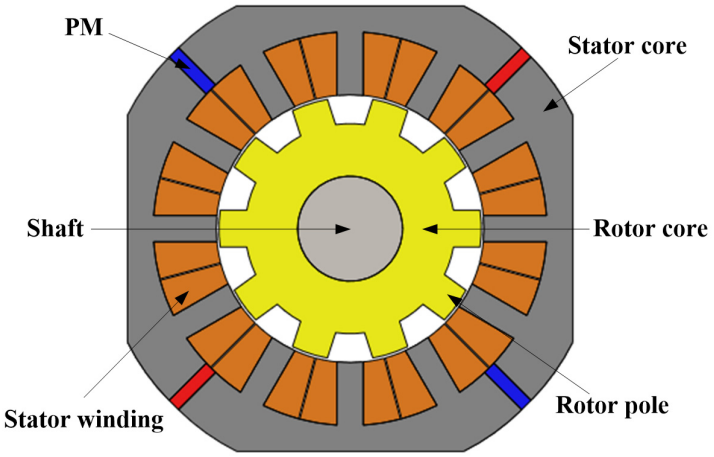

Fig. 1-14. Schematic of doubly salient PM machine.

However, the phase flux-linkage in a DSPM machine it is usually unipolar, resulting in low torque density due to reduced flux-linkage variation range. Although Y. Gong *et al* [88] arranged two reversed sets of coils in every phase to minimise the DC component in flux-linkage, the utilisation of PMs was penalised, resulting in a reduction in torque and power density.

1.3.6.2.2 Flux Reversal Machine

The Flux Reversal Machine (FRM) has PMs located on the surface of the stator teeth with two opposite polarities and employs concentrated windings and a similar salient rotor to SRM [89], as shown in Fig. 1-15. As the salient rotor rotates, the reluctance seen by the stator varies, and thus the PM flux-linkage changes. The polarity of this PM flux-linkage in one stator coil is determined by the rotor position (rotor tooth is closer to the corresponding N pole or S pole). Thus, a bipolar back-EMF is produced with stationary PMs by modulation effects of the salient rotor.

Therefore, the FRM also has the advantages such as simple and robust rotor construction with low inertia, fault-tolerance capability with its natural isolation between the phases in a multiphase configuration, small inductance variation with rotor position and current, and the high-speed capability due to nonrotating magnets [90].

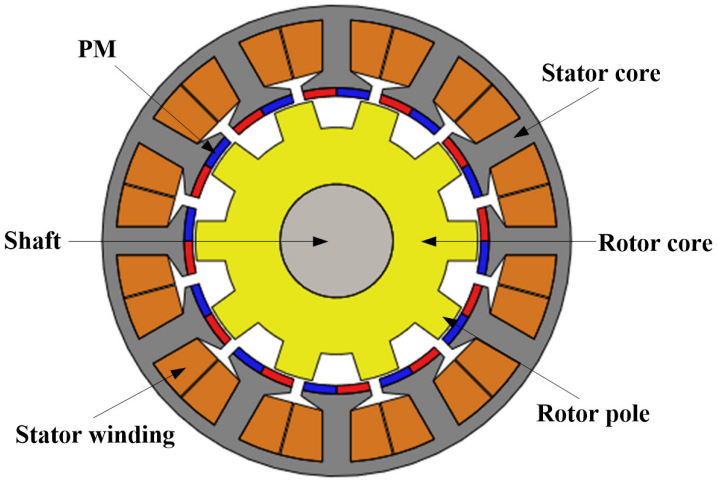

Fig. 1-15. Schematic of flux reversal machine.

However, there is notable flux leakage (fringing) through the teeth on which the magnets are mounted [91]. This flux leakage compromises the performance of the FRM and results in low power density, low torque density, low power factor (due to low back-EMF resulting from high leakage flux) and the poor magnet utilisation. To reduce its flux leakage, a concave-type stator pole and a rotor pole with a flux barrier were used in [92]. Since the magnets are exposed to the alternating armature reaction field directly, the induced-eddy current losses in the magnets and demagnetisation risk are high in this type of machine. These problems have been partly addressed in a new machine type, known as flux switching PM machine that will be discussed in the subsequent section.

1.3.6.2.3 Flux Switching PM Machine

Flux Switching PM Machine (FSPMM) has a similar salient rotor with SRM, but the stator consists of U-shape magnetic cores, PMs, and concentrated winding wound around stator tooth with one PM in the middle, as illustrated in Fig. 1-16. The magnets are magnetised circumferentially in alternating polarity, and the magnetic field is modulated by the relative position of rotating rotor teeth with respect to stationary stator teeth so that the induced flux-linkage by PMs varies periodically. Torque is produced

when the alternating currents are injected in the stator winding appropriately.

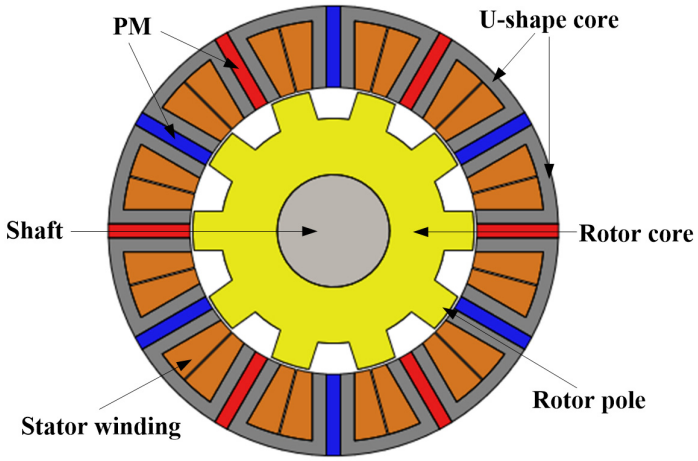

Fig. 1-16. Schematic of flux switching PM machine.

Compared to conventional Rotor-PM machines, placing both PMs and armature windings in the stator is favourable for cooling and is desirable for applications in which the machine ambient temperature is high. The armature reaction flux in a FSPMM flows mainly perpendicular to magnetisation directions of the magnets, and therefore the irreversible demagnetisation risk in PMs is low. This makes FSPMM particularly suitable for field weakening operation. Moreover, FSPMM has a short end-winding with the concentrated winding configuration.

However, owing to the doubly salient structure, high air-gap flux density, and high magnetic saturation in stator, the torque ripple of FSPMM is relatively high compared with other PM machines. To address this problem, W. Xu *et al* [93] devised 6 different combination for the stator pole number and rotor pole number and found that the machine with 6/7 and 12/14 stator and rotor pole number combinations yield low torque ripple, being1.49% and 3.1% respectively. Subsequently, a multi-objective optimisation was performed against the torque production, torque ripple, field weakening capability and efficiency. As a result, the torque ripple for the 6/7 combination and the 12/14 combination are 2.27% and 1.43% respectively. W.

Z. Fei *et al* [94] proposed 3 torque ripple reduction methods on the basis of 3 optimised designs with various rotor topologies, namely, “uniform”, “step skewed”, and “axial pairing”. Compared to the optimised “uniform” design, the “step skewed” counterpart can effectively mitigate both cogging torque and torque ripple. On the other hand, the proposed “axial paring” design can dramatically reduce the cogging torque whereas does not have considerable effects in torque ripple reduction. They reported that the torque ripple of FSPMM can be reduced to approximately 1.8% of rated torque in experiment.

Another issue of concern for FSPMM is extremely high iron loss at high speed, due to the high flux density in stator caused by magnetic saturation, and high order harmonics in the rotor since the air-gap field distributions are far from sinusoidal. Although the high level of saturation can be alleviated by using of ferrite instead of NdFeB, the torque density will drop dramatically due to low magnetic loading. W. Xu *et al* [95] proposed an Axially Laminated Flux Switching Permanent-magnet Machine (ALFSPMM) with the 12/14 stator and rotor pole number combination, which utilises a stator lamination in parallel with the direction of permanent-magnet flux-linkage to make full use of permanent-magnets and reduce relevant flux leakage and iron loss especially in high speed region. With the same PM size, the maximal flux density, 1.91T, occurs in edge of the stator tooth or the rotor pole in the ALSFSPMM, being slightly lower than 2.03T of the radial field FSPMM. They showed that the ALSFSPMM could reduce localised magnetic saturation in edges/tips of stator teeth and rotor poles at the expense of a more complex structure. Due to lower electromagnetic saturation and low iron loss especially in rotor, the rated torque of ALSFSPMM is near 4.1% higher than that of the radial field FSPMM.

In addition, the armature reaction field significantly affects the winding inductance due to the magnetic saturation. For example, the inductance in the FSPM machine is significantly reduced compared to rotor-PM counterpart, and the rotor positions for minimum and maximum

inductances are reversed. These will have adverse effects on the performance in field weakening operation at high speeds.

A fundamental problem with this machine topology is that the stator windings compete for space with the magnets. This compromises peak torque capability and torque density. Since the stator cores are separated by the magnets, the mechanical integrity of the machine is relatively poor and the manufacturing cost will be high.

1.3.6.2.4 Flux Mnemonic PM Machine

Flux Mnemonic PM Machine (FMPMM) was proposed via applying the memory machine concept to the doubly fed doubly salient PM machine. The stator of an FMPMM consists of an outer-layer stator where the armature windings are wound on teeth, and an inner-layer stator where both the PMs and field windings are located, as shown in Fig. 1-17 for an external rotor topology. The rotor structure is similar to an SRM rotor. The PM material used in this type of machine is online tuneable flux-mnemonic PMs, such as aluminium nickel cobalt AlNiCo alloy which can offer a high remanent flux density to enable high air-gap flux density and a low coercive force to enable online magnetisation and demagnetisation [96].

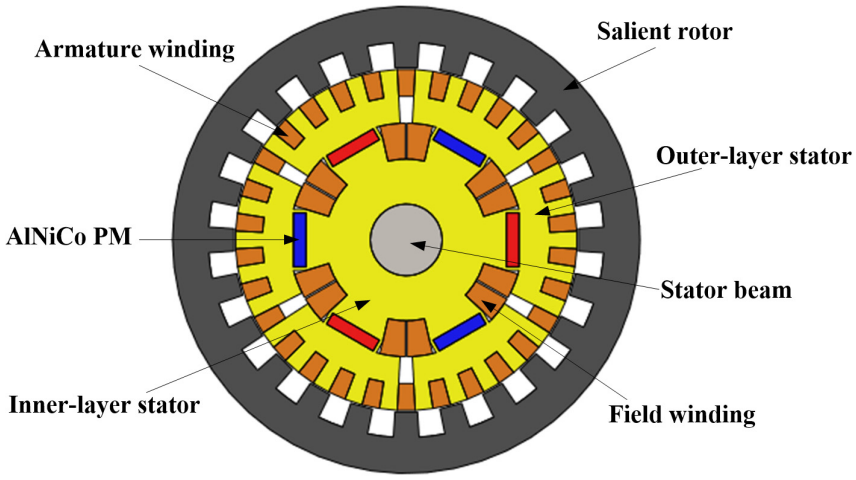

Fig. 1-17. Schematic of flux mnemonic PM machine.

FMPMM has inherited the advantages of both DSPMM and memory machines. The field control of FMPMM is extremely flexible due to the

presence of both the field windings and online tuneable flux-mnemonic PMs. Thus, a very wide constant-power operation range can be achieved. Besides, given that the PMs and the armature windings are located in different stator layers, the chance of irreversible demagnetisation due to armature reaction is very low [97]. Furthermore, FMPMM exhibits high fault tolerance capability when the fault scenario of short-circuit occurs. This is because its PMs can be demagnetised deliberately so as to reduce the short-circuit current [98].

However, the introduced field windings and also their corresponding inverter reduce the power density of the machine and drive system. Apart from that, the complex structure of FMPMM degrades the manufacturability and reliability. Moreover, extra costs are incurred by the manufacture, field windings and also their corresponding inverter.

1.4 Qualitative Comparison among Candidate Machine Technologies

To select the most competitive machine technologies for EV traction, the candidate machines discussed previously are compared in terms of a set of figure-of-merits, viz, torque and power density, torque ripple, efficiency, controllability, reliability, maturity, cost, manufacturability, and the fault tolerance. The comparison will be performed among the basic machine technologies in the following section.

1.4.1 Comparison among Basic Machine Topologies

On the basis of the operating principles shown in Table 1-1 and the essential components given in Table 1-2, the basic machine technologies can be compared with each other in the following aspects.

Table 1-2. Components Requirement in Basic Machine Technologies

Item	BDCM	IM	SM	SRM	SynRM	PMM
Brushes	Y	N	Y	N	N	N
Commutators	Y	N	N	N	N	N
Position sensor	N	N	N	Y	Y	Y
Permanent-magnets	Y/N	N	N	N	N	Y

(1) For the torque and power density, PMM is of great advantages against other options due to the effective and efficient generation of magnetic field by permanent-magnets. On the contrary, BDCM has to provide space for the brushes, commutators and field windings, hence having the lowest torque and power density. For SRM and SynRM, they can be designed to operate at relatively higher speed and thus have a higher power density ranking than that for torque density.

(2) In terms of the torque ripple, BDCM is among the best one due to the static magnetic field and the low level of saturation in magnetic circuit. On the other hand, with the sequential commutation of coils and the doubly salient geometric structure, SRM has the highest torque ripple even if additional reduction methods are employed.

(3) With respect to the efficiency, PMM inherently outperforms others in that the establishment and retention of magnetic field consumes no energy from the power supply. Copper loss will be incurred in order to generate magnetic field in other machine technologies where the BDCM is the worst one.

(4) When it comes to the controllability, the inherent decoupling between the armature current and the field current makes BDCM more preferable than others which have to employ vector control or field oriented control to obtain a relatively good dynamic response.

(5) Concerning the reliability, IM and SRM outweigh other machine technologies since both of them have a robust and simple rotor structure. Besides, SynRM possesses a high reliability in that its rotor has no magnets and windings. In contrast, the presence of the brushes

and commutators in BDCM leads to high maintenance cost and low reliability.

(6) Regarding to the maturity, BDCM, IM and SM are among the best ones with the mature production technologies for decades, whereas other machine technologies still have rooms for improvements.

(7) In the aspect of the cost, less components, low cost materials and established mass-production technologies turn IM into the best option. In contrast, PMM is expensive in both material and manufacture.

(8) From the perspective of manufacturability, SRM is the easiest to be manufactured due to its simple rotor structure. Conversely, the brittleness of the magnets results in a high possibility of being broken in process, and needs specifically designed jigs to handle the assembly and magnetisation processes.

(9) With regard to the fault tolerance, SRM is superior to other machine topologies owing to both the concentrated windings and their sequential excitations. Thus, a failure in one phase will not seriously affect the operation of other phases other than increase in torque ripple. Moreover, SynRM is a good option as well in that there are no magnets on rotor and thereby no induced voltage when inverter fails at high speed.

According to the above analysis, the appropriateness of each basic machine technology for EV traction can be summarised by figures of merits from 1 to 10, 10 being the best while 1 being the worst, as presented in Table 1-3. A similar approach was adopted in [4, 99, 100].

As can be seen from Table 1-3, PMM and IM are more competitive for EV traction relative to other machine technologies, which can also be concluded from the commercial applications of electrical machines for EVs where PMM and IM are dominant machine technologies among the options of automobile companies, as presented in Table 1-4.

Table 1-3. Qualitative Comparison among Basic Machine Technologies

Item	BDCM	IM	SM	SRM	SynRM	PMM
Torque density	5	7	8	7	8	10
Power density	5	7	8	8	9	10
Torque ripple	10	9	8	4	6	8
Efficiency	6	7	8	7	8	10
Controllability	10	7	8	7	8	8
Reliability	5	10	7	10	9	8
Maturity	10	10	10	7	7	8
Cost	7	10	8	7	8	6
Manufacturability	8	9	8	10	8	7
Fault tolerance	6	6	7	10	9	8
Total	72	82	80	77	80	83

Table 1-4. Commercial Applications of EV Electrical Machines

EV models	EV electrical machines
Fiat Panda Elettra	DC machine
Mazda Bongo	DC machine
Conceptor G-Van	DC machine
Tesla Roadster	Induction machine
Fiat Seicento Elettra	Induction machine
Ford Think City	Induction machine
GM EVI	Induction machine
Tesla Model S	Induction machine
Renault Zoe	Synchronous machine
Chloride Lucas	Switched reluctance machine
Hyundai Sonata	Surface-mounted permanent-magnet machine
Honda EV Plus	Interior permanent-magnet machine
Nissan Altra	Interior permanent-magnet machine
Toyota RAV4	Interior permanent-magnet machine
Nissan LEAF	Interior permanent-magnet machine
Volkswagen E-Up	Interior permanent-magnet machine
BMW i3	Interior permanent-magnet machine

In summary, in the competitive electrical machine technologies for EV traction, IM is potentially the lowest cost, and possesses the highest reliability and maturity as well. However, it has a lower torque density and inferior power factor and efficiency compared to PMM. Thereby, in general, PMM is preferred for EV traction applications where the energy efficiency and power density are the most important attributes.

1.4.2 Comparison among PM Machine Topologies

1.4.2.1 Rotor-PM Machine versus Stator-PM Machine

Without magnets and windings in rotor, Stator-PM machines have attracted increasing attention in the past decade owing to its robust rotor structure. Conceptually, Stator-PM machines employ the polarised reluctance principle, in which the torque and back-EMF are the resultant from the flux-switching action of rotor saliencies on a unipolar or bipolar flux produced by PMs in the stator, leading to a relatively simple and robust rotor structure which can withstand high-speed or intermittent operation with high acceleration.

Another advantage of the Stator-PM machine is that the temperature rise of the magnets resulting from eddy current loss is more easily managed since the magnets are on the stator. Moreover, the inherent non-overlapping concentrated armature windings employed in Stator-PM machine is conducive to the reduction of end-winding length and copper loss and also the enhancement of the fault tolerance, compared to the conventional Rotor-PM machines with overlapping windings.

However, to reverse the polarities of the flux-linkage in the stator windings as the rotor rotates, both the stator teeth and rotor poles in a Stator-PM machine are usually salient. Owing to this nature, stator-PM machines suffer from higher torque ripple and greater iron loss in high speed operation than traditional Rotor-PM machines.

Another disadvantage of the Stator-PM machine is that the magnets have to compete with copper windings for the stator space, resulting in lower torque density and lower peak overloading capacity. Further, the distortion of the flux density in the air-gap due to the doubly salient structure also has an adverse effect on the torque density owing to the high saturation level in stator but relatively low magnetic loading. Furthermore, the reluctance torque in this type of machine is negligible because of the inherent doubly

salient structure whereas Rotor-PM machine can utilise reluctance torque to improve the torque density and hence efficiency. This characteristic would ultimately penalise inverter VA rating if a maximum EMF limit has to be imposed for safety in the event of inverter failures.

On the basis of the above analysis, the appropriateness of the Stator-PM machine and Rotor-PM machine for EV traction can be evaluated by the figures of merits from 1 to 10, 10 being the best and 1 being the worst, as shown in Table 1-5.

Table 1-5. Qualitative Comparison between Stator-PM Machines and Rotor-PM Machines

Item	Stator-PM machine	Rotor-PM machine
Torque density	9	10
Power density	10	10
Torque ripple	6	8
Efficiency	9	10
Controllability	7	8
Reliability	9	8
Maturity	8	8
Cost	6	6
Manufacturability	6	7
Fault tolerance	9	8
Total	79	83

As seen from Table 1-5, although the Stator-PM machine is superior to the Rotor-PM counterpart in terms of the reliability and fault tolerance, the drawbacks on the relatively low peak torque density, high torque ripple, low efficiency and comparatively poor controllability of the Stator-PM machine hinders itself being considered as a better candidate for EV traction. Thereby, the following section will perform a comprehensive comparison among Rotor-PM machine topologies to select the appropriate one for EV application.

1.4.2.2 Comparison among Rotor-PM machines

Similarly, Rotor-PM machine topologies can be compared with each other in the following aspects.

(1) As for the torque density, SPM and IPM are among the best ones with the utilisation of high energy product magnets such as sintered NdFeB. Besides, PMCPM can also reach a very high torque density even if employing low energy product magnets such as ferrites or bonded NdFeB because its topology allows the pole pair number to be designed higher without compromising MMF per pole if leakage flux can be minimised. Nevertheless, PMA-SynRM is slightly inferior to the above three options in terms of torque density since it usually adopts ferrites or bonded NdFeB with low remanence. With a DC coil in stator, CPPMM has lower torque density compared to others.

(2) Regarding the power density, PMA-SynRM can compete with SPM and IPM in that the former can operate at higher speed than the latter two due to lower back-EMF in PMA-SynRM. With an additional field coil in stator, CPPMM has relatively high field weakening capability which allows it operates at relatively high speed. Therefore, CPPMM exhibits high power density, given that machine power density is proportional to its operation speed. However, due to the field coil in CPPMM occupies space in stator, its power density is considered to be slightly lower than those of SPM, IPM and PMA-SynRM. On account of the mechanical limitation of the SMC material used in the rotor of PMCPM, this type of machine cannot operate at high speed. Hence, PMCPM is of inferior power density than other rotor-PM machine technologies.

(3) In terms of the torque ripple, SPM is advantageous over other rotor-PM machine technologies in that its rotor structure is almost non-salient and the reluctance variation is both small and smooth.

(4) With respect to the efficiency, CPPMM is less efficient than others because of the extra copper loss due to DC coil whereas other machine technologies employ pure magnetic excitation.

(5) When it comes to the controllability, CPPMM is the best one among rotor-PM machine technologies, owing to the ability to adjust DC field

winding current. In contrast, IPM and PMA-SynRM need relatively complex and robust control due to their torque-current non-linearity which results from the presence of reluctance torque.

(6) Concerning the reliability, PMCPM is the worst due to the mechanical limitation of the SMC material used in its rotor. SPM and CPPMM are slightly less reliable than IPM and PMA-SynRM in that the former two may suffer from more demagnetisation risk. This is because rotor magnets in SPM and CPPMM exposed to air-gap whereas those in IPM and PMA-SynRM are embedded in rotor iron which can provide magnetic filtering effects.

(7) Regarding to the maturity, SPM and IPM belong to conventional PMM and have already been used widely in various applications, whereas others are relatively new and applied in limited applications, particularly for PMCPM and CPPMM.

(8) In the aspect of the cost, PMA-SynRM is the best option since it does not need a strong magnetic field and can still provide good performance even with ferrite or bonded NdFeB magnets. On the contrary, without reluctance torque, SPM uses the largest volume of high energy product magnets. Furthermore, the inverter cost for SPM is relatively high in that a high VA rating is needed to reconcile the conflicting requirements for high torque at low speeds and for low back-EMF at high speeds to guarantee safety in the event of inverter failure in SPMs. Therefore, SPM is less favourable than others regarding cost.

(9) From the perspective of manufacturability, IPM and PMA-SynRM are easier than SPM in that an SPM rotor usually needs to be protected from the centrifugal force by utilising a retaining sleeve (either stainless steel or non-metallic fibre). On the other hand, CPPMM has the most complicated structure in both rotor and stator, thereby being the most difficult to be manufactured.

(10) With regard to the fault tolerance, PMCPM and PMA-SynRM are among the best ones in that they have a relatively low flux level which will not induce high voltage even if the inverter fails at a high speed. In contrast, with the highest flux level, SPM is less fault tolerant than others. However, its fault tolerant capability can be improved by using concentrated windings which are isolated with each other.

According to the above analysis, the appropriateness of each Rotor-PM machine topology for EV traction can be evaluated by the figures of merits from 1 to 10, 10 being the best and 1 being the worst, as shown in Table 1-6.

Table 1-6. Qualitative Comparison among Rotor-PM Machine Technologies

Item	SPM	IPM	PMCPM	CPPMM	PMA-SynRM
Torque density	10	10	10	8	9
Power density	10	10	8	9	10
Torque ripple	9	8	7	7	7
Efficiency	10	10	10	8	10
Controllability	8	7	8	9	7
Reliability	8	9	7	8	9
Maturity	9	9	7	7	8
Cost	4	6	7	6	8
Manufacturability	6	7	6	5	7
Fault tolerance	7	8	9	8	9
Total	81	84	79	75	84

From Table 1-6, it can be seen that IPM and PMA-SynRM are the most competitive candidates for EV traction due to their high torque/power density, high efficiency, broad speed range, and acceptable cost. Moreover, SPM can also be considered, particularly for its fractional-slot and concentrated winding configuration for low speed applications, such as in-wheel motors.

In summary, based on the above qualitative comparison, IPM and PMA-SynRM are considered as the most appropriate machine topologies for the EV traction applications.

1.5 Outline of Thesis

The thesis will be mainly focused on developing potential PM machine topologies, design optimisation and advanced modelling techniques for the foregoing most viable machine candidates (i.e. IPM and PMA-SynRM). This thesis is structured as follows:

Chapter 1 performs comparative studies of electrical machine topologies and technologies for EV traction applications, including the current-state-of-art of candidate machine topologies and the qualitative comparison among prominent candidate machine topologies. The outline and major contribution of the thesis as well as a list of publications as a result of the studies are presented.

Chapter 2 investigates the impacts of vehicle dynamics on electrical machine design aspects. A vehicle dynamic state-space model is developed to investigate the influence of the tyre slip and torque split ratio on the machine sizing. An optimum control strategy for the torque split ratio with distributed tractions is developed to maximise the whole vehicle energy efficiency and thereby reduce the battery size and cost. The failsafe behaviour is also evaluated.

Chapter 3 proposes PMA-SynRMs with fractional-slot winding configurations. Three typical fractional-slot windings are considered, including concentrated non-overlapping (12-slot 10-pole), conventional non-overlapping (12-slot 8-pole), and the overlapping (18-slot 8-pole) windings. All of these three PMA-SynRMs are globally optimised against New European Driving Cycle (NEDC) efficiency with a semi-FE approach and subsequently compared quantitatively to evaluate their overall performance for EV traction applications. A new reluctance torque evaluation approach with the frozen permeability concept is presented to improve prediction accuracy of the reluctance torque ratio against the total torque.

Chapter 4 proposes a generic approach to reduction of MMF Harmonics in PM Machines with concentrated, multiple 3-phase windings. A general expression of MMF with respect to forward and backward harmonics is derived. Subsequently, the MMF harmonic cancellation principles using both time and space phase shifts are presented. Then, the multiple 3-phase winding configurations are devised to realise the MMF harmonic cancellation scheme. The proposed approach is validated via FEA and its application is also presented. Based on this proposed approach, a new 9-phase 18-slot 14-pole IPM machine is developed and designed. A global optimisation against NEDC driving cycle efficiency is performed and this is followed by more detailed analysis and evaluation of the electromagnetic performance, thermal behaviour, mechanical stress, and rotor-dynamics. A 10kW machine prototype has been built to validate the proposed design. The experimental tests include the no-load back-EMF tests, no-load loss tests, load tests in generating mode and thermal steady-state tests.

Chapter 5 establishes a high-fidelity and computationally efficient model for IPM machines, considering the magnetic saturation, spatial harmonics and iron loss effects. The predicted electromagnetic behaviour using the proposed model and the conventional IPM model are analysed and compared. The proposed model is validated by both FEA and experimental tests of a 10kW 36-slot 6-pole IPM machine. Furthermore, the temperature effects are incorporated in the electromagnetic model to form a high-fidelity and computationally efficient electro-thermally coupled IPM machine model. The electro-thermal behaviour of the machine under NEDC and Artemis urban driving cycles are evaluated and compared with and without considering temperature effects. The electro-thermally coupled model has also been validated by experimental results.

Chapter 6 presents a global optimisation technique incorporating mechanical stress constraints for high power, high speed and rare-earth free IPM machines. The mechanical stress model is built based on the maximum

von Mises stress results via FEA with rotor leading parameter variations. The effectiveness of the proposed mechanical stress model is validated by two design examples, including a 50kW 18-slot 16-pole 9-phase IPM machine with single layer V-shaped magnet arrangements and a 160kW 48-slot 8-pole 3-phase IPM machine with double layer V-shaped magnet arrangements.

Chapter 7 summarises the finding of the studied described in the thesis and points out the scopes of the further research.

1.6 Major Contributions of Thesis

The major contributions of this thesis include two aspects. The one is the proposed generic approach to reduction of MMF harmonics in permanent-magnet machines with concentrated, multiple 3-phase windings. The proposed winding configuration cancels out all the MMF sub-harmonics and some high order MMF harmonics. The reduction in MMF harmonics leads to a number of benefits. Firstly it reduces both stator and rotor iron losses, particularly at high speeds, and hence, prevents excessive rotor temperature. Furthermore it improves reluctance torque capability of IPM machines with concentrated windings, and machine efficiency. In addition, the technique also reduces torque ripple since the torque ripples associated with a specific set of harmonics may be cancelled in a multiple 3-phase machine. A 9-phase 18-slot 14-pole machine is devised based on the proposed generic MMF harmonic reduction technique. A 10kW machine prototype is built and tested for experimental validation. Compared to the MMF harmonic reduction techniques in literature, the proposed machine topology in this thesis retains the advantages of the concentrated windings and exhibits a high winding factor, low torque ripple, low manufacture cost, high torque density and the high efficiency over wide torque and speed ranges. The proposed MMF harmonics reduction technique is also applicable to other slot-pole combinations with concentrated windings except for those with slot number being equal to 1.5 times the pole number.

The other one is the proposed high-fidelity and computationally efficient machine model for IPMs. The model captures all significant effects associated with the electromagnetic behaviour of the machines, including magnetic saturation, spatial harmonics, iron loss effect and temperature effects, and has been validated by both FE analysis and experiments. The proposed model provides an accurate means of assessing the drive performance of an IPM machine. It has been shown that torque ripple may increase significantly in the field weakening region due to current waveform distortions resulting from the inverter voltage limit. It is important to capture these adverse effects in drive system simulations in order to develop a robust control for high efficiency operations in both constant-torque and field weakening regions. Furthermore, by taking into account of the temperature effects on both the *d*- and *q*-axis flux-linkages and the torque, the proposed machine model allows for accurate prediction of the electromagnetic behaviour at any feasible given temperature. This model is conducive to developing correct maximum torque per ampere control strategy for IPMs when temperature varies. Moreover, a high-fidelity and computationally efficient electro-thermally coupled model has been subsequently established by integrating the proposed temperature-dependent, high-fidelity electromagnetic model with a state-space lumped parameter thermal model. The proposed electro-thermally coupled model provides a useful platform to assess the temperature effect on electromagnetic behaviour of IPMs during design and over driving cycles.

1.7 List of Publications

Journal papers:

[J1] **X. Chen**, J. Wang, V. I. Patel and P. Lazari, "A Nine-Phase 18-Slot 14-Pole Interior Permanent-magnet Machine with Low Space Harmonics for Electric Vehicle Applications," *Energy Conversion, IEEE Transactions on*, in revision.

[J2] **X. Chen**; J. Wang and A. Griffo, "A High-Fidelity and Computationally Efficient Electro-thermally Coupled Model for Interior Permanent-magnet Machines in Electric Vehicle Traction Applications," *Transportation Electrification, IEEE Transactions on*, in press.

[J3] **X. Chen**; J. Wang; B. Sen; P. Lazari and T. Sun, "A High-Fidelity and Computationally Efficient Model for Interior Permanent-Magnet Machines Considering the Magnetic Saturation, Spatial Harmonics, and Iron Loss Effect," *Industrial Electronics, IEEE Transactions on*, vol.62, no.7, pp.4044,4055, July 2015.

[J4] **X. Chen**, J. Wang and V. I. Patel, "A Generic Approach to Reduction of Magnetomotive Force Harmonics in Permanent-Magnet Machines With Concentrated Multiple Three-Phase Windings," *Magnetics, IEEE Transactions on*, vol.50, no.11, pp.1,4, Nov. 2014.

[J5] T. Sun, J. Wang and **X. Chen**, "Maximum Torque Per Ampere (MTPA) Control for Interior Permanent Magnet Synchronous Machine Drives Based on Virtual Signal Injection," *Power Electronics, IEEE Transactions on*, vol.30, no.9, pp.5036,5045, Sept. 2015.

[J6] V. I. Patel, J. Wang, W. Wang and **X. Chen**, "Six-Phase Fractional-Slot-per-Pole-per-Phase Permanent-Magnet Machines With Low Space Harmonics for Electric Vehicle Application," *Industry Applications, IEEE Transactions on*, vol.50, no.4, pp.2554,2563, July-Aug. 2014.

[J7] P. Lazari, B. Sen, J. Wang and **X. Chen**, "Accurate d-q Axis Modeling of Synchronous Machines with Skew Accounting for Saturation," *Magnetics, IEEE Transactions on*, vol.50, no.11, pp.1,4, Nov. 2014.

[J8] T. Sun; J. Wang, M. Koc and **X. Chen**, "Self-Learning MTPA Control of Interior Permanent Magnet Synchronous Machine Drives Based on Virtual Signal Injection," *Industry Applications, IEEE Transactions on*, accepted.

Conference papers:

[C1] **X. Chen**, J. Wang, P. Lazari and L. Chen, "Permanent Magnet Assisted Synchronous Reluctance Machine with Fractional-slot Winding Configurations," *Electric Machines & Drives Conference (IEMDC), 2013 IEEE International*, pp.374,381, 12-15 May 2013.

[C2] **X. Chen**, J. Wang, V. I. Patel, P. Lazari, L. Chen and P. Lombard, "Reluctance Torque Evaluation for Interior Permanent Magnet Machines using Frozen Permeability," *Power Electronics, Machines and Drives (PEMD 2014), 7th IET International Conference on*, pp.1,6, 8-10 April 2014.

[C3] L. Chen, **X. Chen**, J. Wang and P. Lazari, "A Computationally Efficient Multi-physics Optimization Technique for Permanent Magnet Machines in Electric Vehicle Traction Applications," *Electric Machines & Drives Conference (IEMDC), 2015 IEEE International*, in press.

[C4] V. I. Patel, J. Wang, W. Wang and **X. Chen**, "Thermal Design and Analysis of 6-phase Fractional Slot Permanent Magnet Machines Considering Driving Cycles," *Power Electronics, Machines and Drives (PEMD 2014), 7th IET International Conference on*, pp.1,6, 8-10 April 2014.

[C5] P. Lazari, J. Wang, L. Chen and **X. Chen**, "Design Optimisation and Performance Evaluation of a Rare-earth-free Permanent Magnet Assisted Synchronous Reluctance Machine for Electric Vehicle Traction," *Power Electronics, Machines and Drives (PEMD 2014), 7th IET International Conference on*, pp.1,6, 8-10 April 2014.

[C6] L. Chen, J. Wang, P. Lazari and **X. Chen**, "Optimizations of a Permanent Magnet Machine Targeting Different Driving Cycles for Electric Vehicles," *Electric Machines & Drives Conference (IEMDC), 2013 IEEE International*, pp.855,862, 12-15 May 2013.

[C7] V. I. Patel, J. Wang; W. Wang and **X. Chen**, "Analysis and Design of 6-phase Fractional Slot per Pole per Phase Permanent Magnet Machines with

Low Space Harmonics," *Electric Machines & Drives Conference (IEMDC), 2013 IEEE International*, pp.386,393, 12-15 May 2013.

CHAPTER 2 Impacts of Vehicle Dynamics on Electrical Machine Design Aspects

2.1 Introduction

Electric vehicles with an electrical machine as a propulsion drive which is fed by batteries on board are increasingly commercialised by the automotive industries [101, 102]. It is of utmost importance to design the electrical machine satisfying all the operational requirements of a vehicle, and predict its fault behaviour. The specifications of an electrical machine for EV traction application are determined by the torque and the power requirements over a representative driving cycle together with other requirements such as acceleration and hill-climbing. Therefore, the first step in a machine design process is to calculate the torque and power requirements which are subject to the vehicle mass and acceleration profile. In [103], the rolling resistance force, climbing resistance force, and aerodynamic drag force were also taken into account as braking forces to determine the machine torque requirement. In [104, 105], another braking force component, the viscous friction force which is proportional to the vehicle speed, was introduced to improve the fluid force model which cannot be fully depicted by the aerodynamic drag force. However, the effect of the tyre slip is usually neglected as reported in the literature.

As an intrinsic character for tyres, the tyre slip is due to the tyre non-uniform deformation with the imposed torque [106]. The resultant speed difference between the tyre and the vehicle leads to the corresponding power loss. Therefore, the machine torque and power requirements need to be increased to compensate this power loss due to tyre slip [107]. The tyre-wheel model was established in [108], whereas no quantification has been performed to evaluate the influence of the tyre slip on the machine sizing, and overall performance of the powertrain system for EV tractions.

After calculating the required total torque and power, the powertrain topologies regarding the power distribution need to be determined, such as the number of electrical machines and also their individual power ratings. One of the selection criteria is their failsafe behaviour [109]. To perform the fault behaviour simulation, a four-wheel vehicle dynamic model with both longitudinal and lateral tyre-wheel models need to be established [110, 111]. The failsafe behaviour of an electric vehicle with the four-wheel independent drive was simulated in [112, 113]. However, the power distribution selection criteria of various powertrain topologies has not been investigated.

Based on the state-space method, this chapter improves already established vehicle dynamic model with a four-wheel drive by considering (a) the longitudinal and lateral motion of four wheels, (b) nonlinear relationship between the tyre force and the tyre slip ratio, and (c) the impact of the acceleration on the vertical load. Subsequently, the influence of the tyre slip on machine sizing is evaluated and quantified. Furthermore, according to the driver reaction time, the power distribution selection criteria of various powertrain topologies is determined based on their failsafe behaviour.

2.2 Conventional Method of Machine Sizing

In literature, the conventional method of machine sizing is to calculate the torque and power requirements without taking the tyre slip effect into account. Considering no climbing requirements, the braking forces of the conventional model in this section only include the rolling resistance force F_r and aerodynamic drag force F_{ae} which are given in (2.1) and (2.2) respectively. The specifications of the vehicle body, wheel and tyre, representing a small EV, are given in Table 2-1 and Table 2-2.

Table 2-1. Vehicle Body Specification

Parameters	Symbol	Unit	Value
Vehicle Mass	m	kg	800
Vehicle moment of inertia	I_v	kg·m^2	1350
Front axle length	d_1	m	1.48
Rear axle length	d_2	m	1.46
Distance between front axle and CG	l_1	m	1.2
Distance between rear axle and CG	l_2	m	1.4
Height of CG	H	m	0.5
Front area	A	m^2	0.7
Wind drag coefficient	C_d		0.5

Table 2-2. Wheel and Tyre Specification

Parameters	Symbol	Unit	Value
Tyre size			165/50 R15
Effective rolling radius of the tyre	r_e	m	0.273
Rolling resistance coefficient	C_r		0.007
Wheel and tyre moment of inertia	I_w	kg·m^2	1.118
Gear ratio	n		7
Efficiency of gear and differential	η		0.975

$$F_r = C_r mg \tag{2.1}$$

where the rolling resistance coefficient C_r and vehicle mass m can be found in Table 2-1 and Table 2-2, and the acceleration of gravity g=9.81m/s^2.

$$F_{ae} = \frac{1}{2}\rho C_d A u^2 \tag{2.2}$$

where the wind drag coefficient C_d and vehicle front area A can be found in Table 2-1 and Table 2-2, u is the vehicle longitudinal speed, and the air density ρ=1.225kg/m^3.

The driving force of the vehicle F_m is supplied by the electric machine, and this can be described in (2.3).

$$F_m = \begin{cases} n\eta \dfrac{T_m}{r_e}, driving \\ n\dfrac{T_m}{r_e \eta}, braking \end{cases} \tag{2.3}$$

where T_m is the machine output torque, the effective rolling radius of the tyre r_e, the gear ratio n and the efficiency of the gear and differential η can be found in Table 2-2. The F_m expression is subject to the vehicle operation condition in that the power flow is opposite in the driving and braking conditions while the gear and differential always consumes power.

According to Newton's second law of motion, the equation (2.4) can be derived.

$$F_m - F_r - F_{ae} = m\frac{du}{dt} \tag{2.4}$$

where u is the vehicle longitudinal speed, and t is time. The profile of the vehicle speed u in a New European Driving Cycle (NEDC) which contains 4 urban driving cycles (ECE 15) and 1 extra urban driving cycle (EUDC), is illustrated in Fig. 2-1 (a). The maximum vehicle speed is 120km/h.

According to (2.4), the required machine output torque can be calculated, as in (2.5).

$$T_m = \begin{cases} \dfrac{\left(m\dfrac{du}{dt} + C_r mg + \dfrac{1}{2}\rho C_d A u^2\right) r_e}{n\eta}, driving \\ \dfrac{\left(m\dfrac{du}{dt} + C_r mg + \dfrac{1}{2}\rho C_d A u^2\right) r_e \eta}{n}, braking \end{cases} \tag{2.5}$$

Based on the vehicle speed profile shown in Fig. 2-1 (a) and also the torque expression given by (2.5), the required machine output torque can be obtained, as shown in Fig. 2-1 (b). Furthermore, the total required torque and power for the electrical machine with respect to the vehicle speed are given in Fig. 2-1 (c) and (d). The peak torque and peak power are 59.44Nm and 21.17kW respectively.

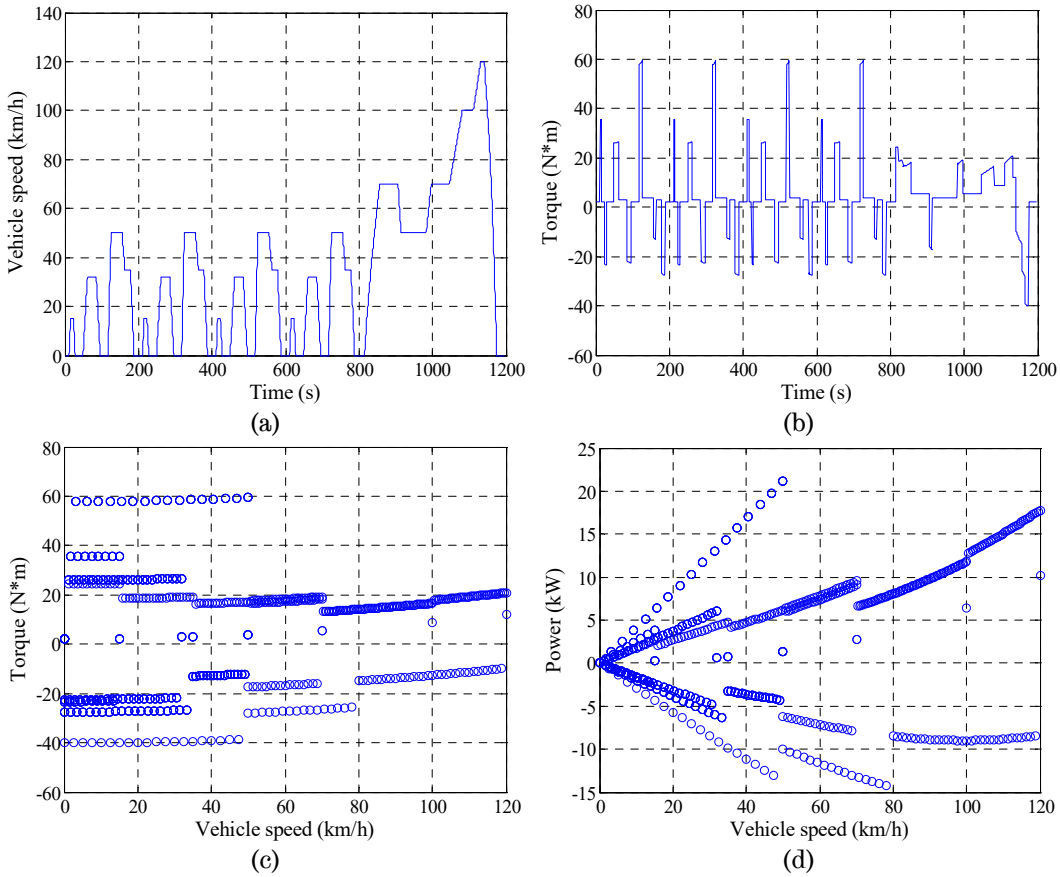

Fig. 2-1. Theoretical calculation results in a whole NEDC cycle. (a) Vehicle speed versus time. (b) Total electrical machine torque versus time. (c) Total electrical machine torque versus vehicle speed. (d) Required electrical machine power versus vehicle speed.

2.3 Tyre Characteristic

In a vehicle, tyres convert the torque supplied by wheels into the driving or braking force to accelerate or decelerate the vehicle. With an imposed torque from a wheel, a tyre exhibits a non-uniform deformation, resulting in the speed slip between the vehicle and the wheel. This phenomenon is the so-called "tyre slip" [106].

To describe the tyre slip, a practical slip ratio k is introduced, as shown in (2.6).

$$k = \begin{cases} \dfrac{r_e\Omega - V\cos\theta}{r_e\Omega}, driving \\ \dfrac{V\cos\theta - r_e\Omega}{V\cos\theta}, braking \end{cases} \tag{2.6}$$

where, Ω is the wheel angular speed, V is the magnitude of the vehicle speed and θ is the tyre slip angle which is defined as the angle between the vehicle speed direction (tyre movement direction) and the tyre longitudinal direction, as shown in Fig. 2-2.

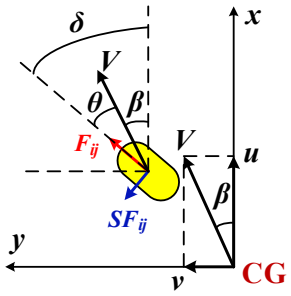

Fig. 2-2. Quantities of a tyre model in the vehicle body coordinate system.

The vehicle speed V can be calculated by (2.7).

$$V = \sqrt{u^2 + v^2} \tag{2.7}$$

where u is the vehicle speed in the x direction (vehicle longitudinal direction) while v is the vehicle speed in the y direction (vehicle lateral direction).

With the tyre slip expressed by (2.6), the driving force applied to the ground will be produced. This driving force is a complex function with respect to the tyre slip [114]. A widely used semi-empirical tyre model is based on the so-called Magic Formula in which the tyre slip is modelled from a physical view point while the empirical coefficients are also employed [115]. The tyre driving forces include both the longitudinal and lateral components. The longitudinal tyre force F_{ij} can be expressed as (2.8). The subscript ij denotes the tyre (wheel) number with 4 combinations: 11, 12, 21 and 22, corresponding to the front left, front right, rear left and rear right tyre (wheel), respectively.

$$F_{ij} = \mu_x(\sigma_{xij}) F_{zij} \tag{2.8}$$

where F_{zij} is the tyre vertical load and $\mu_x(\sigma_{xij})$ is the equivalent longitudinal adhesive coefficient which is expressed by (2.9).

$$\mu_x(\sigma_{xij}) = \sin\left\{C_x \arctan\left[B_x\sigma_{xij} - E_x\left(B_x\sigma_{xij} - \arctan B_x\sigma_{xij}\right)\right]\right\} \cdot D_{xij} \tag{2.9}$$

where B_x, C_x, E_x are longitudinal stiffness factor, shape factor and curvature factor of the tyre respectively, D_{xij} is expressed by (2.10), σ_{xij} is the theoretical longitudinal slip ratio defined in (2.11).

$$D_{xij} = \begin{cases} \dfrac{-|\sigma_{xij}|\mu}{\sqrt{\sigma_{xij}^{\ 2} + \sigma_{yij}^{\ 2}}}, driving \\ \dfrac{|\sigma_{xij}|\mu}{\sqrt{\sigma_{xij}^{\ 2} + \sigma_{yij}^{\ 2}}}, braking \end{cases} \tag{2.10}$$

where μ is the kinetic friction coefficient between the tyre and the road surface and σ_{yij} is the theoretical lateral slip ratio defined in (2.12).

$$\sigma_{xij} = \frac{k_{ij}}{1 + k_{ij}} \tag{2.11}$$

$$\sigma_{yij} = \frac{\tan\theta_{ij}}{1 + k_{ij}} \tag{2.12}$$

The lateral tyre force SF_{ij} can be expressed as (2.13).

$$SF_{ij} = \mu_y(\sigma_{yij}) F_{zij} \tag{2.13}$$

where $\mu_y(\sigma_{yij})$ is the equivalent lateral adhesive coefficient which is expressed by (2.14).

$$\mu_y(\sigma_{yij}) = \sin\left\{C_y \arctan\left[B_y\sigma_{yij} - E_y\left(B_y\sigma_{yij} - \arctan B_y\sigma_{yij}\right)\right]\right\} \cdot D_{yij} \tag{2.14}$$

where B_y, C_y, E_y are lateral stiffness factor, shape factor and curvature factor of the tyre respectively, and D_{yij} can be expressed by (2.15).

$$D_{yij} = \frac{|\sigma_{yij}|\mu}{\sqrt{\sigma_{xij}^{\ 2} + \sigma_{yij}^{\ 2}}} \tag{2.15}$$

The empirical coefficients for the tyre 165/50 R15, such as B_x, C_x, E_x, B_y, C_y, E_y and μ are listed in Table 2-3 [106].

Table 2-3. Tyre Model Coefficients

Parameters	Symbol	Value
Kinetic friction coefficient	μ	0.9
Longitudinal stiffness factor	B_x	11
Longitudinal shape factor	C_x	1.55
Longitudinal curvature factor	E_x	0.2
Lateral stiffness factor	B_y	8.0
Lateral shape factor	C_y	1.3
Lateral curvature factor	E_y	-0.2

The relationships between the tyre equivalent adhesive coefficients and the theoretical longitudinal slip ratio at various tyre slip angles, $\mu_x(\sigma_{xij})$ and $\mu_y(\sigma_{xij})$, are shown in Fig. 2-3 (a) and (b) respectively. The relationship between $\mu_y(\sigma_{xij})$ and $\mu_x(\sigma_{xij})$ is illustrated in Fig. 2-4. It can be seen that relationship between the tyre force and tyre slip exhibits a strong nonlinearity. The linearity region of $\mu_x(\sigma_{xij})$ is approximately $\sigma_{xij}\in[0, 0.1]$. It should be noted that although the characteristic curves in Fig. 2-4 are not smooth when $\mu_x=0$, their trends coincide with those of a practical tyre.

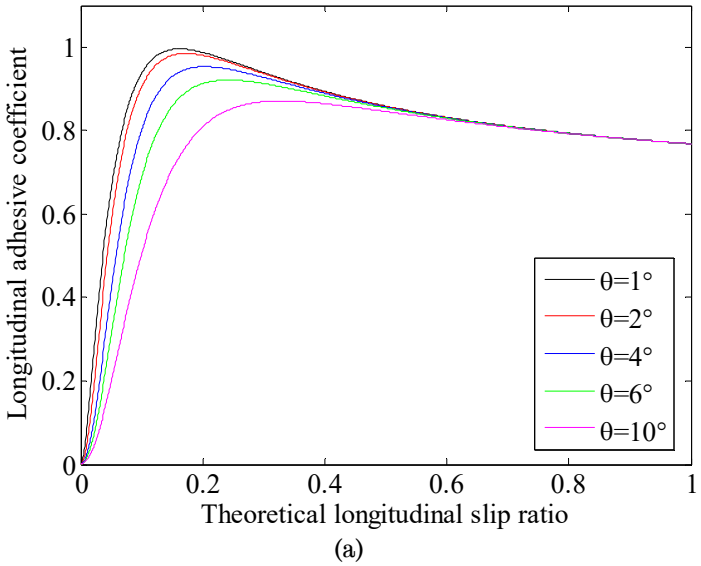

(a)

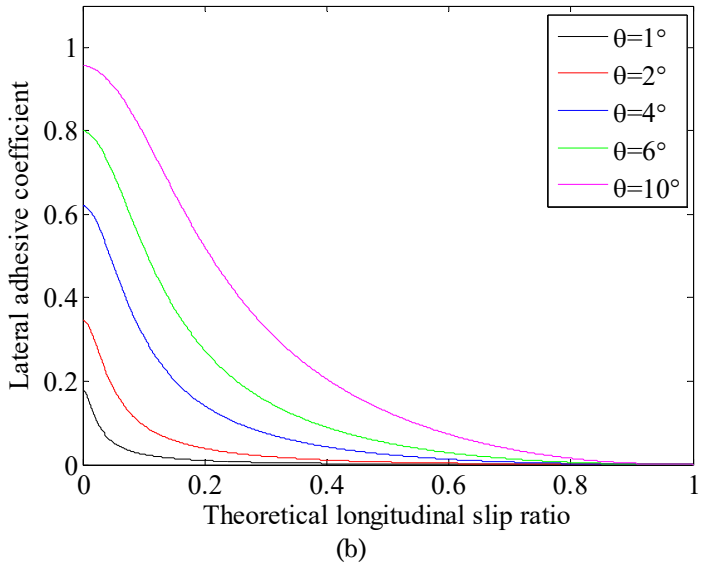

(b)

Fig. 2-3. Relationships between the tyre equivalent adhesive coefficients and the theoretical longitudinal slip ratio at various tyre slip angles. (a) Longitudinal adhesive coefficient. (b) Lateral adhesive coefficient.

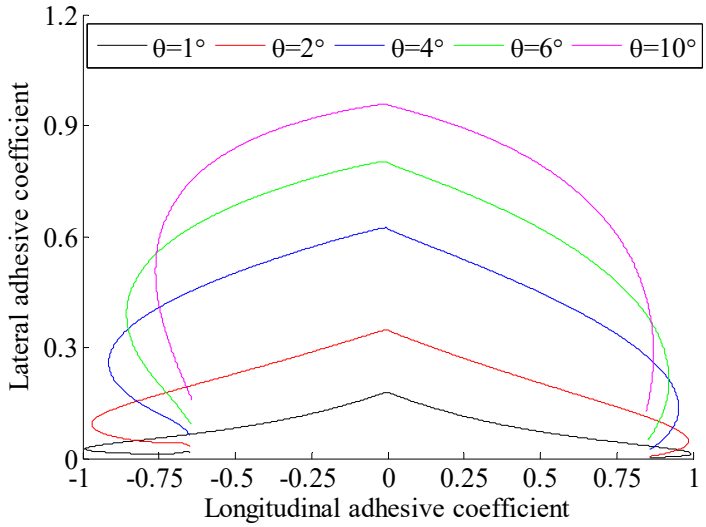

Fig. 2-4. Relationship between the equivalent longitudinal and lateral adhesive coefficients at various tyre slip angles.

2.4 Four-wheel Vehicle Dynamics State-space Model

The four-wheel vehicle model consists of a vehicle body model, a wheel model and a tyre model. The latter two can be combined together for manual simplification. To establish the vehicle body model, two coordinate systems (X, Y) and (x, y) are introduced. (X, Y) is the static global coordinate system

while (x, y) is vehicle body coordinate system whose centre is located at the vehicle gravity centre, as shown in Fig. 2-5.

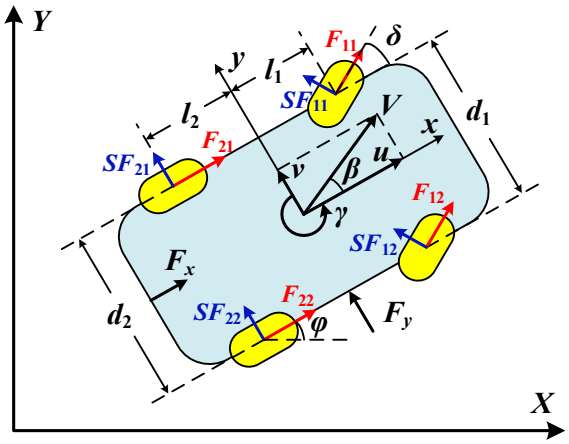

Fig. 2-5. Quantities in the global coordinate system (X, Y) and the vehicle body coordinate system (x, y).

2.4.1 Vehicle Body Model

The function of the vehicle body model is to determine the vehicle locus according to the driving force supplied by 4 wheels and the steer angle governed by the driver. The vehicle speed and the acceleration are treated as the intermediate variables.

According to Newton's second law of motion, the relationship between the acceleration and the driving force can be described by (2.16)-(2.18).

$$m\alpha_x = \sum_{j=1}^{2} F_{1j}\cos\delta + \sum_{j=1}^{2} F_{2j} - \sum_{j=1}^{2} SF_{1j}\sin\delta - \frac{1}{2}\rho A C_d u^2 \operatorname{sgn}(u) \tag{2.16}$$

$$m\alpha_y = \sum_{j=1}^{2} F_{1j}\sin\delta + \sum_{j=1}^{2} SF_{1j}\cos\delta + \sum_{j=1}^{2} SF_{2j} \tag{2.17}$$

$$\begin{aligned} I\dot{\gamma} = {} & \sum_{j=1}^{2} l_1 F_{1j}\sin\delta + \sum_{j=1}^{2} l_1 SF_{1j}\cos\delta - \sum_{j=1}^{2} l_2 SF_{2j} + \frac{d_1}{2}\cos\delta\left(F_{12} - F_{11}\right) \\ & + \frac{d_1}{2}\sin\delta\left(SF_{11} - SF_{12}\right) + \frac{d_2}{2}\left(F_{22} - F_{21}\right) \end{aligned} \tag{2.18}$$

where δ is the steering angle, α_x and α_y are the acceleration in the x and y directions, γ is the yaw rate, I is the vehicle moment of inertia, d_1 and d_2 are the front and rear axle length, and l_1 and l_2 are the distance between the centre of gravity and the front and rear axle. These parameters are illustrated in Fig. 2-5.

The vehicle speed can be determined by the acceleration calculated by (2.16)-(2.18), as expressed in (2.19).

$$\begin{aligned} \dot{u} &= \alpha_x + v\gamma \\ \dot{v} &= \alpha_y - u\gamma \end{aligned} \tag{2.19}$$

The vehicle locus can subsequently be calculated from (2.20).

$$\begin{aligned} \dot{\varphi} &= \gamma \\ \dot{X} &= u\cos\varphi - v\sin\varphi \\ \dot{Y} &= u\sin\varphi + v\cos\varphi \end{aligned} \tag{2.20}$$

where X and Y denote the location of the vehicle centre in the X-Y coordinate system, and φ represents the angle between the x axis and X axis.

To calculate the tyre force F_{ij} and SF_{ij}, given by (2.8) and (2.13), the vertical load and tyre slip angle need to be solved in the vehicle body model, and the results are given in (2.21) and (2.22).

$$F_{zij} = \frac{mgl_{2/i}}{l_1 + l_2} + \frac{(-1)^i m\alpha_x H}{l_1 + l_2} + \frac{(-1)^j m\alpha_y H}{(d_1 + d_2)} \tag{2.21}$$

where i=1,2, j=1,2.

$$\theta_{ij} = \delta_{ij} - \beta \tag{2.22}$$

δ_{2j}=0 since the steering angle only applies to the front wheels, and β is the body slip angle which can be calculated by (2.23).

$$\beta = \begin{cases} \arctan\frac{v}{u}, u > 0 \\ \pi + \arctan\frac{v}{u}, u < 0 \end{cases} \tag{2.23}$$

2.4.2 Wheel-tyre Model

The wheel-tyre model is used to calculate the driving force which will be applied to the vehicle body model, according to the torque from the axle, the vertical load in each wheel, the tyre slip angle and the vehicle speed.

The motion of each wheel can be determined by (2.24).

$$\dot{\Omega} = \frac{1}{I_w}\left(T_{in} - r_e F_{ij} - r_e F_{rij}\right) \tag{2.24}$$

where the calculation of tyre longitudinal force F_{ij} has been described in the tyre model in section 2.3, T_{in} is the input torque from the axle, I_w is the total moment of inertia of the wheel and tyre, and F_{rij} is the rolling resistance which can be calculated via (2.25).

$$F_{rij} = C_r F_{zij} \tag{2.25}$$

2.5 SIMULINK Model

2.5.1 Model Description

The foregoing equations in section 2.3 and section 2.4 can be solved via a state-space method in MATLAB/SIMULINK environment [116]. The wheel-tyre model and vehicle body model are implemented in the form S-functions. The schematic of the four-wheel vehicle dynamic model in SIMULINK is illustrated in Fig. 2-6.

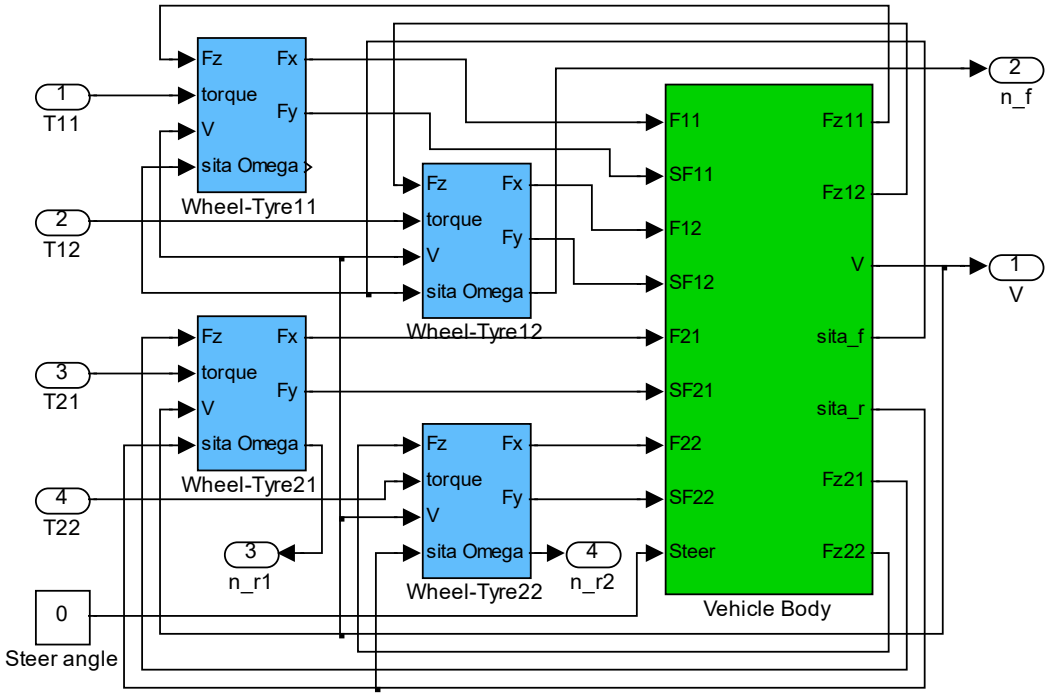

Fig. 2-6. Schematic of the four-wheel vehicle model.

2.5.2 Algebraic Loop

The dynamic equations of the motor, gear box, axle and wheel are coupled together, resulting in an algebraic loop for determination of wheel or rotor speed. Since SIMULINK employs ordinary differential equation (ODE) based solvers, the solution of the algebraic loop is dealt iteratively and results in significant increase in simulation time.

To avoid the algebraic loop, the explicit differential equations for both driving and braking are derived via simplifying these equations manually, as in (2.26) and (2.28), respectively.

$$\dot{\Omega}=\frac{1}{I_e}\left(T_{in}\eta-r_eF_{ij}-r_eF_{rij}\right) \tag{2.26}$$

where I_e is the equivalent moment of inertia for the rotor system seen from the wheel when driving and is given by (2.27).

$$I_e=I_w+\frac{n^2\eta I_m}{q} \tag{2.27}$$

where I_m is the moment of inertia for the electrical machine and q represents the number of wheels that a motor drives, equal to 1 or 2. During braking, the wheel acceleration is governed by (2.28).

$$\dot{\Omega} = \frac{1}{I_e}\left(\frac{T_{in}}{\eta} - r_e F_{ij} - r_e F_{rij}\right) \tag{2.28}$$

where I_e is the equivalent moment of inertia for the rotor system seen from the wheel when braking, given in (2.29).

$$I_e = I_w + \frac{n^2 I_m}{\eta q} \tag{2.29}$$

2.6 Model Verification

At a given total torque, the vehicle dynamic model should have a unique steady-state speed no matter how the torque is distributed in the front and rear wheels (assuming the torque is symmetrically distributed in left and right wheels).

To verify the vehicle model, the total input torque is fixed to be 80N·m, with 3 different torque split ratio, 1:3, 1:1 and 3:1, and the resultant vehicle speed curves are compared in Fig. 2-7. It can be seen that all the three curves superpose each other and have the same steady-state speed 116.92km/h.

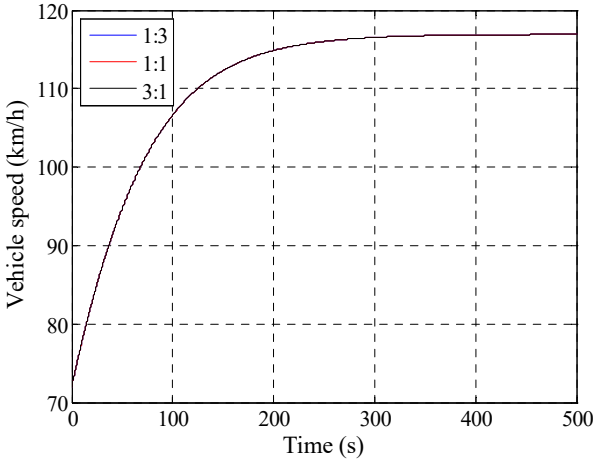

Fig. 2-7. Vehicle speed curves with different torque split ratio.

Furthermore, the vehicle model can also be verified by the theoretical analysis. Using the vehicle motion equation in the steady-state shown in (2.30), the theoretical steady-state speed is 32.48m/s (i.e. 116.94km/h), slightly higher than the simulation result 116.92km/h. This is because theoretical equation of (2.30) does not consider the nonlinear tyre slip which leads to a portion of power loss. This effect is however fully accounted in the vehicle dynamic model in the SIMULINK environment.

$$\frac{T_{total}\eta}{r_e}-\frac{1}{2}\rho A C_d u^2 - C_r mg = 0 \tag{2.30}$$

Therefore, it is reasonable to justify that the simulation result coincides with theoretical analysis, which also supports the verification of the vehicle dynamic model.

2.7 Influence of Tyre Slip on Machine Sizing

In this section, the machine size will be determined by the vehicle dynamic model shown in Fig. 2-6 which accounts the tyre slip effect. To reduce simulation time, only 1 ECE 15 cycle and 1 EUDC cycle are considered in the following simulation. Assuming that the front wheels are driven by a traction motor via a differential while the rear wheels are passive (concentrated powertrain topology), the resultant vehicle speed and machine torque are shown in Fig. 2-8 (a) and (b), respectively. The traction motor output power is calculated by the product of its speed and torque, as shown in Fig. 2-8 (c) and (d). It can be seen that the peak power is 23.19kW, 9.5% higher than that, 21.17kW, predicted by the conventional method when the effect of tyre slip is neglected. Therefore, the influence of the tyre slip on machine sizing is not negligible.

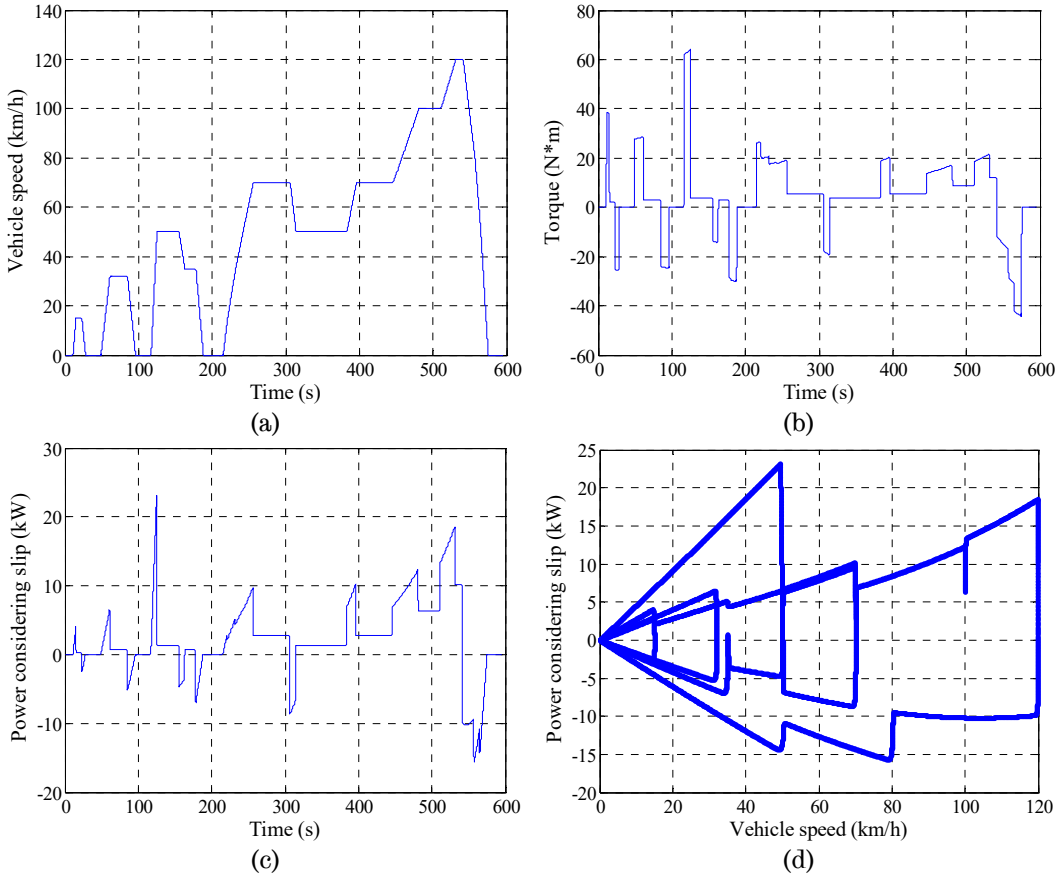

Fig. 2-8. Electrical machine output power considering tyre slip. (a) Vehicle speed versus time. (b) Total electrical machine torque versus time. (c) Electrical machine output power versus time. (d) Electrical machine output power versus vehicle speed.

If the vehicle is driven by 2 traction machines (distributed powertrain topology), one coupled to the front axle and the other to the rear via two differentials, the similar machine sizing simulation can also be performed. In this case, the peak total output power of the electrical machines is 22.97kW, 1% lower than that of the powertrain topology with a single machine (concentrated powertrain topology). Therefore, compared to the concentrated powertrain topology, the distributed one can reduce the extra power loss induced by the tyre slip, and thereby save the power supplied by the electrical machines and also improve the efficiency of the whole system.

The foregoing simulation result also indicates that the torque split ratio between the front and rear wheels can affect both the machine size and the

system efficiency by influencing the tyre slip. This will be investigated in the following section.

2.8 Influence of Torque Split Ratio

2.8.1 Influence of Torque Split Ratio on Machine Sizing

The torque split ratio is defined as the ratio of the front machine torque with respect to the total torque. By varying the torque split ratio, the total power of the front and rear electrical machines is calculated as depicted in Fig. 2-9. The interpolation data is obtained via cubic spline method to predict the required minimum peak power. The optimum ratio for the rating power of the front motor and rear motor is 51.6%:48.4%, where the total peak power required can reach its minimum 22.972kW.

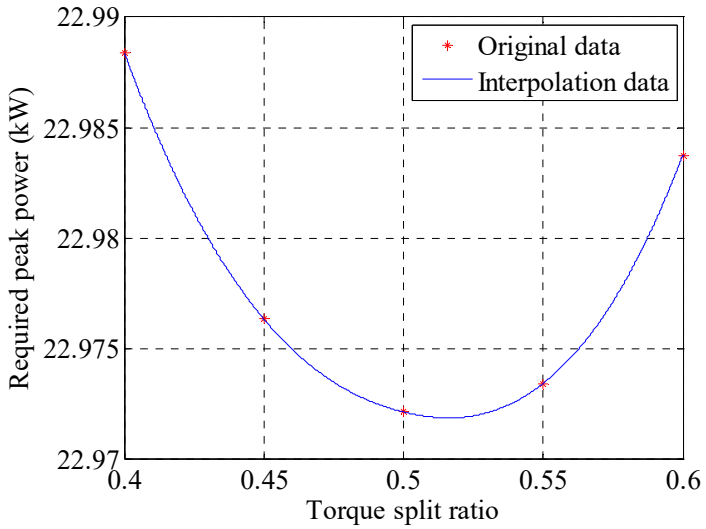

Fig. 2-9. Relationship between the required total power required and the torque split ratio.

The existence of the optimum torque split ratio is fundamentally due to the non-linearity in the tyre characteristic, i.e. the non-linear relationship between the tyre force and tyre slip. An optimum torque split ratio is approached when the total loss caused by the slip in both front and rear tyres reaches its minimum.

It should be noted that the optimum ratio always exists to minimise the total size of electrical machines albeit the influence of the torque split ratio on the power rating is quite small. Furthermore, after sizing the front and rear machines, the optimum control for the torque split ratio can also be realised. This will be discussed in the following section.

2.8.2 Optimum Control of Torque Split Ratio

2.8.2.1 Influence of Vehicle Acceleration on Optimum Torque Split Ratio

According to (2.21), the vertical load on front and rear tyres is subject to the location of the centre of gravity which varies with vehicle acceleration. Therefore, the optimum torque split ratio will be affected by the vehicle acceleration in that the tyre vertical load influences tyre slip. The relationship between the optimum torque split ratio and the vehicle acceleration is illustrated in Fig. 2-10.

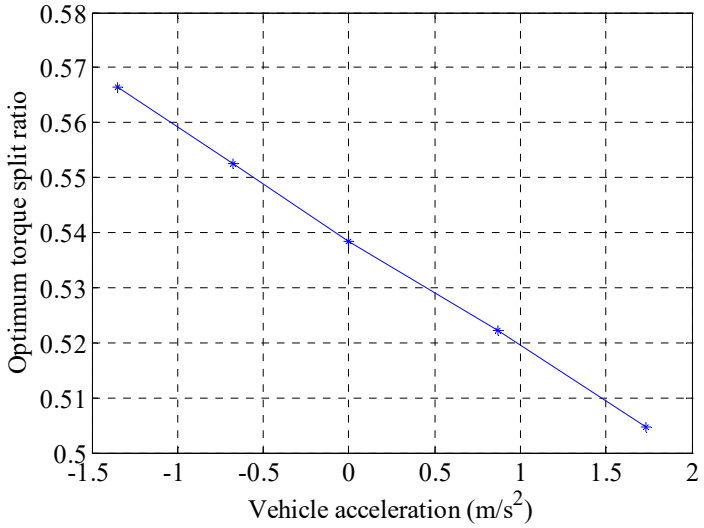

Fig. 2-10. Optimum torque split ratio versus vehicle acceleration.

It can be seen that the optimum torque split ratio is inversely proportional to the vehicle acceleration. Thereby, a linear equation can be employed to approximately describe the relationship between the optimum torque split ratio and the vehicle acceleration as given in (2.31).

$$K_T = \frac{l_2}{l_1 + l_2} - k_s a_x \tag{2.31}$$

where K_T is the optimum torque split ratio and k_s is the average slope of the optimum toque split ratio with respect to vehicle acceleration, which can be derived from Fig. 2-10, i.e. -0.0195s^2/m.

2.8.2.2 Influence of Speed on Optimum Torque Split Ratio

The influence of vehicle speed on optimum torque split ratio is also investigated. At a given vehicle acceleration, the relationship between the optimum torque split ratio and the vehicle speed is shown in Fig. 2-11 with a same scale for vertical axis in Fig. 2-10.

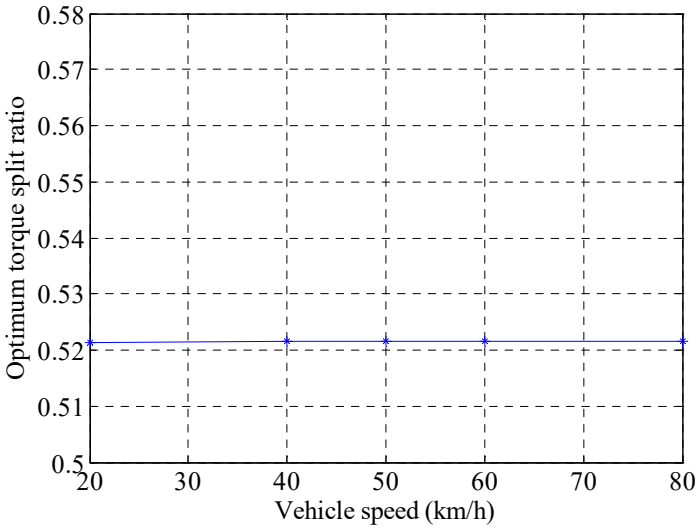

Fig. 2-11. Optimum torque split ratio versus vehicle speed.

It is shown that the influence of vehicle speed on the optimum torque split ratio can be neglected with respect to the influence of vehicle acceleration. This is because the vehicle speed cannot result in uneven tyre slips in front and rear tyres.

2.8.2.3 Optimum Control of Torque Split Ratio

Based on the foregoing analysis, if the toque command signals for the front and rear electrical machines are determined by the vehicle acceleration

in real time according to (2.31), the optimum control for the torque split ratio can be realised to save the energy consumed by the tyre slip.

With the implementation of the optimal torque split, the torque distribution in the front and rear motors can be seen in Fig. 2-12. During a NEDC cycle, with the optimal torque distribution controller, the total energy consumption is reduced by 14.27kJ compared to the single motor drive, as shown in Table 2-4. With the toque split controller, 0.87% of the total energy consumed is saved when operating under a NEDC cycle.

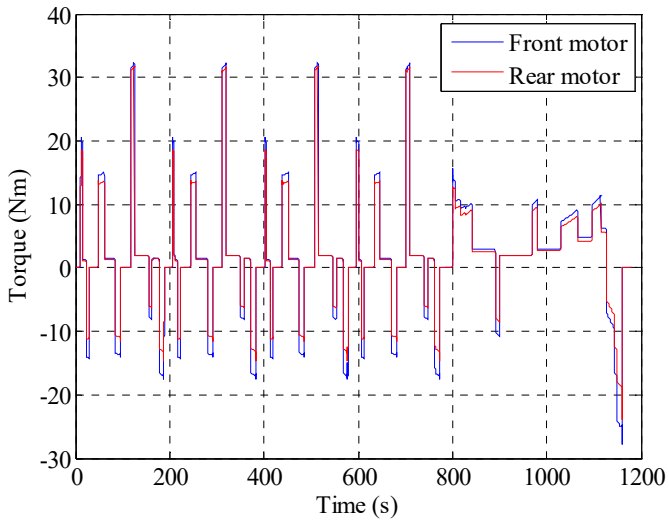

Fig. 2-12. Torque for the front and rear motor versus time.

Table 2-4. Energy Consumption Comparison for a Whole NEDC Cycle

Item	Unit	Value
Total energy consumed in the single motor drive	kJ	1643.31
Total energy consumed with the split ratio controller	kJ	1629.04
Energy saved with the split ratio controller	kJ	14.27

2.9 Fault Behaviour

Although distributed powertrain topology can enhance the fault-tolerant capability for the EV drive system, the failure of unilateral drive will result in an unbalanced vertical torque on the vehicle body. Consequently, the vehicle will deviate from the desired trajectory, even dashing against other

vehicles in adjacent lanes, especially if a failure occurring when the vehicle is cruising or overtaking in highway.

2.9.1 Fault Behaviour when Cruising at a High Speed

In this section, the allowable reaction time for the driver after failure will be calculated according to the principle that the vehicle body cannot be outside the lane boundary.

Given that the vehicle width will cancel out some part of the actual lane width, as demonstrated in Fig. 2-13, the equivalent lane width is calculated by (2.32).

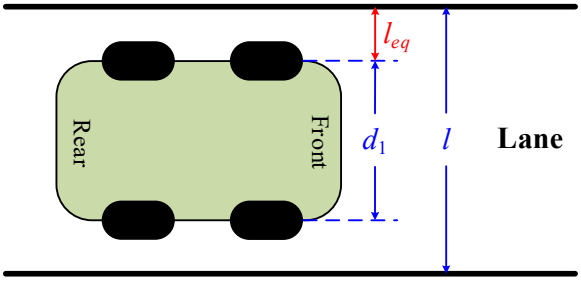

Fig. 2-13. Demonstration of the equivalent lane width l_{eq}.

$$l_{eq} = \frac{l - d_1}{2} = 0.51\text{m} \tag{2.32}$$

where, l_{eq} is the equivalent lane width, d_1 is the front axle length 1.48m, and l is the lane width which is assumed to be 2.5m considering the worst situation.

Consider a distributed powertrain in which the front axle is driven by one motor, and each rear wheel is driven by a motor. Assume that the front wheels are driven by a single motor which contributes 40% of the total toque whereas the rear wheels are driven by two motors and each contributes 30%, as shown in Fig. 2-19 (b). The SIMULINK diagram for the distributed power is shown in Fig. 2-14. With a failure occurring at the right rear motor at a high speed 120km/h, the torque profile is shown in Fig. 2-15. It can be seen that the

torque in the front motor and left rear motor increases greatly when the failure occurs at the right rear motor.

The vehicle locus is given in Fig. 2-16. It can be observed that the time interval between failure occurring and critical point is 1.45s, i.e. the allowable reaction time. The transient yaw rate and body slip angle after failure are given in Fig. 2-17 (a) and (b).

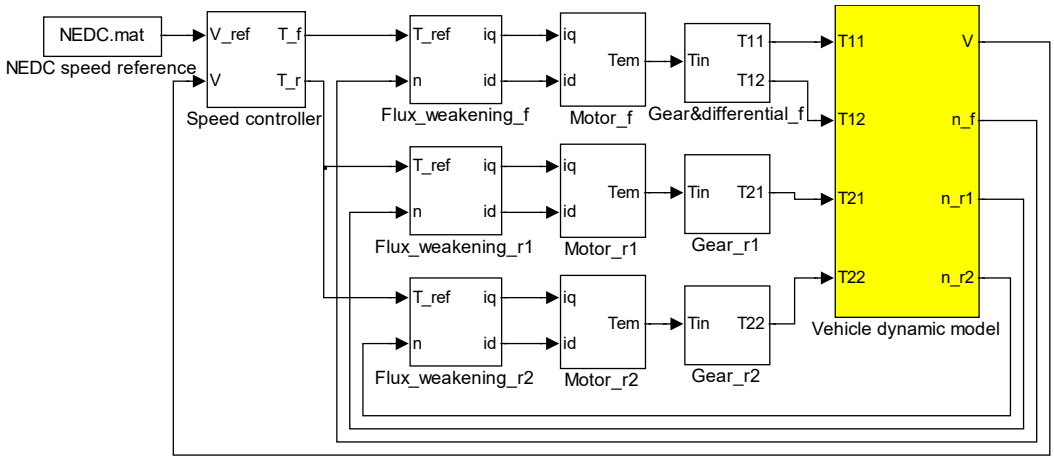

Fig. 2-14. Distributed drive powertrain model.

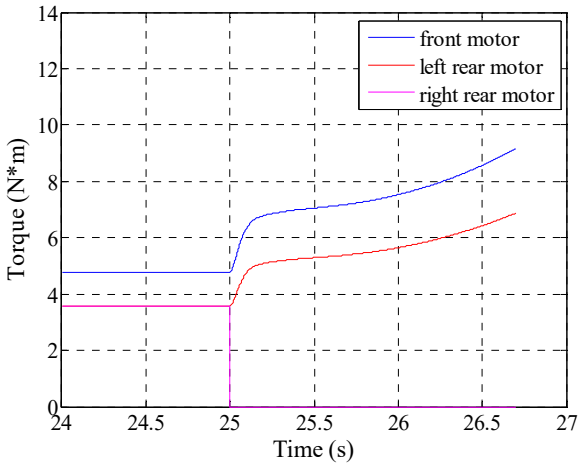

Fig. 2-15. Torque of each motor with a failure at right rear motor at high speed.

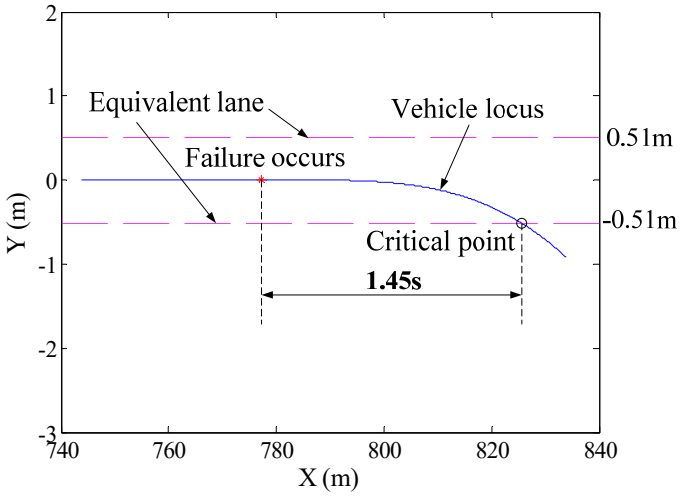

Fig. 2-16. Vehicle locus with a failure at right rear motor when cruising at a high speed.

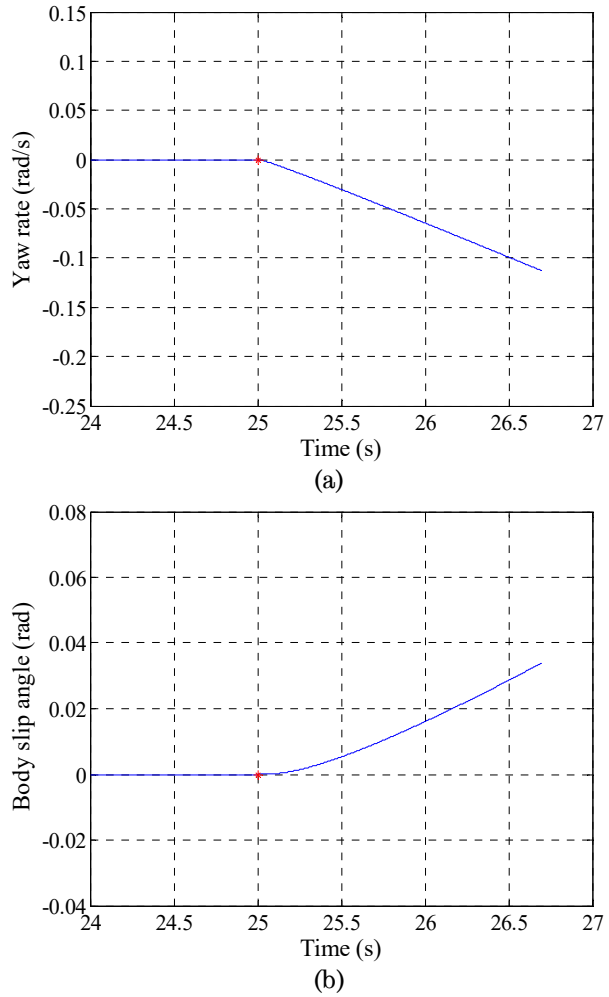

Fig. 2-17. Yaw rate and body slip angle when cruising at a high speed. (a) Yaw rate versus time. (b) Body slip angle.

2.9.2 Fault Behaviour when Overtaking at a High Speed

Similar with the previous calculation, the fault behaviour when the vehicle is overtaking at 115km/h with an acceleration of 0.278m/s^2 (coinciding with the speed trajectory in NEDC cycle) is calculated as shown in Fig. 2-18. It can be seen that the allowable reaction time for the driver is 1.27s, smaller than the one cruising at 120km/h. Thereby, overtaking at a high speed would be the most dangerous operation if one of the rear motors failed suddenly.

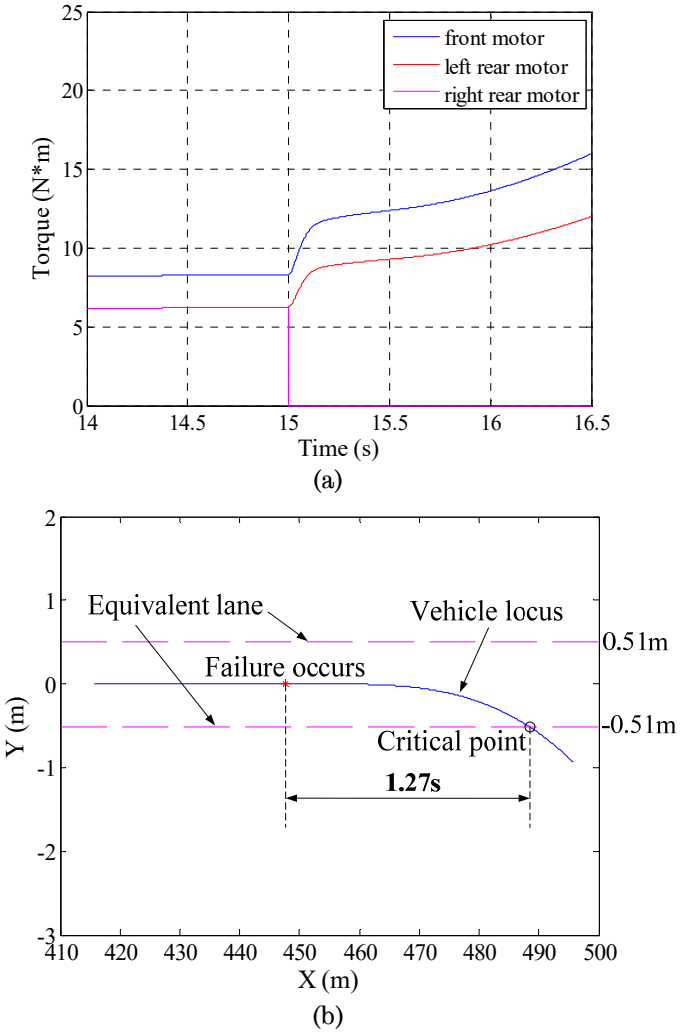

Fig. 2-18. Failsafe behaviour when overtaking at a high speed. (a) Torque versus time. (b) Vehicle locus.

2.9.3 Fault Behaviour of Various Powertrain Topologies

Compared with traditional single motor drive, electric vehicle employing distributed drive with more than one motor can continue its operation when one motor drive system fails suddenly. Nevertheless, the fault behaviour of various distributed power train configurations vary, which will be analysed in this section. Fig. 2-19 illustrates three powertrain topologies.

With an assumption that the right rear motor of each vehicle in Fig. 2-19 fails and cannot supply any mechanical torque, the reaction time left for the driver before the vehicle exceeding the lane boundary is calculated and shown in Table 2-5.

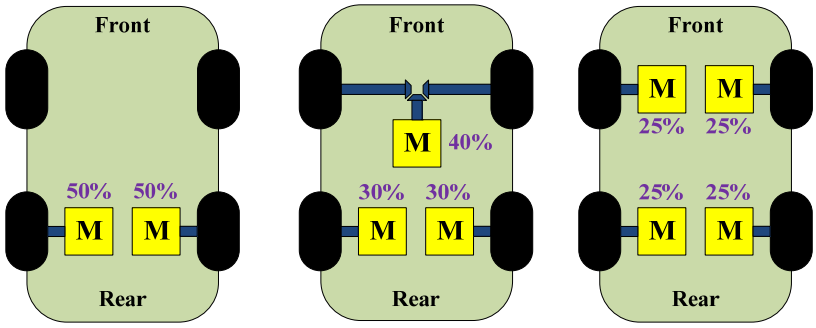

Fig. 2-19. Various powertrain topologies for EV drive. (a) 2 rear. (b) 1 front and 2 rear. (c) 2 front and 2 rear.

Table 2-5. Reaction Time Left for Drivers

Powertrain topology	Reaction time left (s)
Fig. 15 (a)	0.97
Fig. 15 (b)	1.27
Fig. 15 (c)	1.43

It can be seen that the 4-wheel drive will give the driver more reaction time than the other two topologies. However, if a sudden failure occurs at one of the front motors, the vehicle body will have to bear the similar unbalance torque as long as the other front motor is not disabled from the powertrain.

If the failure occurs at the right front motor, the reaction time is calculated to be 1.26s, smaller than that for the rear failure. It indicates that the failure at the front motor will result in a more serious consequence than at the rear when the toque split ratio for the front and rear motors is 50%:50%.

Table 2-6 illustrates driver response times against unexpected events [117, 118]. It can be seen that the probability of a driver unable to react to the fault and make correction to avoid the vehicle excursion into a neighbouring lane is very high.

Table 2-6. Driver Reaction Time

Driver	Reaction time (s)
Best driver	0.7
Realistic driver	1.0
Lethargic driver	2.0

2.10 Conclusion

Due to the power loss induced by the tyre slip, the size of electrical machines is increased by a certain percentage (9.5% in this study), which is subject to the maximum tyre slip ratio in acceleration and cannot be neglected.

Compared to the concentrated powertrain topology with a single machine drive, the distributed one can reduce the extra power loss incurred in the tyre slip, and thereby save the power consumption and also improve the efficiency of the whole system.

In a distributed powertrain topology, the torque split ratio between the front and rear wheels can affect both the machine size and the system efficiency by influencing the tyre slip. An optimum torque split ratio exists to minimise the total size of electrical machines. This optimum torque split ratio is subject to both the location of the vehicle centre of gravity and the vehicle acceleration, and the relationship between them is approximately

linear without considering the influence of the motor efficiency. The optimum control for the torque split ratio can be realised with a real-time calculation according to the vehicle acceleration. The percentage of energy saved depends on the tyre nonlinear characteristics, and is approximately 0.87% in this analysis.

Overtaking at a high speed would be the most dangerous operation if one of the rear motors fails suddenly for the powertrain topology with one motor in the front and two in the rear. Among the distributed powertrain topologies, the 4-wheel drive option with each motor contributing 25% of the total torque can leave more reaction time for the driver than that of 3-motor powertrain topology and 2-rear motor powertrain topology when the failure occurs suddenly at one motor drive system. For the 4-wheel distributed power train, the failure at the front motor will result in a more serious consequence than that at the rear when the toque split ratio for the front and rear motors is 50%:50%.

CHAPTER 3 Permanent-magnet Assisted Synchronous Reluctance Machine with Fractional-slot Winding Configurations

3.1 Introduction

Electrical machines with rare-earth permanent-magnets (such as sintered NdFeB) are of high torque density and good efficiency over a wide operation range, which are preferable attributes for EV traction application [2]. However, the high cost and limited reserves of the rare-earth material indicate that it might not be a sustainable strategy to develop this machine technology for EV traction where the demand on the rare earth material would be enormous in the future [1]. On the other hand, although induction machine possesses the advantages such as low cost, high reliability and high maturity, its inferior power factor and relatively lower efficiency [11] increase energy consumption and battery cost which is dominant in the total cost of EVs. Therefore, considering both cost and energy efficiency, it is worthwhile to develop electrical machines with low cost permanent-magnets (such as ferrite and bonded NdFeB) for EV traction [119]. Against this background, Permanent-magnet Assisted Synchronous Reluctance Machine (PMA-SynRM) may offer a good solution [120], since not only the amount of permanent-magnets being used is low due to a large reluctance torque contributed by the high saliency ratio in the rotor [68, 121-123], but also the efficiency and torque density are relatively high owing to the presence of permanent-magnets [69, 124-126].

In literature, most PMA-SynRMs utilise distributed winding because they are evolved from Synchronous Reluctance Machine (SynRM) where the torque is purely reluctance torque and the distributed winding yields more reluctance torque than fractional-slot winding [57, 70, 127, 128]. However, PMA-SynRM relies on both alignment torque (i.e., torque due to permanent-

magnet) and reluctance torque, and thereby the appropriateness of fractional-slot winding for PMA-SynRMs needs to be comprehensively evaluated.

Therefore, this chapter will investigate the performance of PMA-SynRMs with three typical fractional-slot winding configurations, viz., concentrated non-overlapping (12-slot 10-pole), conventional non-overlapping (12-slot 8-pole), and the overlapping (18-slot 8-pole) winding. All three candidate machines are optimised against the same specification and volumetric constraints. Their performances are comprehensively compared in terms of the efficiency map, loss distribution, torque ripple, reluctance torque contribution and the field weakening capability. Moreover, to more accurately evaluate the reluctance torque, a new torque component separation approach based on frozen permeability concept is developed in this chapter.

3.2 Fractional-slot Winding Configurations

For permanent-magnet machines with fractional-slot winding, a variety of feasible slot/pole number combinations exist. This chapter will evaluate three typical fractional-slot winding configurations for PMA-SynRMs with slot-pole combinations being 12-slot 10-pole, 12-slot 8-pole and 18-slot 8-pole. The 12-slot 10-pole machine topology is widely employed in SPMs due to its non-overlapping winding, high winding factor and also low cogging. The machine design with 12-slot 8-pole is usually associated with so-called brushless DC machines in that the winding span is 120° electrical degree. With respect to 18-slot 8-pole, it is a new fractional-slot winding configuration proposed in [129], where the slot number is doubled from 9-slot 8-pole machine so as to eliminate odd order magneto-motive force (MMF) harmonics and unbalance magnetic pull while preserve the advantages of the fractional-slot winding configuration.

Fig. 3-1 compares the normalised stator MMF harmonic spectra of the three winding configurations. The harmonic order is defined as the number of periods over 2π mechanical radians. The working harmonics for the 12-slot, 10-pole machine and the other two candidate machines is the 5^{th} and 4^{th}, respectively. It can be seen that both the 12-slot 10-pole and 18-slot 8-pole machines contains a sub-harmonic (its order is lower than that of the working harmonic) in their stator MMF, whereas the harmonic order for the 12-slot 8-pole machine is the integer multiple of its pole pair number, viz. 4, as listed in Table 3-1. The harmonic order numbers in bold represent those whose magnitude is larger than 5% of its fundamental.

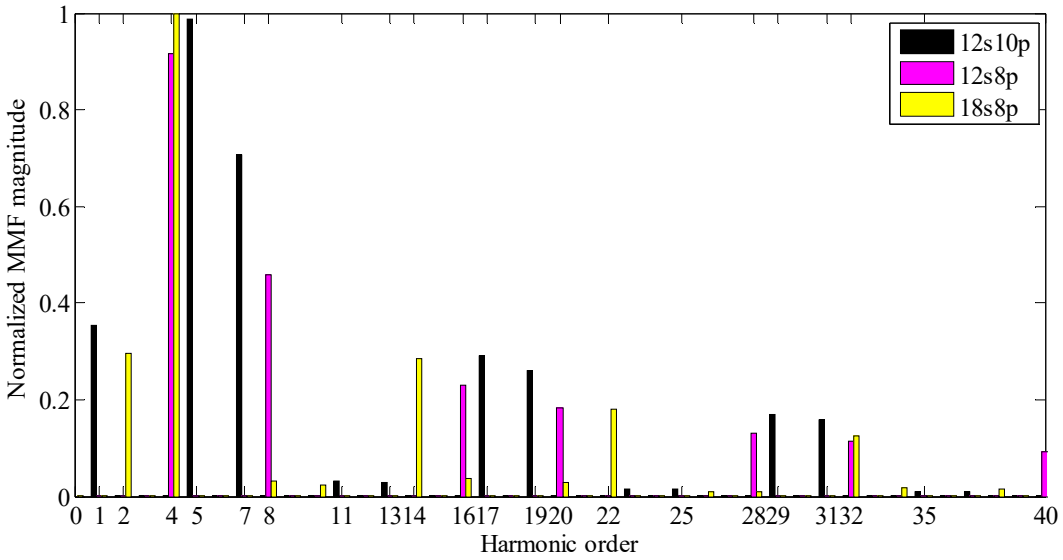

Fig. 3-1. Comparison of stator MMF Harmonic spectrum for three candidate machines.

Table 3-1. Stator MMF Harmonic Order Comparison

Winding configuration	Stator MMF harmonics order
12-slot 10-pole	**1**, **5**, **7**, 11, 13, **17**, **19**, 23, 25, **29**, **31**, 35, 37, ···
12-slot 8-pole	**4**, **8**, **16**, **20**, **28**, **32**, **40**, ···
18-slot 8-pole	**2**, **4**, 8, 10, **14**, 16, 20, **22**, 26, 28, **32**, 34, 38, ···

Although the number of harmonic orders for 12-slot 10-pole and 18-slot 8-pole are similar, the 18-slot 8-pole has less total harmonic distortion than the 12-slot 10-pole, which can be observed in Fig. 3-1.

The above stator MMF analysis and comparison can be utilised to explain the performance difference among these candidate machines with different winding configurations in Section 3.4.

3.3 Optimisation Process

In order to perform a comprehensive comparative study of the three typical fractional-slot winding configurations for PMA-SynRMs, the corresponding candidate machines are optimised against the same objective and within the same electrical and volumetric constraints.

The optimisation objective is to maximise NEDC driving cycle efficiency over 12 representative operating points as described in [130]. The optimisation constraints include performance specifications, volume limit, current limit, DC-link voltage (Line-to-line voltage) limit and the limit on the no-load back-EMF at the maximum speed as listed in Table 3-2. The power rating and operating range are described in the toque-speed profile shown in Fig. 3-2, where the 12 representative points for the energy consumption over NEDC are also illustrated.

Table 3-2. Specification and Optimisation Constraints

Quantity	Unit	Value
Peak power	kW	6.6
Rated power	kW	3.7
Base speed	r/min	2100
Maximum speed	r/min	8200
Peak torque at base speed	Nm	30
Rated torque at base speed	Nm	17
Peak torque at maximum speed	Nm	7.7
Continuous torque at maximum speed	Nm	4.4
Volume limit	m^3	4.75×10^{-3}
Current limit	A	130
Line-to-line voltage limit	V	120
No-load back-EMF limit	V	270
Cooling		Air-cooled

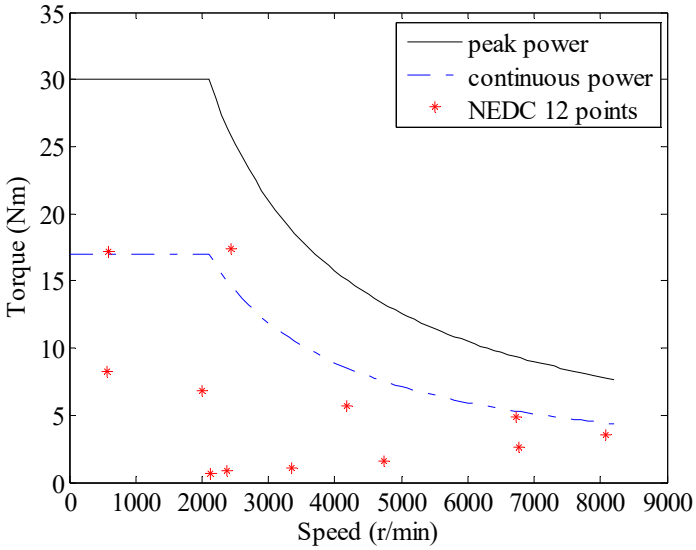

Fig. 3-2. Torque-speed profile for machine design and optimisation.

The optimisation is performed using an FE-based software package, FLUX2D, from CEDRAT [131] together with the optimisation tool GOT-IT [132] also from CEDRAT. A parameterised FE model is constructed in FLUX2D and it is called by the optimisation process which evaluates the objective functions and constraints and selects the most promising designs via a combination of genetic algorithm and sequential surrogate programming technique. The parameters to be optimised and their ranges are described in Table 3-3 and Fig. 3-3. Six parameters, viz., stack length, split ratio, insulation ratio, tooth width, back-iron thickness and the number of turns per coil, will be optimised. As indicated in Fig. 3-3, the split ratio K_s is defined as the ratio of the rotor outer radius R_i to the stator outer radius R_o, whilst the insulation ratio is defined as the total thickness of the magnets (h_{m1}+h_{m2}+h_{m3}) divided by the depth of magnets against the rotor surface d_m. Bonded NdFeB magnets with remanence B_r = 0.56 and relative recoil permeability μ_r=1.2 are employed for the candidate machines.

Table 3-3. Parameters to be Optimised and Their Ranges

Quantity	Symbol	Unit	Range
Stack length	L_a	mm	70.0-110.0
Split ratio	K_s		0.5-0.75
Insulation ratio	K_i		0.52-0.68
Tooth width	h_t	mm	5.0-15.0
Back-iron thickness	h_i	mm	5.0-7.0
Number of turns per coil	N_t		5.0-10.0

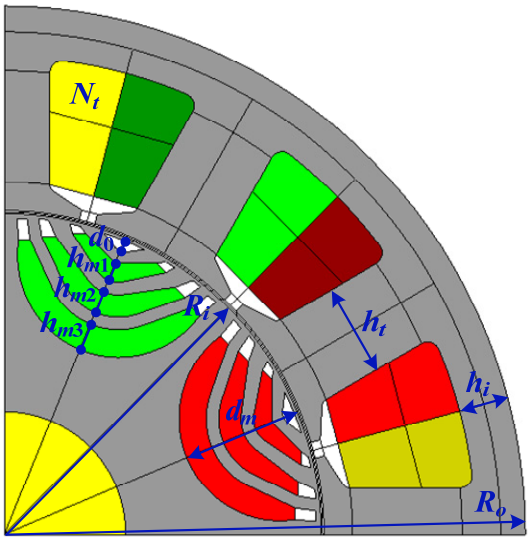

Fig. 3-3. Geometry parameters description.

The optimisation is performed via the similar procedure described in [133]. The optimisation results and the corresponding geometries can be found in Table 3-4 and Fig. 3-4. It can be seen that the optimised geometries exhibit a large difference in split ratio. The 12-slot 10-pole machine exhibits much larger split ratio than the other two machines, and the 18-slot 8-pole machine has the lowest one. This may be explained by reluctance torque production capability differences of these three machines. Regarding the reluctance torque production capability, the 18-slot 8-pole machine is the best while the 12-slot 10-pole one is the worst, which can be observed in Table 3-6 in Section 3.4.4. Therefore, the 12-slot 10-pole machine needs a larger split ratio to produce more torque but compromise efficiency performance to satisfy all the design requirements shown in Table 3-2. In contrast, the 18-slot 8-pole machine has a better reluctance torque capability, and thus does not need a large split ratio to meet the design requirements. The large difference

in split ratio between these three machines also indicates that conventional approaches to performing comparative studies in literature, by employing similar or same split ratio for these three machines may result in a considerably different outcome.

Table 3-4. Optimised Parameters

Parameters	Unit	12-slot 10-pole	12-slot 8-pole	18-slot 8-pole
L_a	mm	85.0	91.2	90.0
K_s		0.7125	0.608	0.567
K_i		0.68	0.68	0.66
h_t	mm	13.5	11.3	7.0
h_i	mm	6.8	6.2	6.6
N_t		8.0	9.0	6.0

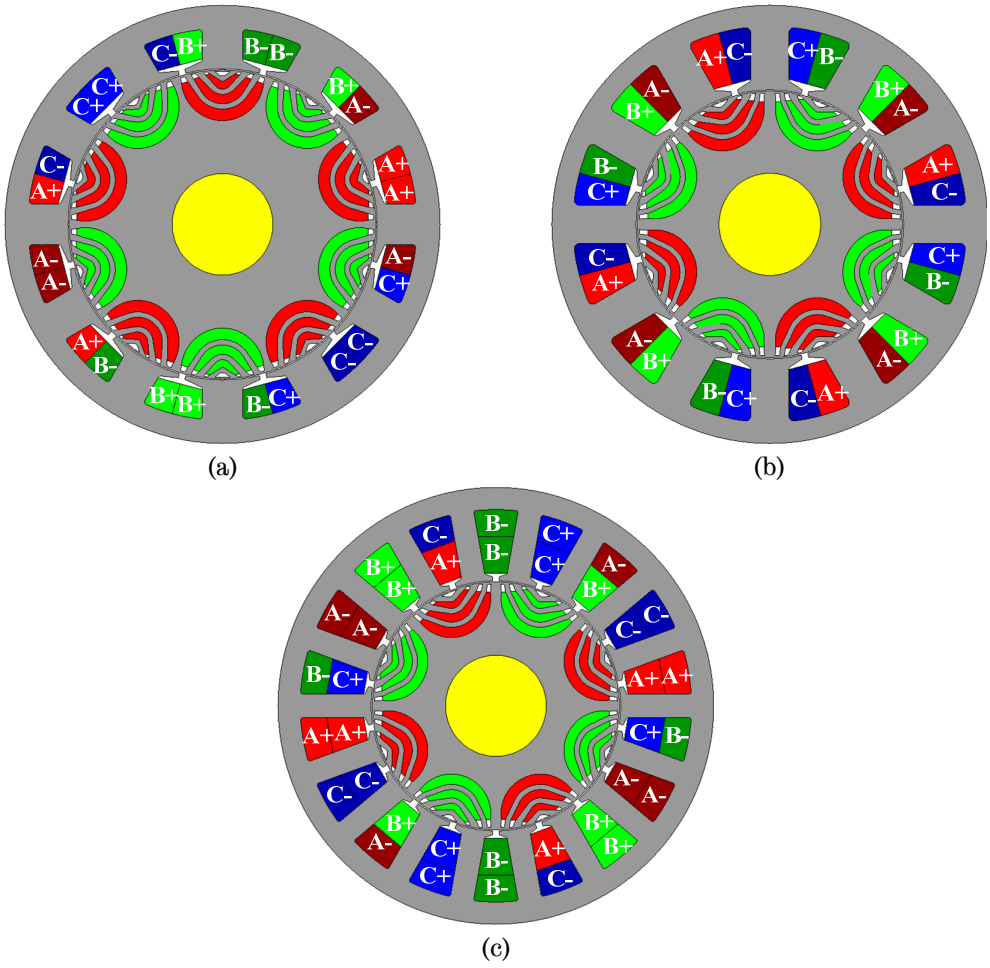

(a) (b) (c)

Fig. 3-4. Geometry cross-section of optimised designs. (a) 12-slot 10-pole. (b) 12-slot 8-pole. (c) 18-slot 8-pole.

3.4 Performance Evaluation

Based on the previous optimisation results, a comprehensive evaluation on the performance of these three PMA-SynRMs with different fractional-slot winding configurations can be made in terms of efficiency map, loss distribution, torque ripple, reluctance torque contribution and the field weakening capability.

3.4.1 Efficiency Map

The loss and efficiency at the peak torque, rated torque and the 12 NEDC operating points are listed in Table 3-5. The efficiency maps over the torque and speed operating range are shown in Fig. 3-5 where only the region with efficiency greater than 80% is displayed. Minimum loss per ampere strategy is employed when the line-to-line voltage is lower than the voltage limit, and field weakening strategy is utilised when the voltage limit is reached. The *d*- and *q*-axis current references are determined by Newton-Raphson method to satisfy both the torque demand and voltage constraint when Space Vector Pulse Width Modulation (SVPWM) is employed.

Table 3-5. Loss and Efficiency at Different Working Points

Operating point	Quantity	Unit	12-slot 10-pole	12-slot 8-pole	18-slot 8-pole
Peak torque & base speed	Copper loss	W	863.5	775.9	860.0
	Rotor iron loss	W	29.0	19.8	15.0
	Stator iron loss	W	56.4	47.8	46.6
	Efficiency	%	87.5%	88.7%	87.8%
Rated torque & base speed	Copper loss	W	269.7	218.5	259.0
	Rotor iron loss	W	21.6	13.7	11.1
	Stator iron loss	W	42.5	35.1	36.3
	Efficiency	%	91.8%	93.3%	92.5%
NEDC 12 points	Copper loss in constant-torque region	J	21601	20299	24223
	Copper loss in field weakening region	J	7213	4210	4923
	Rotor iron loss	J	16798	11003	8656
	Stator iron loss	J	29125	20826	18895
	Cycle efficiency	%	92.7%	94.4%	94.3%

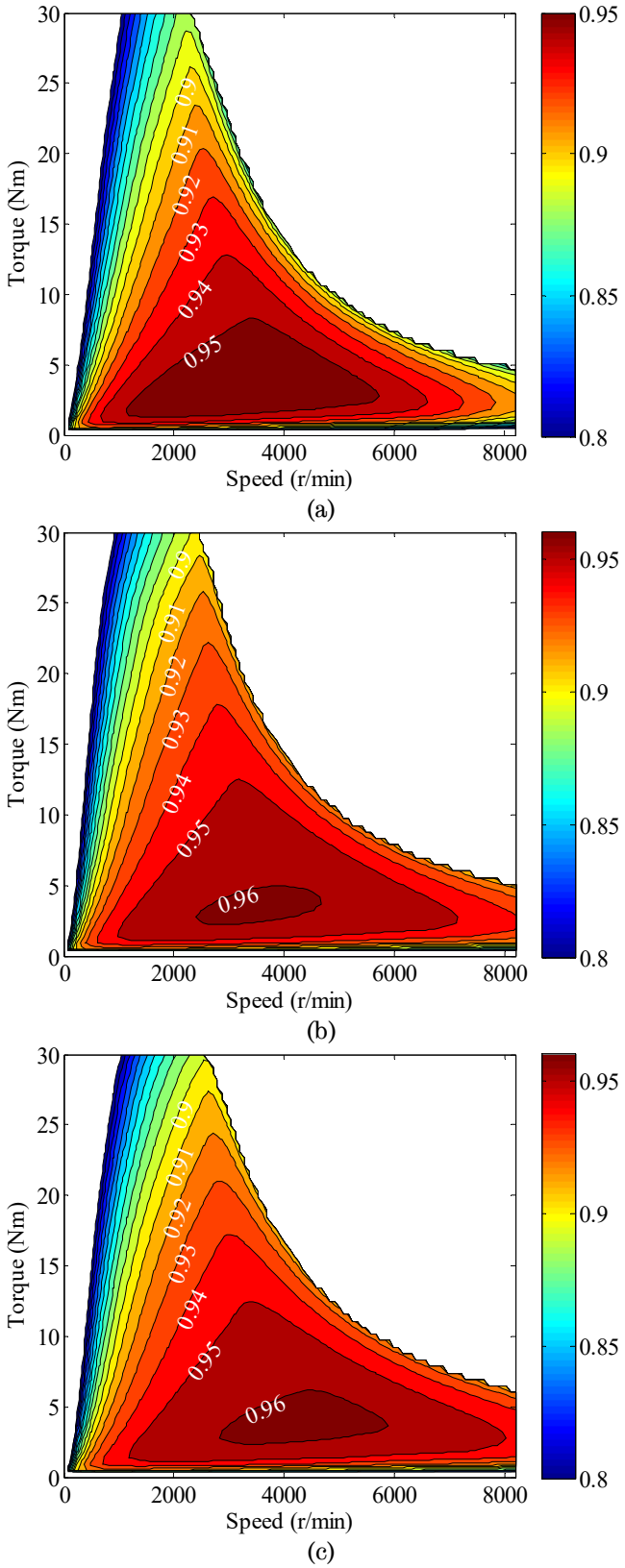

Fig. 3-5. Efficiency maps of PMA-SynRMs with different fractional-slot winding configurations. (a) 12-slot 10-pole. (b) 12-slot 8-pole. (c) 18-slot 8-pole.

It can be seen that the 18-slot 8-pole and the 12-slot 8-pole machines have a very competitive NEDC cycle efficiency greater than 94% at a power rating of 6.6kW. The cycle efficiency can be expected to be higher than 96% if a machine with a power rating of 20kW is designed by employing PMA-SynRM with fractional-slot winding, such as the 12-slot 8-pole and 18-slot 8-pole. However, the 12-slot 10-pole machine suffers from lower NEDC cycle efficiency due to higher stator and rotor iron loss which results from the presence of a large number of sub- and high order stator MMF harmonics.

3.4.2 Loss Distribution

The loss distributions between copper loss, stator iron loss and rotor iron loss at the peak torque, rated torque and over 12 NEDC points for the three design options are also given in Table 3-5. It can be seen that the 12-slot 8-pole machine has the lowest copper loss due to high copper packing factor, short end-winding length and the high reluctance torque, whilst the copper loss of the 12-slot 10-pole machine is similar to that of the 18-slot 8-pole machine. While the 12-slot 10-pole machine has higher copper packing factor and lower end-winding length, the 18-slot 8-pole machine exhibits the higher reluctance torque, which can be shown in Section 3.4.4.

In terms of the rotor iron loss, the 12-slot 10-pole machine is the highest, being ~2 times of that of the 18-slot 8-pole machine, while the 12-slot 8-pole machine is in between, around 30% more than that of the 18-slot 8-pole one. This can be understood by the stator MMF harmonic contents given in Fig. 3-1, where the 12-slot 10-pole winding exhibits the highest total harmonic distortion in MMF, whilst the 18-slot 8-pole one is the lowest.

Moreover, the high rotor iron loss of the 12-slot 10-pole machine presents a particular challenge for rotor heat dissipation. Fig. 3-6 illustrates the harmonic distributions of the rotor iron loss associated with eddy current component for the three candidate machines. It can be seen that the dominant loss harmonic component for the 12-slot 10-pole machine is 12^{th}

order resulting from the interaction of the 7th and 17th stator MMF harmonics in Fig. 3-1 with the 5th rotor MMF working harmonic.

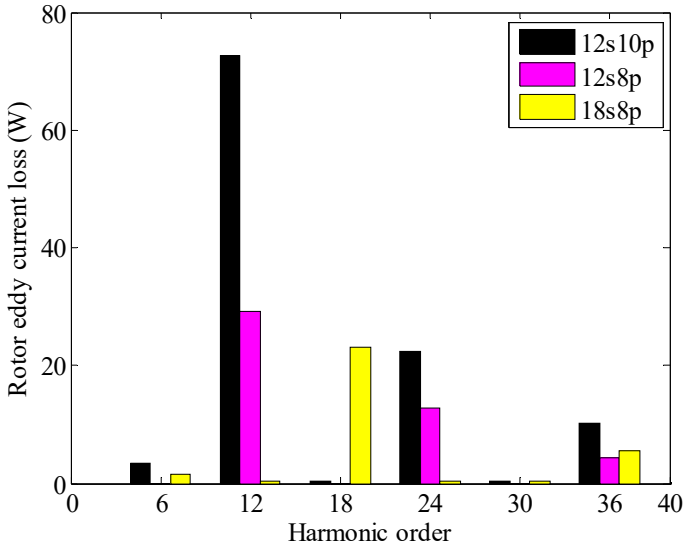

Fig. 3-6. Eddy current component of rotor iron loss at the 12th NEDC operating point.

3.4.3 Torque Ripple

The torque waveforms of the three designs at the peak torque and base speed are compared in Fig. 3-7. As will be seen, the 12-slot 8-pole machine produces a very large torque ripple. This is the most significant disadvantage of the winding configuration. Its peak-to-peak torque ripple ratio against the average peak torque reaches 49%. The other two machines, 12-slot 10-pole and 18-slot 8-pole on the other hand, have a much lower torque ripple with the peak-to-peak torque ripple ratios being 16% and 14%, respectively. Relatively large torque ripples of these three machines may be attributed to the fact that the optimisation objective in this study is against energy efficiency whereas the conditions for reducing losses during field weakening operation may conflict with the conditions for reducing the torque ripple of IPM machines, according to the conclusion in [65].

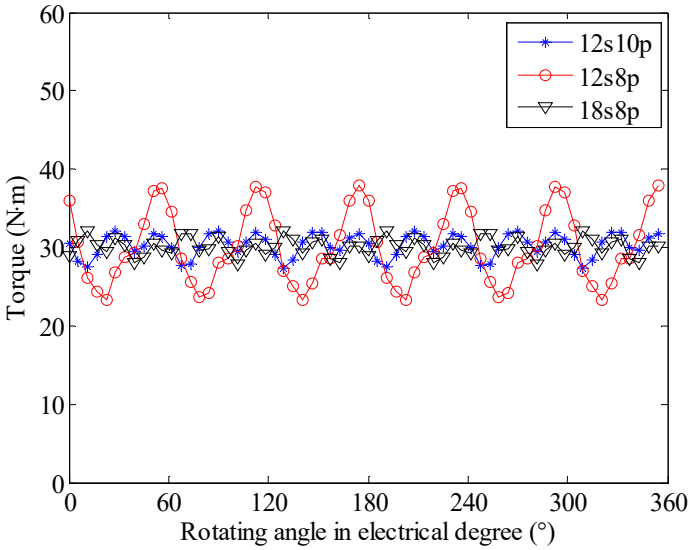

Fig. 3-7. Torque waveform at peak torque & base speed.

Fig. 3-8 shows the comparison of torque harmonic components for these three machines. The dominant torque ripple harmonic for 12-slot 10-pole, 12-slot 8-pole and 18-slot 8-pole machines are the 12^{th}, 6^{th} and 18^{th} order, respectively, with respect to the electrical frequency. The high order harmonics, such as the 12^{th} for the 12-slot 10-pole machine and the 18^{th} for the 18-slot 8-pole machine can be reduced significantly using skew technique without compromising average torque much. However, in order to reduce the 6^{th} order torque ripple in the 12-slot 8-pole PMA-SynRM, other techniques need to be investigated further.

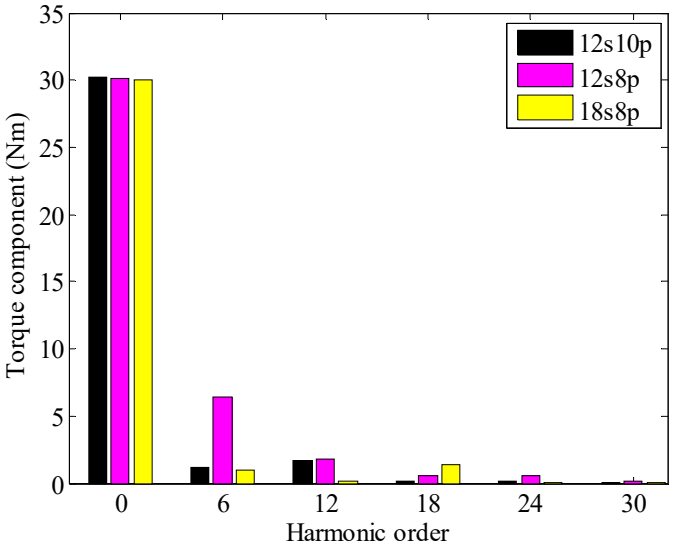

Fig. 3-8. Torque harmonic components at peak torque and base speed.

3.4.4 Reluctance Torque Contribution

The reluctance torque is calculated by removing the alignment torque from the total torque using FE with frozen permeability. To be more specific, a transient FE analysis with both magnets and armature current is performed, and permeability in each element at each time step is recorded. The second transient FE analysis is taken with the recorded permeability in each element at a given time and the remanence of the magnets being set to zero. The resultant torque without magnets will give the reluctance torque. The reluctance torque evaluation process will be described in detail in Section 3.5.

The reluctance torque contribution at the peak and rated operating points are listed in Table 3-6. It can be observed that both the 18-slot 8-pole and 12-slot 8-pole machines can produce significant reluctance torque, whilst the attainable reluctance torque from the 12-slot 10-pole winding configuration is slightly lower but also considerable.

Table 3-6. Reluctance Torque Ratio

Operating point	12-slot 10-pole	12-slot 8-pole	18-slot 8-pole
Peak torque & base speed	66.6%	74.3%	75.4%
Rated torque & base speed	57.6%	68.3%	68.2%

The high reluctance torque obtained from the 12-slot 10-pole machine is not known in literature. Most studies [57, 70], to date, show that IPM machine designs with the 12-slot 10-pole combination result in relatively small reluctance torque and this phenomenon is explained by the fact that the coil span of the concentrated winding, e.g. 12-slot 10-pole, is close to its pole pitch giving rise to a relatively small reluctance variation seen by the coil due to the filtering effect of the flux density integral over a slot-pitch. However, this may only be true when the rotor structure is not specifically designed to enhance reluctance torque. Nevertheless, the presence of the relatively high 1st and 7th order MMF harmonics in the 12-slot 10-pole design give rise to localised saturation in both stator and rotor iron, which may

reduce the permeability difference in the *d*-axis and *q*-axis. Hence, the reluctance torque contribution of the 12-slot 10-pole machine is the smallest among these three fractional-slot PMA-SynRMs. However, it is still considerable compared with the reluctance torque contribution of conventional IPM machines with the concentrated non-overlapping winding configuration.

The reluctance torque variations of the three candidate machines are shown in Fig. 3-9, where the 12-slot 8-pole machine generates a high reluctance torque but with a large ripple. This explains the cause of the large torque ripple shown in Fig. 3-7 for the 12-slot 8-pole machine from another perspective.

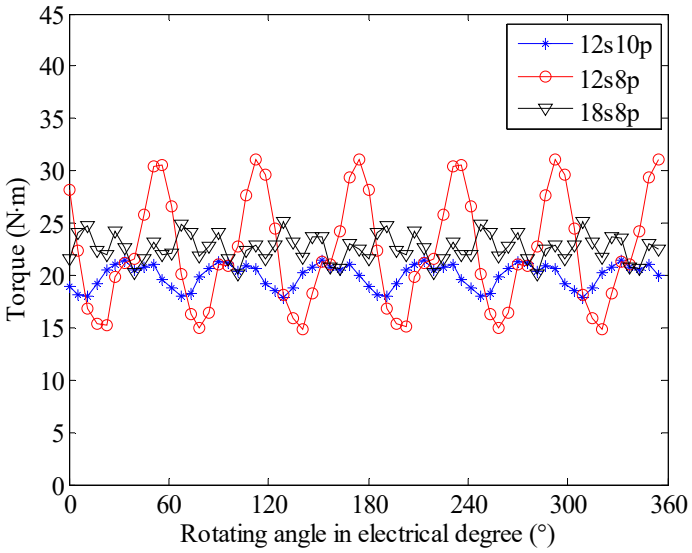

Fig. 3-9. Reluctance torque waveform at peak torque & base speed.

3.4.5 Field Weakening Capability

In literature, the field weakening capability is usually evaluated by the characteristic current or short-circuit current which is defined by the ratio of PM flux-linkage to *d*-axis inductance. Hence, the relationships between the *d*-axis flux-linkage and *d*-axis current for the three candidate machines are established and shown in Fig. 3-10. The characteristic currents are represented by the intersections of the flux-linkage curves with the *d*-axis current axis (the dashed line) in Fig. 3-10.

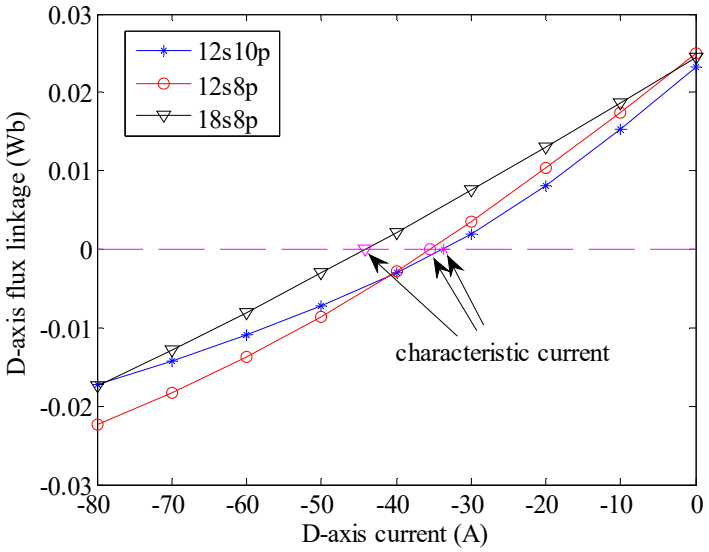

Fig. 3-10. Relationship between *d*-axis flux-linkage and *d*-axis current.

It can be seen that the 18-slot 8-pole machine exhibits the highest characteristic current, being about 30% larger than the other two, due to its relatively lower *d*-axis inductance, as listed in Table 3-7.

Table 3-7. Characteristic Current

Quantity	Unit	12-slot 10-pole	12-slot 8-pole	18-slot 8-pole
No-load PM flux-linkage	mWb	22.4	23.4	24.5
d-axis inductance at short-circuit condition	mH	0.663	0.659	0.554
Characteristic current	A	-33.7	-35.5	-44.2

However, the characteristic current only represents one operating point, viz. the short-circuit point, which cannot fully describe the real machine behaviour in the field weakening region. Therefore, the current trajectories during field weakening are drawn in Fig. 3-11, with load torque fixed to 4.4 Nm and speed increasing from the base speed of 2100r/min to the maximum speed of 8200r/min. The current amplitude variation with speed during field weakening at the same load condition is illustrated in Fig. 3-12. It is shown that all the three currents increase slowly before reaching the field weakening region due to the fact that the controller employs the minimum loss per ampere strategy rather than the maximum torque per ampere (MTPA) strategy.

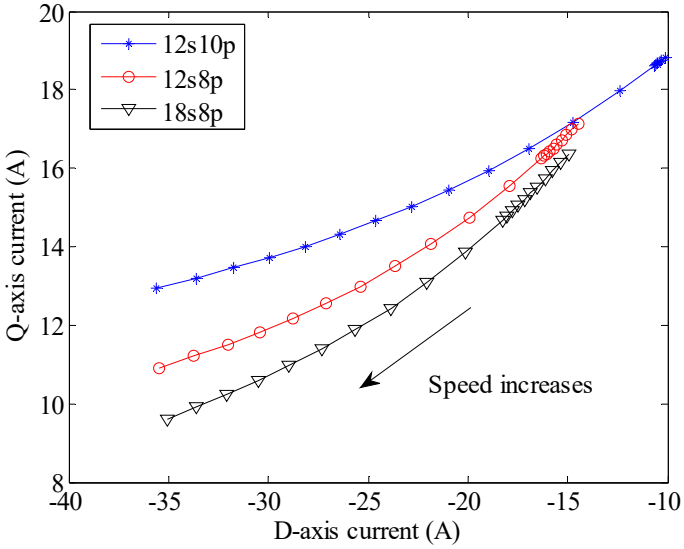

Fig. 3-11. Current trajectory during field weakening at continuous torque.

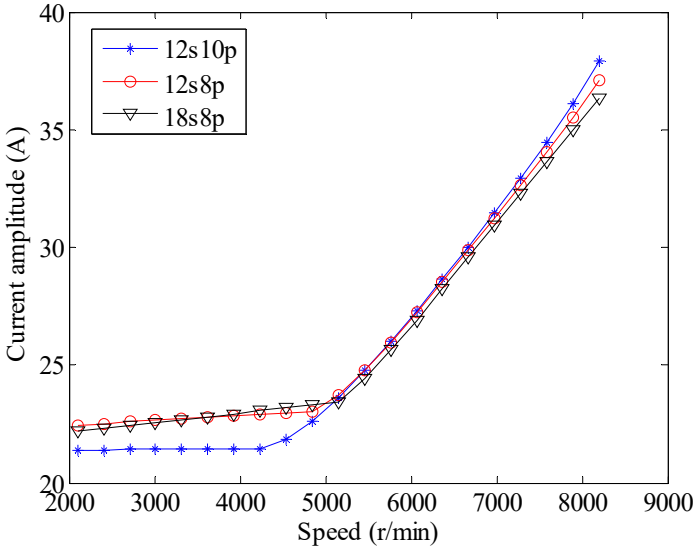

Fig. 3-12. Current amplitude variation with speed during field weakening at continuous torque.

However, after reaching voltage limit, *d*-axis current magnitude needs to be increased to reduce voltage whereas *q*-axis current may decrease slightly to maintain the torque. Due to the fact that the *q*-axis current contributes to both alignment torque and reluctance torque while the *d*-axis current only relates to reluctance torque, the decrease of *q*-axis current is less than the increase of *d*-axis current magnitude, resulting in the increase of the total current magnitude in order to guarantee the torque production within the fixed voltage limit. Further, the total current and *d*-axis current variation

from the base speed to the maximum speed is listed in Table 3-8. It can be observed that the current required at a given speed and torque is virtually the same for all three machines, although it is slightly high with the 12-slot 10-pole machine. Thus the field weakening capability of the three machines is similar, even though the 18-slot 8-pole machine has a relatively high characteristic current.

The above analysis also indicates that a good field weakening capability is not necessarily associated with a low characteristic current. This is because a low characteristic current may compromise the field weakening capability when the *d*-axis flux-linkage becomes negative, or the required *d*-axis current exceeds the characteristic current. Thus the increase of *d*-axis current magnitude will not reduce but increase the *q*-axis voltage.

Table 3-8. Current Variation during Field Weakening

Quantity	Unit	12-slot 10-pole	12-slot 8-pole	18-slot 8-pole
d-axis current at base speed	A	-10.1	-14.4	-15.0
d-axis current at max speed	A	-35.6	-35.4	-35.1
Total current at base speed	A	21.4	22.4	22.2
Total current at max speed	A	37.9	37.1	36.4
Total current increase	%	77.1%	65.6%	64.0%

The foregoing observation can be illustrated by comparing the field weakening capability of two hypothetical models *A* and *B* which have the same no-load PM flux-linkage, saliency ratio and the pole pair number but different *d*-axis inductance, as listed in Table 3-9. Assuming that the inductance variation and the voltage drop on the resistance are negligible, the voltage limit ellipse and the torque profile at the load torque of 4.4 Nm and the speed of 8000r/min are drawn on the *d*-axis and *q*-axis current plane for the two models, as shown in Fig. 3-13. It can be seen that although model *B* has a much lower characteristic current than model *A*, the current amplitude of model *B* is actually higher than that of model *A*, as listed in Table 3-10, in that the *d*-axis current of model *B* has already been beyond its

characteristic current in negative direction whereas the *d*-axis current of model *A* is below its characteristic current.

Table 3-9. Lumped Parameters of Hypothetical Models

Quantity	Unit	Model *A*	Model *B*
No-load PM flux-linkage	mWb	24.0	24.0
d-axis inductance	mH	0.5	0.7
Saliency ratio		2.0	2.0
Pole pair number		4.0	4.0

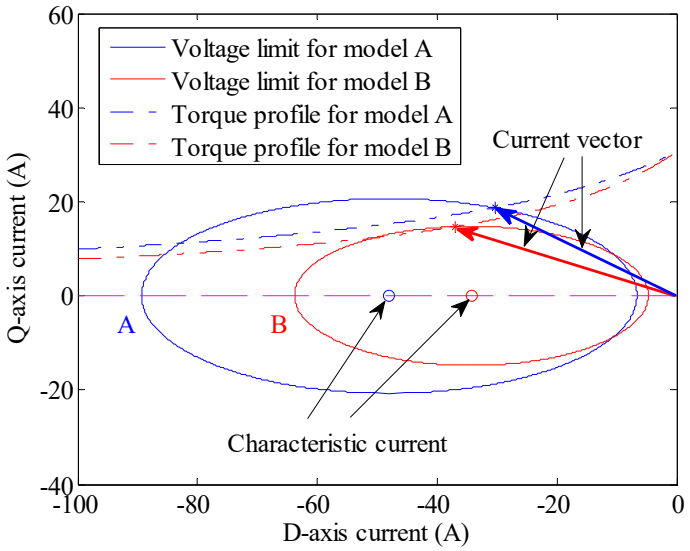

Fig. 3-13. Current trajectory comparison among two hypothetical models at the same torque and speed operating point in field weakening region.

Table 3-10. Current Components of Hypothetical Models

Quantity	Unit	Model *A*	Model *B*
Characteristic current	A	-48.0	-34.3
d-axis current	A	-30.4	-36.9
q-axis current	A	18.7	14.7
Current amplitude	A	35.7	39.7

3.5 Reluctance Torque Evaluation Using Frozen Permeability

The torque production of an IPM (including PMA-SynRM) is contributed by both the alignment torque due to magnets and the reluctance torque due to rotor saliency. From the machine design point of view, a high reluctance torque ratio can increase torque production and overloading capability,

enhance power density, and improve field weakening performance of an IPM machine [68, 69, 122]. Therefore, an accurate evaluation of reluctance torque contribution is important to the IPM design.

The classic torque equation given in (3.1) consists of two terms. The first term, known as alignment torque, is associated with the torque due to permanent-magnet field, and the second term, known as reluctance torque, results from the difference in rotor *d*- and *q*-axis reluctances.

$$T_{em} = \frac{m}{2} p \left\{ \Psi_m(i_d, i_q, \theta) i_q + \left[L_d(i_d, i_q, \theta) - L_q(i_d, i_q, \theta) \right] i_d i_q \right\} \tag{3.1}$$

where T_{em} is the electromagnetic torque, m is the number of phases, p is the number of pole pairs, Ψ_m is the PM flux-linkage, L_d and L_q are the *d*- and *q*-axis inductances respectively, i_d and i_q are the *d*- and *q*-axis currents respectively, and θ is the rotor position angle.

In literature, a few methods have been presented to separate torque components, which include (a) modelling machine assuming constant PM flux-linkage, (b) modelling machine assuming the PM flux-linkage varies with *q*-axis current only [134] and (c) using frozen permeability (FP) concept [135-139]. The first two methods cannot separate PM flux-linkage from the *d*-axis flux-linkage correctly because the superposition principle is no longer valid in a non-linear system. In contrast, the FP concept is more preferable for torque separation. However, the torque separation is performed with the FP concept on average sense, not instantaneously in [139].

In this section, an analytical model in transient FP process is presented, accounting for saturation effects in both *d*- and *q*-axis magnetic circuits. Subsequently, the electromagnetic torque is separated into various components according to (a) classic torque equation, (b) classic torque equation derived from the FP concept and (c) the proposed torque equation also based on the FP approach. The torque calculated by these three different

methods are then compared to show the improved torque prediction achieved by the proposed model.

3.5.1 Analytical Model

Magnetic saturation in electrical machines can vary considerably with the electric loading of the machine. Under low load condition the magnetic saturation is low, and therefore the *d*- and *q*-axis magnetic circuits are effectively independent and their mutual coupling is negligible. Hence, the *d*- and *q*-axis flux-linkages are expressed by (3.2).

$$\begin{aligned} \Psi_d &= \Psi_m(i_d, i_q, \theta) + L_d(i_d, i_q, \theta) i_d \\ \Psi_q &= L_q(i_d, i_q, \theta) i_q \end{aligned} \tag{3.2}$$

However, when the torque demand is high, the shared magnetic paths of *d*- and *q*-axis fluxes will be highly saturated and therefore the *d*- and *q*-axis cross-coupling effect has to be taken into account for a high-fidelity machine model. It is arguable that the *d*- and *q*-axis cross-coupling effect may be represented in (3.2) with variations of Ψ_m, L_d and L_q as functions of the *d*- and *q*-axis currents. However, it implies that the *d*-axis current does not contribute to the *q*-axis flux-linkage and vice versa. This relationship is not consistent with observations from FEA in that if a large positive *d*-axis current is injected while the *q*-axis current is kept zero, the resultant *q*-axis flux-linkage may not be zero, due to magnetic coupling between the *d*- and *q* axes at high saturation level. To account for the cross-coupling effect, mutual inductances are introduced to the *d*- and *q*-axis flux-linkages given in (3.3).

$$\begin{aligned} \Psi_d &= \Psi_{md}(i_d, i_q, \theta) + L_d(i_d, i_q, \theta) i_d + M_{dq}(i_d, i_q, \theta) i_q \\ \Psi_q &= \Psi_{mq}(i_d, i_q, \theta) + M_{qd}(i_d, i_q, \theta) i_d + L_q(i_d, i_q, \theta) i_q \end{aligned} \tag{3.3}$$

where Ψ_{md} and Ψ_{mq} are the *d*- and *q*-axis PM flux-linkages respectively, and M_{dq} and M_{qd} are the mutual inductances between *d*- and *q*-axis magnetic paths.

The electromagnetic torque can be calculated by either Maxwell stress tensor method or virtual work principle. However, the Maxwell stress tensor method is sensitive to mesh density and quality as well as selection of the surface on which the Maxwell stress tensor is evaluated. Therefore, in this section only the virtual work principle is employed in the torque calculation and all the FEA results are obtained via FLUX2D software developed by CEDRAT [131].

The well-known equation for the torque production in the *dq* frame is shown in (3.4). Substituting (3.3) into (3.4), the torque equation can be written as (3.5).

$$T_{em} = \frac{m}{2} p\left[\Psi_d(i_d, i_q, \theta) i_q - \Psi_q(i_d, i_q, \theta) i_d\right] \tag{3.4}$$

$$T_{em} = \frac{m}{2} p\left[\Psi_{md} i_q - \Psi_{mq} i_d + \left(L_d - L_q\right) i_d i_q + M_{dq} {i_q}^2 - M_{qd} {i_d}^2\right] \tag{3.5}$$

However, (3.5) cannot be directly applied to the FP process, since it does not include the torque produced as a result of variation of magnetic co-energy [140] when the *d*- and *q*-axis currents are zero. To separate torque components accurately, a new torque equation in the FP process is proposed, as shown in (3.6).

$$T_{em} = \frac{m}{2} p\left[\Psi_{md} i_q - \Psi_{mq} i_d + \left(L_d - L_q\right) i_d i_q + M_{dq} {i_q}^2 - M_{qd} {i_d}^2\right] + T_{mr} \tag{3.6}$$

where T_{mr} represents the torque component contributed by the interaction of the rotor permanent-magnet field with unequal reluctances in the *d*- and *q*-axis directions in the stator iron. The physical interpretation of this torque component is understood by the fact that when permeability in an IPM machine is frozen for a given set of *d*- and *q*-axis currents at a given rotor position, the reluctances in the *d*- and *q*-axes in the stator will be different due to saturation effect, as shown in Fig. 3-14. Fig. 3-14 (a) and (b) illustrate the relative permeability contour of the rotor and stator laminations at 0°

and 5° (half slot pitch) rotor positions with respect to phase *A* winding axis for a 10kW IPM machine with 36-slot 6-pole winding configuration. The selected working point is the rated torque at the base speed and the machine specification and design details are listed in Table 3-11.

From Fig. 3-14 it can be seen that the permeability in the *d*- and *q*-axes in the stator are different, and the average *q*-axis stator permeability is higher than that of the *d*-axis at both 0° and 5°. The unequal reluctances in the *d*- and *q*-axis magnetic paths in the stator iron interact with the rotor permanent-magnetic field, giving rise to the torque component T_{mr} in the same principle as a synchronous reluctance machine. However, this torque component occurs even if the currents are zero.

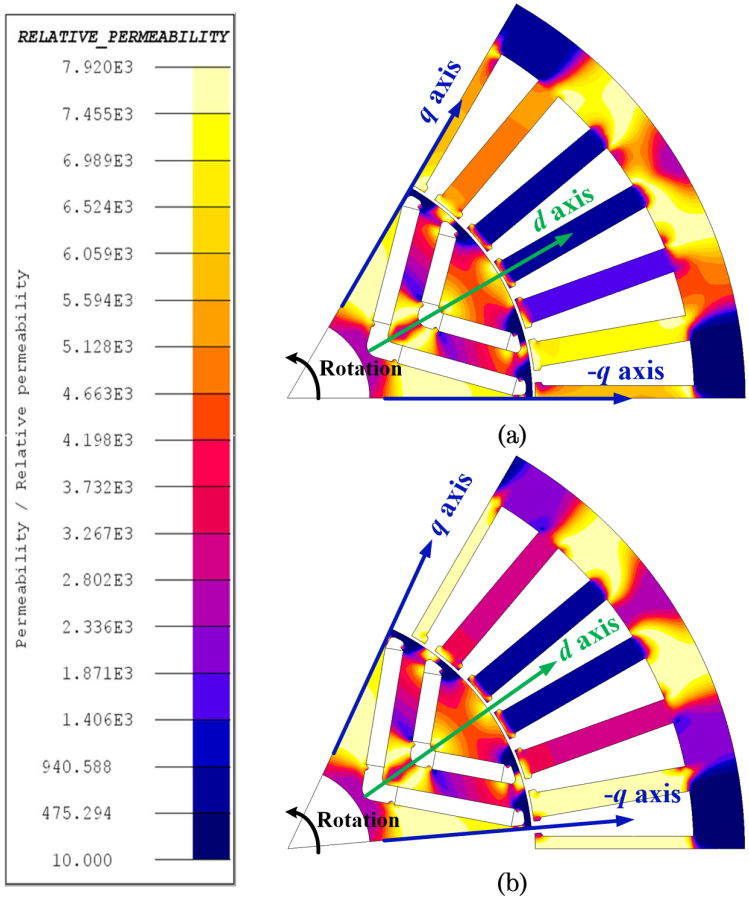

Fig. 3-14. Relative permeability contour at rated torque and base speed working point. (a) Rotor position θ=0°. (b) θ=5°.

Table 3-11. Machine Specifications and Design Parameters

Quantity	Unit	Value
Peak torque	Nm	70
Rated torque	Nm	35
Base Speed	r/min	1350
Max Speed	r/min	4500
Peak power	kW	9.9
Rated power	kW	5
DC link voltage	V	120
Peak current	A	125
Number of pole-pairs	--	3
Number of slots	--	36
Active stack length	mm	118
Stator outer diameter	mm	150
Rotor outer diameter	mm	80

3.5.2 Torque Separation

To separate the instantaneous torque components in (3.6), the specific FP process is needed, as described in the following sub-sections.

3.5.2.1 FP Concept

The basic FP concept is illustrated in Fig. 3-15, where the subscripts "*PM*", "*i*" and "*combined*" denote PM excitation, current excitation and both PM and current excitation, respectively [139]. The combined magneto-motive (magnetic field strength) $H_{combined}$ is the sum of H_{PM} and H_i.

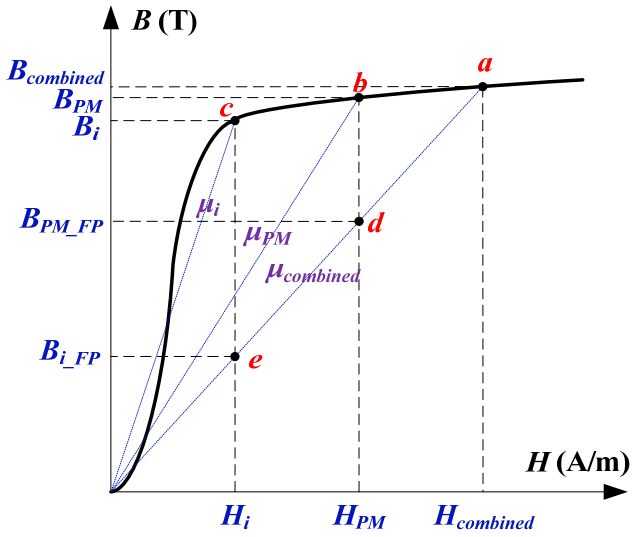

Fig. 3-15. FP concept diagram.

The working points on the B-H curve under the three excitations $H_{combined}$, H_{PM} and H_i are marked as "*a*", "*b*" and "*c*", respectively, and the resultant flux densities are denoted by $B_{combined}$, B_{PM} and B_i, respectively. It can be seen that $B_{PM}+B_i>B_{combined}$, indicating that the flux density of the combined field cannot be obtained by superimposing those from the PM and current excitations separately.

However, if the concept of FP is employed, the apparent relative permeability will be fixed at a specific value $\mu_{combined}$. In other words, the B-H relationship is no longer a non-linear B-H curve but a straight line with a slope of $\mu_{combined}$. Therefore, the working points under H_{PM} and H_i excitations are points "*d*" and "*e*", where the flux densities are B_{PM_FP} and B_{i_FP}. In this case, the $B_{combined}$ equals to the sum of B_{PM_FP} and B_{i_FP}. Hence the superposition principle can be used under FP condition.

3.5.2.2 FP process

In order to separate the torque components in (3.6) using the concept of frozen permeability, a sequence of dedicated processes in one electrical period as illustrated in the flow chart of Fig. 3-16 has to be performed.

First, the magnetic fields in the machine at a given operating condition are solved by time-stepped FE over one electrical period. At each time step, relative permeability of each element in the stator and rotor cores are stored as spatial quantities. Thereafter, the magnetic properties of the stator and rotor cores are replaced by the spatial quantities at the current time step. Subsequently, the excitation sources are changed according to the descriptions in the 2nd column in Table 3-12. By way of example, to calculate "*A*", FE analysis is performed by "Remove magnets" or setting the remanence of the magnets to zero while the current excitation is kept as required. After all the components in Table 3-12 are computed, the permeability of stator and rotor cores will be updated using the spatial quantities at the next time

step. This process will continue until one electrical period is over. Fig. 3-16 shows the complete process for the proposed FP technique.

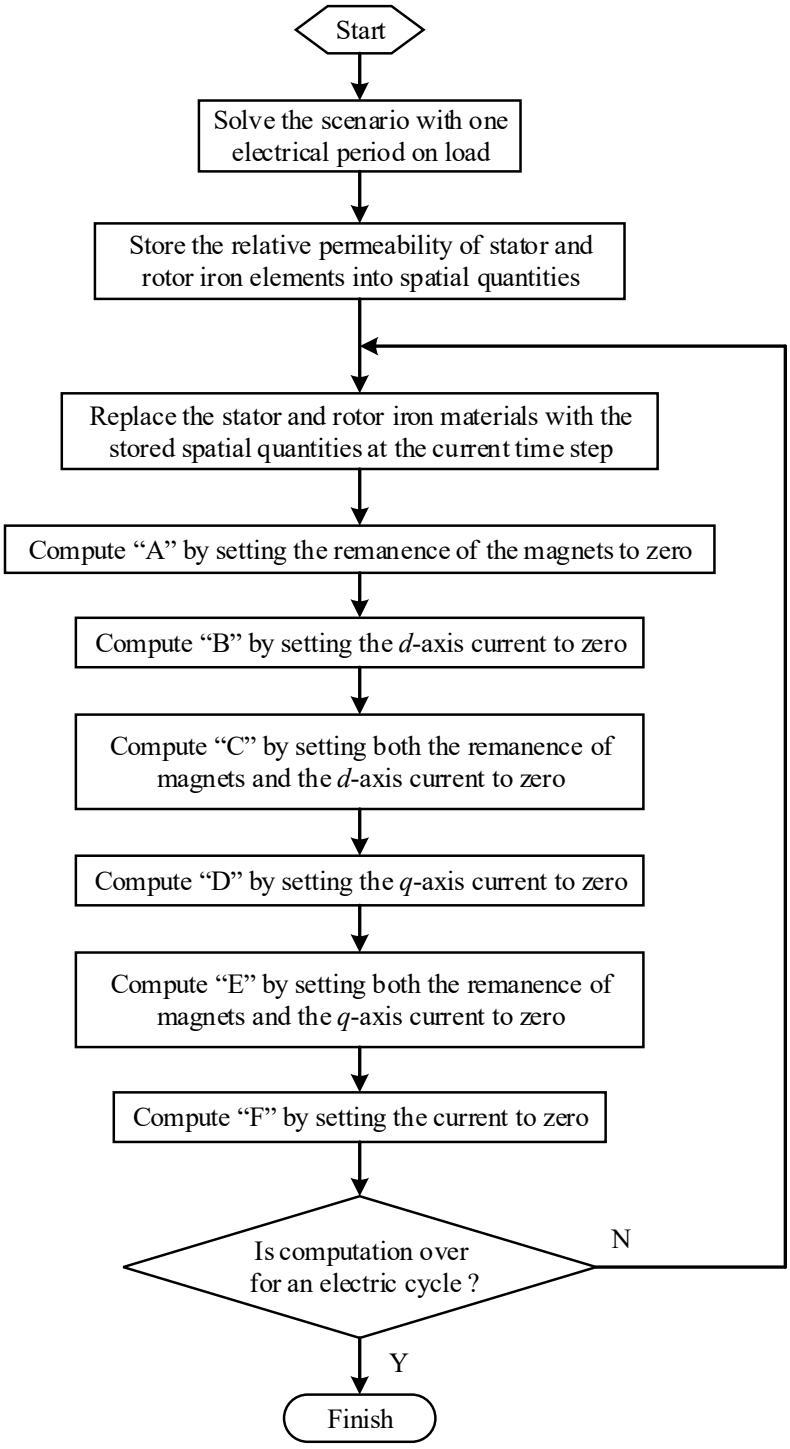

Fig. 3-16. Flow chart of transient FP process.

Table 3-12. Torque Components Separation in the FP Process

Torque terms	Description	Equation
A	Remove magnets	$\frac{m}{2}p\left[\left(L_d - L_q\right)i_d i_q + M_{dq}i_q{}^2 - M_{qd}i_d{}^2\right]$
B	No *d*-axis current	$\frac{m}{2}p\left[\Psi_{md}i_q + M_{dq}i_q{}^2\right] + T_{mr}$
C	Remove magnets & no *d*-axis current	$\frac{m}{2}pM_{dq}i_q{}^2$
D	No *q*-axis current	$\frac{m}{2}p\left[-\Psi_{mq}i_d - M_{qd}i_d{}^2\right] + T_{mr}$
E	Remove magnets & no *q*-axis current	$-\frac{m}{2}pM_{qd}i_d{}^2$
F	No current	T_{mr}

3.5.2.3 Torque components

Based on the FP process described in Fig. 3-16, the torque in (3.6) can be reconstructed by the components listed in Table 3-12 and rewritten as (3.7):

$$T_{em} = A + B - C + D - E - F \tag{3.7}$$

The torque components as listed in Table 3-12, at the rated torque and the base speed working point, are plotted in Fig. 3-17 and the average values are tabulated in Table 3-13. It can be seen that the component "*B*" has the largest contribution because it contains the alignment torque given by $m/2{\cdot}p\Psi_{md}i_q$. The component "*A*" also exhibits significant contribution because it contains reluctance torque terms. The components "*C*" and "*E*" resulting from the cross-coupling effect of *d*- and *q*-axis magnetic paths are relatively small. It should be noted that the component "*F*" resulting from the interaction of the rotor magnetic field with unequal *d*- and *q*-axis reluctances in the stator iron is negative. As seen from the permeability contours in Fig. 3-14, the region from –*q*-axis to *d*-axis in the stator iron exhibits higher permeability than the region from *d*-axis to *q*-axis. This unequal reluctance in these two regions interacts with the magnetic field produced by the permanent-magnets in the rotor, resulting into a negative torque.

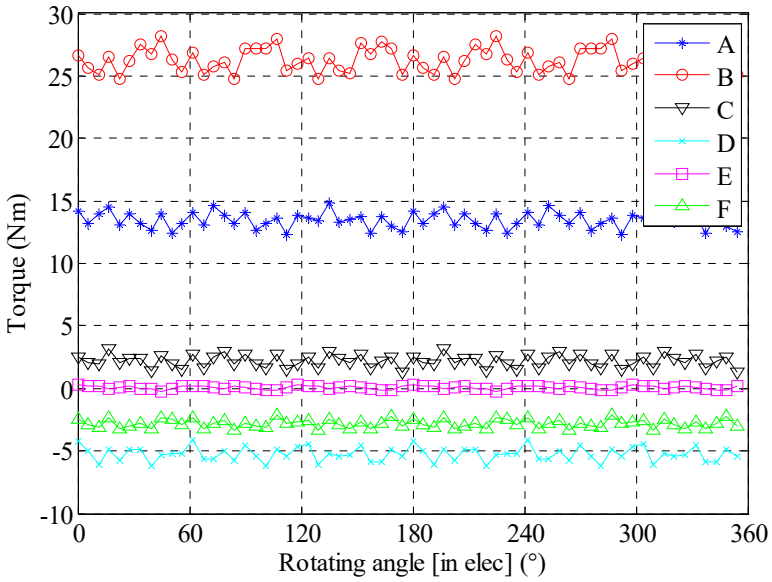

Fig. 3-17. Torque component waveforms at rated torque and base speed.

Table 3-13. Mean Values of Torque Components at Rated Torque and Base Speed

Torque components	Mean torque (Nm)	Mean torque ratio (%)
A	13.5	38.6%
B	26.3	75.1%
C	2.2	6.3%
D	-5.3	-15.1%
E	0.1	0.3%
F	-2.8	-8.0%
Total (*A*+*B*-*C*+*D*-*E*-*F*)	35	100.0%

3.5.2.4 Torque reproduction

To validate the foregoing torque components separation, their sum according to (3.7)is compared with that calculated directly by transient FEA in Fig. 3-18. It can be seen that the analytical model in (3.6) based on the FP concept can accurately represent the torque production mechanism of the IPM machine.

In contrast, the classic torque equation in (3.8), which neglects the *d*- and *q*-axis cross-coupling effect and the term '*F*' in Table 3-12, can be obtained by the torque components listed in Table 3-12. However, the use of this equation with the FP concept results in a relatively large error when compared with the torque obtained by direct FEA or (3.6), as shown in Fig. 3-18. This is due to the fact that the classic torque equation in (3.8) neglects the contribution of

the *d*- and *q*-axis mutual inductance to the reluctance torque and the influence of the unequal reluctances of the *d*- and *q*-axis magnetic circuit in the stator iron on the alignment torque.

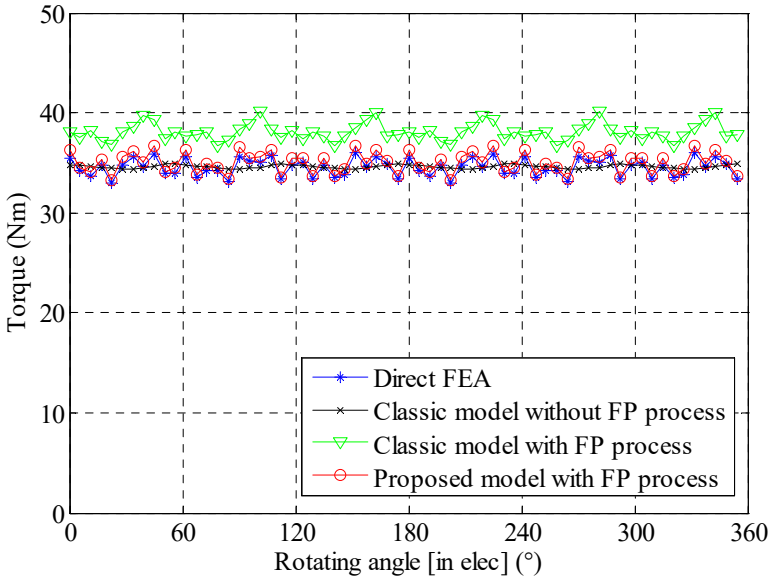

Fig. 3-18. Comparison of reproduced torque waveforms with direct FEA.

$$T_{em} = \frac{m}{2} p\left[\Psi_{md} i_q + \left(L_d - L_q\right) i_d i_q\right] = A + B - 2C - E - F \tag{3.8}$$

The alignment torque and reluctance torque in (3.8) can also be separated by assuming that the *d*-axis flux-linkage due to permanent-magnets only varies with *q*-axis current, viz. the classic model without FP in Fig. 3-18. However, the total torque obtained with this assumption only matches the average torque of the direct FEA. A large deviation in the instantaneous torques waveforms between the two exists, as shown in Fig. 3-18. This is because the torque components due to the cross-coupling effect and the non-uniform reluctance in the stator core are not accounted in the classical model without FP. The high frequency torque ripples in the both components are therefore not present in the torque waveform obtained from the classical model.

Therefore, only the proposed (3.6) can accurately represent the torque production mechanism of the IPM machine using the FP concept.

3.5.3 Reluctance Torque Evaluation

In this section, the reluctance torque calculation based on the classic torque equations and the proposed model is carried out and compared.

The reluctance torque according to the classic torque equation is given in (3.9). This torque component may be obtained by assuming that the *d*-axis flux-linkage due to permanent-magnets is independent of *d*-axis current, or by computing terms "*A*", "*C*" and "*E*" as shown in (3.9) with FP process. The reluctance torque based on the proposed equation can be evaluated according to (3.10), or by computing term "*A*" with FP process. The reluctance torque comparison is shown in Fig. 3-19 and Table 3-14.

$$T_{rel} = \frac{m}{2} p\left[\left(L_d - L_q\right) i_d i_q\right] = A - C - E \tag{3.9}$$

$$T_{rel} = \frac{m}{2} p\left[\left(L_d - L_q\right) i_d i_q + M_{dq} i_q^{\,2} - M_{qd} i_d^{\,2}\right] = A \tag{3.10}$$

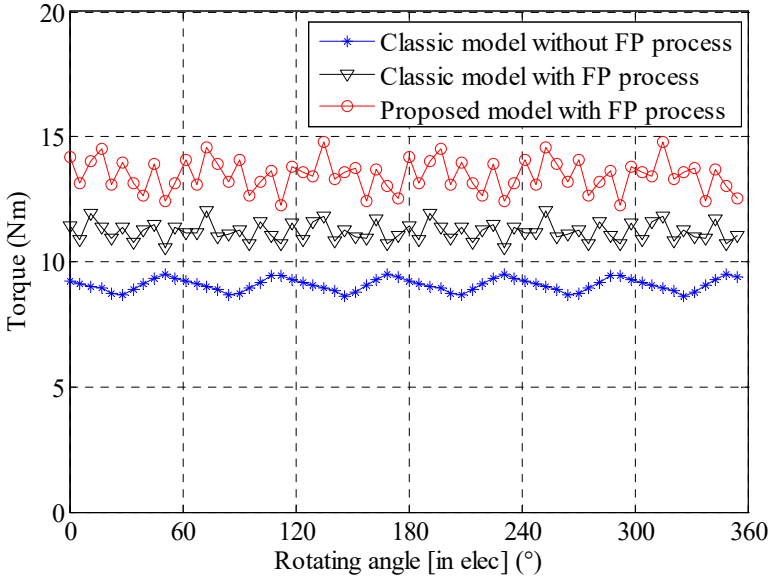

Fig. 3-19. Reluctance torque waveform comparison.

Table 3-14. Reluctance Torque Comparison

Item	Classic model without FP process	Classic model with FP process	Proposed model with FP process
Mean reluctance torque (Nm)	9.1	11.2	13.5
Mean reluctance torque ratio (%)	25.9%	32.0%	38.5%

It can be seen that the reluctance torque calculations based on the classic models with and without the FP process under-estimate the reluctance torque compared with the proposed model with the FP process. This is attributable to two reasons. First, the classic models neglect the torque component contributed by the mutual inductance, viz. component "*C*" and "*E*" whose mean values are positive, which can be observed in Fig. 3-17 and Table 3-13. Secondly, the negative torque component T_{mr} shown in Fig. 3-17 resulting from the FP process is attributed to the alignment torque rather than the reluctance torque in both the classic model and proposed model with the FP process. This component is not present in the classical model without FP given by (3.1). Consequently, the alignment torque predicted by the FP process is lower while the reluctance torque is higher compared with those predicted using the classical model without FP.

Separation of the two torque components with non-linear machine characteristics has to be based on an assumption, and the FP process is no exception. However, the torque separation based on the proposed FP concept should be more accurate than the classic approach that neglects the torque due to mutual coupling and assumes the PM flux-linkage is independent with the *d*-axis current, both of which deviate more from the real physical condition at a high level of saturation.

3.6 Conclusion

PMA-SynRM with concentrated fractional-slot non-overlapping winding (12-slot 10-pole) has advantages such as short end-winding, high copper packing factor, low manufacturing cost and the low torque ripple. However,

it exhibits relatively high iron loss, slightly low reluctance torque ratio and the low efficiency over NEDC. Therefore, this winding configuration is more suited for in-wheel motor application where the maximum speed is low and the disadvantage of high iron loss is less significant.

PMA-SynRM with conventional fractional-slot non-overlapping winding (12-slot 8-pole) is of competitive energy efficiency, short end-winding, high copper packing factor, low manufacturing cost and the good field weakening capability. However, excessive torque ripple is a major issue of concern for EV traction applications. This problem needs to be addressed in future.

PMA-SynRM with fractional-slot overlapping winding (18-slot 8-pole) has slightly longer end-winding and higher manufacturing cost compared with the other two candidate fractional-slot PMA-SynRM machines. However, it possesses high efficiency over a very wide operating region, low torque ripple, high reluctance torque ratio and good field weakening capability, and therefore it is attractive for high speed and low torque ripple EV applications.

Moreover, this study shows that significant reluctance torque can be produced in PMA-SynRMs with concentrated fractional-slot non-overlapping windings. The attainable reluctance torque from these winding configurations is comparable to that from PMA-SynRMs with conventional distributed windings. Therefore, the reluctance torque component is more to do with the rotor topology and design. The high salience feature of the PMA-SynRM rotor tends to reduce the influence of stator MMF harmonics on the attainable reluctance torque. However, the presence of these harmonics in the stator and rotor does increase iron loss, particular in high speeds. This is one drawback of PMA-SynRMs with the concentrated non-overlapping windings.

Additionally, the characteristic current cannot be taken alone as a criterion to evaluate the field weakening capability for PMA-SynRMs. In this type of machines, the characteristic current is usually lower than the

maximum permissible current. With a low characteristic current, the *d*-axis current may exceed the characteristic current, and produce a *q*-axis voltage component which may compromise the performance of the machine in deep field weakening regions.

Regarding the reluctance evaluation, this chapter also shows that using the classic models which assume that the PM flux-linkage is independent with *d*-axis current, can only match the average total torque but not the instantaneous torque waveform. However, the proposed model based on FP can match both average and instantaneous torque very well with the direct FEA results. Therefore, a more accurate model which allows for separation of torque components via FP process for IPM machines is presented. The proposed model can reproduce the instantaneous torque waveform at any load condition, and hence provides a more accurate evaluation of reluctance torque compared to the conventional methods.

CHAPTER 4 A Generic Approach to Reduction of Magneto-motive Force Harmonics in Permanent-magnet Machines with Concentrated, Multiple 3-phase Windings

4.1 Introduction

Permanent-Magnet Synchronous Machines (PMSMs) exhibit high torque density and high energy efficiency over a wide operation range, which are preferable attributes for EV traction applications [1].

In PMSMs, SPMs produce electromagnetic torque purely from the interaction of the permanent-magnet field with armature currents [141, 142]. Without flux focusing effect in SPMs, rare-earth permanent-magnets with a high remanence (such as sintered NdFeB) are usually employed to improve torque density and this often results in relatively more magnet material usage. However, the limited reserves and high cost of the rare-earth materials restrict the potential of PM machine topologies, such as SPMs, which uses more rare-earth magnets, in EV traction applications [143-145]. Further, the conflicting requirements for high torque at low speeds and low back-EMF at high speeds in EV tractions are very difficult to meet without increase in inverter VA rating.

In contrast, IPMs with low cost magnet material (such as ferrite and bonded NdFeB) provide more flexibility to strike a good balance between performance and cost, due to both the reluctance torque contribution and flux focusing effect [146, 147]. Hence, IPMs, including PMA-SynRMs, proposed in recent years, present a promising solution for EV traction applications [67, 148, 149].

Compared to the conventional distributed winding configurations, the advantages of the fractional-slot non-overlapping (concentrated) winding

configurations include the high copper packing factor (slot fill factor) particularly with segmented stator structure, short end-winding length, low cogging torque, good field weakening capability due to relatively large *d*-axis inductance, and good fault tolerant capability owing to low mutual inductance [150]. However, one of the key challenges of utilising concentrated winding in IPMs is the high rotor eddy-current losses in both magnets and rotor iron due to the presence of a large number of lower and higher order space harmonics in the stator MMF [45, 151]. These MMF harmonics also result in other undesirable effects, such as acoustic noise and vibrations, and the localised core saturation that tend to reduce reluctance torque.

In literature, a number of methods have been proposed to cancel or reduce MMF harmonics, such as employing non-uniform tooth width, using asymmetric number of turns, and applying phase shift by doubling slot numbers [50, 152, 153]. The first two methods compromise the machine performance and the third technique no longer has the manufacture advantage of concentrated windings. A delta-star connection is utilised to reduce MMF harmonics by shifting the current phase angle in the delta and star connected windings in [154]. However, the shift angle is restricted to 30°, 150° and 270°, due to the phase angle limits of the delta-star connection, and hence it compromises the MMF harmonic cancellation effect. Moreover, this technique yields a very low winding factor for the working harmonic. Special magnetic flux barriers in stator yoke are introduced in [155] to reduce flux density sub-harmonics in air-gap by changing the magnetic reluctance in specific stator core location. Nevertheless, the mechanical stiffness of the stator is reduced significantly with presence of the flux barriers. This will result in a lower stator natural frequency and increase the risk of resonance within a speed operating range. Multiple 3-phase sets with an appropriate phase shift between them have also been devised to cancel out the undesirable MMF harmonics [156, 157]. However, this approach leads to an

overlapping winding configuration, compromising advantages of the concentrated windings.

To reduce the undesirable MMF harmonics while retain the advantages of the concentrated windings, this chapter proposes a general approach to cancelling out all the MMF sub-harmonics and some higher order harmonics in concentrated windings by employing multiple 3-phase sets. Subsequently, a 9-phase 18-slot 14-pole IPM machine is devised based on the proposed MMF harmonic cancellation approach using multiple 3-phase winding configurations. A global optimisation against NEDC cycle efficiency is performed before the machine performances are evaluated. A 10kW machine prototype is built and tested in generating mode for the experimental validation.

4.2 Generic Harmonic-based MMF Expressions of Conventional 3-Phase Windings

Assuming *ABC* windings are symmetric and have the same number of turns, the MMF distribution of each phase due to unit current, known as the winding function, can be expressed as Fourier series given in (4.1).

$$\begin{aligned} n_A(\theta_m) &= \sum_h \left[N_h \cos\left(h\theta_m + \beta_h\right) \right] \\ n_B(\theta_m) &= \sum_h \left[N_h \cos\left(h\theta_m - h\theta_{phm} + \beta_h\right) \right] \\ n_C(\theta_m) &= \sum_h \left[N_h \cos\left(h\theta_m + h\theta_{phm} + \beta_h\right) \right] \end{aligned} \tag{4.1}$$

where h denotes the harmonic order with respect to one mechanical revolution, N_h is the magnitude of the h^{th} order harmonic, β_h is the phase angle of the h^{th} order harmonic of phase A, θ_{phm} is the mechanical angular displacement between two adjacent phases of a 3-phase winding, and θ_m denotes the space angle at a point of interest in the air-gap with respect to phase A axis as shown in Fig. 4-1. Due to the symmetrical distribution of a 3-

phase winding, θ_{phm}=120° or -120°, depending on the direction of rotation of the MMF working harmonic.

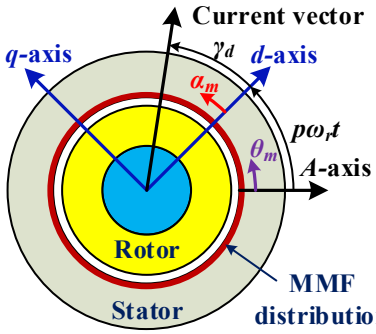

Fig. 4-1. Current vector diagram in *dq*0 and *ABC* coordinate systems.

Assuming the current amplitudes in all the phases are identical, the phase currents are expressed by (4.2).

$$\begin{aligned} i_A &= I\cos\left(p\omega_r t+\gamma_d\right) \\ i_B &= I\cos\left(p\omega_r t+\gamma_d-120°\right) \\ i_C &= I\cos\left(p\omega_r t+\gamma_d+120°\right) \end{aligned} \tag{4.2}$$

where I is the current amplitude, p is the pole pair number, ω_r is the rotor angular speed, t is the time, and γ_d is the phase angle between the current vector and the rotor reference axis (d-axis) as shown in Fig. 4-1.

The combined MMF of all the 3 phase windings, F_s, is given in (4.3). It should be noted that F_s in (4.3) is derived in a stationary coordinate system in that θ_m denotes the space angle with respect to phase A axis as shown in Fig. 4-1. To investigate the influence of stator MMF on rotor eddy-current loss more conveniently, F_s is rewritten with respect to the rotary coordinate system which is synchronous with the rotor, as given by (4.4).

$$
\begin{aligned}
F_s &= n_A i_A + n_B i_B + n_C i_C \\
&= \sum_h N_h I \cos(h\theta_m + \beta_h)\cdot\cos(p\omega_r t + \gamma_d) \\
&\quad + \sum_h N_h I \cos(h\theta_m - h\theta_{phm} + \beta_h)\cdot\cos(p\omega_r t + \gamma_d - 120°) \\
&\quad + \sum_h N_h I \cos(h\theta_m + h\theta_{phm} + \beta_h)\cdot\cos(p\omega_r t + \gamma_d + 120°) \\
&= \frac{1}{2}\sum_h N_h I[\cos(h\theta_m - p\omega_r t + \beta_h - \gamma_d) + \cos(h\theta_m + p\omega_r t + \beta_h + \gamma_d)] \\
&\quad + \frac{1}{2}\sum_h N_h I[\cos(h\theta_m - p\omega_r t + \beta_h - \gamma_d - h\theta_{phm} + 120°) \\
&\qquad\qquad + \cos(h\theta_m + p\omega_r t + \beta_h + \gamma_d - h\theta_{phm} - 120°)] \\
&\quad + \frac{1}{2}\sum_h N_h I[\cos(h\theta_m - p\omega_r t + \beta_h - \gamma_d + h\theta_{phm} - 120°) \\
&\qquad\qquad + \cos(h\theta_m + p\omega_r t + \beta_h + \gamma_d + h\theta_{phm} + 120°)] \\
&= \frac{1}{2}\sum_h N_h I[1 + 2\cos(h\theta_{phm} - 120°)]\cdot\cos(h\theta_m - p\omega_r t + \beta_h - \gamma_d) \\
&\quad + \frac{1}{2}\sum_h N_h I[1 + 2\cos(h\theta_{phm} + 120°)]\cdot\cos(h\theta_m + p\omega_r t + \beta_h + \gamma_d)
\end{aligned}
\tag{4.3}
$$

$$
\begin{aligned}
F_s &= \frac{1}{2}\sum_h N_h I[1 + 2\cos(h\theta_{phm} - 120°)]\cdot\cos[h\alpha_m + (h-p)\omega_r t + \beta_h - \gamma_d] \\
&\quad + \frac{1}{2}\sum_h N_h I[1 + 2\cos(h\theta_{phm} + 120°)]\cdot\cos[h\alpha_m + (h+p)\omega_r t + \beta_h + \gamma_d]
\end{aligned}
\tag{4.4}
$$

where α_m is the space angle with respect to the d-axis as shown in Fig. 4-1, and hence $\alpha_m = \theta_m - \omega_r t$.

Therefore, the forward and backward rotating MMF harmonics are given in (4.5) and (4.6) respectively.

$$
F_f = \frac{1}{2}\sum_h N_h I[1 + 2\cos(h\theta_{phm} - 120°)]\cdot\cos[h\alpha_m + (h-p)\omega_r t + \beta_h - \gamma_d] \tag{4.5}
$$

$$
F_b = \frac{1}{2}\sum_h N_h I[1 + 2\cos(h\theta_{phm} + 120°)]\cdot\cos[h\alpha_m + (h+p)\omega_r t + \beta_h + \gamma_d] \tag{4.6}
$$

For a machine with Q slots and p pole pairs, its periodicity r is subject to the greatest common divider between Q and p, as described in (4.7).

$$
r = \mathrm{GCD}\{Q, p\} \tag{4.7}
$$

The orders of harmonics with non-zero magnitudes for the single phase winding function in (4.1) are summarised in Table 4-1. By way of example, in a double layer winding with the even Q/r, the orders of harmonics with non-zero magnitudes for the single phase winding function are odd numbers $2(h\text{-}1)r$ except jQ, $j\in\mathbf{Z}$, where $\mathbf{Z}$ denotes the positive integer set. This is because the even Q/r can form a symmetric pattern with opposite phasors that are π radians out of phase [158]. The integer multiples of the slot number, jQ, are the numbers of harmonic orders which are cancelled out by the mechanical periodicity. For a 3-phase configuration, windings are uniformly displaced in space with respect to each other by 120° electrical degrees. Therefore, all triplen MMF harmonics of the 3-phase windings are eliminated in Q/r slots. This can also be observed in (4.5) and (4.6), where the terms $[1+2\cos(h\theta_{phm}\text{-}120°)]$ and $[1+2\cos(h\theta_{phm}+120°)]$ are derived from the 3-phase configuration. Given that jQ is a subset of $3jr$, the orders of MMF harmonics with non-zero magnitudes for a double layer 3-phase winding with an even Q/r are odd numbers $2(h\text{-}1)r$ except $3jr$. The harmonic order numbers of the other winding configurations in Table 4-1 can also be derived in the same way.

Table 4-1. Orders of Harmonics with Non-zero Magnitudes

Winding type	Double layer winding		
Condition	Q/r is even		Q/r is odd
Non-zero harmonic orders for winding function	$(2h\text{-}1)r$ except $jQ, j\in\mathbf{Z}$		hr except $jQ, j\in\mathbf{Z}$
Non-zero harmonic orders for 3-phase MMF	$(2h\text{-}1)r$ except $3jr, j\in\mathbf{Z}$		hr except $3jr, j\in\mathbf{Z}$
Winding type	Single layer winding		
Condition	$Q/(2r)$ is even	$Q/(2r)$ is odd	Q/r is odd & r is even
Non-zero harmonic orders for winding function	$(2h\text{-}1)r$ except $jQ, j\in\mathbf{Z}$	hr except $jQ, j\in\mathbf{Z}$	$hr/2$ except $jQ, j\in\mathbf{Z}$
Non-zero harmonic orders for 3-phase MMF	$(2h\text{-}1)r$ except $3jr$, $j\in\mathbf{Z}$	hr except $3jr$, $j\in\mathbf{Z}$	$hr/2$ except $3jr/2$, $j\in\mathbf{Z}$

Compared to conventional distributed windings, the periodicity r in factional-slot concentrated windings is relatively small. Therefore, the latter exhibits more low-order MMF harmonics than the former. To reduce the

MMF harmonics in concentrated windings, a new "degree of freedom" in the MMF harmonic cancellation mechanism will be introduced in Section 4.4.

4.3 MMF Harmonic Cancellation Principle

4.3.1 Basic Concentrated Winding Types

A single coil in Fig. 4-2 (a) exhibits a rectangular MMF waveform, as illustrated in Fig. 4-3. Therefore, the MMF spectrum of a single coil contains all the integer order harmonics, as shown in Fig. 4-4.

To cancel out the most MMF harmonics, a second coil with 180° mechanical phase shift in space with respect to the first coil is introduced, as shown in winding type 1 in Fig. 4-2 (b) and winding type 2 in Fig. 4-2 (c). For the odd pole pair number, the second coil should have opposite polarity with respect to the first coil, in order that both coils produce torque in the same direction. In doing so, the MMF of the second coil cancels out all the even MMF harmonics of the first coil, and hence the MMF of winding type 1 only contains odd order harmonics, as presented in Fig. 4-4. When the pole pair number is even, the winding type 2, shown in Fig. 4-3 where the two coils have the same polarity should be selected, to cancel out all the odd order harmonics, as shown in Fig. 4-4.

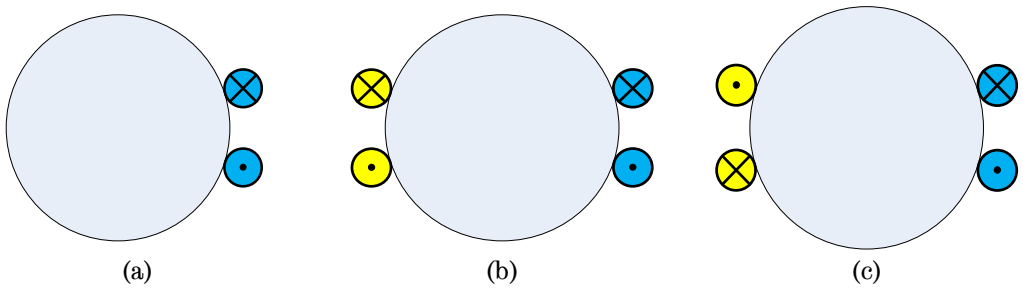

Fig. 4-2. Basic concentrated winding type schematics. (a) Single coil. (b) Winding type 1: opposite polarity. (c) Winding type 2: same polarity.

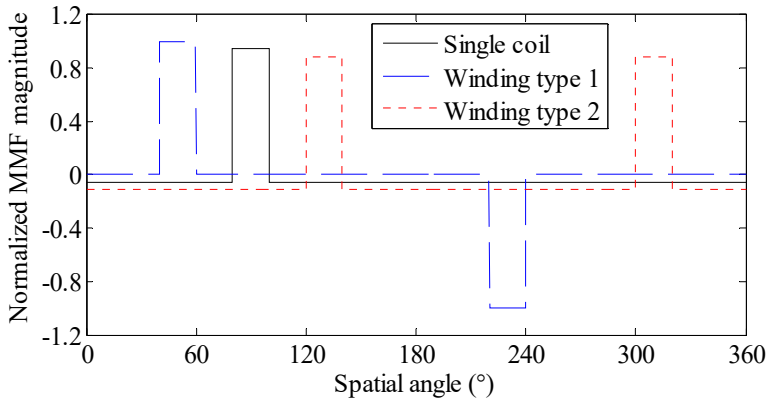

Fig. 4-3. MMF waveforms of basic concentrated winding types.

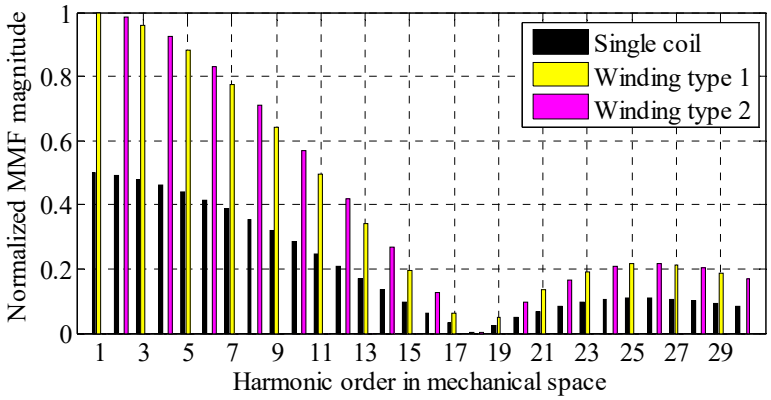

Fig. 4-4. MMF spectra of basic concentrated winding types.

4.3.2 Single 3-phase Harmonic Cancellation

In a conventional 3-phase machine, three phase windings are uniformly displaced in space with respect to each other by 120° electrical degrees. Therefore, all triplen MMF harmonics of the 3-phase windings are eliminated. Fig. 4-5 compares the MMF spectra of single phase winding and 3-phase windings with an odd pole pair number. The MMF harmonic magnitudes of a 3-phase winding are 1.5 times those of a single phase winding.

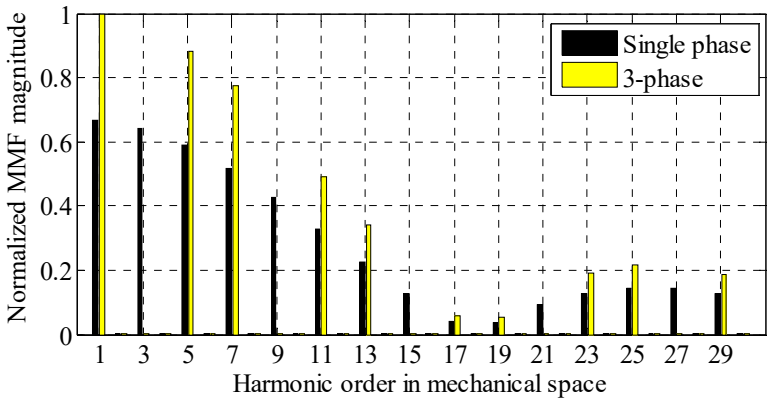

Fig. 4-5. MMF spectra comparison of single and 3-phase windings, with an odd pole pair number.

4.3.3 Multiple 3-phase Harmonic Cancellation

As shown in (4.5) and (4.6), the forward and backward MMFs of a conventional 3-phase winding are travelling waves, and the terms $[1+2\cos(h\theta_{phm}-120°)]$ and $[1+2\cos(h\theta_{phm}+120°)]$ lead to the cancellation of all triplen MMF harmonics. To eliminate more MMF harmonics, this chapter employs a multiple 3-phase winding configuration to introduce an additional "degree of freedom" in the MMF harmonic cancellation mechanism.

If one phase contains a minimum of two coils, it is possible to devise multiple 3-phase configurations if the total number of slots is no less than 12. By way of example, for an 18-slot 14-pole combination, three 3-phase windings can be developed. The three 3-phase windings are uniformly arranged in space but with a specific spatial phase angle with respect to each other, as shown in Fig. 4-6 (a). In addition, the phase shift in time for the currents in each 3-phase set can also be selected in order to eliminate unwanted harmonics. The condition to cancel out a given order MMF harmonic is to select appropriate space and time phase shifts so that the MMF vectors produced by the three 3-phase windings form a balanced 3-phase system, as illustrated in Fig. 4-6 (c), while their working harmonic vectors overlap with each other, as shown in Fig. 4-6 (b).

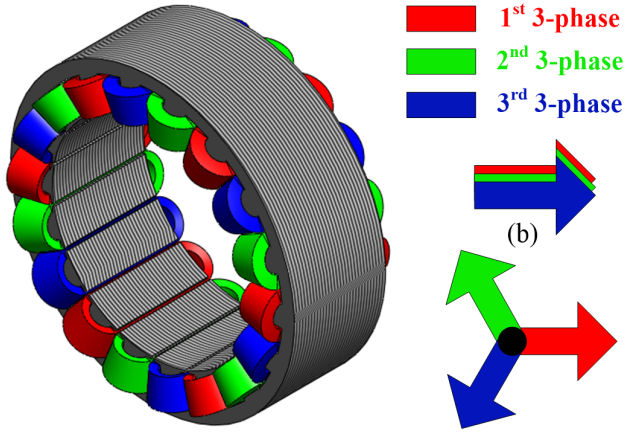

Fig. 4-6. Schematics for the three 3-phase concentrated winding configuration with 18 coils. (a). Winding arrangement. (b). MMF vectors for the working harmonic. (c). MMF vectors for unwanted harmonics.

Based on the foregoing discussion, -260° phase shift in space and 20° phase shift in time are selected for the 18-slot 14-pole 9-phase (three 3-phase) configuration. The MMF spectra of the single 3-phase and three 3-phase windings are shown in Fig. 4-7. It can be seen that the 1st, 5th, 13th, 17th, 19th, 23rd ··· order harmonics are cancelled out whereas the 7th (working harmonics for 14-pole), 11th, 25th, 29th ··· order harmonics are combined. Quantitative determination of the space and time phase shifts will be described in the following section.

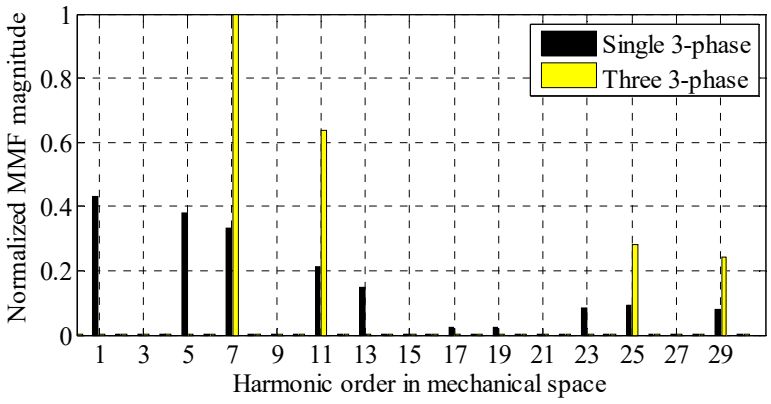

Fig. 4-7. MMF spectra comparison of single 3-phase and three 3-phase windings, with 18-slot 14-pole configuration.

4.4 Generic Harmonic-based MMF Expressions of Multiple 3-Phase Windings

This section will derive the generic expressions of the MMF in a multiple 3-phase winding. Firstly, assuming all 3-phase windings are symmetric and have the same number of turns, the generic MMF distribution of a phase winding in the k^{th} 3-phase set due to unit current, known as the winding function, can be expressed as a Fourier series given in (4.8).

$$n_k(\theta_m) = \sum_h \left[N_h \cos\left(h\theta_m + \beta_{kh}\right) \right] \tag{4.8}$$

where k denotes the k^{th} 3-phase set, β_{kh} is the phase angle of the h^{th} order spatial harmonic of the k^{th} set 3-phase winding.

Therefore, the winding functions of each phase (Ak, Bk and Ck) of the k^{th} 3-phase set can be written as (4.9).

$$\begin{aligned} n_{Ak} &= n_k(\theta_m) \\ n_{Bk} &= n_k\left(\theta_m - \theta_{phm}\right) \\ n_{Ck} &= n_k\left(\theta_m + \theta_{phm}\right) \end{aligned} \tag{4.9}$$

Assuming the current amplitudes in all the phases are identical, the phase currents of the k^{th} 3-phase set are expressed by (4.10).

$$\begin{aligned} i_{Ak} &= I\cos\left[p\omega_r t + \gamma_d - (k-1)\theta_\Delta \right] \\ i_{Bk} &= I\cos\left[p\omega_r t + \gamma_d - (k-1)\theta_\Delta - 120^\circ \right] \\ i_{Ck} &= I\cos\left[p\omega_r t + \gamma_d - (k-1)\theta_\Delta + 120^\circ \right] \end{aligned} \tag{4.10}$$

where θ_Δ is the phase shift angle of the currents between the $(k+1)^{\text{th}}$ and k^{th} 3-phase sets.

The combined MMF distribution of multiple 3-phase windings is given in (4.11).

$$F_s = \sum_k \left(n_{Ak} i_{Ak} + n_{Bk} i_{Bk} + n_{Ck} i_{Ck} \right) \tag{4.11}$$

Substituting (4.9) and (4.10) into (4.11), the forward and backward MMF equations can be derived and given in (4.12) and (4.13) respectively.

$$\begin{aligned} F_f = \frac{1}{2} \sum_h \Big\{ & N_h I [1 + 2\cos(h\theta_{phm} - 120°)] \\ & \cdot \sum_k \cos[h\alpha_m + (h-p)\omega_r t + \beta_{kh} - \gamma_d + (k-1)\theta_\Delta] \Big\} \end{aligned} \tag{4.12}$$

$$\begin{aligned} F_b = \frac{1}{2} \sum_h \Big\{ & N_h I [1 + 2\cos(h\theta_{phm} + 120°)] \\ & \cdot \sum_k \cos[h\alpha_m + (h+p)\omega_r t + \beta_{kh} + \gamma_d - (k-1)\theta_\Delta] \Big\} \end{aligned} \tag{4.13}$$

Assuming that the currents in each 3-phase set are independently controlled, the h^{th} order MMF harmonic can be cancelled out, if the combined phase shift angles between the k^{th} and $(k+1)^{\text{th}}$ 3-phase sets denoted as θ_{fw} and θ_{bw} for the forward and backward MMF harmonics satisfy (4.14) and (4.15), respectively.

$$\theta_{fw} = \beta_{(k+1)h} - \beta_{kh} + \theta_\Delta = \pm 360° / K + q_f 360°, q_f \in \mathbf{Z} \tag{4.14}$$

$$\theta_{bw} = \beta_{(k+1)h} - \beta_{kh} - \theta_\Delta = \pm 360° / K + q_b 360°, q_b \in \mathbf{Z} \tag{4.15}$$

where K is the number of 3-phase sets. The above conditions lead to the second summation in (4.12) and (4.13) becoming zero and hence the h^{th} order harmonic is eliminated. Thus, the condition, which satisfies (4.14) and (4.15), is a new "degree of freedom" in the MMF harmonic cancellation mechanism. It should be noted that realisation of the conditions in (4.14) and (4.15) requires appropriate phase shifts between two neighbouring 3-phase sets in both space and time, denoted by $\beta_{(k+1)h}$-β_{kh} and θ_Δ, respectively.

The selection of K (the number of 3-phase sets) should follow the principle that the single phase winding function N_h only contains even or

order harmonics. Therefore, it is recommended that the number of slots per phase should be an even number.

4.5 Application to 18-slot 14-pole

Based on the foregoing multiple 3-phase winding technique, a 9-phase 18-slot 14-pole winding configuration (three 3-phase sets) is developed in this section. The 9-phase, 18-slot instead of 6-phase or 18-phase is employed such that the number of slots per phase is 2 in a 9-phase configuration and thereby the single phase winding function N_h only contains odd order harmonics. In this way, minimal MMF harmonic contents can be reached.

-260° phase shift in space and 20° phase shift in time are selected in the proposed 9-phase 18-slot 14-pole winding configuration. The selection of space and time phase shifts will be described later. Fig. 4-8 depicts the detailed winding arrangements of the conventional 3-phase and the proposed 9-phase 18-slot 14-pole windings.

To demonstrate the MMF harmonic cancellation effects in the proposed 9-phase 18-slot 14-pole winding configuration, Table 4-2 lists the spatial shift angle $\beta_{(k+1)h}$-β_{kh} for MMF harmonic orders up to 29. The spatial shift of the 1st order MMF harmonic is -260° because phase *D* is 13 slots lagging phase *A* and each slot occupies 20° mechanical degrees in space, as shown in Fig. 4-8 (b). When the current phase shift angle θ_Δ is selected to be 20°, the combined MMF harmonic phase shift angle θ_{fw}= $\beta_{(k+1)h}$-β_{kh}+θ_Δ becomes -240° (or 120°), and satisfies (4.14). Hence the 1st order forward rotating harmonic is eliminated. It should be noted that the 1st order backward rotating harmonic does not exist in the machine, and this is denoted by "×" in Table 4-2. Similarly, the combined phase shift angles θ_{fw} and θ_{bw} of the 5th, 13th, 17th, 19th, 23rd ··· order MMF harmonics satisfy (4.14) and (4.15), and therefore they are cancelled out.

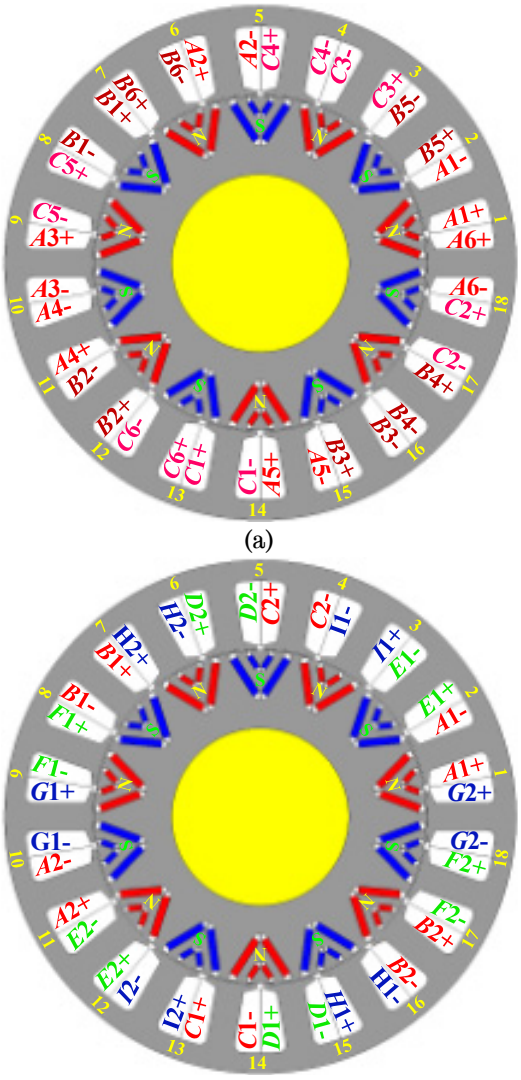

(a)

(b)

Fig. 4-8. Schematics of the conventional 3-phase and the proposed 9-phase 18-slot 14-pole winding configurations. (a) 3-phase. (b) 9-phase.

Table 4-2. Cancellation of Forward and Backward MMF Harmonics for 9-phase 18-slot 14-pole Winding Configuration

Harmonic order h	Shift spatial angle $\beta_{(k+1)h}$-β_{kh}	Forward phase angle $\theta_{fw}=\beta_{(k+1)h}$-$\beta_{kh}+\theta_{\Delta}$	Backward phase angle $\theta_{bw}=\beta_{(k+1)h}$-$\beta_{kh}-\theta_{\Delta}$
1	-260° (or 100°)	120°	×
5	-1300° (or 140°)	×	120°
7	-1820° (or 340°)	0°	×
11	-2860° (or 20°)	×	0°
13	-3380° (or 220°)	240°	×
17	-4420° (or 260°)	×	240°
19	-4940° (or 100°)	120°	×
23	-5980° (or 140°)	×	120°
25	-6500° (or 340°)	0°	×
29	-7540° (or 20°)	×	0°

The reduction in MMF harmonics can also be observed in the comparison of 3-phase and 9-phase MMF waveforms shown in Fig. 4-9 and MMF spectra shown in Fig. 4-10. The waveforms in Fig. 4-9 are normalised to the fundamental MMF magnitude of the conventional 3-phase 18-slot 14-pole machine. It can be seen that the MMF waveform of the proposed 9-phase winding configuration exhibits more variation steps and hence less harmonics. From Fig. 4-10, it can also be seen that by employing the proposed winding configuration, the 1st, 5th, 13th, 17th, 19th, 23rd ··· order harmonics are cancelled out while the 7th (working harmonic for 14-pole), 11th, 25th, 29th ··· order harmonics slightly increase due to higher winding distribution factors.

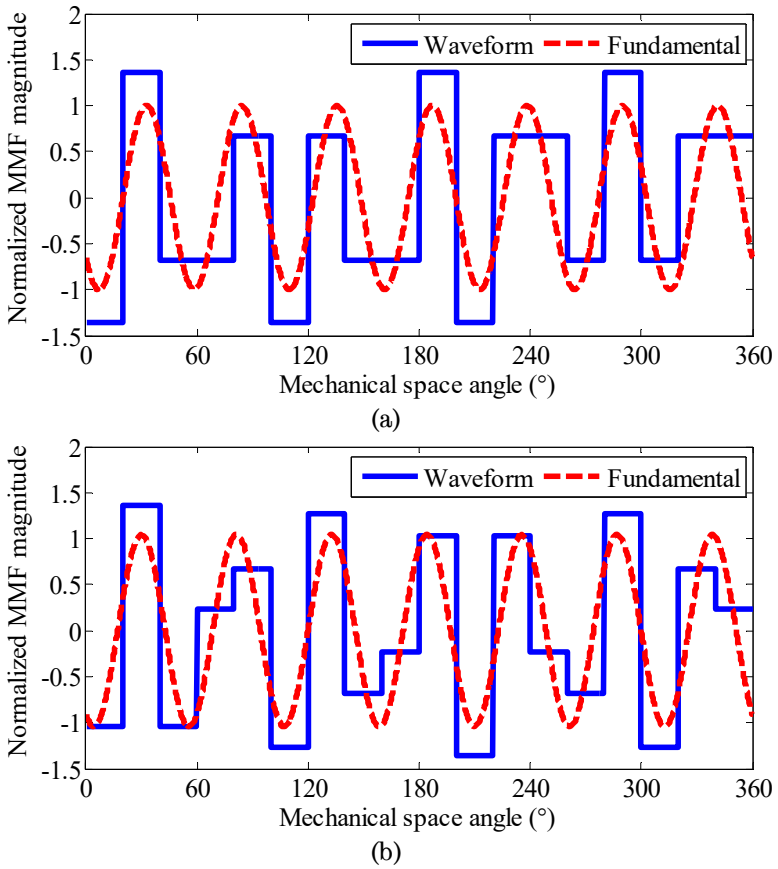

Fig. 4-9. Comparison of normalised MMF waveforms of 3-phase and 9-phase 18-slot 14-pole winding configurations. (a) 3-phase. (b) 9-phase.

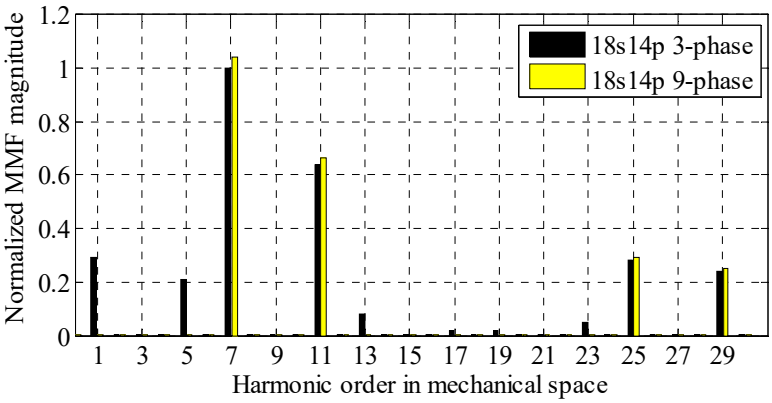

Fig. 4-10. Comparison of normalised MMF spectra of 3-phase and 9-phase 18-slot 14-pole winding configurations.

The foregoing theory is validated by the FEA results shown in Fig. 4-11. To eliminate distortions caused by saturation and rotor asymmetry, linear B-H curve of the iron-core and isotropic rotor are employed. It can be seen that the normalised air-gap flux density spectra from the FEA are very similar to the analytical MMF results in Fig. 4-10. The minor difference in the 11th and 25th order harmonics are due to the slotting effects which are not considered in the analytical calculation, because the stationary 18 slots can produce the backward 11th and forward 25th order harmonics seen from the rotor with 7 pole-pairs rotating in the forward direction.

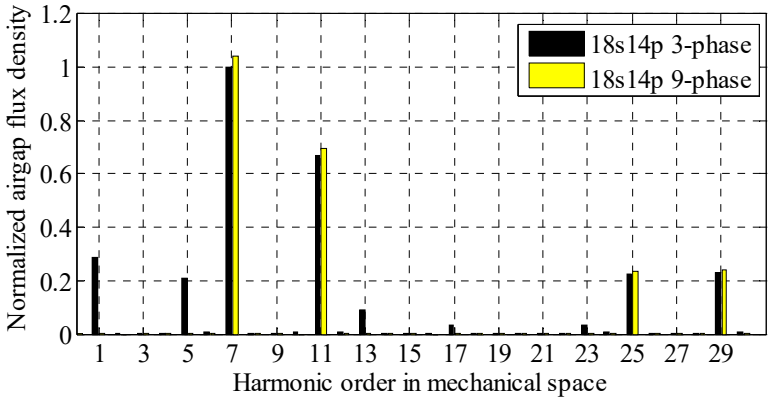

Fig. 4-11. Comparison of normalised air-gap flux density spectra of 3-phase and 9-phase 18-slot 14-pole winding configurations.

4.6 Machine Design and Global Optimisation

On the basis of the proposed multiple 3-phase winding configuration, a new 9-phase 18-slot 14-pole IPM machine is designed and optimised. The

design specifications and constraints are listed in Table 4-3. The optimisation objective is to maximise the NEDC efficiency over 12 representative working points as proposed in [159]. The 12 representative points for the energy consumption over NEDC are illustrated in the torque-speed profile shown in Fig. 4-12, where the peak and continuous power envelopes are also demonstrated. It should be noted that design optimisation against any other representative driving cycle can be performed in a similar manner.

Table 4-3. Design Specification and Optimisation Constraints

Quantity	Unit	Value
Peak power	kW	10
Rated continuous power	kW	5.0
Base speed	r/min	1350
Maximum operation speed	r/min	4500
Maximum cruise speed	r/min	5050
Peak torque at base speed	Nm	70
Rated torque at base speed	Nm	35
Peak torque at maximum speed	Nm	21.0
Continuous torque at maximum speed	Nm	10.5
Current limit	A	22
Current density limit (RMS)	A/mm^2	8.0
DC-link voltage(Line-to-line voltage limit)	V	320
No-load line-to-line back-EMF limit	V	600
Cooling		Air-cooled

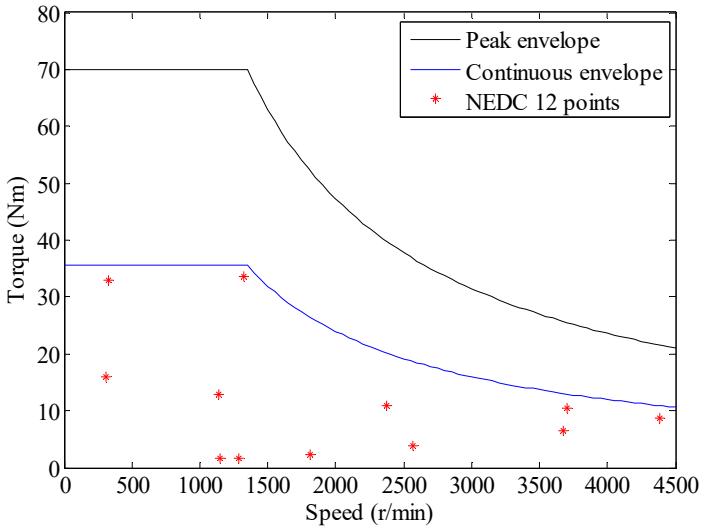

Fig. 4-12. Torque-speed profile and NEDC 12 representative operating points.

The optimisation constraints include performance specifications, current limit, current density limit corresponding to the thermal constraint, DC-link voltage (Line-to-line voltage) limit and the limit on the no-load back-EMF at the maximum speed for safety in the event of inverter or control failures, as listed in Table 4-3. The mechanical strength constraint has not been included in this optimisation since the maximum speed is relatively low and the maximum mechanical stress on rotor is much lower than the material strength limit. This can be observed by the mechanical stress analysis results in Section 4.7.4. The mechanical strength constraints will be considered in the optimisation of high speed and high power machines in Chapter 6.

The optimisation is performed using an FE-based software package, FLUX2D, from CEDRAT [131] together with the optimisation tool GOT-IT [132] also from CEDRAT. A parameterised FE model is constructed in FLUX2D and it is called by the optimisation process which evaluates the objective functions and constraints, and selects the most promising designs via a combination of genetic algorithm and sequential surrogate programming technique.

The leading design parameters to be optimised are shown in Fig. 4-13. Seven parameters including split ratio, pole arc, pole depth ratio, magnet thickness, tooth width, back-iron thickness and the number of turns per coil, will be optimised. The split ratio K_s is defined as the ratio of the rotor outer radius R_i to the stator outer radius R_o. The pole arc β_p is defined in electrical degree, and hence β_p=p·β_p where p is the pole pair number. The pole depth ratio K_p is defined as the pole depth D_p divided by the rotor outer radius R_i, as indicated in Fig. 4-13. Bonded NdFeB magnets with remanence B_r=0.56 and relative recoil permeability μ_r=1.1 are employed for the proposed machine.

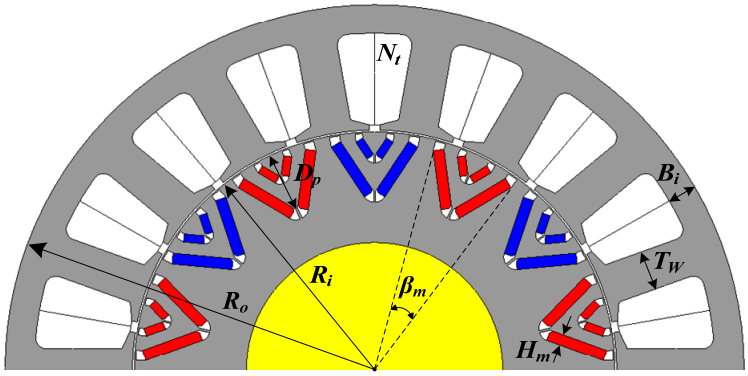

Fig. 4-13. Geometry parameters illustration.

The evolution of the energy efficiency over the NEDC and the parameter conversion process during the optimisation are shown in Fig. 4-14. As can be seen, a global optimum is reached after three generations of GA iterations. The total number of designs evaluated in the optimisation is 283 and it took 70 hours to complete on a typical PC. It can also be observed that in the region close to the global optimum, there are a large number of different design parameter combinations which yield very similar efficiency while satisfying all constraints.

Fig. 4-15 illustrates the cross-section of the optimised 9-phase 18-slot 14-pole IPM machine with outer diameter of 200mm and active length of 66.4mm. The optimisation results are listed in Table 4-4.

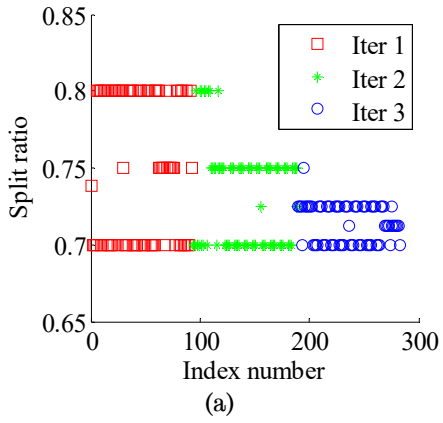

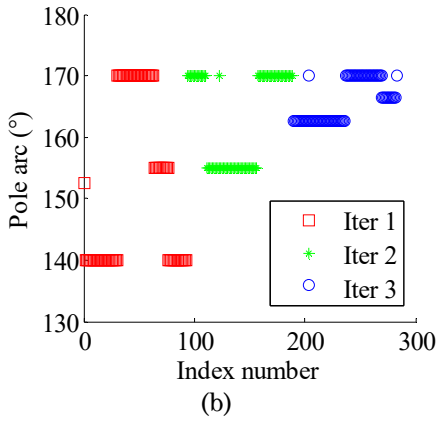

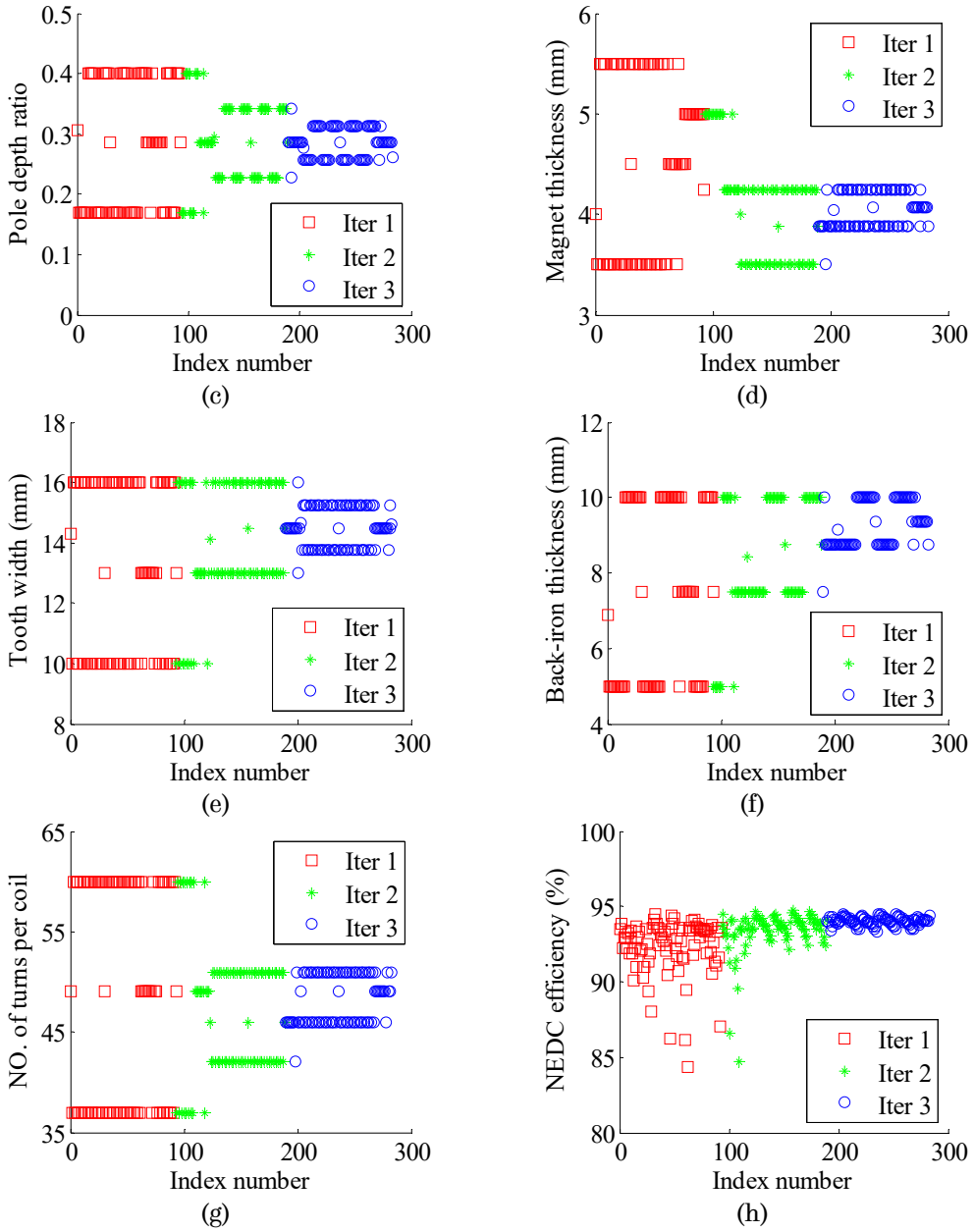

Fig. 4-14. Optimisation trends of variables and objective. (a) Split ratio. (b) Pole arc. (c) Pole depth ratio. (d) Magnet thickness. (e) Tooth width. (f) Back-iron thickness. (g) NO. of turns per coil. (h) NEDC energy efficiency.

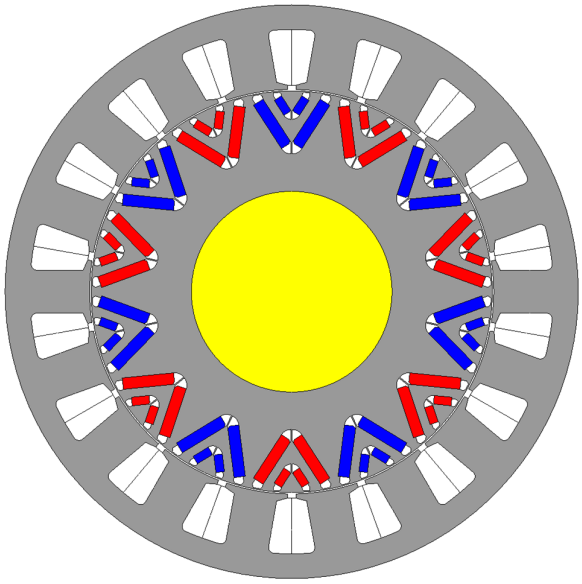

Fig. 4-15. Cross-section of the optimised 9-phase 18-slot 14-pole IPM machine.

Table 4-4. Optimised Parameters

Quantity	Symbol	Unit	Value
Split ratio	K_s		0.7
Pole arc	β_p	°	162.6
Pole depth ratio	K_p		0.2565
Magnet thickness	H_m	mm	3.875
Tooth width	T_w	mm	15.26
Back-iron thickness	B_i	mm	8.75
NO. of turns per coil	N_t		51

4.7 Performance Evaluation

4.7.1 Electromagnetic Performances

The phase back-EMF waveforms and spectrum at the maximum cruise speed 5050r/min are illustrated in Fig. 4-16. It can be seen that the phase shift angle between phase D and phase A is 20°, which coincides with the θ_Δ in (4.10). Due to absence of constraints on back-EMF harmonics during the global optimisation, the phase back-EMF contains a large 7^{th} order harmonic component shown in Fig. 4-16 (b). However, this is the optimal design against NEDC cycle efficiency, as shown in Section 4.6. Therefore, no further fine tuning on rotor geometry is performed to make the phase back-EMF more sinusoidal.

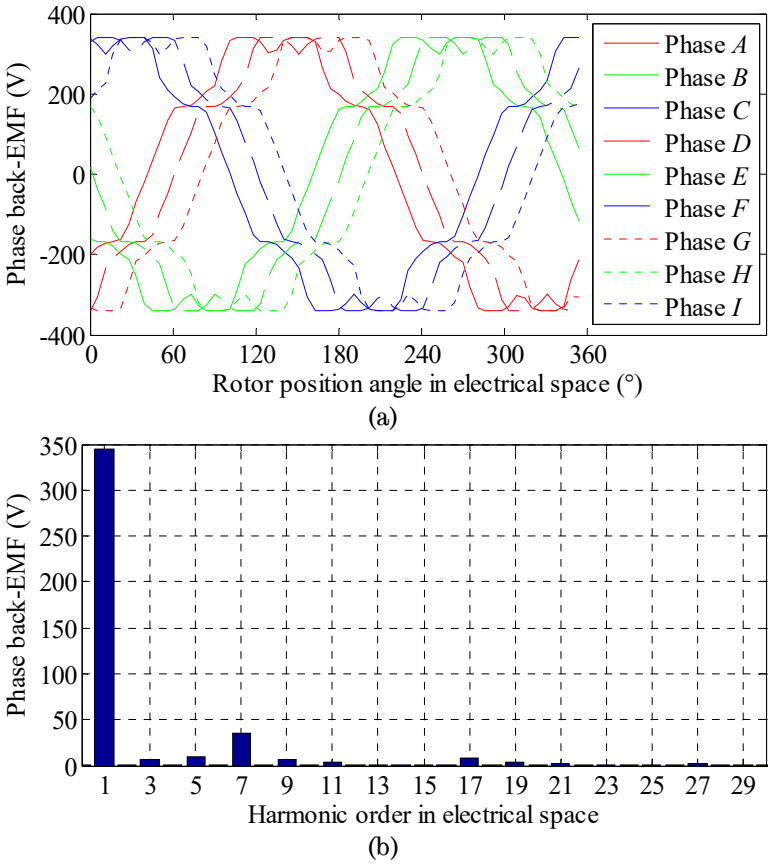

Fig. 4-16. FE-predicted phase back-EMF waveforms and spectrum at maximum cruise speed 5050r/min. (a) Waveforms. (b) Spectrum.

Fig. 4-17 shows the torque and power envelopes against speed. The constant-torque region is from 0 to 1350r/min while the constant-power region is from 1350r/min to 3523.5r/min. The maximum output power cannot reach 10kW when the operation speed is beyond 3523.5r/min. At the maximum operation speed, i.e. 4500r/min, the maximum output power is 9.5kW, 5% lower than the peak power. The reduction of the maximum output power at high speeds is due to the low characteristic current which is represented by the intersection of the *d*-axis flux-linkage curve with the *d*-axis current axis (the dashed line) in Fig. 4-18. A low characteristic current may compromise the field weakening capability when the *d*-axis flux-linkage becomes negative, or the required *d*-axis current exceeds the characteristic current. Thus the increase of *d*-axis current amplitude will not reduce but increase the *q*-axis voltage. This phenomenon has been investigated in Section 3.4.5, Chapter 3.

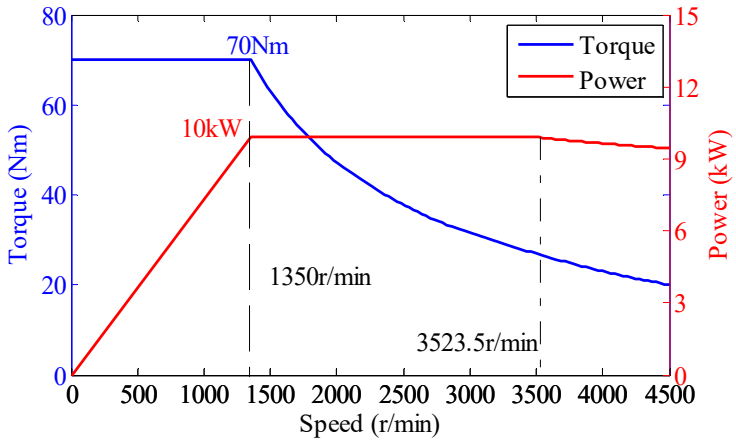

Fig. 4-17. FE-predicted torque and power envelopes against speed.

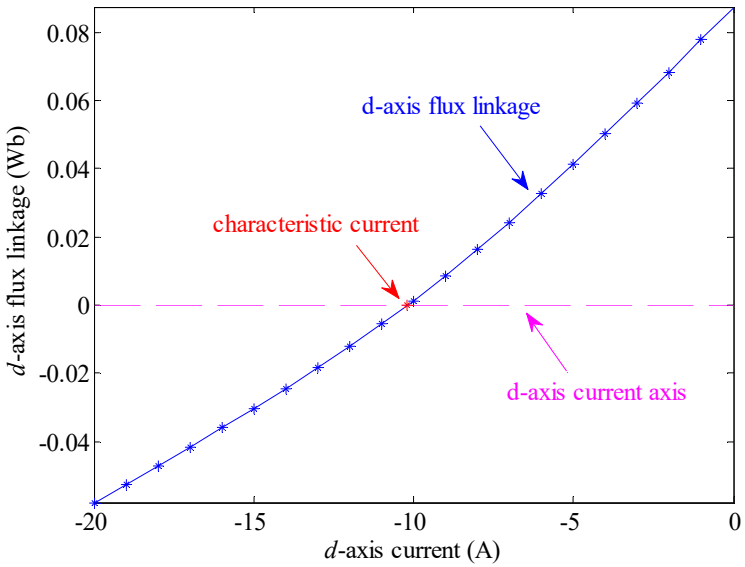

Fig. 4-18. Relationship between *d*-axis flux-linkage and *d*-axis current.

Fig. 4-19 depicts the current trajectory along the peak power envelop shown in Fig. 4-17. From Fig. 4-19, it can be observed that with the increase of operation speed, *d*-axis current magnitude decreases before reaching its minimum. This is because the increase of *d*-axis current magnitude due to field weakening is less than the decrease of that due to torque demand reduction. After this point, the *d*-axis current amplitude increases until the end of the constant-power region, i.e. 3523.5r/min shown in Fig. 4-17. Subsequently, the machine cannot maintain the constant-power operation and thereby *d*-axis current amplitude decreases.

The electromagnetic performances at the rated and peak torques at the base speed and over the NEDC driving cycle are shown in Table 4-5. The FE-predicted efficiency map over the toque and speed envelopes is depicted in Fig. 4-20. It is shown that the proposed machine exhibits high efficiency over wide torque and speed ranges. It should be noted that the copper loss calculation in Table 4-5 does not include skin effect and proximity loss because the machine operating speed is not very high (maximum operating speed 4500r/min) and also the windings employ multi-strand wires with small size. These effects can be quantified by the proposed methods in [160-162].

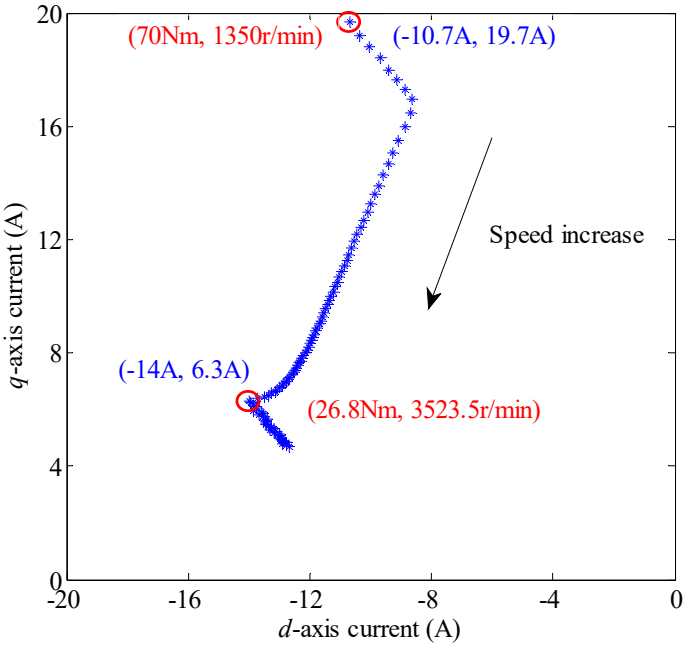

Fig. 4-19. Current trajectory along peak power envelope.

Table 4-5. Performances of Proposed 9-phase 18-slot 14-pole Machine

Quantity	Unit	Value
Rated current	A	11.1
Rated current density	A/mm^2	7.9
Efficiency at rated torque and base speed	%	93.5%
Peak current	A	22.4
Peak torque ripple	%	5.7%
Efficiency at peak torque and base speed	%	89.1%
Peak line-to-line voltage	V	326
Max no-load line-to-line back-EMF	V	564
NEDC efficiency	%	94.2%

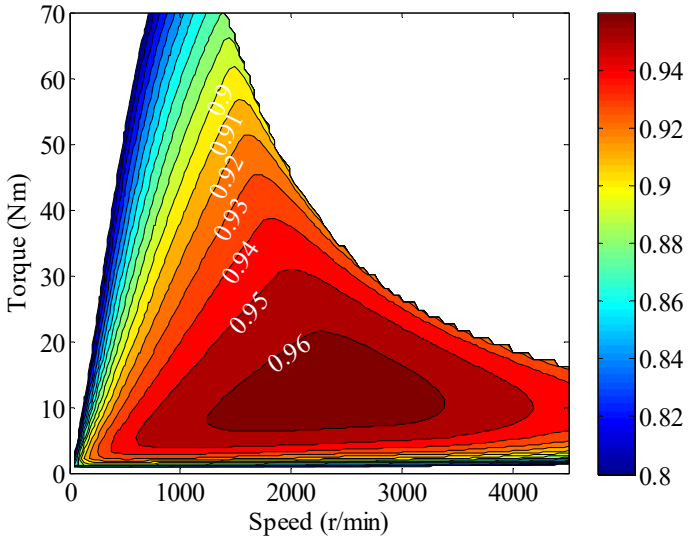

Fig. 4-20. FE-predicted efficiency map.

The machine performances in field weakening region are also evaluated. By way of example, at 10.5Nm (continuous torque at maximum speed) and 4500r/min, the electromagnetic performances are listed in Table 4-6. It can be observed that the machine efficiency can still reach >94%, demonstrating high efficiency in the field weakening operation.

Table 4-6. Performances at 10.5Nm and 4500r/min

Quantity	Unit	Value
Current amplitude	A	6.2
Copper loss	W	86.4
Rotor iron loss	W	77.7
Stator iron loss	W	135.8
Efficiency	%	94.1%
Torque ripple with respect to peak torque	%	1.7%

4.7.2 Comparison with Conventional 3-phase machine

Table 4-7 shows the performance comparison between the conventional 3-phase and the proposed 9-phase 18-slot 14-pole machines. The latter exhibits lower losses and thereby higher efficiency than the former at all the operation conditions (peak, rated and NEDC driving cycle).

By way of example, at peak torque and base speed operation, by using the proposed 9-phase winding configuration, the copper loss, stator iron loss and

rotor iron loss are reduced by 11.7%, 2.6% and 10.9% respectively. Therefore, the efficiency is improved by 1.2% (increase from 87.9% to 89.1%).

Table 4-7. Performance Comparison between Conventional 3-phase and Proposed 9-phase 18-slot 14-pole Machines

Operation condition	Quantity	Unit	3-phase	9-phase
Peak torque and base speed	Copper loss	W	1258.3	1111.5
	Stator iron loss	W	70.0	68.2
	Rotor iron loss	W	28.5	25.4
	Efficiency	%	87.9%	89.1%
	Torque ripple	%	11.5%	5.7%
Rated torque and base speed	Copper loss	W	304.7	274.5
	Stator iron loss	W	48.4	47.7
	Rotor iron loss	W	20.9	19.7
	Efficiency	%	92.9%	93.5%
	Torque ripple	%	7.3%	2.8%
NEDC driving cycle	Copper loss	J	2.7×10^4	2.6×10^4
	Stator iron loss	J	3.0×10^4	2.9×10^4
	Rotor iron loss	J	1.2×10^4	1.1×10^4
	Cycle efficiency	%	93.9%	94.2%

The copper loss reduction is contributed by the winding factor improvement in the proposed 9-phase winding configuration.

The rotor iron loss reduction is attributed to the MMF reduction shown in Fig. 4-10. Fig. 4-21 illustrates the harmonic distributions of the rotor iron loss associated with eddy current component for these two machines. It can be observed that the 6^{th}, 12^{th}, 24^{th}, 30^{th}, 42^{nd}, 48^{th}, 60^{th}, 66^{th}, 78^{th} ··· orders of harmonics in the eddy current loss component of the rotor iron loss are eliminated by using the proposed 9-phase winding configuration. These harmonic orders can be associated with the MMF harmonic orders shown in Fig. 4-10. By way of example, the 6^{th} order harmonic in the rotor eddy current loss is contributed by the 1^{st} and 13^{th} order harmonics in the stator MMF.

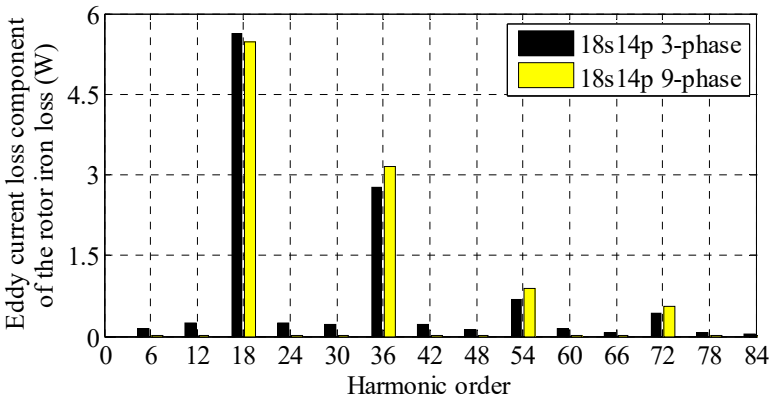

Fig. 4-21. Harmonic distributions of the eddy current loss component of the rotor iron loss.

Fig. 4-22 illustrates the efficiency difference map which is obtained by subtracting the efficiency map of the conventional 3-phase 18-slot 14-pole machine from that of the proposed 9-phase machine. It shows that by using the proposed 9-phase machine, the efficiency is improved at all the torque and speed operation conditions. The efficiency improvement at high torque and low speed region is more than that at low torque and high speed region. This is because the copper loss is dominant in the former region while the iron loss is dominant in the latter one. The iron loss reduction in the proposed 9-phase machine is mainly obtained in the rotor core.

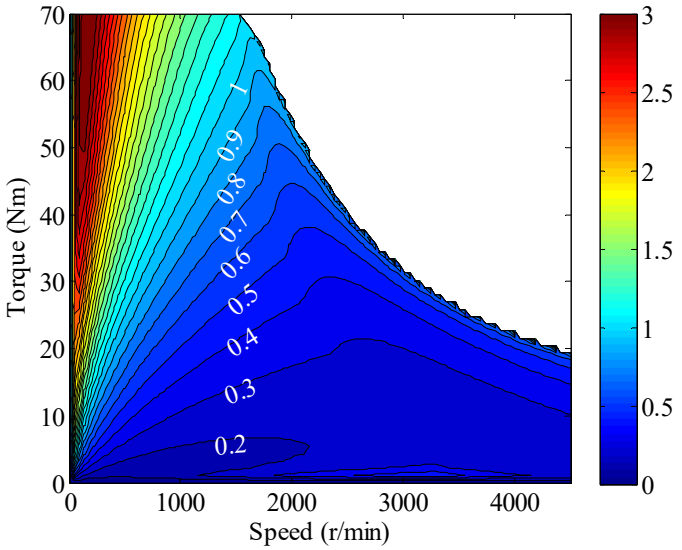

Fig. 4-22. Efficiency difference map between 9-phase and 3-phase 18-slot 14-pole machines (Efficiency difference unit: %).

The torque ripple is also reduced in the proposed 9-phase machine. At the peak torque and base speed, the torque ripple is reduced from 11.5% to 5.7%. This is due to the elimination of the 6^{th}, 12^{th}, 24^{th}, 30^{th} ··· order torque ripple harmonics, as shown in Fig. 4-23. This is because the torque harmonic components produced by the three 3-phase winding sets forms a balanced 3-phase system at these orders. For example, the phase shift of the 6^{th} order torque ripple harmonics between two neighbouring 3-phase sets is 120° and thus they are cancelled out in a three 3-phase machine. This phenomenon can be understood by the fact that the 6^{th} order torque ripple harmonic is produced by the interaction of the 5^{th} and 7^{th} order back-EMF harmonics with the fundamental current. The phase shifts of the 5^{th} and 7^{th} order back-EMF harmonics between two neighbouring 3-phase sets are 5×20°=100° and 7×20°=140°, respectively, while the current phase shift between two neighbouring 3-phase sets is 20°. Consequently, the phase shift of the 6^{th} order torque ripple harmonic contributed by the 5^{th} order back-EMF harmonic is 100°+20°=120°, whilst that of the 7^{th} order back-EMF harmonic is 140°-20°=120°.

From Fig. 4-23 (b), it can also be observed that the 18^{th} order torque ripple harmonic remains in the 9-phase machine. This is because the phase shift of the18^{th} order torque ripple harmonic between two neighbouring 3-phase sets, resulting from the interaction of 17^{th} and 19^{th} back-EMF harmonics with the current is 17×20°+20°=360° or 19×20°-20°=360°. Thus, the torque ripple of each 3-phase set adds up. Moreover, the lowest order of cogging torque harmonic is also 18.

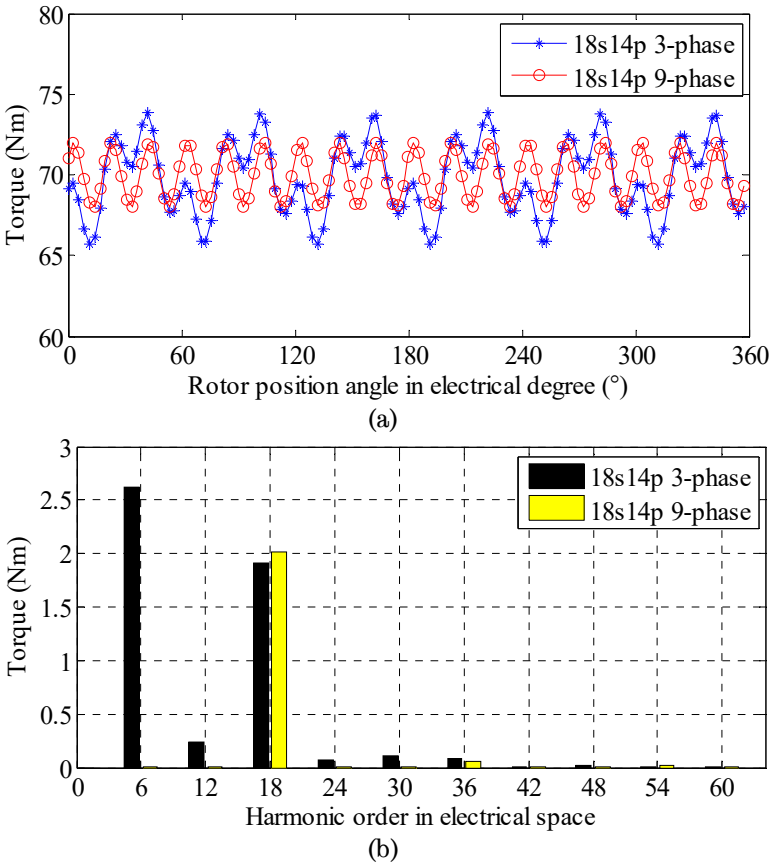

Fig. 4-23. Torque ripple comparison at 70Nm and 1350r/min. (a) Waveforms. (b) Spectra without DC components.

4.7.3 Thermal Analysis

Accurate temperature predictions for permanent-magnet machines are essential to prevent irreversible demagnetisation and undesirable reduction in lifetime. This section will be focused on the thermal analysis of the proposed machine.

The commercial thermal analysis software Motor-CAD developed by Motor Design Limited [163] is employed to predict the thermal behaviour of the proposed machine at various load conditions. The thermal network in Motor-CAD is illustrated in Fig. 4-24. It contains 48 nodes, including the housing, end-plate, end-cap, stator tooth, stator back-iron, 18 winding layers, end-windings, rotor pole, rotor back-iron, magnets, shaft, bearings, and etc.

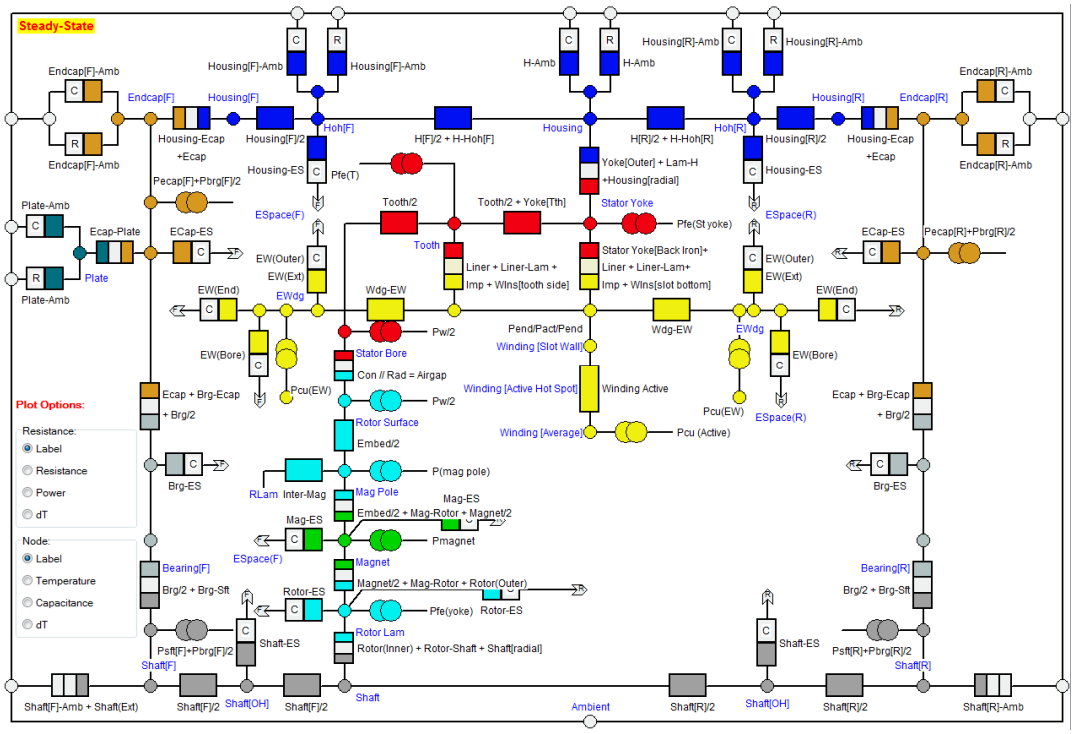

Fig. 4-24. Thermal network in Motor-CAD.

The cooling condition is air-cooled and the air flow rate is proportional to vehicle velocity and thus also machine speed. The air flow rate is 10m/s when the machine operates at 4500r/min, perpendicular to axial direction. The ambient temperature is assumed to be 45°C.

The thermal analysis at two most demanding load conditions are performed. The one is the rated torque and base speed, i.e. 35Nm and 1350r/min, and the other one is the continuous torque at the maximum operation speed, i.e. 10.5Nm and 4500r/min. Both of them deliver rated power. Their thermal analysis results are shown in Fig. 4-25 and Fig. 4-26 respectively.

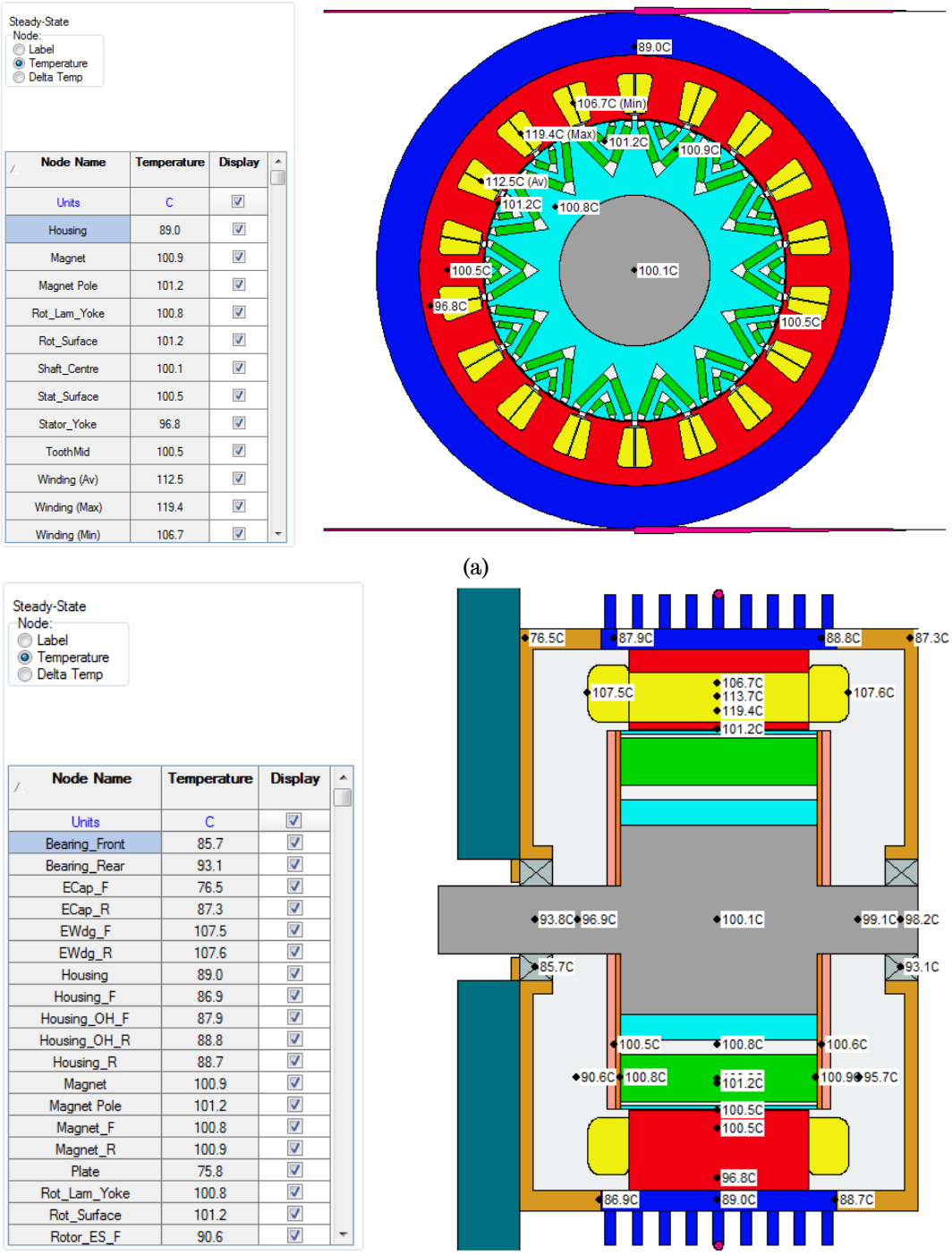

Fig. 4-25. Thermal analysis results at rated torque and base speed (35Nm and 1350r/min). (a). Cross-section. (b) Side view.

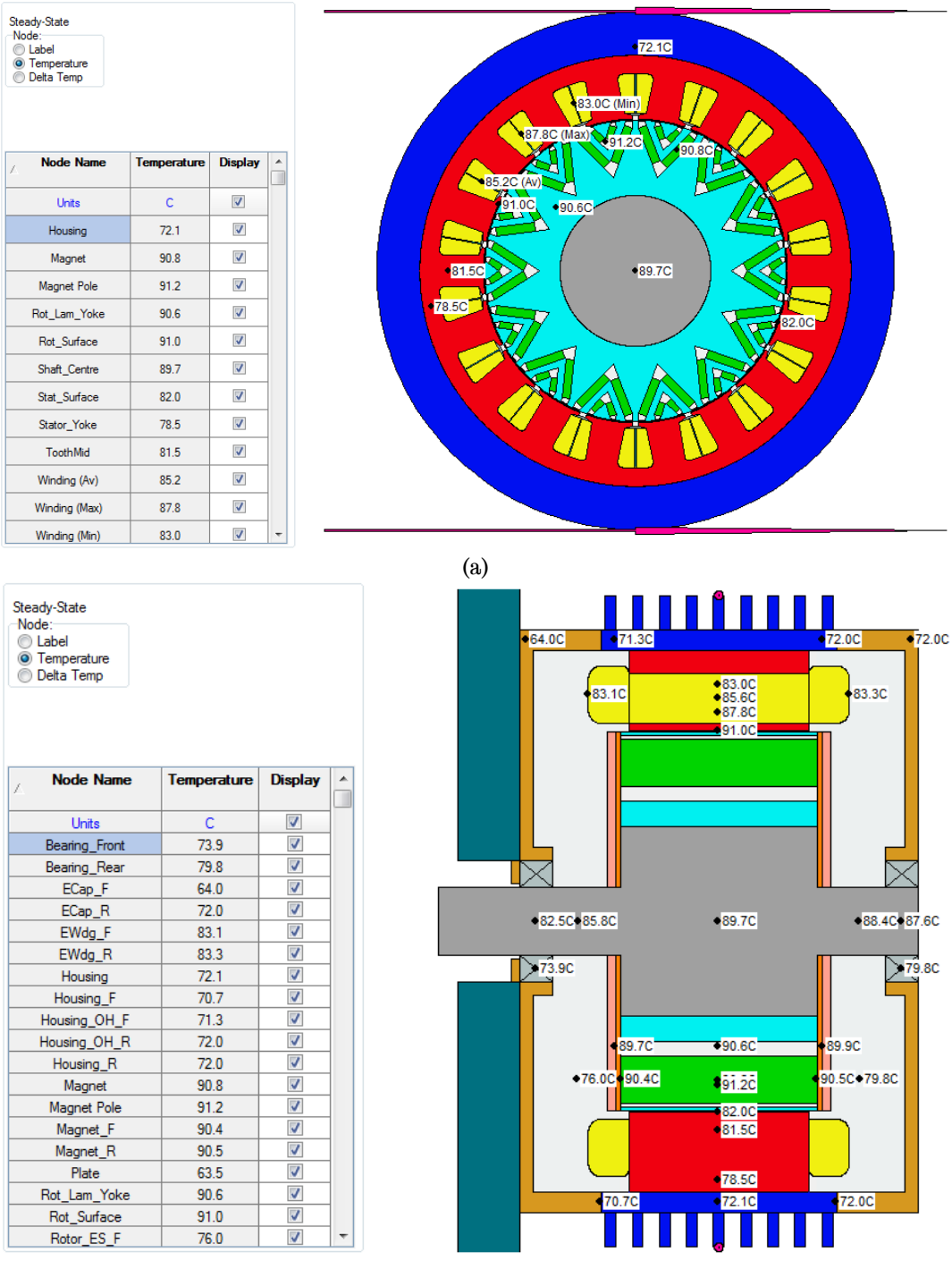

Fig. 4-26. Thermal analysis results at continuous torque and maximum operation speed (10.5Nm and 4500r/min). (a). Cross-section. (b) Side view.

It can be seen that at rated torque and base speed, the maximum temperatures at windings and magnets are 119.4°C and 100.9°C respectively. The winding temperature is higher than the magnet temperature since the

copper loss is high and the rotor iron loss is quite low. A fraction of heat in the stator is dissipated via the rotor. In contrast, at the continuous torque and maximum speed, these temperatures are 87.8°C and 90.8°C respectively. The magnet temperature is higher than the winding temperature because the rotor iron loss is increased and a part of the resultant heat has to be dissipated via the stator.

It can also be observed that in this machine the operation at the rated torque and base speed is more thermally demanding than that at the continuous torque and maximum speed. However, the maximum winding and magnet temperatures at the most demanding load condition are still much less than the permissible temperatures which are both 150°C in this machine.

4.7.4 Mechanical Stress Analysis

Rotating at a high speed, the machine rotor has to sustain a high centrifugal force. The rotor iron and magnets will suffer from mechanical failures if mechanical stresses exceed their strength limits. Therefore, mechanical stress analysis will be performed in this section.

The material of the rotor iron is the silicon-steel M270-35A which is an elastic material. Thus, von Mises stress should be employed to examine its yield strength. On the other hand, the bonded NdFeB used for magnets is a brittle material, and thereby tensile and compressive strengths are the criteria of its mechanical strength justification. The material properties of M270-35A and Magnets are shown in Table 4-8.

Table 4-8. Material Properties of Rotor Iron and Magnets

Item	Unit	M270-35A	Bonded NdFeB
Young modulus	GPa	192	160
Poisson's ratio		0.28	0.24
Density	kg/m^3	7600	5000
Tensile strength	MPa	N/A	80
Compressive strength	MPa	N/A	300
Yield strength	MPa	450	N/A

Due to the mechanical periodicity, only one pole needs to be modelled. The rotor speed is set to be 1.5 times of the maximum cruise speed, i.e. 7575r/min, for safety. Non-linear contact between rotor iron and magnets are considered. Fig. 4-27 illustrates the von Mises contour of the rotor iron, calculated via the commercial FEA software ANSYS Mechanical v12.1 [164]. It can be observed that the maximum stress occurs on the middle bridge of the bottom layer, being 141.1MPa which is much less than the yield strength 450MPa. Therefore, the rotor iron is free of mechanical failure risk.

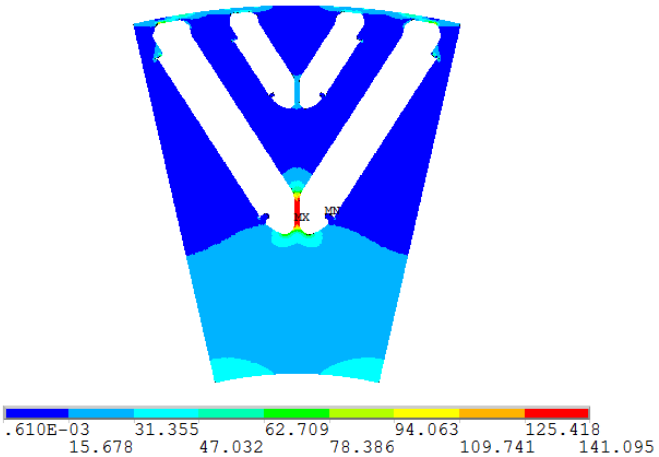

Fig. 4-27. von Mises contour of rotor iron at 7575r/min.

Fig. 4-28 (a) and (b) depict the 1st and 3rd principal stress contours of magnets respectively. It can be seen that the maximum 1st principal stress is 19.5MPa which is much less than the tensile strength 80MPa whilst the maximum 3rd principle stress amplitude is 70.1MPa which is much less than the compressive strength 300MPa. Therefore, the magnets are also free of mechanical failure risk.

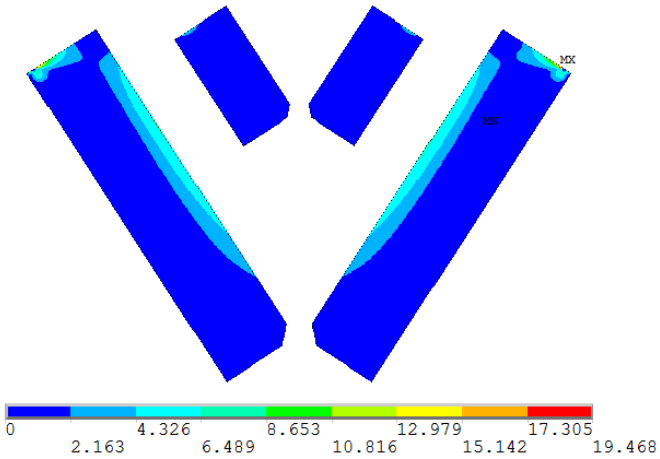

(a)

(b)

Fig. 4-28. Principal stress contours of magnets. (a) 1st principal stress. (b) 3rd principal stress.

4.7.5 Rotor-dynamics Analysis

In a rotor-bearing system, the bearing stiffness is much lower than the rotor one, resulting in a relatively low natural frequency. When the rotation frequency of the rotor, which is usually unbalanced, approaches to its natural frequency, resonance occurs and thus may cause a mechanical failure because the damping in the rotor-bearing is usually small. Therefore, a rotor-dynamics analysis needs to be performed to ensure the maximum cruise speed is much lower than the first order critical speed which corresponds to the first order natural frequency.

3-D 2-node beam elements (BEAM188) are employed to model the rotor whilst spring-damper elements (COMBIN14) are utilised to represent the

bearings via the commercial FEA software ANSYS Mechanical v12.1 [164]. Due to the fact that the rotor-dynamics behaviour of a rotor-bearing system is insensitive to localised geometry variation, the rotor-bearing system model is simplified by combining rotor iron, magnets and rotor end-plates into one equivalent solid cylinder, as shown in Fig. 4-29.

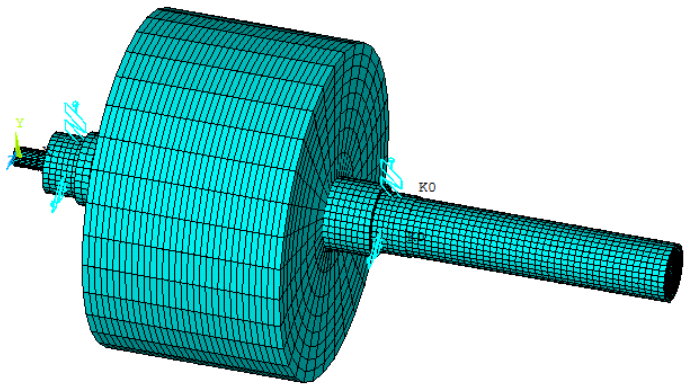

Fig. 4-29. Rotor-bearing system for rotor-dynamics analysis.

According to ISO 1940-1, the balance grade of the electrical machine rotor system is selected to be G16. The permissible eccentricity e_{cc} can be calculated by (4.16).

$$e_{cc} = \frac{G}{\omega_{\max}} = \frac{60G}{2\pi n_{\max}} = 30.26\mu\text{m} \tag{4.16}$$

where G=16mm/s and $n_{\max}$=5050r/min. G is the product of permissible eccentricity and the maximum angular speed $\omega_{\max}$ and is a constant for rotors of the same type. $n_{\max}$ is the maximum cruise speed.

The maximum centrifugal force F_c is given by (4.17).

$$F_c = m_r e_{cc} \omega_{\max}{}^2 = m_r e_{cc} \left(\frac{2\pi n_{\max}}{60} \right)^2 = 93.07\text{N} \tag{4.17}$$

where rotor mass m_r=11.0kg.

Therefore, the radial load for each bearing is calculated by (4.18).

$$F_l = \frac{m_r g + F_c}{2} = 100.49\text{N} \tag{4.18}$$

SKF 61905 bearings whose inner diameter is 25mm are used in this machine. According to the relationship between bearing stiffness and radial load of SKF 61905 bearings, as shown in Table 4-9 (supplied by SKF technical support), the bearing stiffness is 5.15×10^7N/m, calculated via interpolation method.

Table 4-9. Relationship between Bearing Stiffness and Radial Load of SKF 61905

Radial load (N)	Deflection (μm)	Bearing stiffness (N/m)
30	1.305	3.45×10^7
100	2.912	5.15×10^7
500	8.515	8.81×10^7
1000	13.52	1.11×10^8
2000	21.46	1.40×10^8
3000	28.12	1.60×10^8

Based on the model shown in Fig. 4-29 and also the calculated bearing stiffness, rotor-dynamics analysis is performed and the Campbell diagram is depicted in Fig. 4-30. "BW" and "FW" mean "backward" and "forward" respectively.

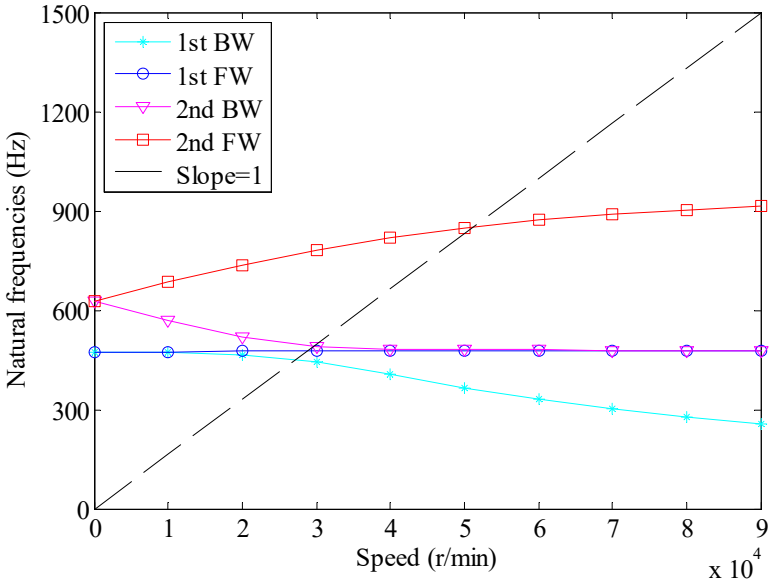

Fig. 4-30. Campbell diagram of the rotor-bearing system.

The critical speed at a given order is obtained at the intersection of the forward natural frequency curve at the corresponding order and the dashed line whose slope is 1 when the X- and Y-axes shown in Fig. 4-30 are converted into the same unit. In this way, the first and second order critical speeds are calculated, and are 28,527r/min and 51,103r/min. The first order critical speed is much higher than the maximum cruise speed, and hence no resonance risk exists.

To illustrate vibration characteristics, the first 6 order vibration modes are shown in Fig. 4-31. The 1st order lateral mode shown in Fig. 4-31 (a) is caused by the low stiffness of bearings and corresponds to the first order critical speed. The 1st conical mode shown in Fig. 4-31 (b) also results from the low stiffness of bearings. The other 4 bending modes reflect the natural vibration characteristics of the rotor body. These 4 natural frequencies are usually very high, and thus they are out of our concern.

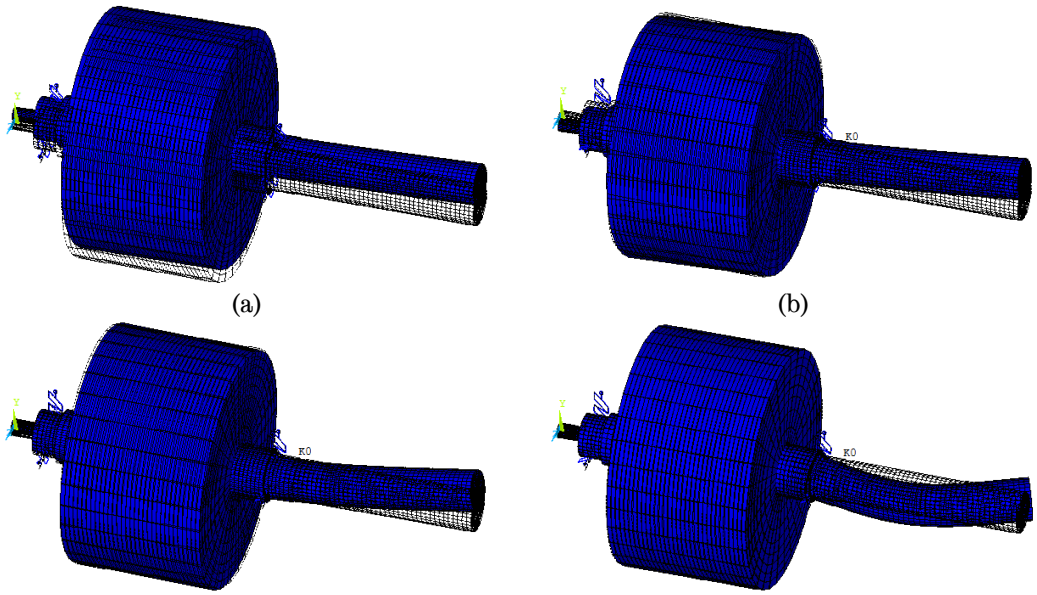

(a) (b)

(c) (d)

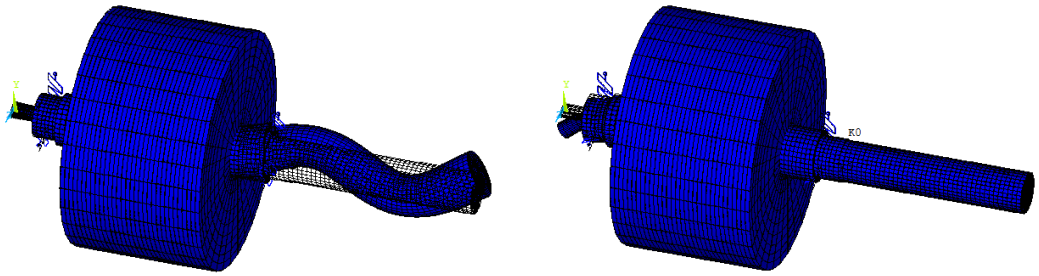

(e) (f)

Fig. 4-31. Vibration modes. (a) 1st order lateral mode. (b) 1st order conical model. (c) 1st order bending mode. (d) 2nd order bending mode. (e) 3rd order bending mode. (f) 4th order bending mode.

4.8 Experimental Validation

4.8.1 Machine Prototype

A 10kW, 9-phase, 18-slot 14-pole IPM machine prototype is built to validate the foregoing FEA and MMF harmonics cancellation effects. The stator and rotor components of the machine prototype are shown in Fig. 4-32.

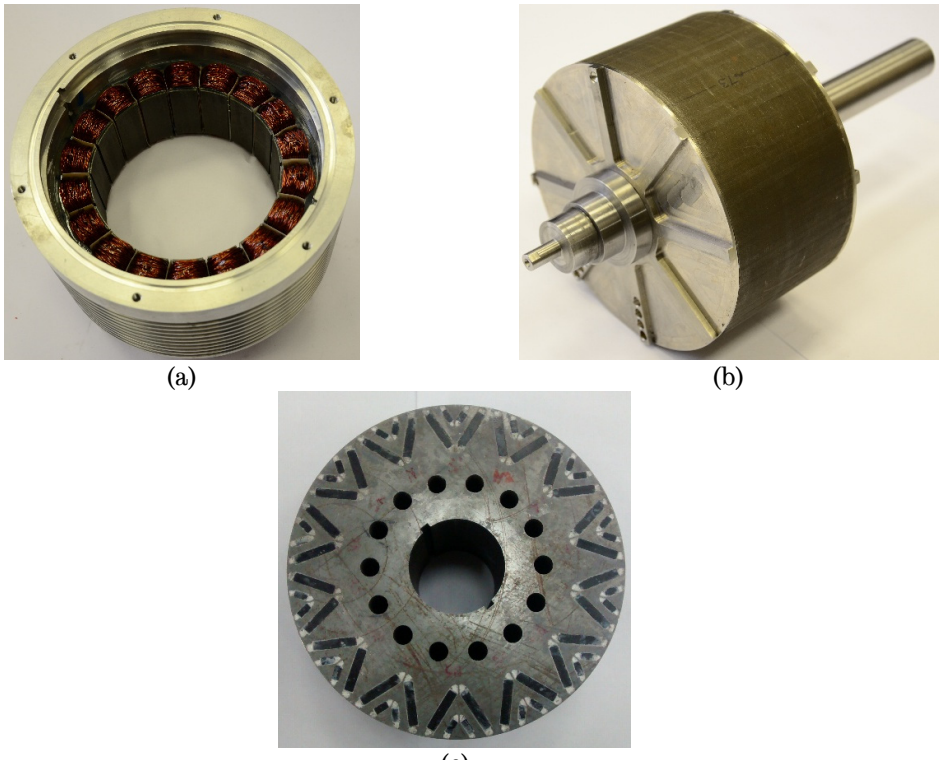

(a) (b)

(c)

Fig. 4-32. Machine prototype. (a) Stator. (b) Rotor. (c) Rotor lamination and magnets.

Table 4-10 lists the measured resistance of each phase at 28°C. Compared to the predicted phase resistance at 28°C, i.e. 0.365Ohm, the measured ones

are 1%-5% lower. This is because the end-windings of the machine prototype are made very compact during a manual winding process.

Table 4-10. Measure Phase Resistances at 28°C

Phase index	Resistance (Ohm)	Difference (%)
A	0.347	-5.00%
B	0.356	-2.50%
C	0.351	-3.90%
D	0.356	-2.50%
E	0.353	-3.30%
F	0.362	-0.90%
G	0.361	-1.10%
H	0.357	-2.20%
I	0.348	-4.70%

4.8.2 No-load Test

First, the machine prototype is driven without load to validate the back-EMF predicted by FEA. The FE-predicted and measured phase back-EMFs are compared in Fig. 4-33. The fundamental back-EMF of the machine prototype is 1.7% higher than the FEA result under the same speed and temperature conditions. This is because the rotor stack length in the prototype machine is 6mm longer than that of the stator in order to compensate potential flux reduction due to 3-D effect which cannot be predicted by 2-D FEA.

The no-load loss is measured by a high precision in-line torque transducer at various speeds, and the comparison between the measured no-load loss and the FE-predicted iron loss is shown in Fig. 4-34. It can be observed that the measured no-load loss is much higher than the FE predicted no-load iron loss. This is due to the fact that the measured no-load loss includes both the iron loss and the mechanical loss (friction and windage) and in addition, the factors that may affect iron loss during manufacturing such as mechanical and thermal stress are not accounted in the FE prediction. Therefore, a build factor (1.3 for this machine) is introduced to calibrate the no-load loss model. It can be seen from Fig. 4-34 that with a build factor of 1.3, the FE-predicted iron loss agrees well with the measurements.

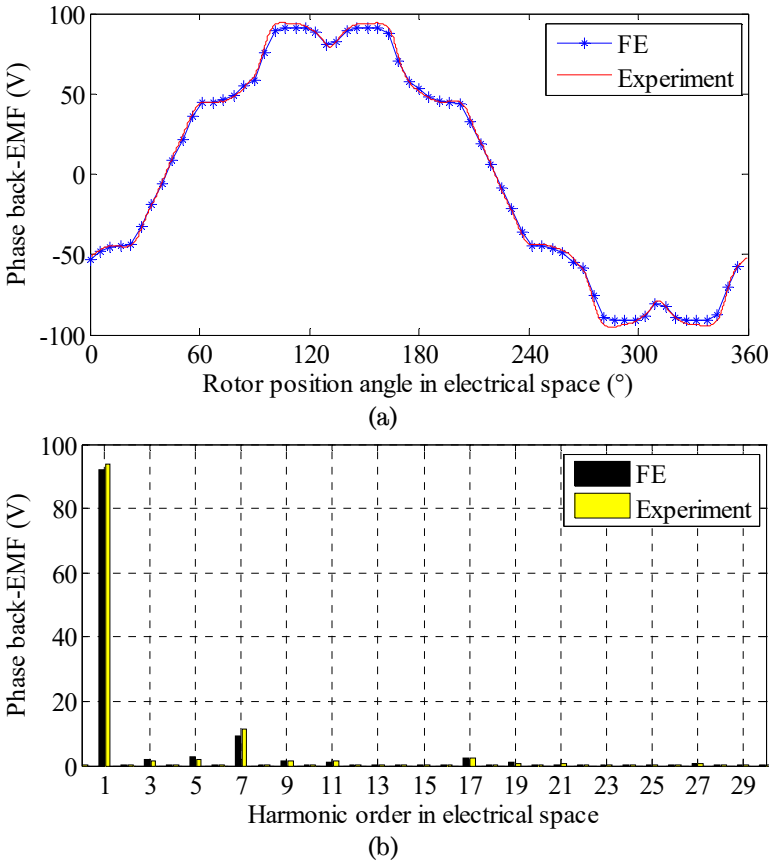

Fig. 4-33. Comparison of measured and FE-predicted phase back-EMF at 1350r/min and 25°C. (a) Waveforms. (b) Spectra.

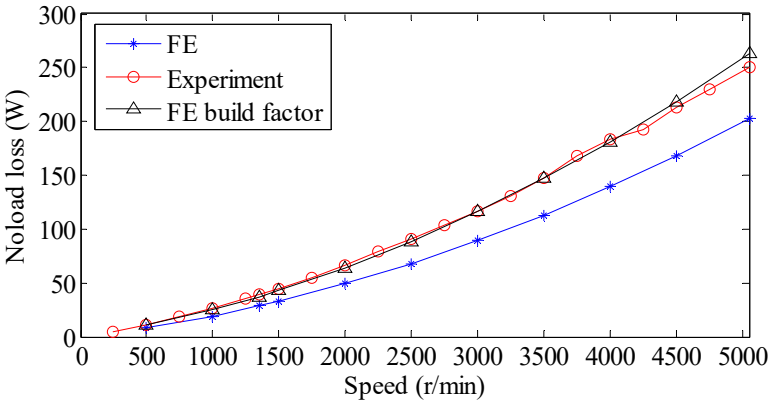

Fig. 4-34. Measured and predicted no-load loss variation with speed.

4.8.3 Load Test

Since a 9-phase inverter is not readily available, the load tests were performed in generating mode of operation. Given that the *d*-axis current is always negative in both motoring and generation and the machine flux-linkage map is almost symmetrical with respect to *q*-axis current, the test

results in generating mode should also be representative of motoring operations, albeit the loss due to high frequency PWM will not be present.

The experimental setup is illustrated in Fig. 4-35. The prototype machine is connected to a dynamometer via a high precision in-line torque transducer, and it is driven by the dynamometer during the tests. Voltage and current waveforms are measured using high precision voltage and current transducers and the data are captured with high resolution oscilloscopes.

Fig. 4-35. Experimental setup. (a) Machine prototype, torque transducer, coupling and dynamometer. (b) Resistive load.

On-load tests are performed against four load conditions with the load resistance at 6.875Ohm, 10Ohm, 22Ohm and 32Ohm, respectively. For each load condition, the speed varies from 250r/min to the speed at which the maximum power is reached. The measured and FE-predicted voltage and current waveforms as well as the average torque are compared. Good agreements are observed for all four operating points between the predictions and measurements.

By way of example, Fig. 4-36 compares the measured and FE-predicted phase voltage and phase current, at 3250r/min with 22Ohm load. The output power of the machine at this load condition is 4.5kW.

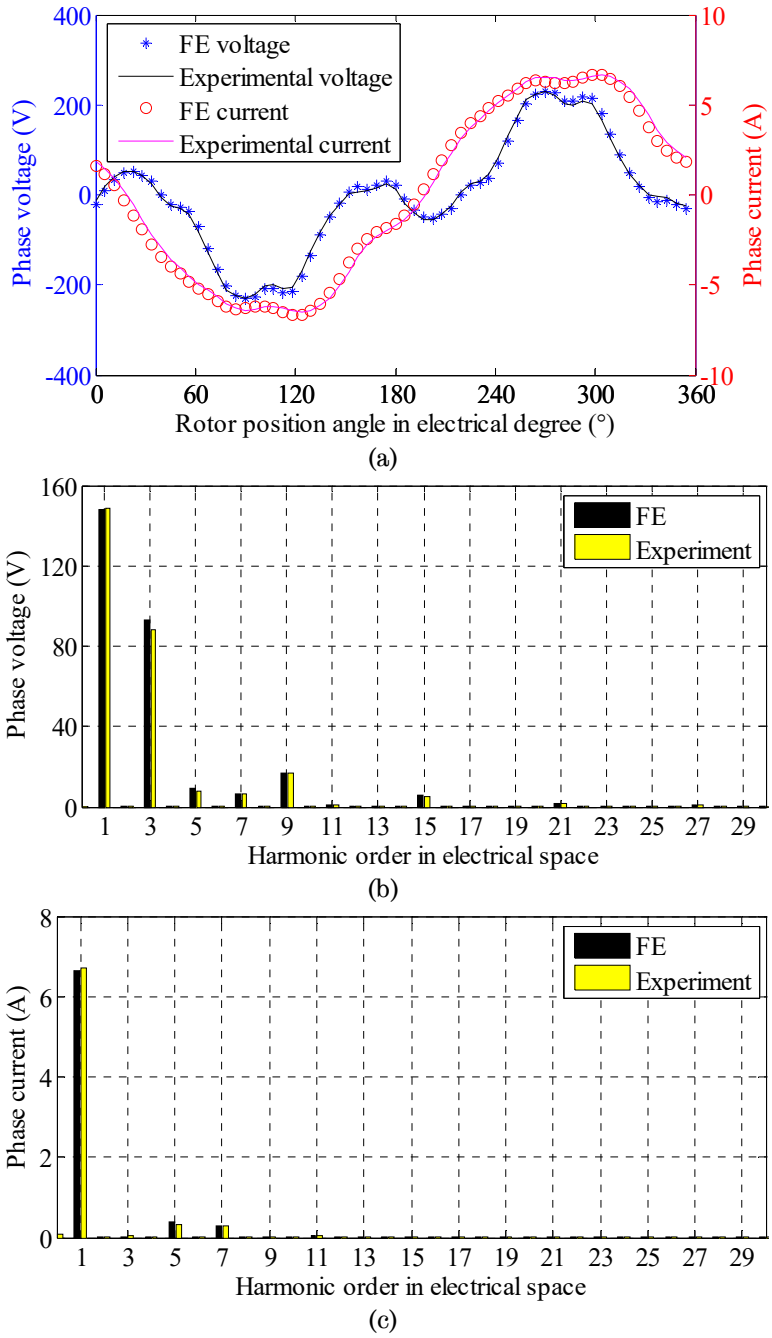

Fig. 4-36. Comparison of measured and FE-predicted phase voltage and current at 3250r/min with 22Ohm load. (a) Waveforms. (b) Phase voltage FFT spectra. (c) Phase current FFT spectra.

It can be seen that both the FE-predicted phase voltage and phase current agree well with the experimental results. The errors in fundamental phase voltage and current are 0.1% and 0.8%, respectively, which might result from the combined effect of modelling and measurement errors. It should be noted that the current and voltage waveforms in Fig. 4-36 (a) contains high

order harmonics which are caused by the harmonics in the back-EMF since the machine operates at the generating mode. These harmonics in the phase current and voltage will result in additional copper loss, iron loss and torque ripple. However, the current waveform will be close to sinusoid in the motoring operation under inverter feedback control.

The comparison of the predicted and measured torque is shown in Fig. 4-37 under the same condition as described for Fig. 4-36. Due to bandwidth limit of the torque transducer, the instantaneous torque waveform at 2.3kHz cannot be captured, and thereby only the mean torque value of the experimental result is shown in Fig. 4-37. The measured mean torque is 3.7% higher than the FE prediction. This is mainly due to the fact that the mechanical loss and iron loss which contributes to the input torque in generating mode is not accounted in the FE-predicted torque. Therefore, the electromagnetic behaviour of the proposed machine are also validated under load conditions.

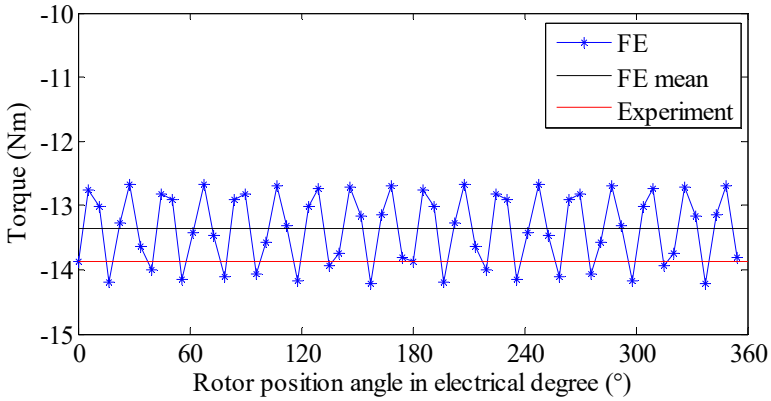

Fig. 4-37. Comparison of the measured and FE-predicted torque at 3250r/min with 22Ohm load.

To demonstrate the effect of the space harmonic cancellation which results with the proposed technique, the on-load tests with only one 3-phase (*ABC*) and with two 3-phases, *ABC* and *DEF* are also performed under the same load condition as the three 3-phase operation in Fig. 4-36 for each 3-phase set. The input and output powers of each test are measured and the resultant total loss is obtained. With measured winding temperature in each

test, the copper loss can be accurately quantified and the sum of the iron loss and mechanical loss is determined by subtracting the copper loss from the total loss. Table 4-11 summarises the test results obtained from one 3-phase, two 3-phase and three 3-phase operations. It can be observed that the ratio of the sum of the iron loss and mechanical loss to the input power are 7.7%, 4.7% and 2.9% for one 3-phase, two 3-phase and three 3-phase operations, respectively. Given that the mechanical loss in each operation should be approximately equal, the increases in the measured mechanical and iron losses in the one 3-phase and two 3-phase operations can only be explained by the presence of more space harmonics which have otherwise been cancelled by the proposed technique in the three 3-phase operation. This observation is indeed supported by FE-predicted iron losses, also given in Table 4-11, for the three operations. It has been shown from the FEA that the presence of the more undesirable space harmonics in the one 3-phase and two 3-phase operations gives rise to more significant distortion in flux density waveforms in the stator and rotor cores, and hence increase in iron loss. This indicates the effectiveness of the MMF harmonics cancellation effect in the proposed machine.

Table 4-11. Power and Losses

Item	*ABC* on	*ABC,DEF* on	*ABC,DEF,GHI* on
Measured mean torque (Nm)	5.6	10.1	13.9
Measured input power (W)	1915.8	3450.2	4722.4
Measured output power (W)	1736.2	3226.8	4498.6
Measured copper loss (W)	32.5	61.2	87.1
Measured Iron loss and mechanical loss (W)	147.1	162.2	136.8
Measured iron loss and mechanical loss ratio	7.7%	4.7%	2.9%
Measured efficiency (%)	90.6%	93.5%	95.3%
FE-predicted iron loss (W)	126.2	140.1	112.8
FE-predicted iron loss ratio	6.6%	4.1%	2.4%

4.8.4 Thermal Steady-state Test

To measure temperatures in all 9-phase windings, 7 thermocouples are embedded in various winding coils. Their position arrangements are given in

Table 4-12. The slot number follows the same sequence of the winding diagram in Fig. 4-8 (b).

The thermal test is performed with a 22Ohm resistive load at 3250r/min. The measured ambient temperature is 25.8°C. The test lasts 5.5 hours to ensure the machine temperatures reach their steady-states. No cooling fan is used in this experiment, whereas an air-conditioner is turned on to maintain the ambient temperature. The air flow rate at the surface of machine prototype is measured by a wind gauge, being 0.5m/s. The measured winding temperatures via thermocouples are depicted in Fig. 4-38. The maximum winding temperature occurs at the middle of slot 4, reaching 75.3°C.

Table 4-12. Thermocouple Position Arrangement

Slot NO.	Phase NO.	Thermocouple position
1	*A*, *G*	Middle of slot
4	*C*, *I*	Middle of slot
8	*B*, *F*	Middle of slot
12	*E*, *I*	Middle of slot
15	*D*, *H*	Middle of slot
5, 6	*D*	Front end-winding
15, 16	*H*	Rear end-winding

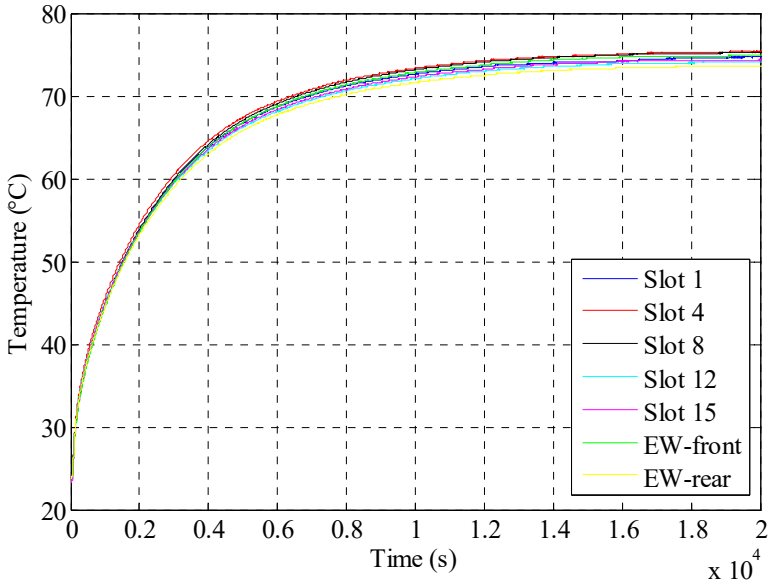

Fig. 4-38. Measured winding temperatures via thermocouples with 22Ohm resistive load at 3250r/min.

The thermal analysis under the same load condition is performed in Motor-CAD with the same air flow rate (0.5m/s) as the measurement. The input copper loss and iron loss are obtained from FEA at 80°C rotor temperature and 75°C winding temperature. This 75°C winding temperature is based on the measurement results shown in Fig. 4-38 while the 80°C rotor temperature is estimated according to the measured winding temperature. Fig. 4-39 shows the thermal steady-state results with 22Ohm resistive load at 3250r/min. The maximum winding temperature is 79.1°C.

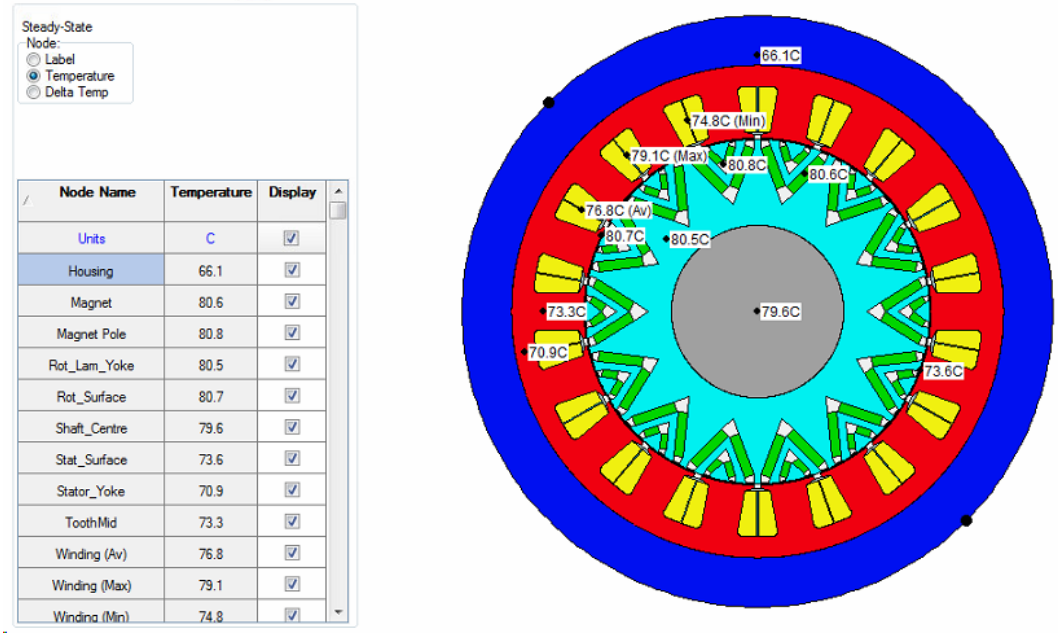

Fig. 4-39. Predicted steady-state temperatures with 22Ohm resistive load at 3250r/min.

Fig. 4-40 compares the transient variations of measured and predicted temperatures. The comparison includes both the maximum and mean temperatures. The measured mean temperature is the average of these temperatures measured from the middle of slots. The predicted maximum winding temperature is 78.8°C which is 4.6% higher than the measured 75.3°C. The predicted mean winding temperature is 76.5°C which is 2.4% higher than the measured 74.7°C. It can also be observed that the measured and predicted winding temperatures also exhibit similar transient waveforms.

It should be noted that the predicted transient winding temperatures in Fig. 4-40 by Motor-CAD are simulated after the measured winding

temperatures are obtained. In other words, the input copper and iron loss of Motor-CAD are calculated based on the measured winding temperatures at thermal steady-states. Therefore, this simulation in Motor-CAD does not represent an electro-thermally coupled simulation. This is also one of the factors resulting in the errors in temperature prediction. The electro-thermally coupled simulation will be performed in Chapter 5.

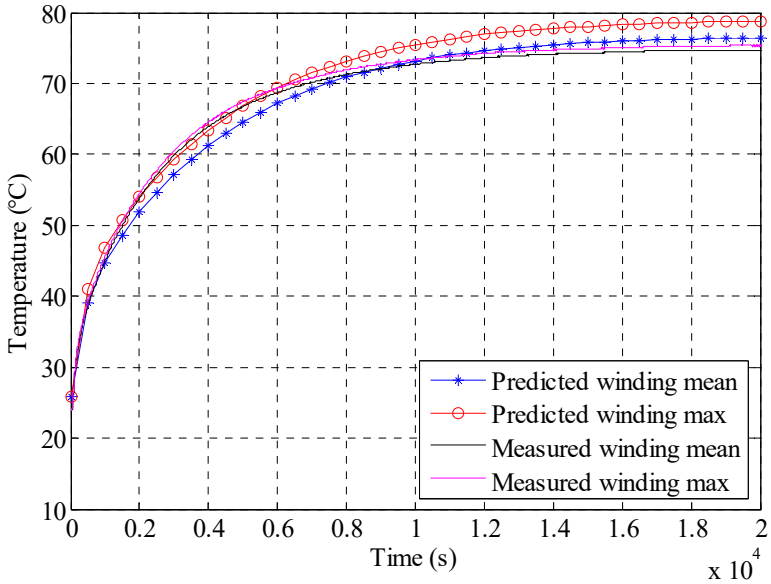

Fig. 4-40. Comparison of measured and predicted winding temperatures with 22Ohm resistive load at 3250r/min.

4.9 Conclusion

A generic approach to reduction of MMF harmonics in permanent-magnet machines with multiple 3-phase concentrated windings has been proposed. The MMF harmonic cancellation is achieved by employing multiple 3-phase windings and selecting appropriate phase shifts in both space and time. The proposed winding configuration cancels out all the MMF sub-harmonics and some high order MMF harmonics.

The reduction in MMF harmonics leads to a number of benefits. Firstly it reduces both stator and rotor iron losses, particularly at high speeds, and hence, prevents excessive rotor temperature. Furthermore it improves

reluctance torque capability of IPM machines with concentrated windings, and machine efficiency.

Compared to the MMF harmonic reduction techniques in literature, the proposed machine topology in this chapter retains the advantages of the concentrated windings and exhibits a high winding factor, low torque ripple, low manufacture cost, high torque density and the high efficiency over wide torque and speed ranges.

To drive the proposed 9-phase 18-slot 14-pole machine, a 9-phase inverter needs to be employed. This 9-phase inverter should be configured as three 3-phase inverters with standard modules, and each 3-phase inverter may be controlled based on conventional field oriented control technique. It should be noted that although the need for multiple 3-phase inverters for the proposed winding configuration might be seen as a disadvantage, the total inverter VA rating is the same as that of a 3-phase machine since the current rating of one 3-phase inverter is proportionally reduced. The use of three 3-phase inverters with low current rating spreads the inverter loss and is conducive to cooling and integration of the inverter into the machine. It also contributes to a degree of fault tolerance in that the machine can continue to operate even if one set of 3-phase winding/drive fails. This is valuable and significant for machines in EV traction application where the safety requirement of the powertrain system is relatively high. Moreover, the torque ripple can be dramatically reduced without skew techniques in that certain torque ripple harmonics can be completely cancelled out. Therefore, it is worthwhile and advantageous to develop multiple 3-phase winding configurations for electrical machines in EV traction application.

The proposed MMF harmonics reduction technique is also applicable to other slot-pole combinations with concentrated windings except for those with slot number being equal to 1.5 times the pole number.

CHAPTER 5 A High-Fidelity and Computationally Efficient Model for Interior Permanent-magnet Machines

NOMENCLATURE

i_d	d-axis current in A
i_q	q-axis current in A
J	Rotor inertia in Kg·m^2
L_d	d-axis inductance in H
L_q	q-axis inductance in H
m	Number of phases
n	Machine speed in r/min
p	Number of pole pairs
R_{load}	Load resistance in Ohm
R_s	Phase resistance in Ohm
s	Derivative operator
t	time in s
T	Rotor magnet temperature in °C
$T_{ambient}$	Rotor magnet temperature in °C
T_{em}	Electromagnetic torque in Nm
T_L	Load torque in Nm
T_w	Winding temperature in °C
V_d	d-axis voltage in V
V_q	q-axis voltage in V
V_s	Voltage magnitude in V
θ	Rotor position angle
Ψ_d	d-axis flux-linkage in Wb
Ψ_q	q-axis flux-linkage in Wb
Ψ_m	Permanent-magnet flux-linkage in Wb
ω	Angular speed in mechanical rad/s
ω_e	Angular speed in electrical rad/s

5.1 Introduction

PMSMs exhibit high torque density and high energy efficiency due to the fact that the magnetic field which facilitates electromechanical energy conversion is mainly produced by permanent-magnets [52, 141]. Therefore, they have increasingly been employed in a variety of applications [143, 165, 166], such as industrial drives, hybrid and electric vehicles, wind turbine, aerospace, marine, and domestic appliances, etc.

In PMSMs, SPMs only have alignment torque component which results from the interaction of the permanent-magnet field with armature currents [142]. The effective air-gap seen by the stator winding is relatively large, being equal to the sum of the air-gap and magnet thickness and hence the armature reaction is not very significant. Further, the winding inductance is virtually independent of rotor position. Therefore, it is relatively simple to model and control SPM machines. However, the magnet usage in SPM machines tends to be large due to absence of reluctance torque contribution [167]. SPM machines are less favoured in applications which require a wide constant-power operating range [147].

To improve field weakening capability and to reduce demand on permanent-magnet usage, IPMs, including both conventional IPMs with rare-earth materials and PMA-SynRMs, have been employed [148, 168]. However, the presence of reluctance torque in IPM machines not only results in the non-linear relationship between the electromagnetic torque and the armature current, but also leads to more spatial harmonics in phase voltages due to the inherently large variation in magnetic energy with rotor position [144, 169]. Therefore, the conventional model using constant d- and q-axis inductances cannot accurately represent the IPM machine behaviour if the spatial harmonics and the magnetic saturation effect in stator and rotor cores are neglected [170], particularly in the field weakening region where the phase voltage harmonics will result in distorted current waveforms due to the limited DC link voltage.

To improve the IPM model fidelity, the circuit-field coupled co-simulation was employed in [170-172]. This approach is, however, very time-consuming due to the involvement of numerical FEA. To avoid the FE computation in the simulation process, the *d*- and *q*-axis flux-linkage variations with *d*- and *q*-axis currents and the rotor position were established via FEA and the results were treated as curve fitted functions in the drive system simulation in [173]. However, it was necessary to compute the derivatives of the flux-linkages with voltage inputs, resulting in the algebraic loop and numerical instability, particularly in a drive simulation system with switching devices. To avoid the derivative computation, the *d*- and *q*-axis current variations with *d*- and *q*-axis flux-linkages and the rotor position were obtained by performing the inverse of the flux-linkages as functions of currents and rotor position computed from FEA in [174-176]. However, the cross-coupling saturation effect was not included in [174], the order of the spatial harmonics considered in flux-linkages was limited to 3 in [175], and the resultant torque was not validated in [176]. Moreover, the temperature effects on both the phase resistance and magnet remanence have not been considered in these models [170-176]. This neglect of the temperature effects can result in large errors in assessing the electromagnetic performance and thermal behaviour since the phase resistance and magnet remanence can vary approximately 39.3% and -12% respectively with a 100°C temperature rise [177].

In literature, the temperature effect on winding resistance has been simply accounted by the temperature coefficient of the wire resistivity if the winding temperature is known. The similar approach may be used for adjusting the permanent-magnet flux-linkage. However, the latter is only valid in SPMs in which the armature reaction is relatively weak and the saturation level in the stator and rotor cores is relatively low. In an IPM, strong armature reaction, high level of magnetic saturation and cross-coupling due to magnetic saturation result in much more complex temperature effects on the electromagnetic behaviour. Consequently, the *d*-

and q-axis flux-linkages and torque are non-linear functions of d- and q-axis currents, rotor position and temperature.

The temperature effect on electromagnetic performances was investigated and considered in the IPM model reported in [178]. However, the thermal model is not included and thus the machine temperatures cannot be predicted. Without an accurate temperature prediction, the losses and electromagnetic performance of the machine cannot be accurately predicted. Further, underestimation of the rotor magnet temperature may significantly increase the risk of irreversibly demagnetisation [179, 180]. This is because when the machine temperature increases, the permanent-magnet remanence will decrease, and so will the torque capability. Hence, the motor currents have to increase in order to meet the same torque demand. The increase in both the armature currents and phase resistance can further lead to even higher temperatures in both windings and rotor magnets. This vicious cycle continues, resulting in a much greater risk of irreversible demagnetisation. Therefore, a high-fidelity electro-thermally coupled machine model is essential for both the machine design and drive simulations in order to avoid this problem in real operations.

A few approaches to modelling machine electro-thermal behaviour have been proposed in [181-184]. However, they predict electromagnetic and thermal coupled machine behaviour by FEA of both electromagnetic and thermal fields, and require tremendous computational and data storage resources. It is therefore not realistic to employ FE-based electro-thermally coupled models in design optimisation and in simulations of EV traction machines which often require performance prediction over driving cycles.

To build a high-fidelity and computationally efficient model for IPMs, this chapter proposes a machine model based on the inverse solution of the flux-linkages extracted via FEA. The proposed model accounts for all physically essential effects, such as magnetic saturation, spatial harmonics, iron loss and temperature influences. This model is subsequently integrated with a

lumped parameter thermal model to establish an electro-thermally coupled model for IPMs. The developed electro-thermally coupled model is experimentally validated. The proposed modelling technique provides a computationally efficient and accurate means for design optimisation and for assessing electromagnetic and thermal behaviour of traction machines at the system-level over driving cycles.

5.2 Conventional IPM Machine Model

In literature, the conventional approach to modelling a PMSM is based on the *d*- and *q*-axis voltage and torque equations shown in (5.1). The corresponding machine model schematic is illustrated in Fig. 5-1.

$$\begin{aligned} V_d &= L_d \frac{di_d}{dt} + R_s i_d - \omega_e L_q i_q \\ V_q &= L_q \frac{di_q}{dt} + R_s i_q + \omega_e \left(\Psi_m + L_d i_d \right) \\ T_{em} &= \frac{m}{2} p \left[\Psi_m i_q + \left(L_d - L_q \right) i_d i_q \right] \end{aligned} \tag{5.1}$$

where *d*-axis inductance L_d, *q*-axis inductance L_q and permanent-magnet flux-linkage Ψ_m are the functions of both *d*-axis current i_d and *q*-axis current i_q, to take into account the magnetic saturation effect.

However, the conventional machine model only captures the effect of fundamental components whereas harmonic fields resulting from the combination of the magnetic saturation, slotting and permeance variation with rotor position are neglected. Secondly, the separation of $L_d i_d$ and Ψ_m from FE-predicted or measured *d*-axis flux-linkage cannot be performed accurately under saturation since the superposition principle is no longer valid. Inaccurate machine model not only affects the performance prediction of the drive system, but also seriously compromises the quality of model-based control for MTPA and field weakening operations.

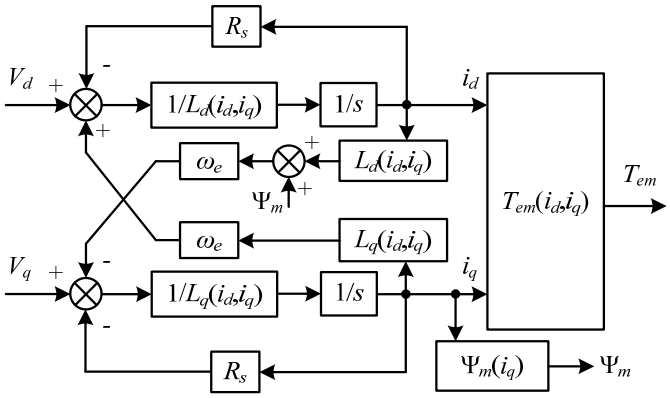

Fig. 5-1. Schematic of the conventional IPM machine model.

5.3 Proposed Electromagnetic Model

5.3.1 Model Description

To address the problems associated with the conventional model as discussed in Section 5.2, a flux-linkage-based machine model, as described by (5.2), (5.3) and (5.4), is employed.

$$\begin{aligned} V_d &= \frac{d\Psi_d}{dt} + R_s i_d - \omega_e \Psi_q \\ V_q &= \frac{d\Psi_q}{dt} + R_s i_q + \omega_e \Psi_d \end{aligned} \tag{5.2}$$

$$\begin{aligned} \Psi_d &= f\left(i_d, i_q, \theta\right) \\ \Psi_q &= g\left(i_d, i_q, \theta\right) \end{aligned} \tag{5.3}$$

$$T_{em} = \frac{m}{2} p\left(\Psi_d i_q - \Psi_q i_d\right) \tag{5.4}$$

where d- and q-axis flux-linkages Ψ_d, Ψ_q are the functions of the d- and q-axis currents i_d, i_q and the rotor position θ. Thus, the effects of both magnetic saturation and the spatial harmonic fields are inherently included in the above flux-linkage functions.

Furthermore, to avoid the derivative calculation, the d- and q-axis flux-linkages can be obtained by integration given in (5.5).

$$\begin{aligned}\Psi_d &= \int \left(V_d - R_s i_d + \omega_e \Psi_q\right) dt \\ \Psi_q &= \int \left(V_q - R_s i_q - \omega_e \Psi_d\right) dt\end{aligned} \tag{5.5}$$

By performing inverses of (5.3) at a given rotor position, the *d*- and *q*-axis currents are determined by (5.6).

$$\begin{aligned}i_d &= f^{-1}\left(\Psi_d, \Psi_q, \theta\right) \\ i_q &= g^{-1}\left(\Psi_d, \Psi_q, \theta\right)\end{aligned} \tag{5.6}$$

To capture all the torque components, including cogging torque which is present even with zero currents [140], the electromagnetic torque computed from FEA can be written as a function of *d*- and *q*-axis currents i_d, i_q and the rotor position θ in (5.7).

$$T_{em} = T\left(i_d, i_q, \theta\right) \tag{5.7}$$

All the functions in (5.6) and (5.7) can be established by either 3-D lookup tables or curve fitting. It should be noted that the instantaneous torque cannot be calculated purely by flux-linkages and currents due to the existence of cogging torque which is determined by the stored energy variation or field solution in the air-gap [140]. Therefore, the torque in the proposed model is determined by (5.7) rather than an explicit equation.

The electromagnetic part of the proposed machine model schematic is illustrated in Fig. 5-2.

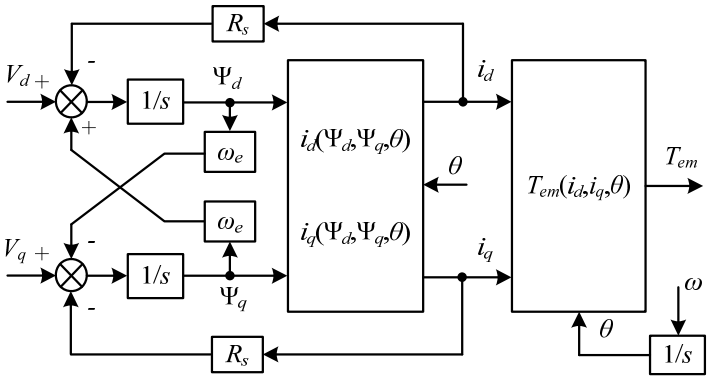

Fig. 5-2. Schematic of the proposed electromagnetic model of IPMs.

As shown in Fig. 5-2, for a given voltage, the d- and q-axis flux-linkages Ψ_d and Ψ_q are calculated by the integrals in (5.5). Subsequently, the d- and q-axis current i_d and i_q are obtained from the functions $i_d(\Psi_d,\Psi_q,\theta)$ and $i_q(\Psi_d,\Psi_q,\theta)$ with the d- and q-axis flux-linkages Ψ_d, Ψ_q, and rotor position θ as the inputs. The resultant electromagnetic torque is acquired from $T_{em}(i_d,i_q,\theta)$. Finally, the angular speed and position of the rotor can be calculated via the mechanical motion equations. It should be noted that the proposed model includes all effects due to magnetic saturation in the stator and rotor cores and spatial harmonics in MMF, as well as torque ripple from variation of magnetic co-energy with rotor position.

To accurately represent the electromagnetic behaviour of a PMSM machine, all the variations of d- and q-axis flux-linkages and torque with d- and q-axis currents and rotor position, viz. $\Psi_d(i_d,i_q,\theta)$, $\Psi_q(i_d,i_q,\theta)$ and $T_{em}(i_d,i_q,\theta)$, are obtained via FEA or measurements. However, to implement the proposed model shown in Fig. 5-2, the d- and q-axis currents, viz. $i_d(\Psi_d,\Psi_q,\theta)$ and $i_q(\Psi_d,\Psi_q,\theta)$, as functions of Ψ_d, Ψ_q, and θ need to be obtained through the inverse of $\Psi_d(i_d,i_q,\theta)$, $\Psi_q(i_d,i_q,\theta)$. This process is described in the following section.

5.3.2 Inverse Solution of Currents versus Flux-linkages

Without loss of generality, a 36-slot 6-pole IPM machine prototype is employed to demonstrate the process and the effectiveness of the proposed modelling technique. The machine specifications and design parameters are listed in Table 5-1 and the schematic is shown in Fig. 5-3.

The d- and q-axis flux-linkages and torque $\Psi_d(i_d,i_q,\theta)$, $\Psi_q(i_d,i_q,\theta)$ and $T_{em}(i_d,i_q,\theta)$ as functions of i_d, i_q, and θ are obtained via FEA by varying i_d, i_q and θ in the ranges of -140~140A, -240~240A and 0~120° (0~360° in electrical degree), respectively. The i_d, i_q and θ samples in FE calculation are 15, 25 and 97 respectively, and hence the total FE steps are 36,375. The off-line

computation time to set up $\Psi_d(i_d,i_q,\theta)$, $\Psi_q(i_d,i_q,\theta)$ and $T_{em}(i_d,i_q,\theta)$ is approximately 32 hours on a quad-core 3.1GHz PC. The computation time also depends on the periodicity condition and mesh density of the FE model.

Table 5-1. Specifications and Design Parameters of the Machine Prototype

Quantity	Unit	Value
Peak torque	Nm	70
Rated torque	Nm	35.5
Base Speed	r/min	1350
Max Speed	r/min	4500
Peak power	kW	9.9
Rated power	kW	5
DC link voltage	V	120
Peak current	A	125
Number of pole-pairs	--	3
Number of slots	--	36
Active stack length	mm	118
Stator outer diameter	mm	150
Rotor outer diameter	mm	80

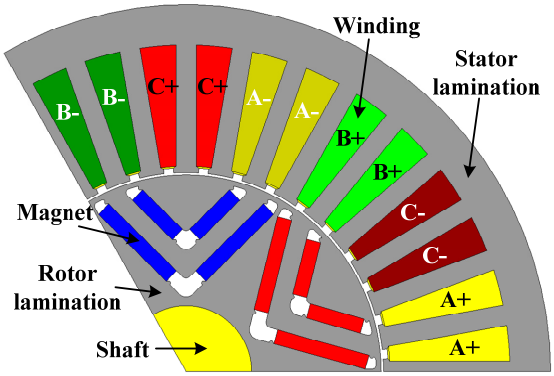

Fig. 5-3. Schematic for IPM 36-slot 6-pole machine prototype (one-third model).

The d- and q-axis flux-linkages and torque maps versus d- and q-axis currents at 0° rotor position referred to phase A axis are shown in Fig. 5-4, whilst the variations of the d- and q-axis flux-linkages and torque with rotor position at i_d=-40A and i_q=60A are illustrated in Fig. 5-5. The magnetic saturation effect is evident in Fig. 5-4 and the spatial harmonics in the flux-linkages and torque can be observed in Fig. 5-5. It should be noted that torque ripple exists even with constant d- and q-axis currents or sinusoidal phase currents. This ripple is present in a real IPM machine, but cannot be predicted by the conventional model in (5.1).

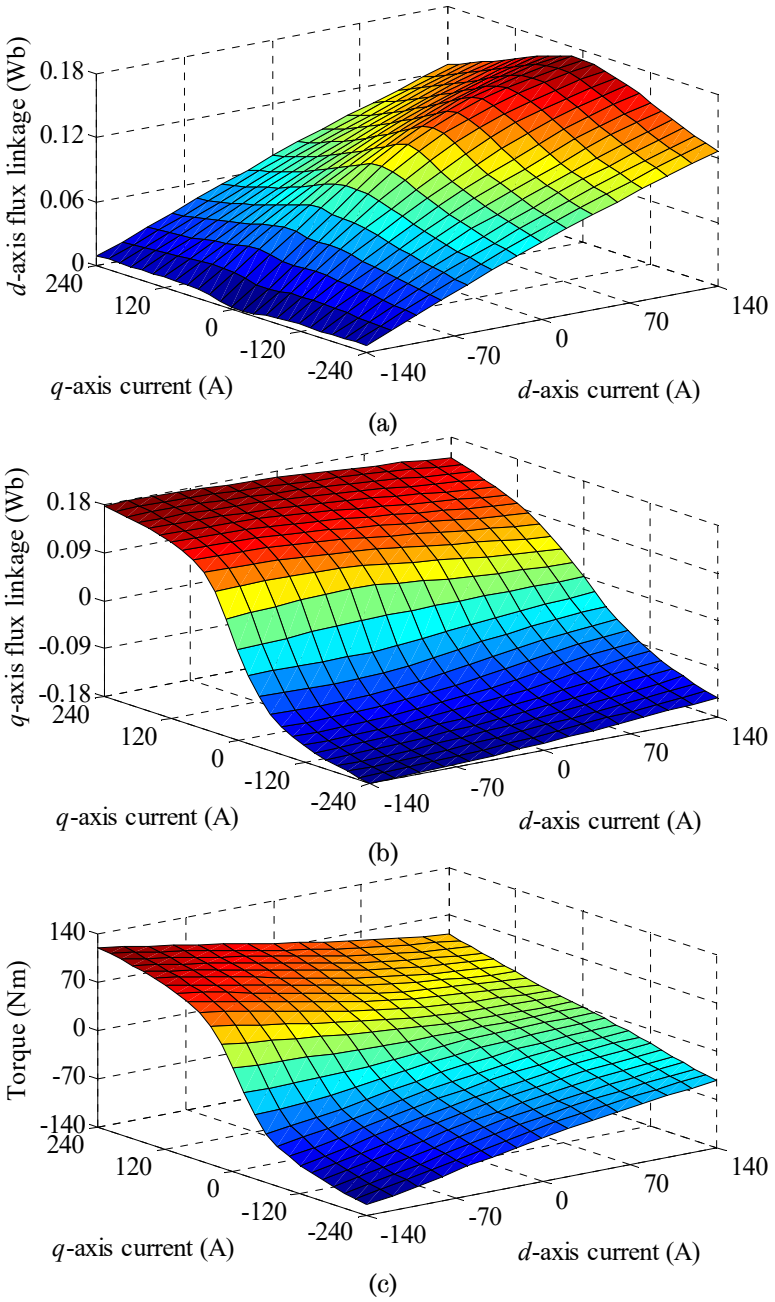

Fig. 5-4. Flux-linkage and torque maps versus *d*- and *q*-axis currents at rotor position = 0°. (a) *d*-axis flux-linkage. (b) *q*-axis flux-linkage. (c) Torque.

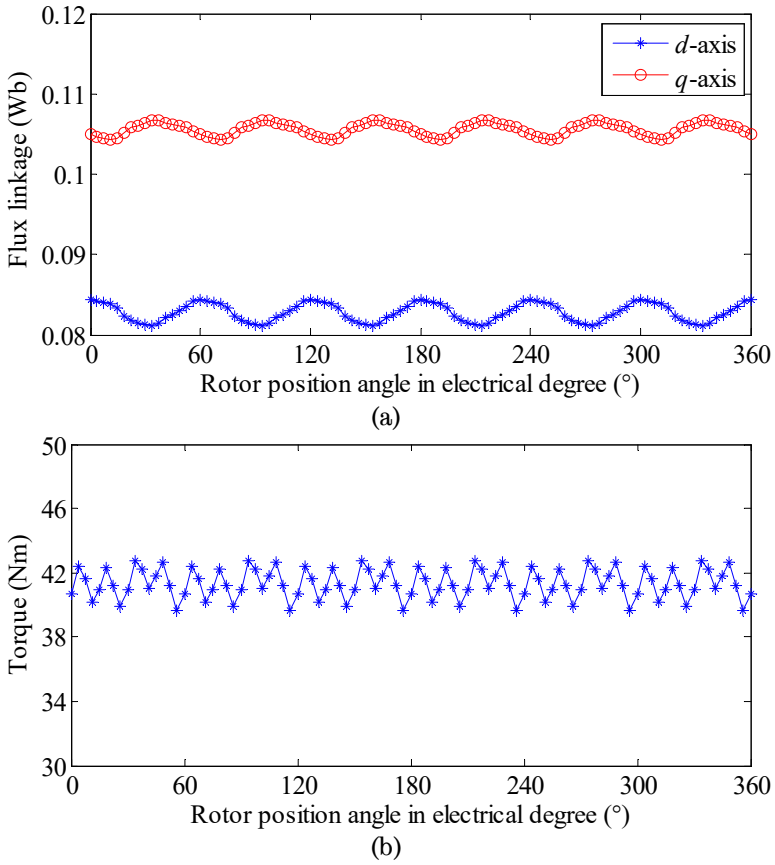

Fig. 5-5. Flux-linkage and torque variations with rotor position at i_d=-40A, i_q=60A. (a) d- and q-axis flux-linkages. (b) Torque.

Based on the $\Psi_d(i_d,i_q,\theta)$ and $\Psi_q(i_d,i_q,\theta)$ maps at a given θ, i_d and i_q can be uniquely found. The solution to the inverse problem, viz., equation (5.6), can be obtained via the minimisation of the residual flux-linkage magnitude Ψ_{eq}, defined in (5.8).

$$\Psi_{eq} = \left|\Psi_d\left(i_d, i_q, \theta_0\right) - \Psi_{d0}\right| + \left|\Psi_q\left(i_d, i_q, \theta_0\right) - \Psi_{q0}\right| \tag{5.8}$$

where the Ψ_{d0} and Ψ_{q0} are the given d- and q-axis flux-linkages at θ_0, and Ψ_d and Ψ_q are obtained from the flux-linkage maps with iterative solutions of the d- and q-axis currents as the inputs at the same rotor position.

To minimise Ψ_{eq}, the unknown i_d and i_q are found through an iterative process until the objective function Ψ_{eq} reduces to the required tolerance. During this process, $\Psi_d(i_d,i_q,\theta_0)$ and $\Psi_q(i_d,i_q,\theta_0)$ are calculated via the 2-D interpolation on the original flux-linkage maps. The employed minimisation

algorithm is the interior-point method [185]. The computation time needed to build (5.6) is approximately 1 hour on a quad-core 3.1GHz PC.

The resultant *d*- and *q*-axis current variations are shown in Fig. 5-6 and Fig. 5-7. Fig. 5-6 depicts the *d*- and *q*-axis current maps versus *d*- and *q*-axis flux-linkages at 0° rotor position, whilst Fig. 5-7 shows the *d*- and *q*-axis current variations with rotor position at Ψ_d = 0.083Wb and Ψ_q = 0.105Wb.

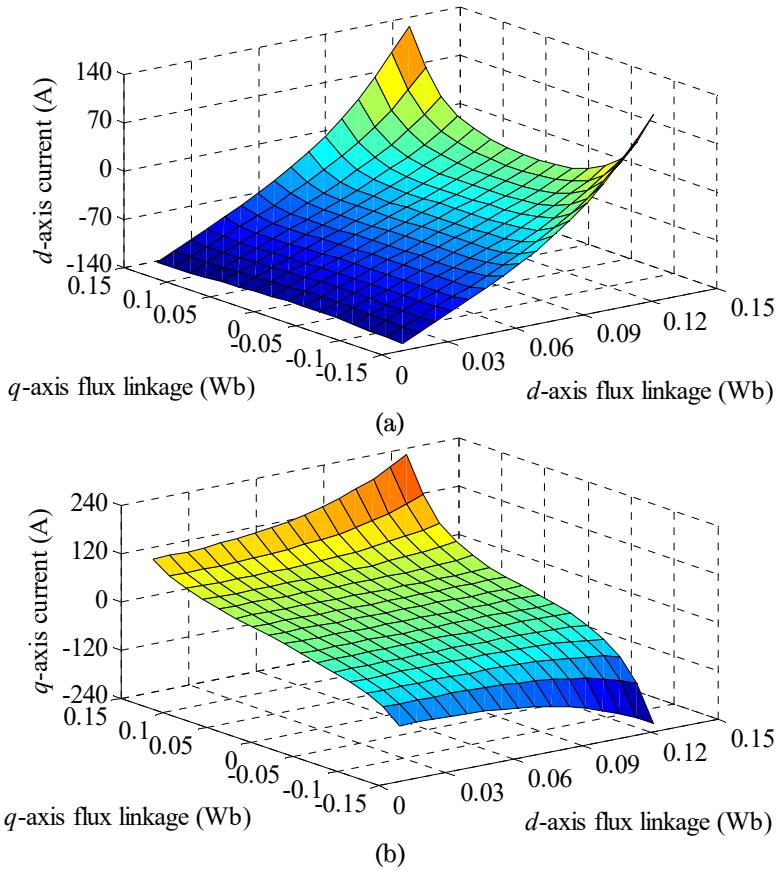

Fig. 5-6. Current maps versus *d*- and *q*-axis flux-linkages at rotor position =0°. (a) *d*-axis current. (b) *q*-axis current.

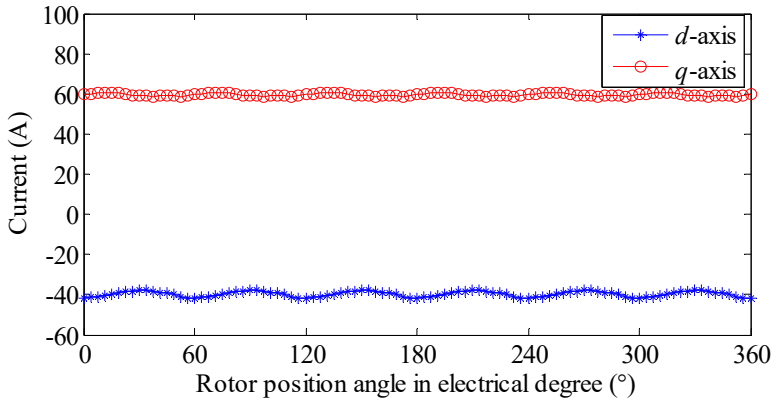

Fig. 5-7. *d*- and *q*-axis current variations with rotor position at Ψ_d=0.083Wb and Ψ_q=0.105Wb.

To validate the accuracy of the inverse, the resultant *d*-axis and *q*-axis currents at given *d*- and *q*-axis flux-linkages and rotor position are used to obtain *d*- and *q*-axis flux-linkages from the original *d*- and *q*-axis flux-linkage maps shown in Fig. 5-4, and the results are compared with the flux-linkages that are used to generate the *d*- and *q*-axis currents from the inverse maps shown in Fig. 5-6. The resultant *d*- and *q*-axis flux-linkage error maps are shown in Fig. 5-8. It can be observed that maximum error of the *d*-axis flux-linkage is 1.5×10^{-5}% whilst that of the *q*-axis flux-linkage is 1.0×10^{-6}%. Flux-linkage errors at other rotor positions were also checked and they are of the similar order of magnitude.

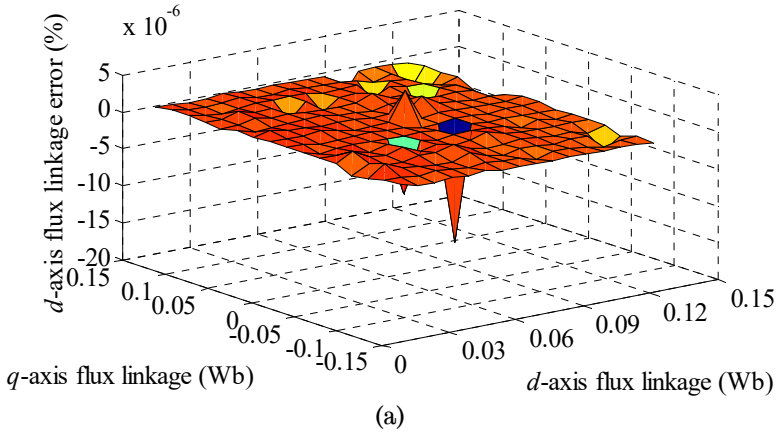

(a)

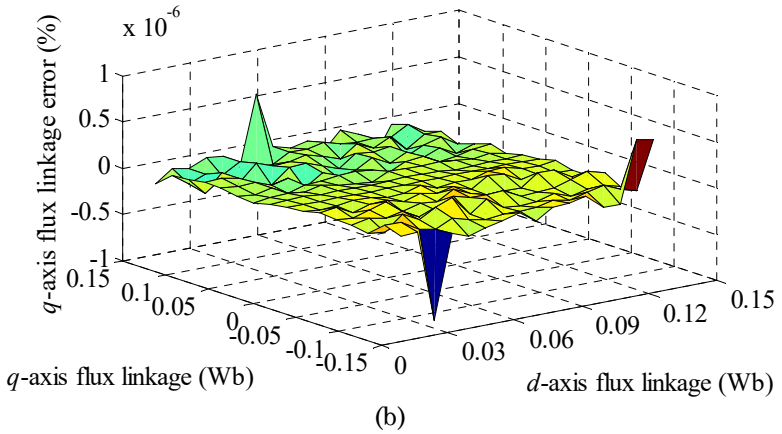

(b)

Fig. 5-8. Flux-linkage error maps versus *d*- and *q*-axis flux-linkages at rotor position =0°. (a) *d*-axis flux-linkage error. (b) *q*-axis flux-linkage.

5.4 Proposed Machine Model Considering Iron Loss Effect

5.4.1 Iron Loss Circuit Model

The iron loss in electrical machines increases or decreases active power depending on whether they operate as motor or generator, and hence affects the phase currents at a given supply voltage.

To consider the iron loss effect on the machine electromagnetic behaviour at different load conditions in a computationally efficient manner, the iron loss model presented in [59, 186] is employed, which can be described by (5.9).

$$p_{Fe\_oc} = a_h \frac{V_m}{2\pi\Psi_m} + a_e \left(\frac{V_m}{2\pi\Psi_m}\right)^2 + a_x \left(\frac{V_m}{2\pi\Psi_m}\right)^{1.5}$$
$$p_{Fe\_sc} = b_h \frac{V_{da}}{2\pi\Psi_m} + b_e \left(\frac{V_{da}}{2\pi\Psi_m}\right)^2 + b_x \left(\frac{V_{da}}{2\pi\Psi_m}\right)^{1.5} \quad (5.9)$$

where the iron loss coefficients (a_h, a_e, a_x) and (b_h, b_e, b_x) are determined by FE analysis at no-load (open-circuit) and short-circuit operations, respectively. The total iron loss at a given operation is the sum of p_{Fe_oc} and p_{Fe_sc}. The voltage magnitude V_m and the voltage due to armature reaction of

d-axis current V_{da} whose phasor diagram is shown in Fig. 5-9 can be calculated by (5.10).

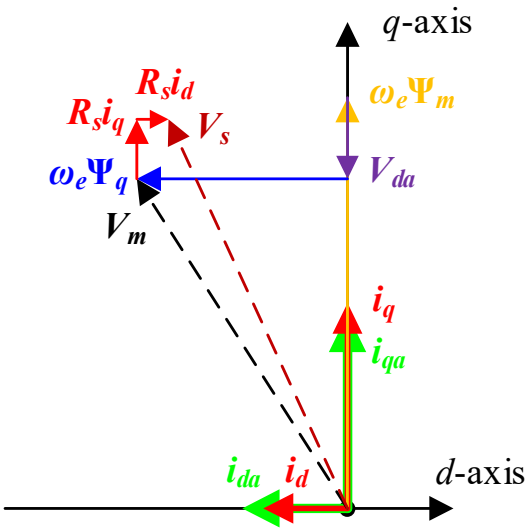

Fig. 5-9. Phasor diagram for an IPM machine.

$$\begin{aligned} V_m &= \omega_e \sqrt{\Psi_d^{\,2} + \Psi_q^{\,2}} \\ V_{da} &= -\omega_e \left(\Psi_d - \Psi_m \right) \end{aligned} \tag{5.10}$$

where Ψ_m is obtained by the Ψ_d at i_d=0 while i_q equals to the on-load *q*-axis current.

The iron loss can be further decomposed into the components associated with the *d*- and *q*-axis flux-linkages, as expressed by (5.11).

$$\begin{aligned} p_{Fe\_d} &= \frac{\Psi_q^{\,2}}{\Psi_d^{\,2} + \Psi_q^{\,2}} p_{Fe\_oc} + p_{Fe\_sc} \\ p_{Fe\_q} &= \frac{\Psi_d^{\,2}}{\Psi_d^{\,2} + \Psi_q^{\,2}} p_{Fe\_oc} \end{aligned} \tag{5.11}$$

In motoring operation, the iron loss consumes power from electrical supply, whereas it reduces electrical output power in generating mode. Therefore, if the iron loss effect is considered as the equivalent currents which incur losses in the equivalent resistors across the *d*- and *q*-axis

induced voltages, as shown in Fig. 5-10, the influence of the iron loss on the *d*- and *q*-axis currents is given in (5.12).

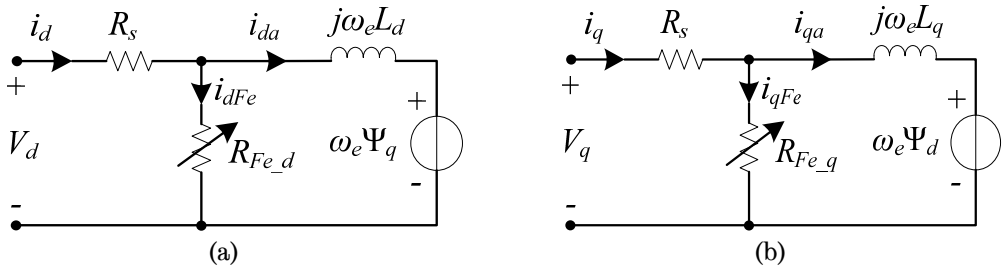

Fig. 5-10. Circuit model with equivalent iron loss components. (a) *d*-axis circuit model. (b) *q*-axis circuit model.

$$i_{da} = i_d \mp \frac{p_{Fe\_d}}{V_d - R_s i_d}$$
$$i_{qa} = i_q \mp \frac{p_{Fe\_q}}{V_q - R_s i_q} \tag{5.12}$$

where i_{da} and i_{qa} are the *d*- and *q*-axis currents which are associated with the armature reaction, "-" is for the motoring mode, and "+" is for the generating mode. The schematic of the IPM model that integrates the iron loss model is shown in Fig. 5-11.

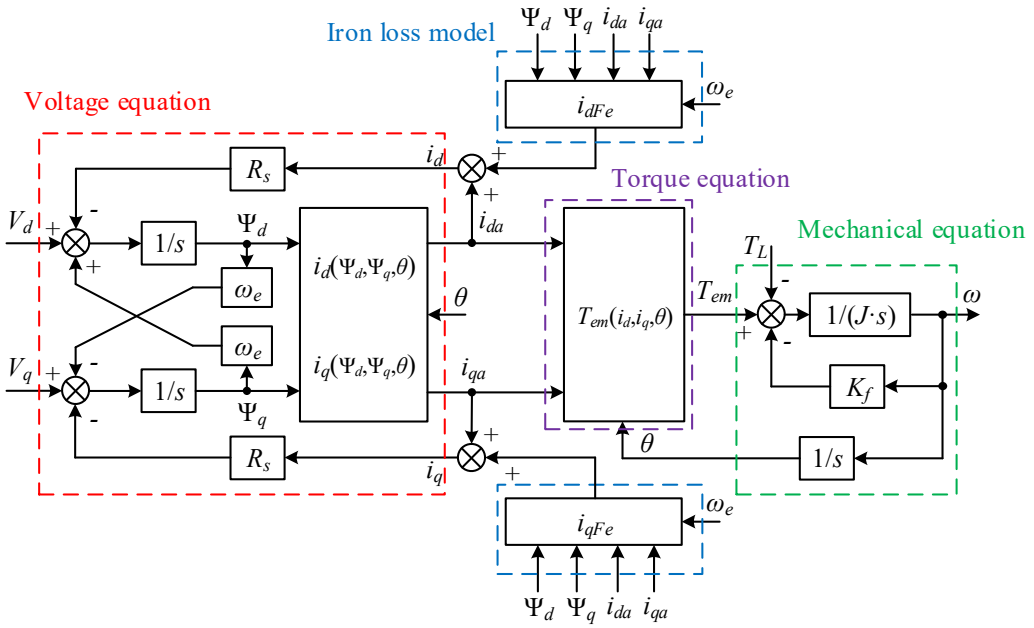

Fig. 5-11. Schematic of the proposed IPM machine model with iron loss effect.

5.4.2 Iron Loss Influence on Electromagnetic Behaviour

The influence of iron loss on the electromagnetic behaviour of the IPM machine is studied using the developed model shown in Fig. 5-11. Fig. 5-12 compares (i_d,i_q) with (i_{da},i_{qa}) at peak torque over the operating speed range in the motoring mode. If the iron loss is neglected, i_d=i_{da}; i_q=i_{qa}. Otherwise, they will be different. It can be seen that in the constant-torque region where the machine operates at the MTPA condition with the current limit, the amplitudes of both *d*- and *q*-axis currents, i_{da} and i_{qa}, associated with electromechanical energy conversion are slightly reduced in the motoring mode when the iron loss is included. Consequently, the electromagnetic torque will be slightly lower. However, in the constant-power region where the machine operates under the field weakening condition, the influence of iron loss on the *d*-axis current is more pronounced with increase in operating speeds. This is because the iron loss increases more than proportionally as the speed increases. It can also be seen that in the field weakening region the influence of iron loss on *q*-axis current is much less than that on the *d*-axis current since the *d*-axis flux-linkage has been weakened and becomes smaller than that of the *q*-axis at high speeds.

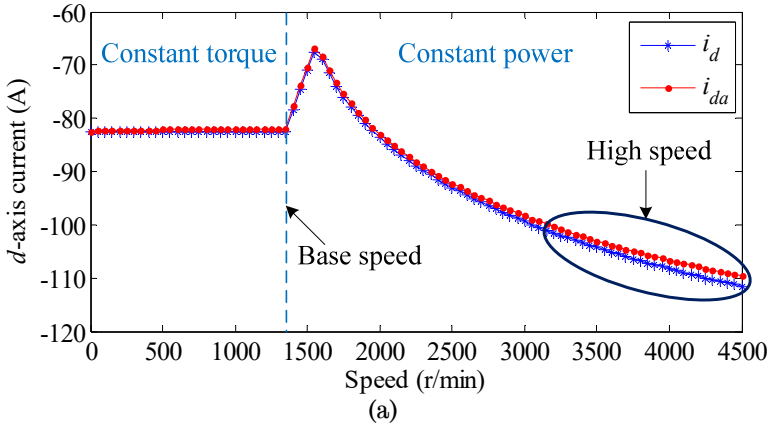

(a)

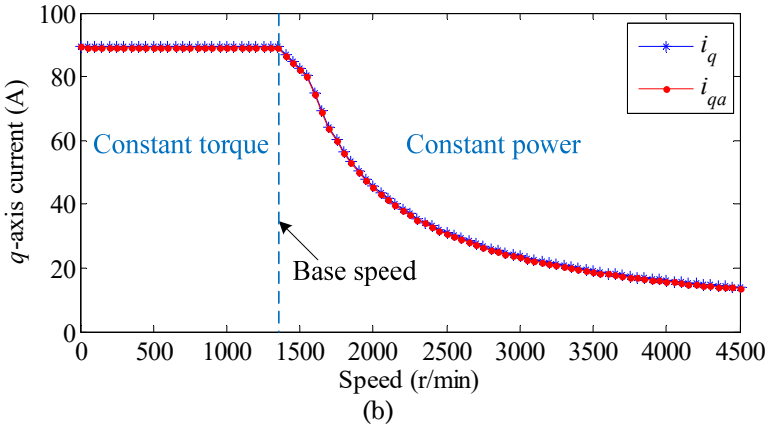

Fig. 5-12. Iron loss influence on *d*- and *q*-axis currents over the peak torque envelope in motoring mode. (a) *d*-axis current. (b) *q*-axis current.

5.5 Comparison with Conventional Model

The utility of the proposed model in Fig. 5-11 is studied in a drive system with the field-oriented control strategy in both constant-torque and field weakening regions, and the results are compared with those obtained from the conventional model given in (5.1) and Fig. 5-1 under the same operating conditions.

If the current control bandwidth is high and the currents can be controlled close to sinusoidal, the resultant differences in flux-linkage and voltage waveforms between the proposed and conventional models are quite significant. By way of example, Fig. 5-13 compares the flux-linkage trajectories predicted by the conventional and proposed models in the field weakening region. The *d*- and *q*-axis currents are -62.6A and 10.4A, respectively, which correspond to the experimental working point in field weakening region in Section 5.8.3. It can be seen that the flux-linkage trajectory predicted by the proposed model is no longer a circle and exhibits fluctuation in magnitude. This fluctuation results in a large distortion in the voltage trajectory, as shown in Fig. 5-14.

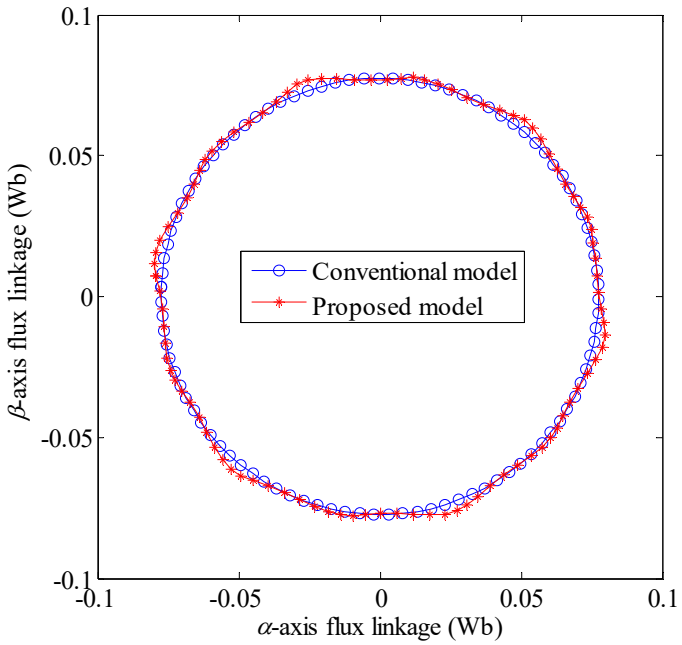

Fig. 5-13. Flux-linkage trajectory comparison between proposed and conventional models under ideal sinusoidal current excitation.

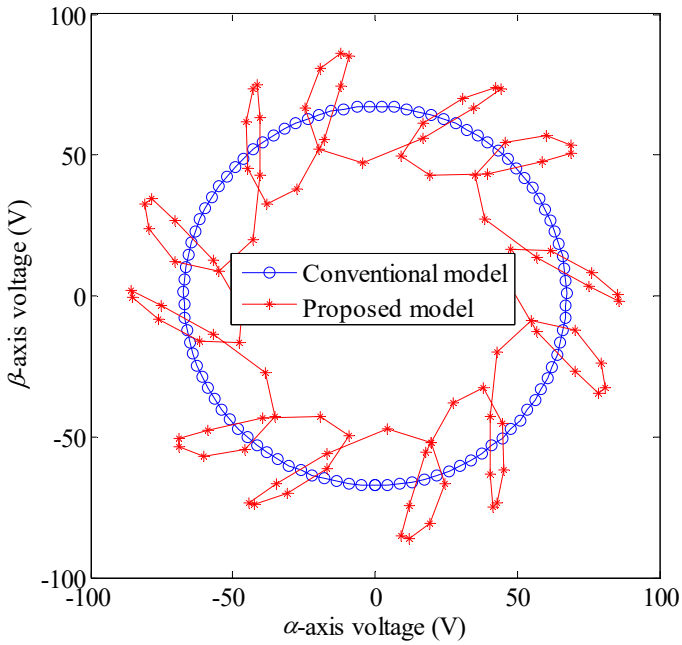

Fig. 5-14. Voltage trajectory comparison between proposed and conventional models under ideal sinusoidal current excitation.

If the currents can be controlled as purely sinusoidal, the voltage will exhibit enormous distortion in the field weakening region. However, the drive has a limited current control bandwidth and is usually fed by a voltage-source inverter with its maximum available voltage being limited. As a result,

the current trajectory becomes distorted, as can be seen in Fig. 5-15. All the three current trajectories are obtained at the same load condition, viz., 10Nm and 2700r/min. It can also be observed that the current trajectory of the proposed model is very close to the measurement. However, the conventional model can neither predict accurately the current amplitude due to neglecting the iron loss nor capture the current ripples resulting from the MMF spatial harmonics.

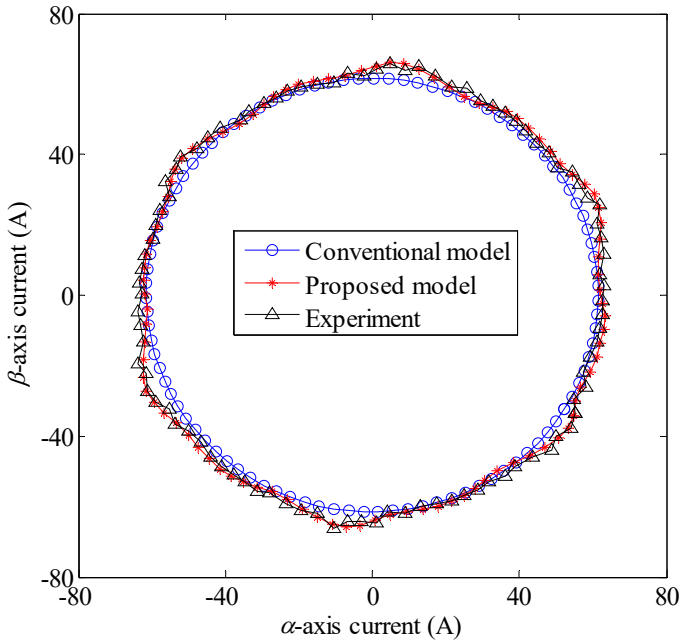

Fig. 5-15. Comparisons of measured and predicted current trajectories with voltage-source inverter at 10Nm and 2700r/min.

Due to the current waveform being distorted as shown in Fig. 5-15, the proposed model predicts a very high torque ripple, which cannot be represented by the conventional machine model, as illustrated in Fig. 5-16. The harmonic distribution of the torque predicted by the proposed model, as shown in Fig. 5-16 (b), suggests that the dominant ripple harmonic is of the 12^{th} order. It is mainly contributed by the 12^{th} order harmonic in the *d*- and *q*-axis currents, shown in Fig. 5-17, which interact with the DC components of the *q*- and *d*-axis flux-linkages respectively.

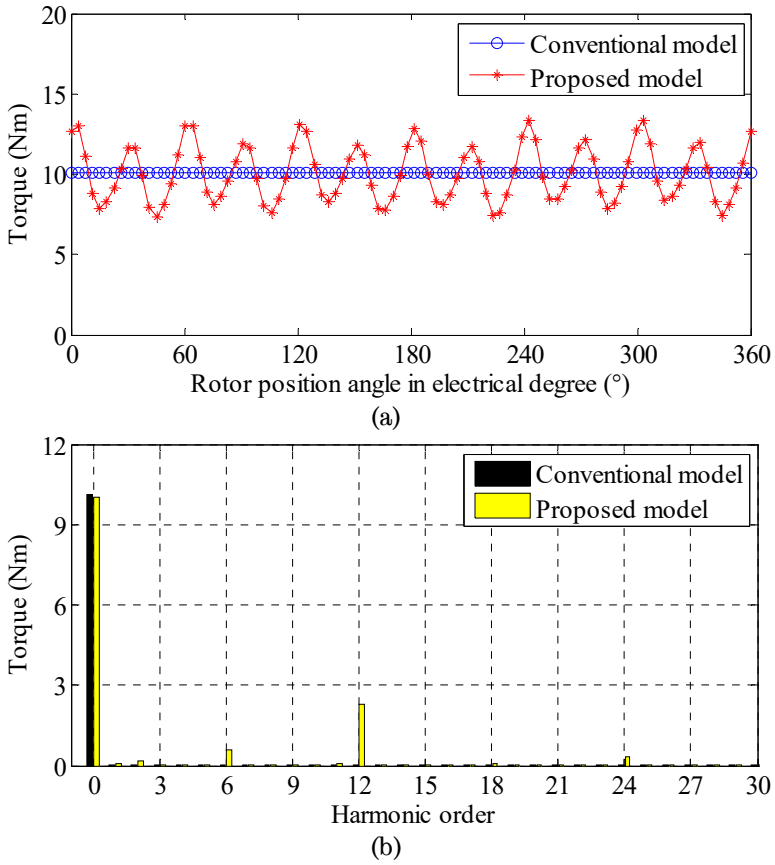

Fig. 5-16. Torque waveform and spectrum comparison for the proposed and conventional models with voltage-fed converter.

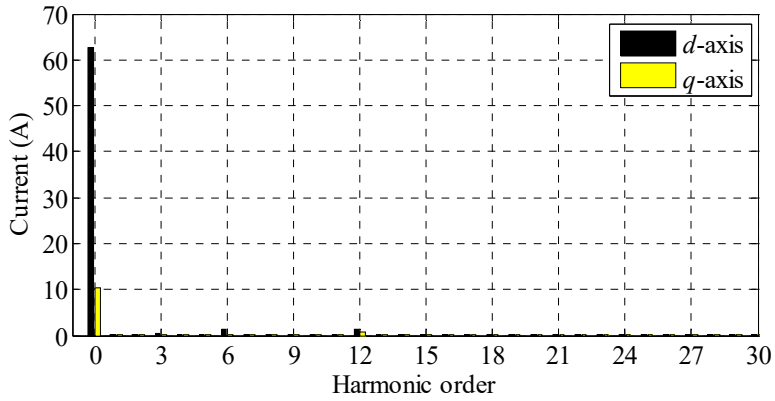

Fig. 5-17. *d*- and *q*-axis current spectra of the proposed model at 10Nm and 2700r/min.

In the constant-torque region, the predicated current waveforms obtained from the proposed model are close to sinusoidal when the current control bandwidth is relatively high. However, the distortions in the flux-linkages and voltages are still significant although the torque ripple is lower than that observed in the field weakening region. Nevertheless, no distortion

is seen in the predicted voltages, currents and flux-linkages by the conventional model in both constant-torque and field weakening regions.

In summary, the conventional inductance-based model neglecting spatial harmonics, position dependent *d*- and *q*-axis flux-linkages and the iron loss effect cannot reflect the real machine behaviour in the simulation, particularly in the field weakening region where the iron loss influence will be large and significant harmonics in current waveforms will be present due to current control error under the voltage limit.

In contrast, the proposed machine model in Fig. 5-11 includes the iron loss effect and captures all these effects in the form of 3-D flux-linkage and torque lookup tables or curve fitted functions. Therefore, the proposed model exhibits high fidelity in predicting the real machine behaviour.

Compared to the circuit-field coupled co-simulation, the order of magnitude of the computation time for the proposed model is reduced from days [170] to seconds. For a 0.5s simulation with 10μs time step, the computation time is 10s on a quad-core 3.1GHz PC.

5.6 Proposed Machine Model Considering Temperature Effect

The temperature effects on machine performance will be investigated in this section. Subsequently, these temperature effects will be incorporated into the proposed machine model.

5.6.1 Temperature Influence

The temperature effect on winding resistance is widely established in literature and can be described in (5.13).

$$R_s = R_{s0}\left[1+\alpha_T\left(T_w - T_0\right)\right] \tag{5.13}$$

where R_{s0} is the phase resistance at winding temperature T_0, and the temperature coefficient for copper α_T=0.393%/°C. It should be noted that the skin effect, proximity loss [160-162] and their temperature effects can also be included in the copper loss calculation. However, these effects are negligible in machines whose speed (electric frequency) is not very high or whose windings employ multi-strand wires with small size. Litz wire configuration can be used to minimise these effects.

In literature, the temperature effect of the magnet remanence is usually accounted only by *d*-axis flux-linkage independent of load conditions. However, this simplification leads to a non-negligible error since three factors are ignored. Firstly, the *d*-axis flux-linkage variation due to temperature change is dependent on *d*- and *q*- axis currents and hence on loads because the magnetic saturation levels vary with the currents. Secondly, the *q*-axis flux-linkage also changes with temperature due to saturation-induced cross-coupling. Thirdly, the magnetic saturation levels vary when the rotor position changes, and hence the rotor position also affects the temperature influence on both the *d*- and *q*-axis flux-linkages and the torque.

Without loss of generality, the foregoing 10kW 36-slot 6-pole IPM machine prototype is employed to demonstrate the three factors. The *d*- and *q*-axis flux-linkage and torque variations with *d*- and *q*-axis currents at rotor position θ=0° when the rotor magnet temperature changes from 20°C to 120°C are illustrated in Fig. 5-18. The percentage values of the *d*- and *q*-axis flux-linkages and the torque in Fig. 5-18 are calculated against their maximum values over the current ranges at 20°C, namely, 0.098Wb, 0.155Wb and 98.4Nm, respectively. It can be observed that the *d*-axis flux-linkage variation is non-uniform while the *q*-axis flux-linkage variation is up to 6% which is not negligible due to saturation induced cross-coupling.

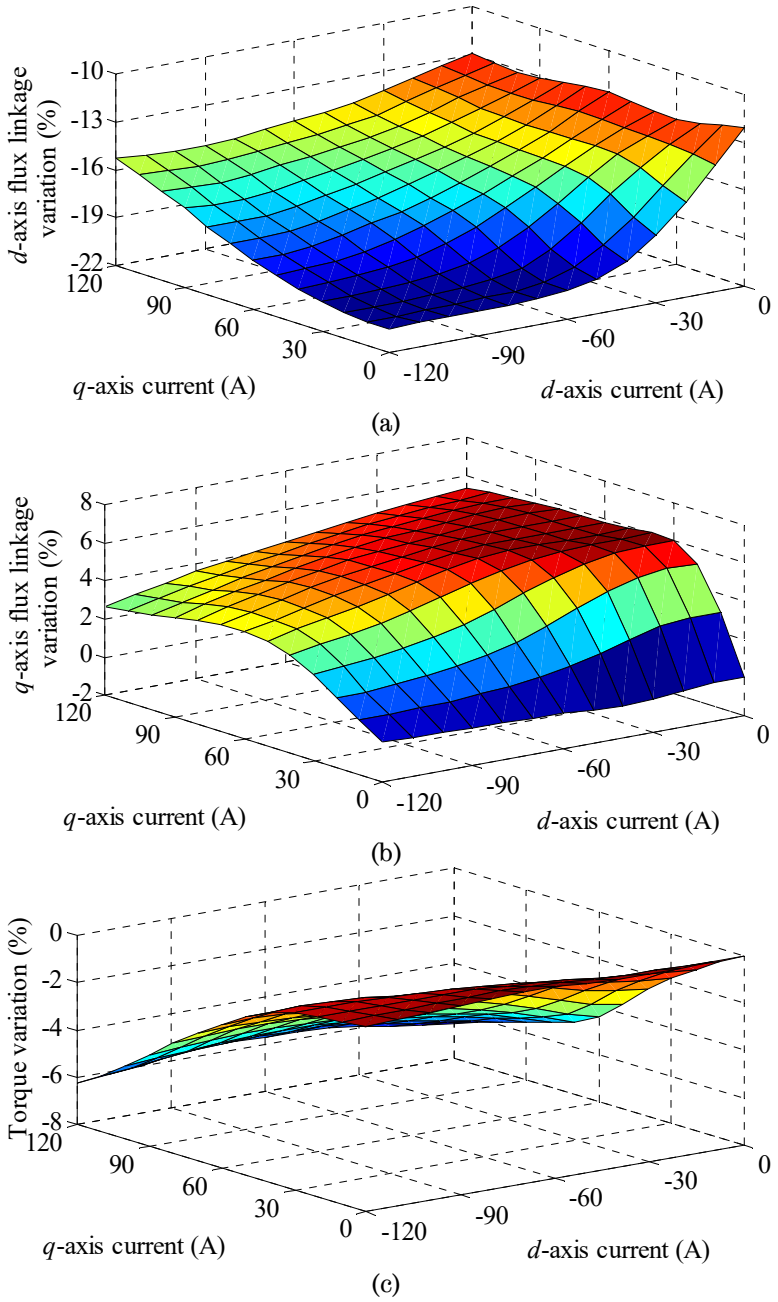

Fig. 5-18. Flux-linkage and torque variations with *d*- and *q*-axis currents at rotor position = 0° when rotor temperature changes from 20°C to 120°C. (a) *d*-axis flux-linkage. (b) *q*-axis flux-linkage. (c) Torque.

Fig. 5-19 shows the flux-linkage and torque variations with rotor position, at i_d=-90A, i_q=90A, when the rotor temperature changes from 20°C to 120°C. It is evident that the temperature influence on the *d*- and *q*-axis flux-linkages and the torque varies with rotor position.

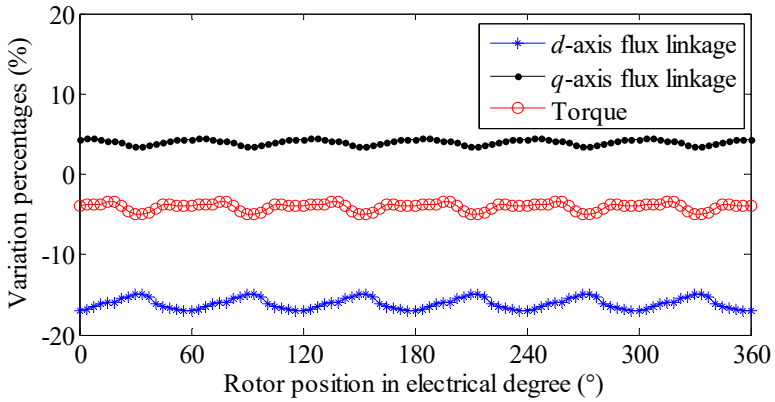

Fig. 5-19. Flux-linkage and torque variations with rotor position at i_d=-90A, i_q=90A when rotor temperature changes from 20°C to 120°C.

Therefore, any modelling technique which accounts the temperature effect of magnets only by introducing a constant $\Delta\Psi_d$ independent of d- and q-axis currents will result in large errors in predicting the electromagnetic performance of an IPM machine.

5.6.2 Temperature Effect Incorporation

According to the foregoing analysis, the magnet temperature influences both d- and q-axis flux-linkages and this influence also varies with currents (load) and rotor position. To consider the temperature effects in the machine model in Fig. 5-11, the d- and q-axis currents need to be corrected according to the rotor magnet temperature variation. This is because the relationship between flux-linkages and armature currents is depicted by $i_d(\Psi_d,\Psi_q,\theta,T)$ and $i_q(\Psi_d,\Psi_q,\theta,T)$ rather than $\Psi_d(i_d,i_q,\theta,T)$ and $\Psi_q(i_d,i_q,\theta,T)$ in the model. Theoretically, $i_d(\Psi_d,\Psi_q,\theta,T)$, $i_q(\Psi_d,\Psi_q,\theta,T)$ and $T_{em}(i_d,i_q,\theta,T)$ are all 4-D functions. However, to reduce the data size in simulations and also save the FEA time, a simplified electromagnetic model that accounts the temperature effects is proposed in this study. Based on Taylor's expansion, the temperature effects on i_d, i_q and T_{em} may be approximated in (5.14) and the schematic of the overall machine model with the temperature effects is shown in Fig. 5-20.

$$
\begin{aligned}
i_d\left(\Psi_d,\Psi_q,\theta,T\right) &= i_d\left(\Psi_d,\Psi_q,\theta,T_0\right)+\Delta i_d\left(\Psi_d,\Psi_q,\theta\right)\cdot\left(T-T_0\right)\\
i_q\left(\Psi_d,\Psi_q,\theta,T\right) &= i_q\left(\Psi_d,\Psi_q,\theta,T_0\right)+\Delta i_q\left(\Psi_d,\Psi_q,\theta\right)\cdot\left(T-T_0\right)\\
T_{em}\left(i_d,i_q,\theta,T\right) &= T_{em}\left(i_d,i_q,\theta,T_0\right)+\Delta T_{em}\left(i_d,i_q,\theta\right)\cdot\left(T-T_0\right)
\end{aligned}
\tag{5.14}
$$

where, T is the operating temperature of the rotor magnets, T_0 is the reference temperature, $\Delta i_d(\Psi_d,\Psi_q,\theta)$, $\Delta i_q(\Psi_d,\Psi_q,\theta)$ and $\Delta T_{em}(i_d,i_q,\theta)$ are the first order slopes of i_d, i_q and T_{em} against temperature change, respectively. These three functions can be obtained by calculating the changes of $i_d(\Psi_d,\Psi_q,\theta)$, $i_q(\Psi_d,\Psi_q,\theta)$ and $T_{em}(i_d,i_q,\theta)$ at two representative temperatures. Fig. 5-21 illustrates the variations of $\Delta i_d(\Psi_d,\Psi_q,\theta)$, $\Delta i_q(\Psi_d,\Psi_q,\theta)$ with Ψ_d, and Ψ_q and the variation of $\Delta T_{em}(i_d,i_q,\theta)$ with i_d, and i_q at θ = 0°, obtained from FE calculations at two rotor temperatures with +1°C temperature variation. Fig. 5-22 shows the variations of $\Delta i_d(\Psi_d,\Psi_q,\theta)$, $\Delta i_q(\Psi_d,\Psi_q,\theta)$ with θ at Ψ_d = 0.09Wb, Ψ_q = 0.1Wb and the variation of $\Delta T_{em}(i_d,i_q,\theta)$ with θ at i_d=-40A, i_q=60A. It can be seen that $\Delta i_d(\Psi_d,\Psi_q,\theta)$, $\Delta i_q(\Psi_d,\Psi_q,\theta)$ and $\Delta T_{em}(i_d,i_q,\theta)$ are all non-linear functions of Ψ_d, Ψ_q and θ, and hence dependent on both load and rotor position.

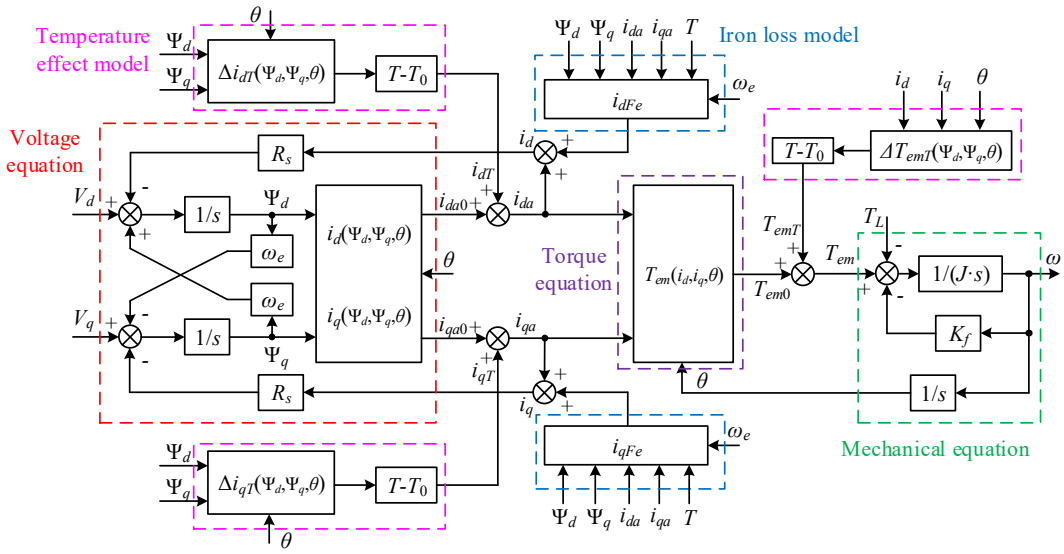

Fig. 5-20. The schematic of the proposed IPM machine model considering temperature effects.

The temperature effect on the iron loss is also considered in the proposed model in Fig. 5-20. The electrical resistivity of the silicon-steel varies with temperature. Therefore, the eddy current loss component of the iron loss is

affected by the temperature. The resistivity temperature coefficient 0.2%/°C is employed for the silicon-steel material M270-35A.

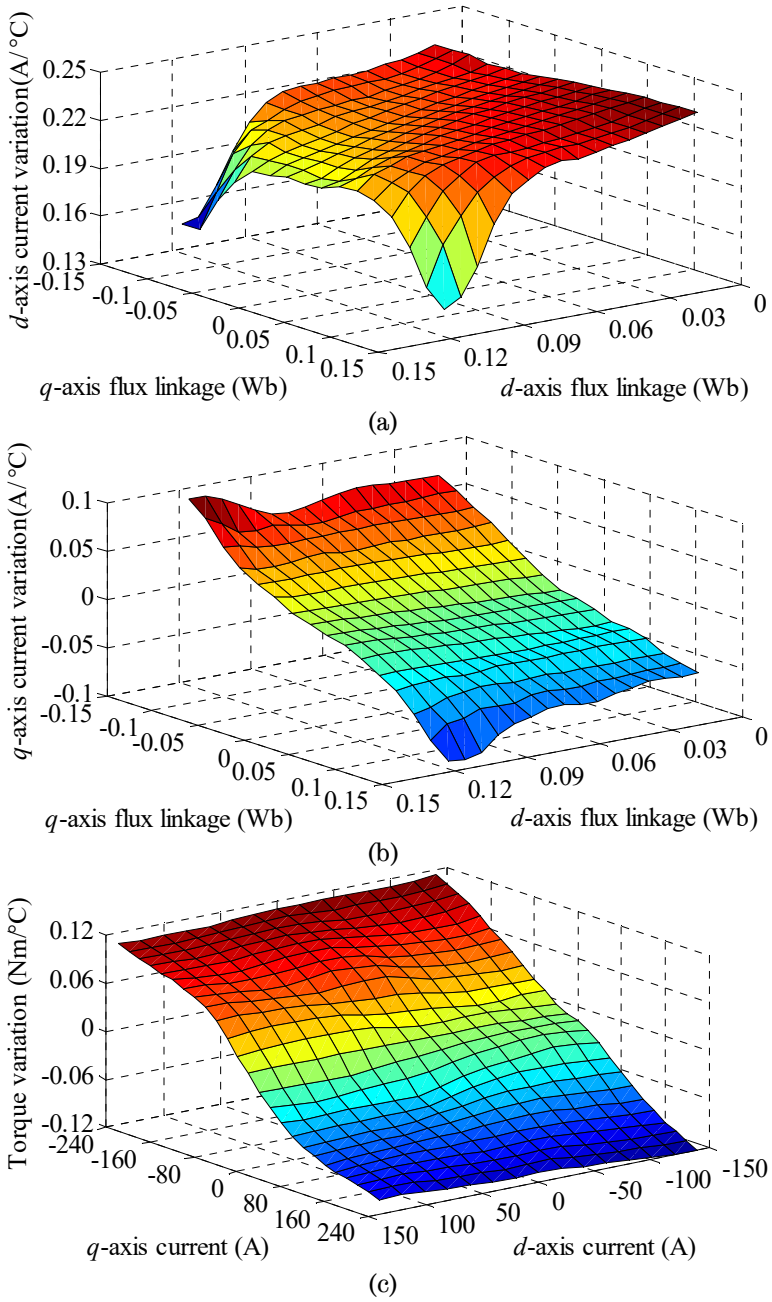

Fig. 5-21. Currents and torque variation maps per degree Celsius at rotor position = 0°. (a) *d*-axis current. (b) *q*-axis current. (c) Torque.

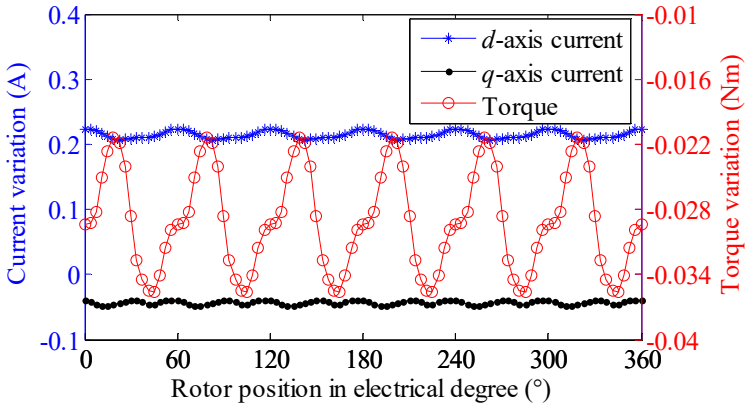

Fig. 5-22. Current and torque variations per degree Celsius with rotor position (current variations are obtained at Ψ_d=0.09Wb, Ψ_q=0.1Wb; torque variation is at i_d=-40A, i_q=60A).

The effects of rotor magnet temperature on machine performance will be illustrated by the following example. Assuming the machine model in Fig. 5-11 is established based on the FEA data at the temperature of 120°C while the machine operating temperature is 180°C, the machine performance with and without considering the temperature effects are compared. The *d*- and *q*-axis current and voltage waveforms over one electric period at 35.5Nm and 1350r/min (rated torque and base speed) are shown in Fig. 5-23 and Fig. 5-24 respectively. The mean values of the currents, voltages, copper losses and iron losses are listed in Table 5-2. The "Reference" waveforms in Fig. 5-23 and Fig. 5-24 and the "Reference" data in Table 5-2 correspond to the FE predicted machine performances at 180°C. It can be observed that the machine model in Fig. 5-11 without temperature effects exhibits ~25% error in copper loss. This is due to ~14% error in the phase resistance and ~6% error in the current magnitude. Moreover, the iron loss error is ~16%. In contrast, the proposed machine model shown in Fig. 5-20 can accurately predict the electromagnetic behaviour when temperature changes. This can be observed from the fact that the *d*- and *q*-axis current and voltage waveforms of the proposed model coincide with the reference waveforms, as shown in Fig. 5-23 and Fig. 5-24. Hence, the copper and iron loss errors which result with the proposed model are reduced to 1.4% and 0.8% respectively.

Therefore, the proposed model in Fig. 5-20 exhibits high-fidelity when temperature varies. This model can be used to accurately predict the

electromagnetic behaviour of an IPM machine at any feasible given temperature.

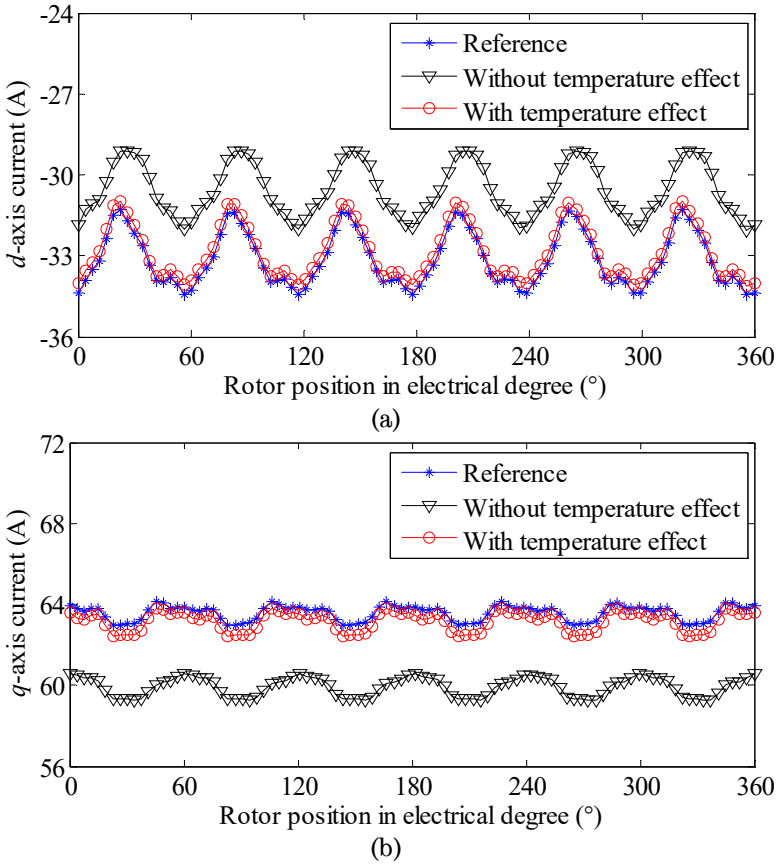

Fig. 5-23. *d*- and *q*-axis current waveforms with and without temperature effects at 35.5Nm and 1350r/min. (a) *d*-axis current. (b) *q*-axis current.

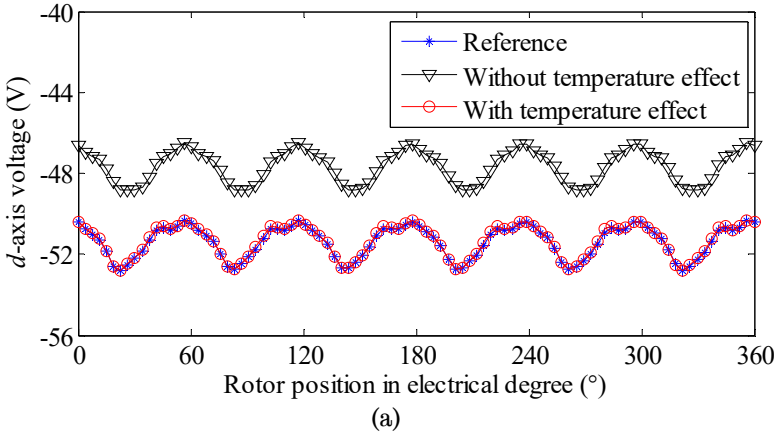

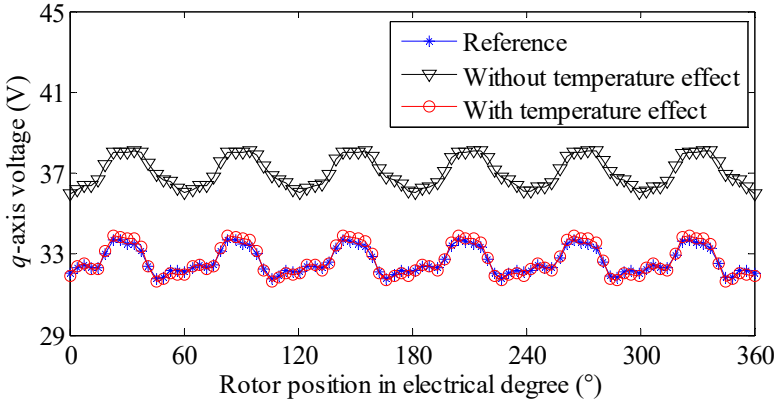

(b)

Fig. 5-24. *d*- and *q*-axis voltage waveforms with and without temperature effects at 35.5Nm and 1350r/min. (a) *d*-axis voltage. (b) *q*-axis voltage.

Table 5-2. Machine Performances with and without Temperature Effect at 35.5Nm and 1350r/min

Quantity	Reference	Without temperature effect	Error 1	With temperature effect	Error 2
d-axis current (A)	-33.1	-30.6	-7.8%	-32.8	-0.9%
q-axis current (A)	63.6	59.9	-5.7%	63.2	-0.7%
d-axis voltage (V)	-51.4	-47.7	-7.2%	-51.3	-0.1%
q-axis voltage (V)	32.7	37.1	13.5%	32.7	0.1%
Resistance (Ohm)	0.0741	0.0634	-14.4%	0.0741	0.0%
Copper loss (W)	571.4	430.3	-24.7%	563.5	-1.4%
Iron loss (W)	87.2	73.0	-16.3%	86.4	-0.8%

5.7 Proposed Electro-thermally Coupled Model

5.7.1 Model Description

The high-fidelity IPM machine model with temperature effects as shown in Fig. 5-20 can be augmented with an appropriate thermal model, such as that derived from Motor-CAD developed by Motor Design Limited [163] to form an electro-thermally coupled model which represents the physical behaviour of the IPM machine with high fidelity. Fig. 5-25 illustrates the schematic of the proposed electro-thermally coupled IPM machine model. The copper loss and iron losses are obtained via the proposed machine model considering temperature effects (as shown in Fig. 5-20) at a given load condition, and subsequently fed into the thermal model which is represented by a set of state-space equations of the thermal network. The thermal

network contains 48 nodes, including the housing, end-plate, end-cap, stator tooth, stator back-iron, 18 winding layers, end-windings, rotor pole, rotor back-iron, magnets, shaft, bearings, and etc. The predicted average temperatures in both stator windings and rotor magnets are fed back to the machine model to take into account the temperature variations. It should be noted that the iron loss p_{Fe} shown in Fig. 5-25 is an array which contains iron loss components in the stator tooth, stator back-iron, rotor pole and rotor back-iron.

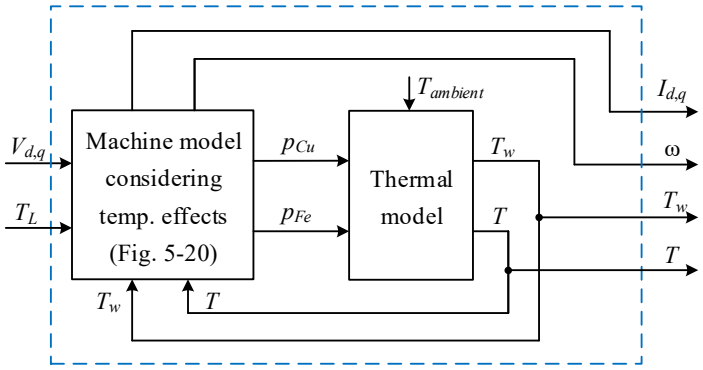

Fig. 5-25. The schematic of the proposed electro-thermally coupled model of an IPM machine.

Fig. 5-26 shows the schematic of the lumped parameter thermal model. The inputs, i.e. the copper loss p_{Cu} and the iron loss p_{Fe}, are converted into a loss vector with 48 components which are fed into a state-space model. However, most components of the loss vector are zero while non-zero components are associated with nodes at which iron loss or copper loss components are injected. Copper loss is distributed in three nodes associated with the active part of the winding and two end-winding parts according to the physical length of each part. Similarly, the iron loss is separated into the losses associated with the stator teeth, stator yoke, rotor pole and rotor yoke. The eddy current loss in the rotor magnets is also included in the loss vector. These loss components are then injected at the relevant nodes. The output of this state-space model is a vector with the temperature rise information of all 48 nodes. Subsequently, the resultant temperatures of all 48 nodes are obtained by adding the ambient temperature on the temperature rise vector.

The outputs are the winding temperature T_w and rotor magnet temperature T.

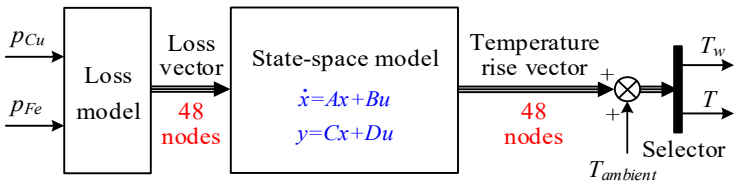

Fig. 5-26. The schematic of the lumped parameter thermal model.

The state-space model shown in Fig. 5-26 is mathematically represented by (5.15), and these vectors and matrixes can be determined by the heat transfer equations given by (5.16). By selecting nodal temperatures as state variables, as shown in (5.17), the input vector u, matrixes A and B are expressed by (5.18), (5.19) and (5.20) respectively. Since the output vector $y=x$, the matrixes C and D are unit and null matrixes respectively.

$$\begin{aligned} \dot{x} &= Ax + Bu \\ y &= Cx + Du \end{aligned} \tag{5.15}$$

where u is input vector, x is state vector, y is output vector, and A, B, C and D are coefficient matrixes whose dimensions are all 48×48 in this model.

$$C_i \frac{dT_i}{dt} = P_i - \sum_j \frac{1}{R_{i,j}} \left(T_i - T_j \right) \tag{5.16}$$

where T_i is the temperature of i^{th} node (i=1, 2, $\cdots$, 48), C_i is the heat capacitance (thermal mass) of i^{th} node, P_i is the power loss of i^{th} node, and $R_{i,j}$ is the thermal resistance between i^{th} and j^{th} nodes (j=1, 2, $\cdots$, 48, $j \neq i$).

$$y = x = \begin{bmatrix} T_1 \\ T_2 \\ \vdots \\ T_{48} \end{bmatrix} \tag{5.17}$$

$$u = \begin{bmatrix} P_1 \\ P_2 \\ \vdots \\ P_{48} \end{bmatrix} \tag{5.18}$$

$$A = \begin{bmatrix} C_1 & 0 & \cdots & 0 \\ 0 & C_2 & \cdots & \vdots \\ \vdots & \vdots & \ddots & 0 \\ 0 & \cdots & 0 & C_{48} \end{bmatrix}^{-1} \begin{bmatrix} -\sum_{j\neq 1} \frac{1}{R_{1,j}} & \frac{1}{R_{1,2}} & \cdots & \frac{1}{R_{1,48}} \\ \frac{1}{R_{2,1}} & -\sum_{j\neq 2} \frac{1}{R_{2,j}} & \cdots & \vdots \\ \vdots & \vdots & \ddots & \frac{1}{R_{47,48}} \\ \frac{1}{R_{48,1}} & \cdots & \frac{1}{R_{48,47}} & -\sum_{j\neq 48} \frac{1}{R_{48,j}} \end{bmatrix} \tag{5.19}$$

$$B = \begin{bmatrix} C_1 & 0 & \cdots & 0 \\ 0 & C_2 & \cdots & \vdots \\ \vdots & \vdots & \ddots & 0 \\ 0 & \cdots & 0 & C_{48} \end{bmatrix}^{-1} \tag{5.20}$$

This thermal model also takes into account the cooling effect which is represented by the variation in the thermal resistance between the machine housing and ambient.

However, to simulate the traction system behaviour over driving cycles, it requires a few hours of time duration to reach a cyclic thermal steady-state while the simulation time step must be much less than the minimum time constant of the system which is usually dependent on the current loop control bandwidth. Therefore, enormous amount of computational and data storage resources is required and this is not realistic even with state-of-the art computing platform.

To improve the computational efficiency, the machine model in Fig. 5-25 is simplified by neglecting the spatial harmonics. In other words, the influence of the rotor position on flux-linkages and torque is ignored. All the 3-D functions shown in Fig. 5-20 are averaged over one electric period and

thereby become 2-D functions. In this way, the simulation time step can be increased and therefore the computational efficiency is improved. It takes ~3 hours on a quad-core 3.1GHz PC to complete a 5.5 hour electro-thermally coupled simulation using MATLAB/SIMULINK [116] with a variable time step. It should be noted that the position dependent effects on flux-linkage and torque at a given temperature can be assessed by the model shown in Fig. 5-20 when the temperature is known from the simulation of the simplified model.

5.7.2 Electro-thermally Coupled Simulation at Rated Torque and Base Speed

To demonstrate the significance of the electro-thermally coupling, simulations at 35.5Nm and 1350r/min (rated torque and base speed) are performed and compared with and without considering temperature effects. The average winding and magnet temperature variations with time over 20,000s duration are shown in Fig. 5-27. The comparisons are listed in Table 5-3. "Thermally coupled" indicates the results obtained from the proposed model in Fig. 5-25; "Without temp. effect" means the predicted machine temperatures in the thermal model are not fed into the machine electric model which is built based on 120°C FEA data; "R_s temp. effect" corresponds to the scenario that only the winding temperature fed into the machine electromagnetic model whereas the rotor magnet temperature is set to the reference temperature 120°C. "R_s temp. effect", indeed, represents one conventional way to account for the temperature effect in an electrical machine, namely, only considering the winding resistance as the temperature dependent parameter while neglecting the temperature influences on the flux-linkages and torque.

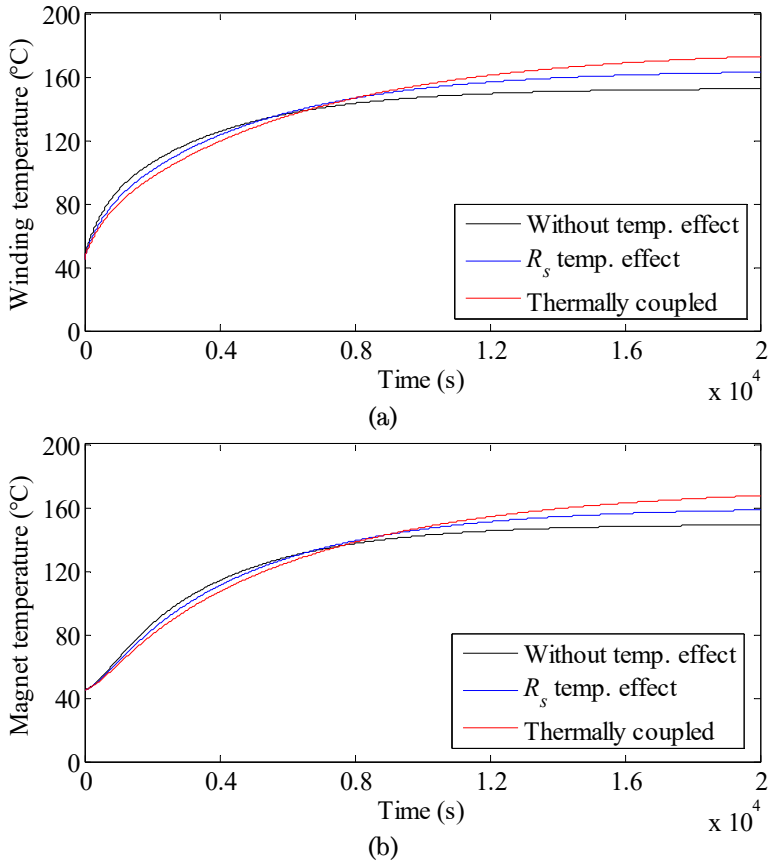

Fig. 5-27. Temperature rise comparisons at 35.5Nm and 1350r/min. (a) Winding temperature. (b) Magnet temperature.

Table 5-3. Machine Performances with and without Thermal Coupling Effect at 35.5Nm and 1350r/min

Quantity	Without temp. effect	R_s temp. effect	Thermally coupled	Difference against without temp. effect	Difference against R_s temp. effect
d-axis current (A)	-38.5	-38.5	-42.1	9.4%	9.4%
q-axis current (A)	54.0	54.0	54.3	0.5%	0.5%
d-axis voltage (V)	-47.0	-47.2	-49.9	6.2%	5.5%
q-axis voltage (V)	34.8	35.3	30.9	-11.3%	-12.3%
Phase resistance (Ohm)	0.0634	0.0711	0.0729	15.0%	2.5%
Copper loss (W)	418.8	469.6	516.6	23.4%	10.0%
Iron loss (W)	69.0	69.0	74.0	7.3%	7.3%
Winding temperature (°C)	152.4	163.0	173.0	13.5%	6.1%
Magnet temperature (°C)	149.1	158.6	167.6	12.4%	5.7%

From Fig. 5-27 and Table 5-3, it can be observed that without temperature effects, the average winding and magnet temperatures are 152.4°C and 149.1°C respectively. If the temperature effect on the winding resistance is

considered, these temperatures will be 163.0°C and 158.6°C respectively. However, the proposed model in Fig. 5-25 shows that these temperatures are significantly higher, reaching 173.0°C and 167.6°C, respectively. Therefore, without considering temperature effects, the winding and magnet temperatures can be under-estimated by approximately 20°C. Even if the temperature effect on the winding resistance is considered, these temperatures can still be under-estimated by approximately 10°C. The under-estimation in winding and magnet temperatures results in much great risk of failure. This is because on one hand, the permanent-magnets may be irreversibly demagnetised. On the other hand, the designed insulation lifespan is reduced to approximately half by every 10°C temperature rise. Therefore, a high-fidelity electro-thermally coupled machine model is essential for machine designers in order to assess potential demagnetisation risk and lifetime of the machine.

Table 5-3 also lists the detailed currents, voltages, resistances, copper losses and iron losses which result with these three models. It shows that the proposed electro-thermally coupled model predicts both higher current amplitude and higher resistance. This is the reason why only considering the temperature effect on the winding resistance is not sufficient to accurately predict the machine temperatures.

From Fig. 5-27, it can also be observed that the winding and magnet temperatures predicted by the machine model which neglects the temperature effects are higher than those predicted by the electro-thermally coupled models at the beginning of the transient (up to ~7,000s). This is mainly due to the fact that when the temperature effects are neglected, the resistances of the winding and lamination, and the magnet remanence are evaluated at the fixed temperature of 120°C. Therefore, when the actual temperatures in these materials are below 120°C, the model over-estimates the resistances and current, and hence the losses and temperatures.

5.7.3 Electro-thermally Coupled Simulation over Given Driving Cycles

In this section, the machine performance will be evaluated over both Artemis urban and NEDC driving cycles, using the proposed electro-thermally coupled model in Fig. 5-25. Table 5-4 lists the EV specification and design parameters. According to these parameters and also the gradient requirements, the torque demand profiles can be derived based on the drive cycle speed profiles.

Table 5-4. Specifications and Design Parameters of the Electric Vehicle

Quantity	Unit	Value
Vehicle Mass including load	kg	950
Front area	m^2	0.7
Wind drag coefficient		0.5
Effective rolling radius of tire	m	0.273
Rolling resistance coefficient		0.007
Gear ratio		4
Efficiency of gear and differential	%	97.5%
Drive train configuration		Distributed (Front & rear)

Since it takes approximately 20,000s for the machine to reach its cyclic thermal steady-state, the simulation is performed over 20 Artemis urban driving cycles with 10° gradient and the results are compared in Fig. 5-28 and Table 5-5. It can be seen that the machine model without considering temperature effects predict 155.2°C and 148.8°C for the peak winding and peak magnet temperatures respectively. The temperatures predicted by the model which only considers the temperature effect on the winding resistance are 168.6°C and 160.7°C respectively. However, the proposed electro-thermally coupled model shows that these temperatures are 178.8°C and 169.6°C respectively, approximately 20°C higher than those predicted by the machine model without considering temperature effects, and approximately 10°C higher than those predicted by the machine model which only considers the temperature effect on the winding resistance. This trend coincides with that observed in the rated torque operation.

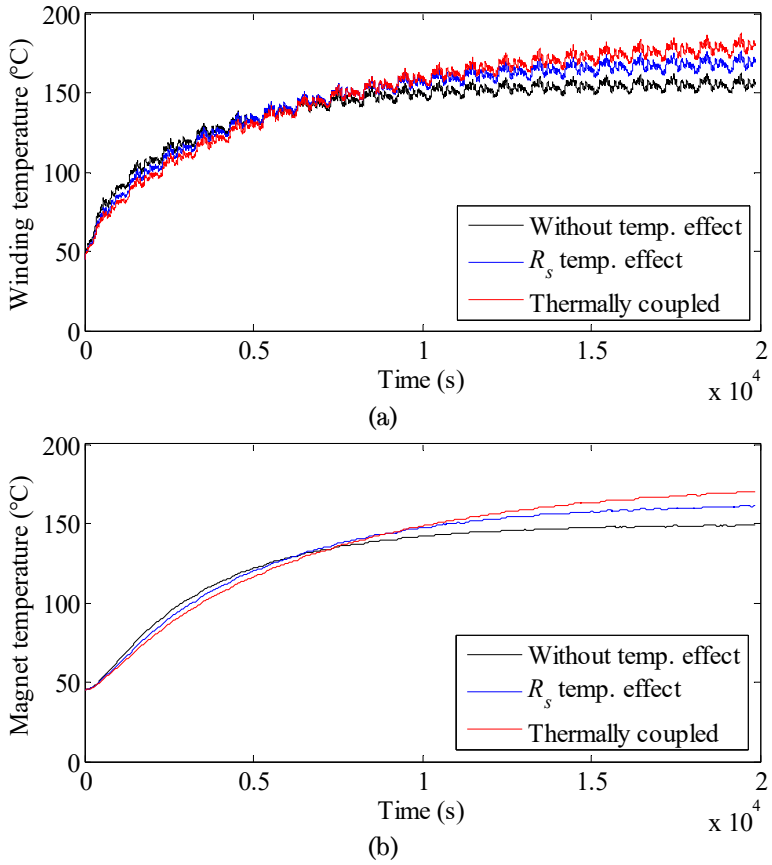

Fig. 5-28. Machine performance comparison over 20 Artemis urban driving cycles with 10° gradient. (a) Winding temperature. (b) Magnet temperature.

Table 5-5. Machine Performance Comparison with and without Thermal Coupling Effect over Artemis Urban Driving Cycle with 10° Gradient

Quantity	Without temp. effect	R_s temp. effect	Thermally coupled	Difference against without temp. effect	Difference against R_s temp. effect
Copper loss in the last cycle (J)	4.6×10^5	5.3×10^5	5.8×10^5	24.9%	9.7%
Iron loss in the last cycle (J)	3.4×10^4	3.4×10^4	3.7×10^4	7.3%	7.3%
Winding temperature (°C)	155.2	168.6	178.8	15.2%	6.0%
Magnet temperature (°C)	148.8	160.7	169.6	14.0%	5.6%

Similar comparisons are made over 20 NEDC driving cycles with 15° gradient. A different trend with respect to the Artemis urban driving cycle, as illustrated in Fig. 5-29 and Table 5-6, is observed. The temperature differences among these three models are reduced. The machine model which neglects the temperature effects under-estimates the winding and magnet temperatures by 17.3°C and 15.8°C respectively compared to the proposed electro-thermally coupled model. However, less than expected

results are obtained from the machine model which only accounts for the temperature effect on the winding resistance. The temperatures predicted by this model are only 2.1°C lower. This is because in the NEDC driving cycle more energy is consumed in the low torque and high speed region (field weakening region) whereas in the Artemis driving cycle more energy is consumed in the high torque and low speed region (MTPA region). In the low torque and high speed region, a higher temperature helps weaken the permanent-magnet field. Consequently, the required *d*-axis current for field weakening is reduced, resulting in less copper loss contribution. Therefore, the temperature rise is compensated and the temperature differences among these three models are reduced.

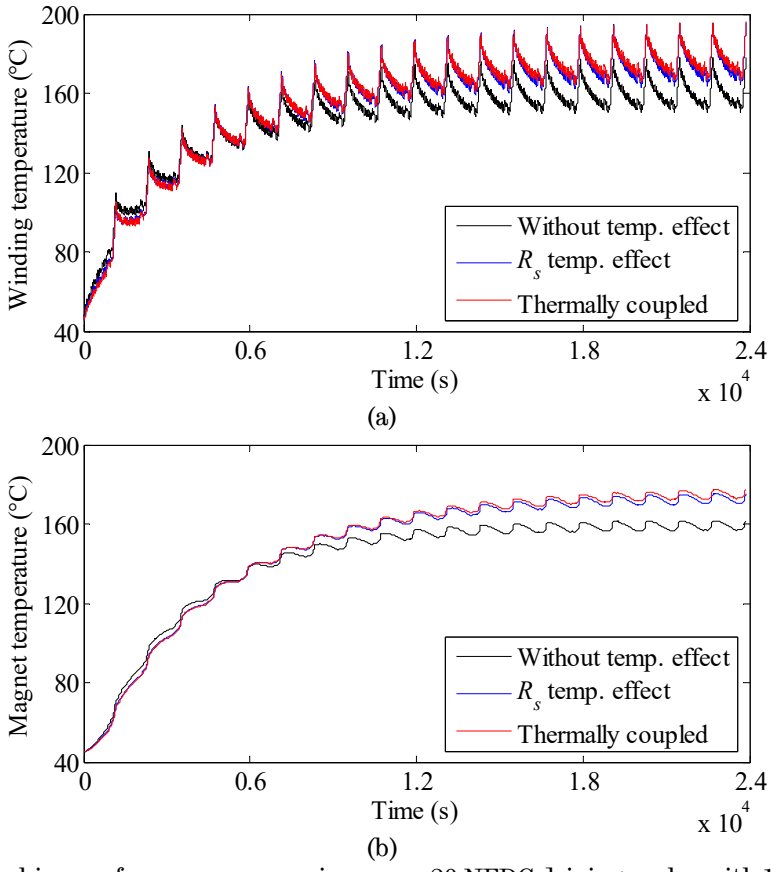

Fig. 5-29. Machine performance comparison over 20 NEDC driving cycles with 15° gradient. (a) Winding temperature. (b) Magnet temperature.

Table 5-6. Machine Performance Comparison with and without Thermal Coupling Effect over NEDC Driving Cycle with 15° Gradient

Quantity	Without temp. effect	R_s temp. effect	Thermally coupled	Difference against without temp. effect	Difference against R_s temp. effect
Copper loss in the last cycle (J)	5.3×10^5	6.1×10^5	6.2×10^5	17.6%	1.4%
Iron loss in the last cycle (J)	8.4×10^4	8.4×10^4	8.8×10^4	4.8%	4.8%
Winding temperature (°C)	159.9	175.1	177.2	10.8%	1.2%
Magnet temperature (°C)	159.3	173.0	175.1	10.0%	1.2%

5.8 Electromagnetic Model Validation

Both the proposed electromagnetic model and electro-thermally coupled model have been validated. This section will be focused on the validation of the electromagnetic model whose schematic is shown in Fig. 5-11.

5.8.1 FE Validation

In most commercial electromagnetic FE tools, iron loss is usually evaluated in post process. Therefore, in the following FE validation, both the SIMULINK model and FE model do not consider the iron loss influence.

A number of representative points are compared for the purpose of validations. Since the ripples on flux-linkages and torque are more significant at high speeds where the machine operates in a deep field weakening region, the comparisons are illustrated for the operating point at 18Nm and 4500r/min.

First, the drive system modelled with the proposed approach in the SIMULINK environment is simulated at a specific operating point and the resulting current waveforms, as shown in Fig. 5-30, are extracted. The current waveforms are then injected into the FE model under the same load condition. Fig. 5-31 and Fig. 5-32 compare SIMULINK and FE-predicted torque and voltage waveforms, respectively.

It can be observed that the torque waveforms predicted by SIMULINK and FE models coincide because the electromagnetic torque depends on the

flux-linkage and current. The injected currents in the FE model are identical to those of the SIMULINK model and the flux-linkage error between the proposed and FE model is virtually negligible as illustrated in Fig. 5-8. Therefore, the FE-predicted torque waveform can be completely reproduced by the SIMULINK model.

As shown in Fig. 5-32, the voltage waveforms predicted by the two models are slightly different since the voltage in FE analysis is calculated from the derivatives of the flux-linkages. The accuracy largely depends on the size of transient steps; this can be understood by the fact that the smaller the step size, the better the FE-predicted voltage accuracy.

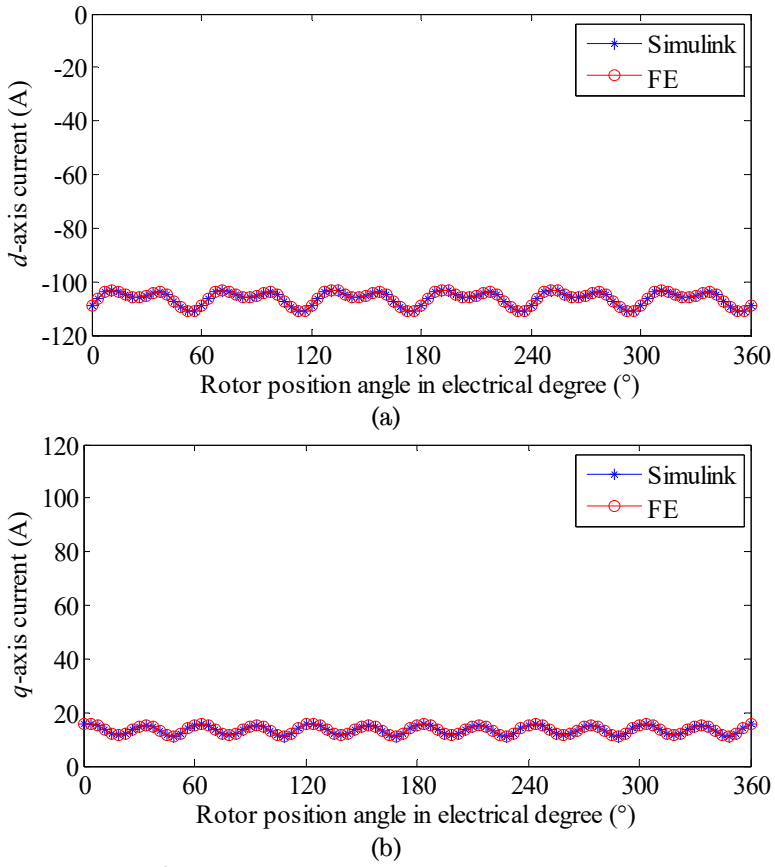

Fig. 5-30. Comparisons of *d*- and *q*-axis current waveforms used in SIMULINK and FE models. (a) *d*-axis current. (b) *q*-axis current.

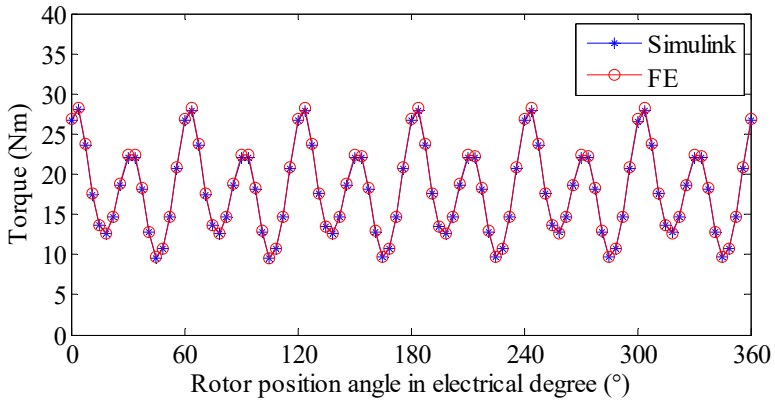

Fig. 5-31. Comparison of SIMULINK and FE-predicted torque waveform.

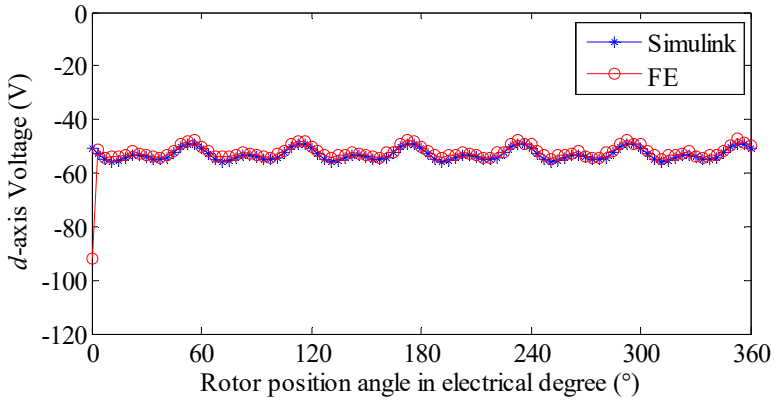

Fig. 5-32. Comparisons of SIMULINK and FE-predicted *d*- and *q*-axis voltage waveforms. (a) *d*-axis voltage. (b) *q*-axis voltage.

5.8.2 Experimental Validation in Generating Mode

To avoid any uncertainties introduced by an inverter, the machine prototype is driven by a dynamometer and operates in the generating mode with a resistive load for the validation of the proposed machine model. The

experimental set-up, including the machine prototype, dynamometer and resistive load are shown in Fig. 5-33.

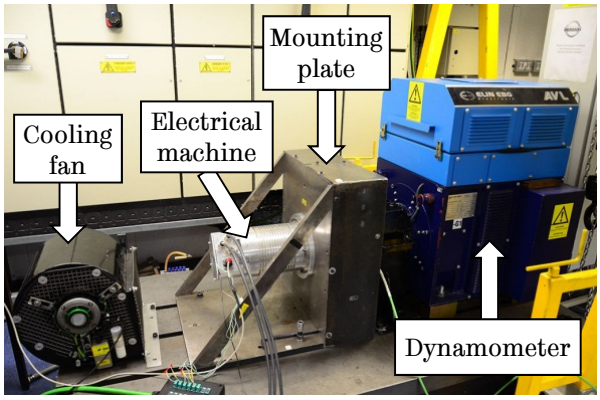

(a)

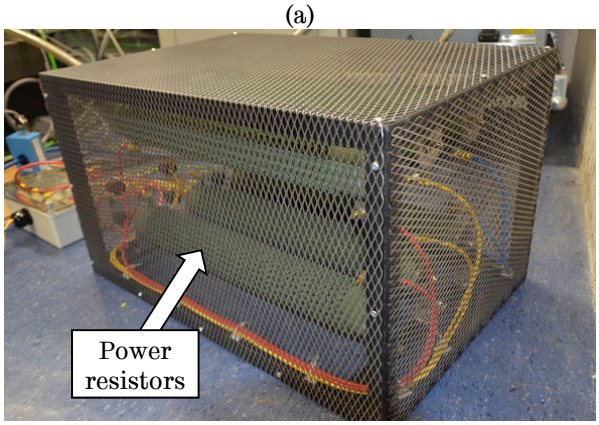

(b)

Fig. 5-33. Generating mode experimental set-up. (a) Electrical machine prototype and dynamometer. (b) Resistive load.

First, the no-load test is performed and the FE-predicted and measured phase back-EMF waveforms at 1350r/min are compared in Fig. 5-34. It is worth noting that the predicted phase back-EMF with ideal 2-D FE model of the machine is approximately 9% higher than the measured value due to the 3-D effect, manufacture tolerance (e.g., assembly gaps between magnets and rotor core), and difference in material properties, etc. The difference between the prediction and measurement is removed by a calibration procedure in which the magnet remanence is adjusted so that the fundamental phase back-EMF of the FE result coincides with the measurement. The calibrated FE model is used to compute the flux-linkage and torque maps for the construction of the proposed SIMULINK model. From Fig. 5-34 (b), it can be

observed that after calibration, the measured and predicted phase back-EMF waveforms match very well except for some high order harmonics.

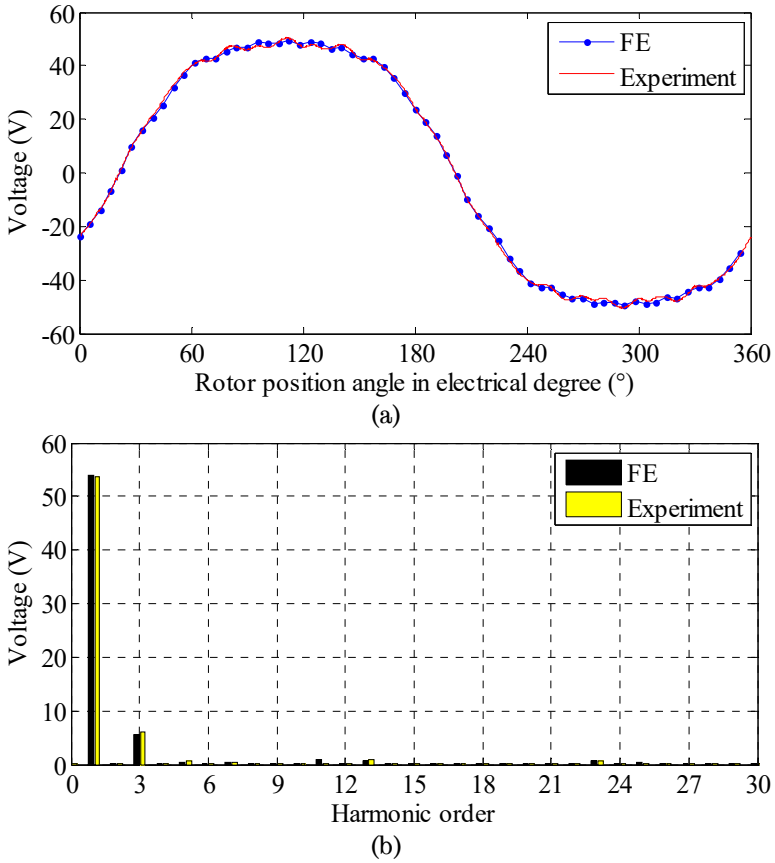

Fig. 5-34. Comparison of measured and FE-predicted phase back-EMF at 1350r/min. (a) Waveforms. (b) FFT spectra.

On-load tests are performed against four load conditions with load resistance at 0.6875Ohm, 1.0Ohm, 2.2Ohm and 3.2Ohm, respectively. For each load condition, the speed varies from 500r/min to the speed at which the maximum power is reached. The measured and SIMULINK model-predicted voltage and current waveforms as well as the average torque are compared. Good agreements are observed for all four operating points between the predictions and measurements.

By way of example, Fig. 5-35 and Fig. 5-36 compare the measured and predicted line-to-line voltage and phase current respectively, at 1350r/min with 0.6875Ohm load. It can be seen that both the predicted line-to-line voltage and phase current agree well with the experimental results. The

errors in fundamental line-to-line voltage and current are 1.6% and 0.7%, respectively, which might result from the load resistance variation due to temperature rise which is not accounted in the model, and/or measurement errors.

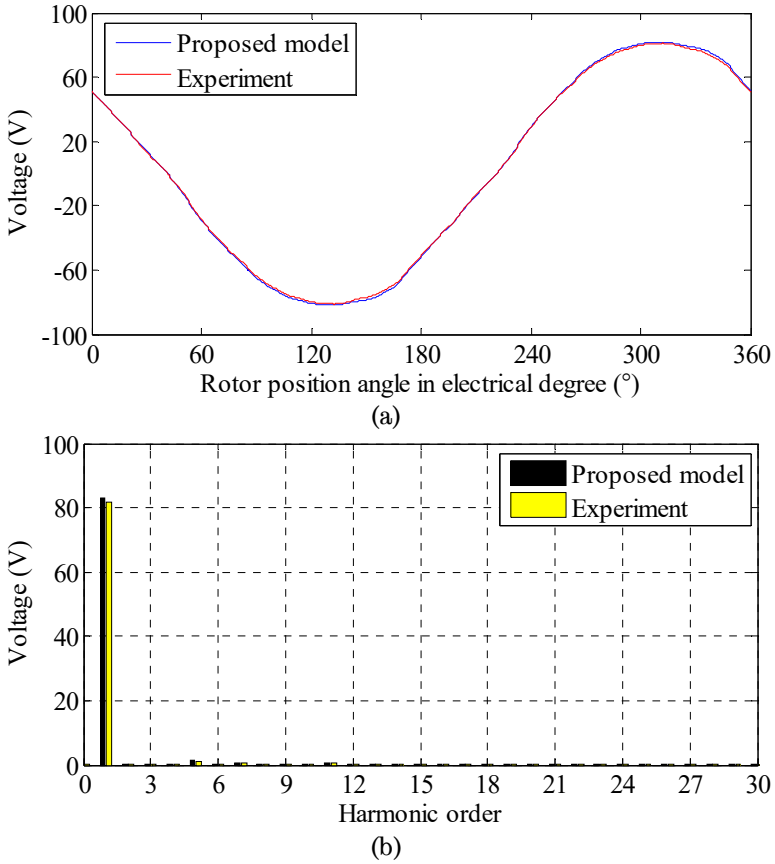

Fig. 5-35. Comparison of measured and predicted line-to-line voltage at 1350r/min with 0.6875Ohm load. (a) Waveforms. (b) FFT spectra.

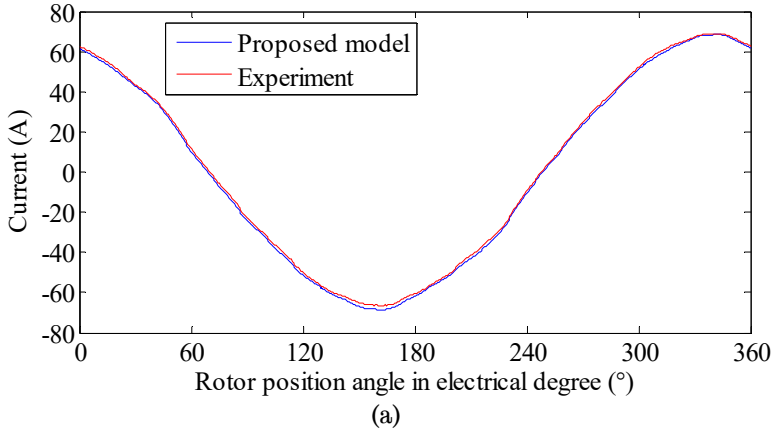

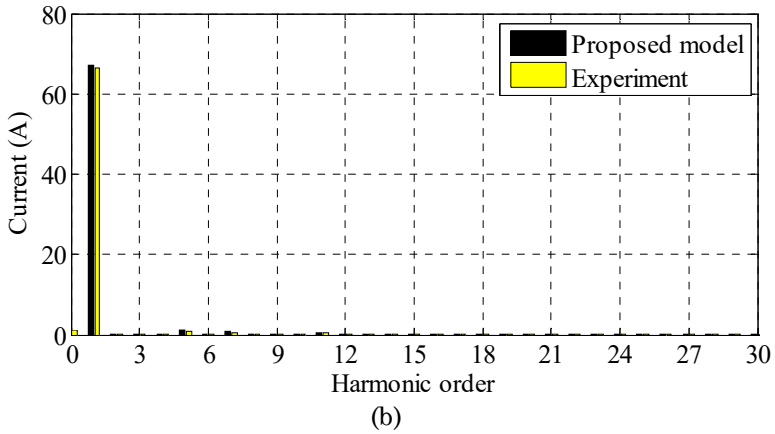

(b)

Fig. 5-36. Comparison of measured and predicted phase current at 1350r/min with 0.6875Ohm load. (a) Waveforms. (b) FFT spectra.

The comparison of the predicted and measured torque is shown in Fig. 5-37. Due to the bandwidth limit of the torque transducer and also the fact that the actively controlled dynamometer itself produces torque ripple, the instantaneous torque waveform of the test machine cannot be captured, and thereby only the mean torque value of the experimental result is shown in Fig. 5-37. The error in the mean torque value is 0.4%.

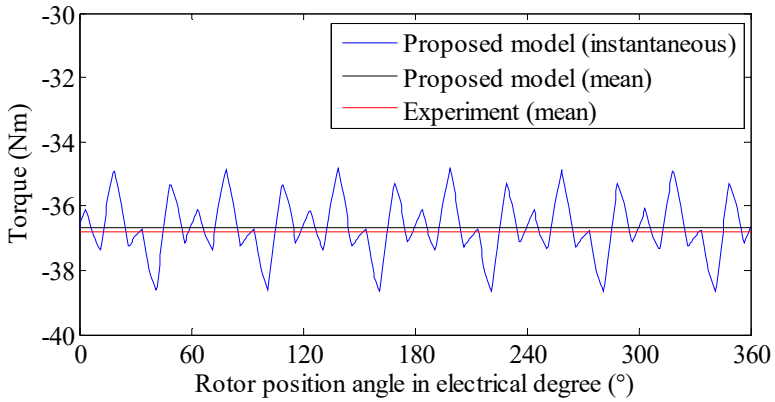

Fig. 5-37. Comparison of the measured and predicted torque at 1350r/min with 0.6875Ohm load.

Therefore, the proposed model exhibits high-fidelity for predicting the electromagnetic behaviour of the IPM machine even under heavy load conditions.

5.8.3 Experimental Validation in Motoring Mode

Tests in inverter-fed motoring operation have also been performed to validate the proposed model. The prototype machine is driven by a 10kW voltage-fed inverter with an 8kHz switching frequency. The experimental set-up is illustrated in Fig. 5-38. The three-phase voltages and currents are captured by high band-width voltage and current transducers.

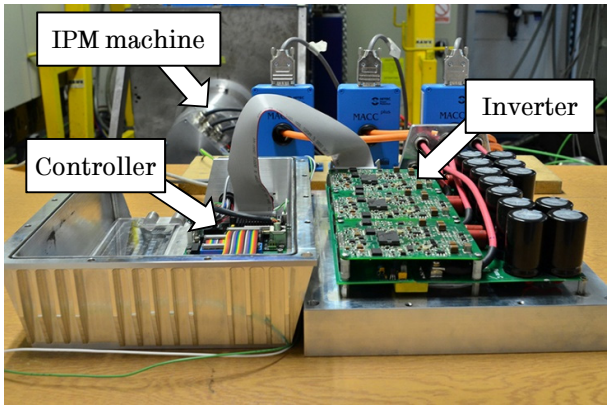

Fig. 5-38. Motoring mode experimental set-up.

The measured three-phase voltage waveforms in one electrical cycle at 10Nm and 2700r/min (field weakening region) were filtered by a 10kHz low pass filter, and the filtered voltages are shown in Fig. 5-39. The filtered voltages are applied to the proposed models with and without inclusion of the iron loss model, and the resultant phase *A* current waveforms and their spectra are compared with the measurement in Fig. 5-40 (a) and (b). Compared to the measured amplitude, 63.49A, of the fundamental current, the model-predicted current amplitudes with and without the iron loss inclusion are 63.32A (-0.3% error) and 61.47A (-3.2% error), respectively, as shown in Table 5-7 and Table 5-8.

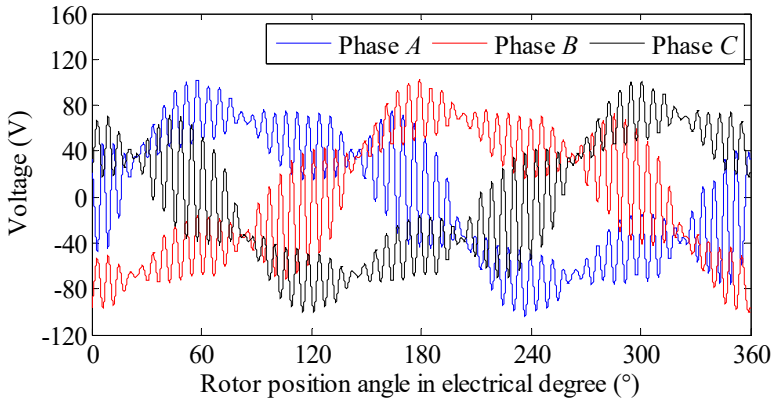

Fig. 5-39. Waveforms of measured three-phase voltages at 10Nm and 2700r/min filtered by a 10 kHz low pass filter.

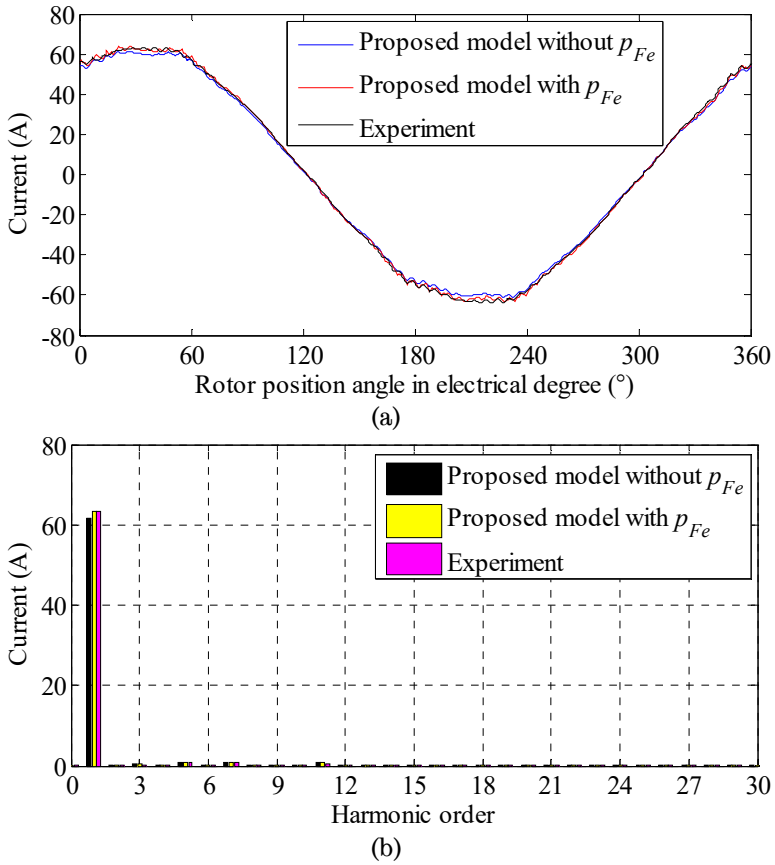

Fig. 5-40. Comparison of measured and predicted phase current at 10Nm and 2700r/min (field weakening region). (a) Waveforms. (b) FFT spectra.

Table 5-7. Comparison of Measured and Predicted Currents at 10Nm and 2700r/min (Field Weakening Region)

Quantity	Without p_{Fe}	With p_{Fe}	Experiment
Fundamental phase current (A)	61.47	63.32	63.49
Mean *d*-axis current (A)	-60.65	-62.47	-62.60
Mean *q*-axis current (A)	9.68	10.33	10.39

Table 5-8. Relative Errors in Predicted Currents at 10Nm and 2700r/min (Field Weakening Region)

Quantity	Without p_{Fe}	With p_{Fe}
Error in fundamental phase current (%)	-3.2%	-0.3%
Error in mean d-axis current (%)	-3.1%	-0.2%
Error in mean q-axis current (%)	-6.9%	-0.6%

The comparison of currents in the d-q system is shown in Table 5-7, Table 5-8 and also Fig. 5-41. It can be seen that the inclusion of iron loss in the model reduces the model errors in the mean d- and q-axis currents from -3.1% and -6.9% to -0.2% and -0.6%, respectively, and hence improves model fidelity. The level of improvement will be dependent on operation conditions. At high speeds, iron loss becomes more significant, and hence neglecting iron loss may result in larger error. For efficiency assessment and thermal evaluation, inclusion of iron loss in the model is indispensable.

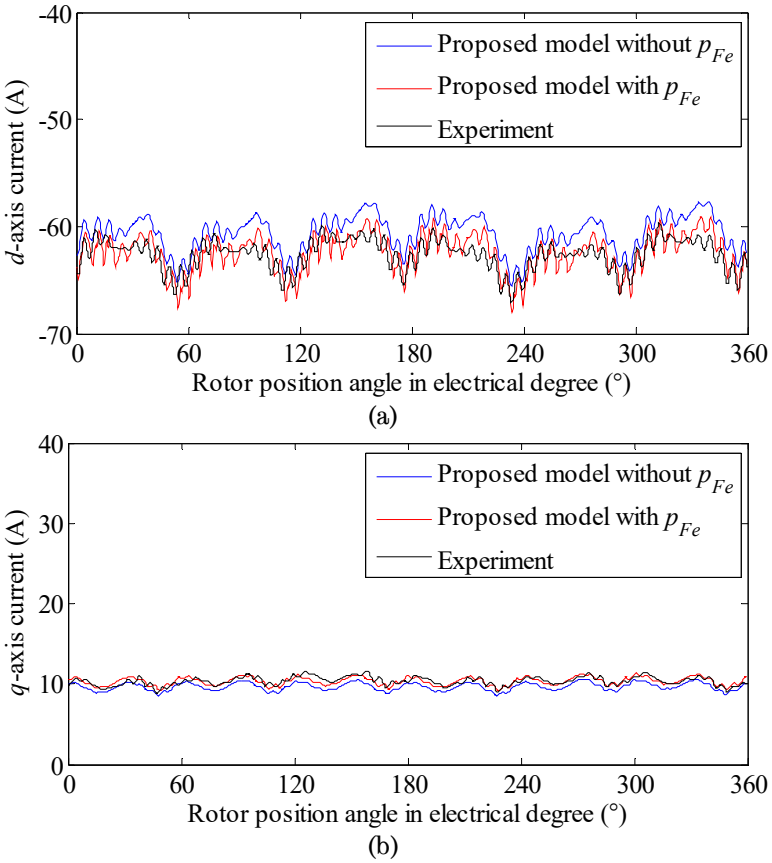

Fig. 5-41. Comparison of measured and predicted d- and q-axis current at 10Nm and 2700r/min (field weakening region). (a) d-axis current. (b) q-axis current.

5.9 Electro-thermally Coupled Model Validation

This section will be focused on the validation of the proposed electro-thermally coupled machine model. The temperature coefficient of the magnet remanence is measured before performing the thermal steady-state test.

5.9.1 Magnet Temperature Coefficient Test

Magnet remanence decreases with increase in temperature and this relationship is characterised by the remanence temperature coefficient of magnets. Although typical values for the temperature coefficient can be found from the manufacturer's datasheet, the actual value may differ significantly. An experimental procedure was performed to measure the temperature coefficient of the prototype machine for constructing the electro-thermally coupled model.

First, the prototype machine is placed in an environmental chamber in which the temperature is set to 20°C for more than 3 hours. The three-phase back-EMFs are subsequently measured when the machine is driven at a given speed. Thereafter, the temperature of the environmental chamber is set to 70°C and the three-phase back-EMFs are measured again after thermal equilibrium is reached after more than 3 hours. The measured three-phase back-EMF waveforms and their spectra at 20°C and 70°C are shown in Fig. 5-42 and Fig. 5-43 respectively. It can be found from the measurements that the back-EMF coefficients at 20°C and 70°C are 0.381V· s/rad and 0.371V· s/rad, respectively.

To derive the temperature coefficient of magnet remanence from the measured back-EMF coefficients at various temperatures, the relationship between back-EMF coefficient and magnet remanence needs to be established. By varying the magnet remanence and acquiring various fundamental component of phase back-EMF in FEA, this relationship is

established as shown in Table 5-9. The "predicted back-EMF coefficient" column is obtained by linearly calculating the back-EMF coefficient based on FE-predicted back-EMF coefficient at magnet remanence=1.07T. By way of example, the FE-predicted back-EMF coefficient is 0.382V·s/rad with 1.07T magnet remanence, and thus the predicted back-EMF coefficient at 1.04T is obtained by 0.382/1.07×1.04=0.371V·s/rad. From Table 5-9, it can be seen that the predicted back-EMF coefficient error at 1.04T is only 0.67%. Although the predicted back-EMF coefficient error at 1.01T magnet remanece is doubled compared to error at 1.04T due to the fact that both of them employs the same reference (i.e. 1.07T data), this error at 1.01T is still very small, only being 1.27%. This infers that the saturation level of the machine at no-load is very low and the relationship between the back-EMF coefficient and magnet remanence is approximately linear.

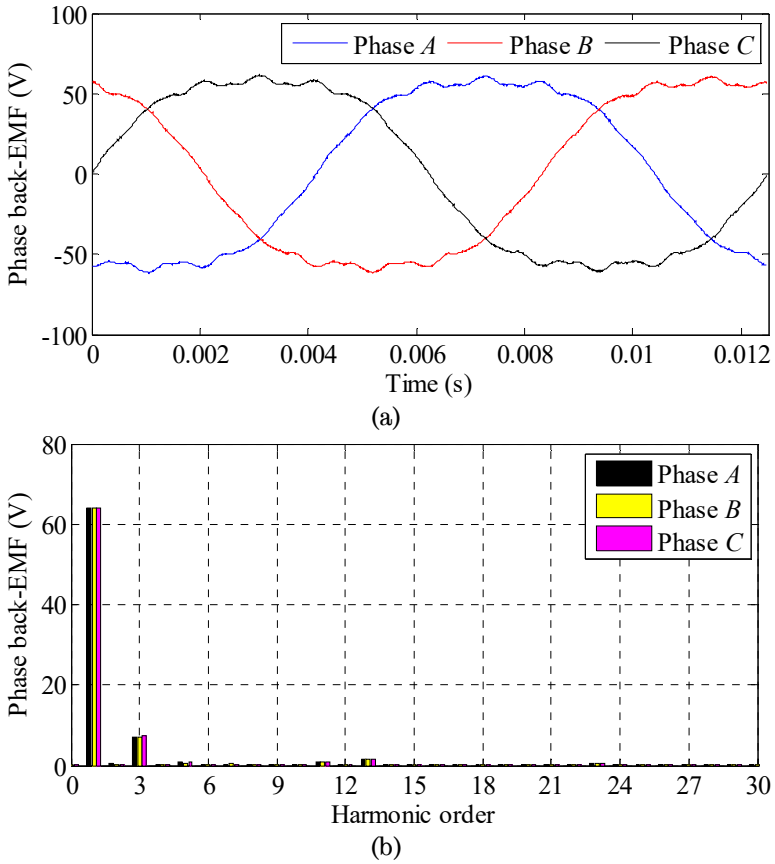

Fig. 5-42. Measured three-phase back-EMF at 1603.3r/min at 20°C. (a) Waveforms. (b) FFT spectra.

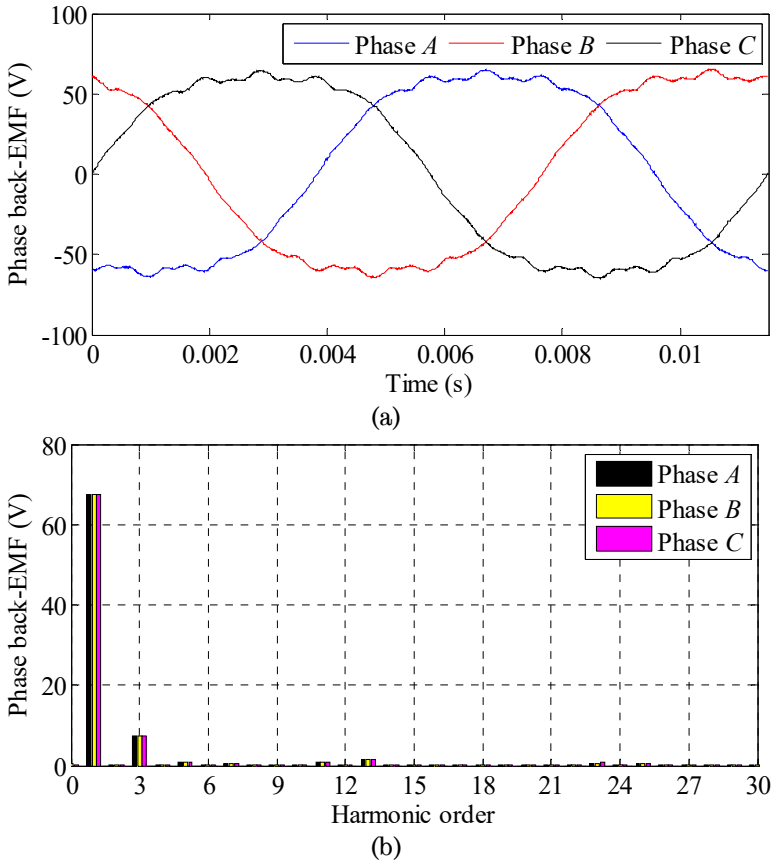

Fig. 5-43. Measured three-phase back-EMF at 1739.1r/min at 70°C. (a) Waveforms. (b) FFT spectra.

Table 5-9. Relationship between Back-EMF Coefficient and Magnet Remanence

Magnet remanence (T)	Back-EMF coefficient via FEA (V·s/rad)	Predicted back-EMF coefficient (V·s/rad)	Predicted back-EMF coefficient Error (%)
1.07	0.382	N/A	N/A
1.04	0.374	0.371	-0.67%
1.01	0.365	0.361	-1.27%

Thus, the resultant magnet temperature coefficient is calculated by the back-EMF coefficient difference divided by the temperature difference, being -0.056%/°C which is much less than a typical value of -0.12%/°C for the magnets being used.

5.9.2 Thermal Steady-state Test

The electro-thermal test is performed to validate the proposed electro-thermally coupled model. The machine prototype is driven by the dynamometer at 1350r/min with 0.71Ohm three-phase resistive loads. The

experiment lasts more than 5 hours to ensure the machine is close to its thermal steady-state. The measured magnet temperature coefficient in Section 5.9.1 is employed to establish the electro-thermally coupled model.

The measured and predicted transient winding temperatures are illustrated in Fig. 5-44. The winding temperatures are measured in each phase by thermocouples, and the measurement results in Fig. 5-44 indicate a non-uniform temperature distribution in three phases. This might be caused by a non-uniform flow distribution in the machine cooling fins and/or the thermocouple in phase *A* being dislocated and not in a good contact with the winding. The predicated average winding temperature agrees reasonably well with the measured temperatures in phases *B* and *C*. Table 5-10 compares the measured and predicted fundamental phase voltage, current and the mean torque at the time when the machine temperatures reach their steady-states. It can be observed that all the errors of the predicted quantities are within 5%, showing a good agreement with experimental results.

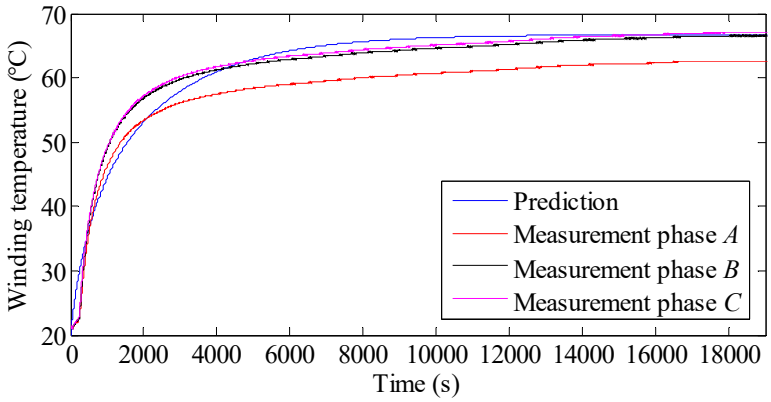

Fig. 5-44. Measured and predicted winding temperature transient waveforms with 0.71Ohm load at 1350r/min.

Table 5-10. Measured and Predicted Machine Performances at Thermal Steady-State with 0.71Ohm Load at 1350r/min

Quantity	Measurement	Simulation	Error
Fundamental phase voltage (V)	46.1	48.1	4.3%
Fundamental phase current (A)	65.0	67.8	4.3%
Mean torque (Nm)	-35.5	-37.0	4.2%
Average winding temperature (°C)	65.5	66.7	1.8%

5.10 Conclusion

A high-fidelity, computationally efficient model for IPM machines has been proposed. The model captures all significant effects associated with the electromagnetic behaviour of the machines, including magnetic saturation, spatial harmonics, iron loss effect and temperature effects, and has been validated by both FE analysis and experiments. The proposed model provides an accurate means of assessing the drive performance of an IPM machine. It has been shown that torque ripple may increase significantly in the field weakening region due to current waveform distortions resulting from the inverter voltage limit. It is important to capture these adverse effects in drive system simulations in order to develop a robust control for high efficiency operations in both constant-torque and field weakening regions.

By taking into account of the temperature effects on both the *d*- and *q*-axis flux-linkages and the torque, the proposed machine model allows for accurate prediction of the electromagnetic behaviour at any feasible given temperature. This model is conducive to developing correct MTPA control strategy for IPMs when temperature varies. A high-fidelity, computationally efficient electro-thermally coupled model has been subsequently established by integrating the proposed temperature-dependent, high-fidelity electromagnetic model with a state-space lumped parameter thermal model. The proposed electro-thermally coupled model provides a useful platform to assess the temperature effect on electromagnetic behaviour of IPMs during design and over driving cycles.

It has been shown through simulation studies at the rated torque and over Artemis urban driving cycle operations that by neglecting temperature effects, the winding and magnet temperatures can be under-estimated by approximately 20°C. Even if the temperature effect on the winding resistance is considered, the predicted temperatures can still be under-estimated by approximately 10°C. Under-estimate of temperatures in magnets and

windings pose a serious risk of irreversible demagnetisation and reduction of machine lifetime. It has also been shown that, in field weakening region, neglect of temperature effect on magnets leads to less significant under-estimate of magnet and winding temperatures since the increase in *q*-axis current and decrease in *d*-axis current when PM field is reduced at high temperature tends to have some cancellation effect.

CHAPTER 6 Global Optimisation Incorporating Mechanical Strength Constraints for High Power, High Speed, Rare-earth Free Interior Permanent-magnet Machines

6.1 Introduction

Due to the high cost and limited reserves of the rare-earth material, rare-earth free IPMs are increasingly employed in industrial applications [72, 168, 187]. As reported in literature, with a proper design the performance of rare-earth free IPMs can compete with that of conventional IPMs with sintered NdFeB [69, 168]. However, the former usually exhibits a larger split ratio (defined by the ratio of rotor outer diameter to the stator outer diameter) to satisfy the same design specifications and constraints as the latter [69, 144]. Therefore, rare-earth free IPMs suffer from more mechanical strength challenges on rotor, particularly in high power and high speed applications.

In literature, the rotor mechanical strength is usually examined after the electromagnetic design [188-191]. If the maximum mechanical stress exceeds the strength limit of the rotor material, the machine rotor has to be re-designed till both electromagnetic and mechanical constraints are satisfied. This, in fact, not only costs more computation time, but also can no longer guarantee the globally optimal design. Therefore, the mechanical strength constraints need to be incorporated into the machine global optimisation.

This chapter will present two design examples of rare-earth free IPMs for EV traction applications. The one is a 53kW 9-phase 18-slot 16-pole IPM machine design. The other one is a 160kW 3-phase 48-slot 8-pole IPM machine design. The latter also includes a comparative study of machines with spoke type rotor and double layer V shape rotor. Analytical mechanical

stress models are established and subsequently incorporated into the global optimisations of all these designs.

6.2 9-phase 18-slot 16-pole IPM Machine Design and Optimisation Incorporating Mechanical Strength Constraints

This section describes the design and optimisation process of a 53kW 9-phase 18-slot 16-pole rare-earth free IPM. Subsequently, an analytical mechanical stress model is presented to take the rotor mechanical strength constraint into account. After this, machine performances are evaluated.

6.2.1 Machine Design and Global Optimisation

To improve the system compactness of electrical machines and drives in EV traction applications, inverters are integrated into machine housing, as shown in Fig. 6-1.

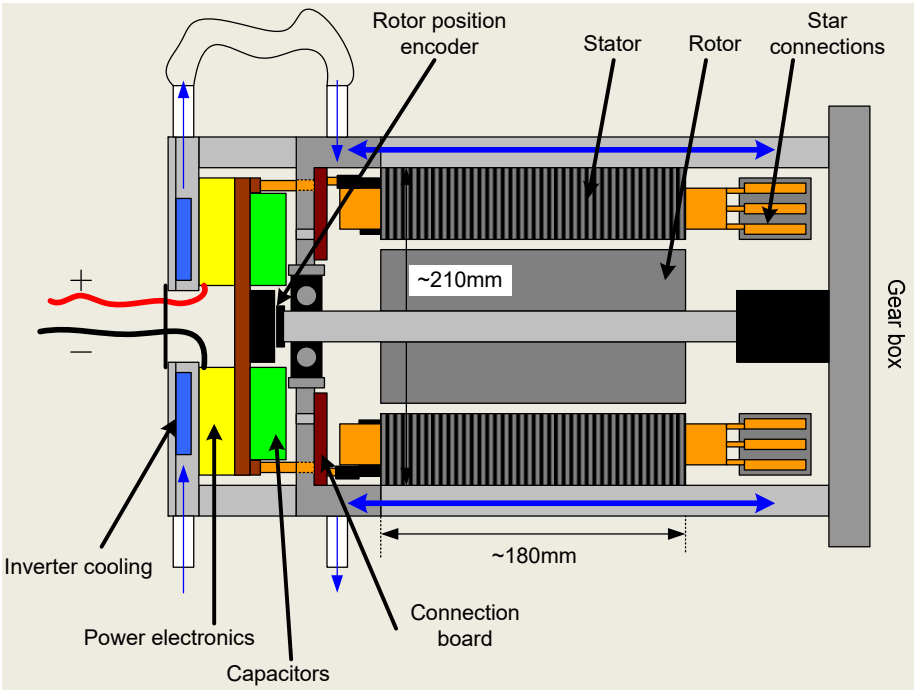

Fig. 6-1. Schematic of the 9-phase 18s-slot 16-pole machine and inverter structure.

Thus, multiple 3-phase inverters are employed in order to fully utilise the space in machine housing. This winding configuration reduces the current

rating in each phase and facilitates the use of small power electronic modules that ease the integration and connections with phase terminals. The small power modules distributed around the disc housing/cooling spreads the heat (loss) and minimises hot spot temperature. Thus, the corresponding multiple 3-phase winding configuration needs to be used in the electrical machine. On the other hand, a factional-slot concentrated winding configuration is preferable in this application in which the compactness is the priority, since the end-winding length of the concentrated winding is significantly shorter than that of a conventional distributed winding. Therefore, a 9-phase 18-slot 16-pole winding configuration is devised as illustrated in Fig. 6-2.

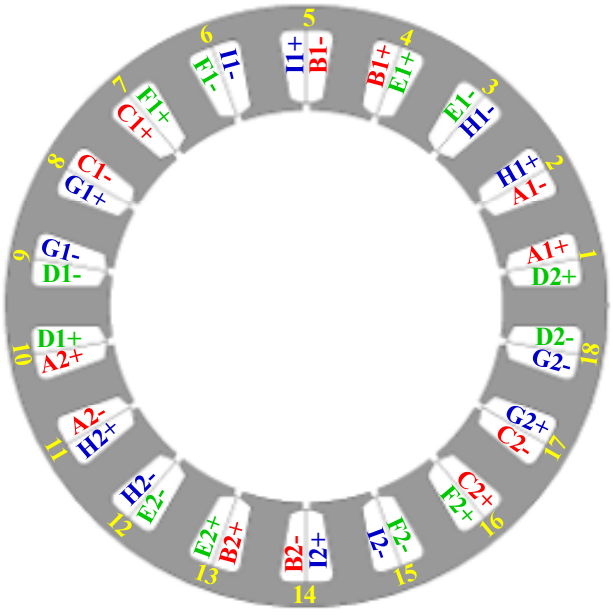

Fig. 6-2. Schematic of the 9-phase 18-slot 16-pole winding configuration.

This winding configuration also follows the MMF harmonic reduction principle proposed in Chapter 4. The three 3-phase winding sets (*ABC*, *DEF* and *GHI*) have 20° phase shift between two neighbouring 3-phase sets. Thus, compared to conventional 3-phase winding, not only the fundamental of MMF is improved, but also all the sub-harmonics and part of high order MMF harmonics are eliminated. This can be observed in the MMF spectrum comparison between the 3-phase and 9-phase 18-slot 16-pole winding

configurations shown in Fig. 6-3. The orders of eliminated harmonics include 2^{nd}, 4^{th}, 14^{th}, 16^{th}, 20^{th}, 22^{nd} ….

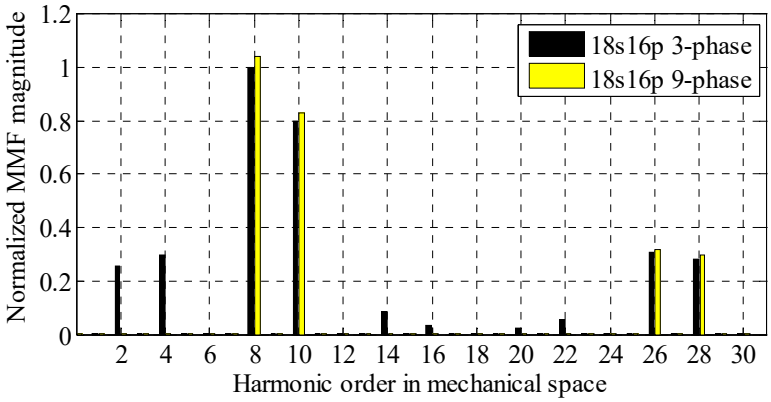

Fig. 6-3. MMF harmonic spectrum comparison between 3-phase and 9-phase 18-slot 16-pole winding configurations.

The design specifications and optimisation constraints are listed in Table 6-1. Due to the strictly limited volume in this design, the optimisation objective is to maximise the output torque (or torque density). Therefore, the peak power and peak torque are listed as "desirable peak power" and "desirable peak torque" respectively in Table 6-1. Fig. 6-4 depicts the prospective peak envelop and continuous envelop on torque-speed plane.

Table 6-1. Design Specifications and Optimisation Constraints of 9-phase 18-slot 16-pole Machine

Quantity	Unit	Value
Desirable peak power	kW	47
Rated power	kW	40
Base speed	r/min	3000
Rated speed	r/min	4200
Maximum operation speed	r/min	11300
Desirable peak torque	Nm	150.0
Rated torque	Nm	91.0
Continuous torque at maximum speed	Nm	33.8
Phase current limit	A	140
DC-link voltage (Line-to-line voltage limit)	V	354
No-load line-to-line back-EMF limit	V	520
Current density limit (in RMS)	A/mm^2	9.6
Rotor mechanical stress limit (M235-35A)	MPa	460
Cooling		Water-cooled

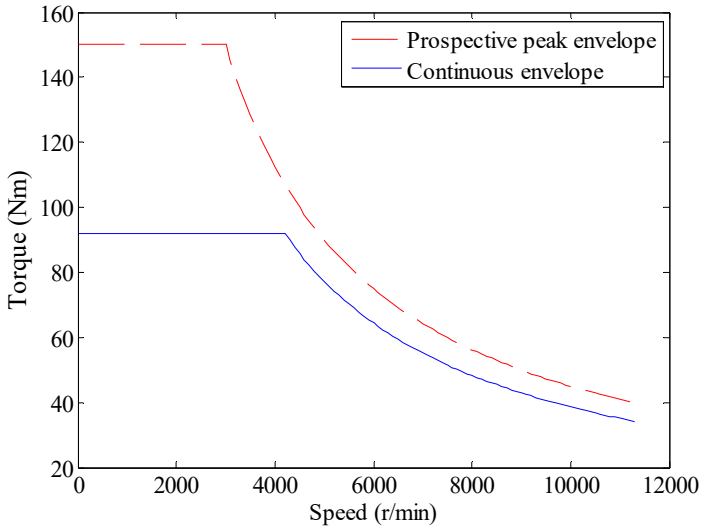

Fig. 6-4. Torque-speed profile of the 9-phase 18-slot 16-pole machine.

The optimisation constraints include performance specifications, current limit, DC-link voltage (Line-to-line voltage) limit, the limit on the no-load back-EMF at the maximum speed for safety in the event of inverter or control failures, current density limit corresponding to the thermal constraint, and also the rotor mechanical stress limit, as listed in Table 6-1. The incorporation of the mechanical strength constraint will be presented in the next section.

The optimisation is performed using the same tool as in Chapter 4. The flow chart of the machine design and optimisation process is illustrated in Fig. 6-5. First, the range of parameters to be optimised needs to be defined. Then, the optimisation tool GOT-IT by CEDRAT [132] determine values for these parameters. After this, the mechanical stress model calculates the appropriate rotor bridge thicknesses based on the current rotor geometry and then these thicknesses are changed accordingly in FEA. Subsequently, the electromagnetic performances are evaluated via the semi-FE model developed in [133] before the optimisation objective and constraints are fed back to GOT-IT. Then, optimisation trends of parameters are determined via GA and SSO algorithms by GOT-IT. If the optimisation has not finished, updated valued will be assigned to parameters and the above processes will continue. However, if it has finished, the optimal design will be obtained. A

mechanical stress analysis in FEA needs to be performed and the rotor geometry may be finely tuned if needed. Finally, the machine performances of the final design are evaluated.

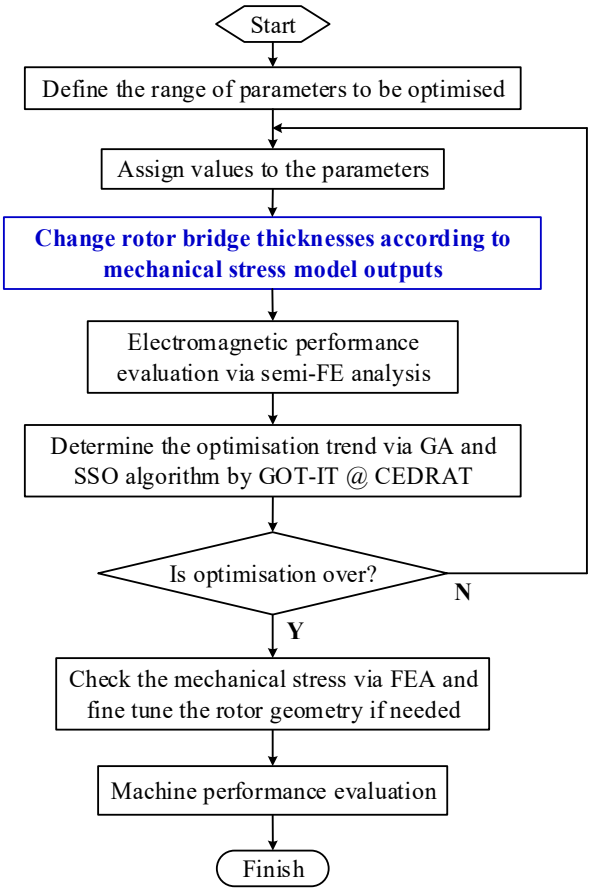

Fig. 6-5. Flow chart of machine design and optimisation incorporating mechanical strength constraints.

The leading design parameters to be optimised in this design are shown in Fig. 6-6. Six parameters including split ratio, pole arc, pole depth ratio, tooth width, back-iron thickness and the number of turns per coil, will be optimised. The split ratio K_s is defined as the ratio of the rotor outer radius R_i to the stator outer radius R_o. The pole arc β_p is defined in electrical degree, and hence $\beta_p=p\cdot\beta_p$ where p is the pole pair number. The pole depth ratio K_p is defined as the pole depth D_p divided by the rotor outer radius R_i, as indicated in Fig. 6-6. The parameter variation ranges are listed in Table 6-2. Ferrite magnets with remanence B_r=0.395 and relative recoil permeability μ_r=1.14 are employed for this machine.

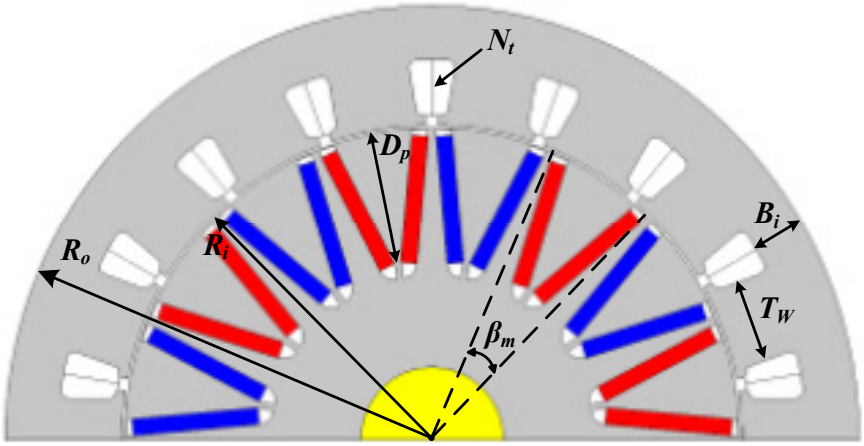

Fig. 6-6. Geometry parameters illustration of 9-phase 18-slot 16-pole machine.

Table 6-2. Parameter Variation Ranges of 9-phase 18-slot 16-pole Machine

Quantity	Symbol	Unit	Range
Split ratio	K_s		0.638~0.752
Pole arc	β_p	°	155~175
Pole depth ratio	K_p		0.4~0.6
Tooth width	T_w	mm	13~20
Back-iron thickness	B_i	mm	7~15
NO. of turns per coil	N_t		5,6,7,8

The evolution of the peak torque and the parameter conversion process during the optimisation are shown in Fig. 6-7. As can be seen, a global optimum is reached after three generations of GA iterations. The total number of designs evaluated in the optimisation is 139 and it took 35 hours to complete on a typical PC. It can also be observed that in the region close to the global optimum, there are a large number of different design parameter combinations which yield very similar efficiency while satisfying all constraints. The last sample is selected as the final design.

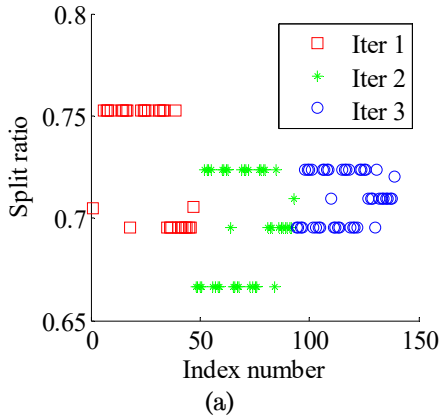

(a)

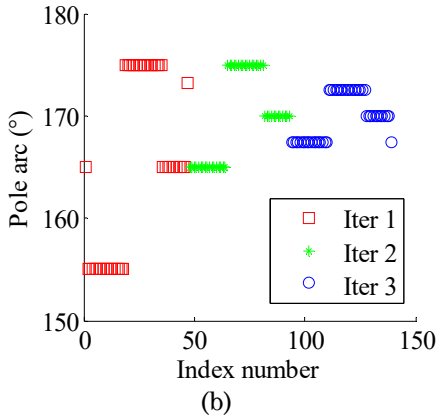

(b)

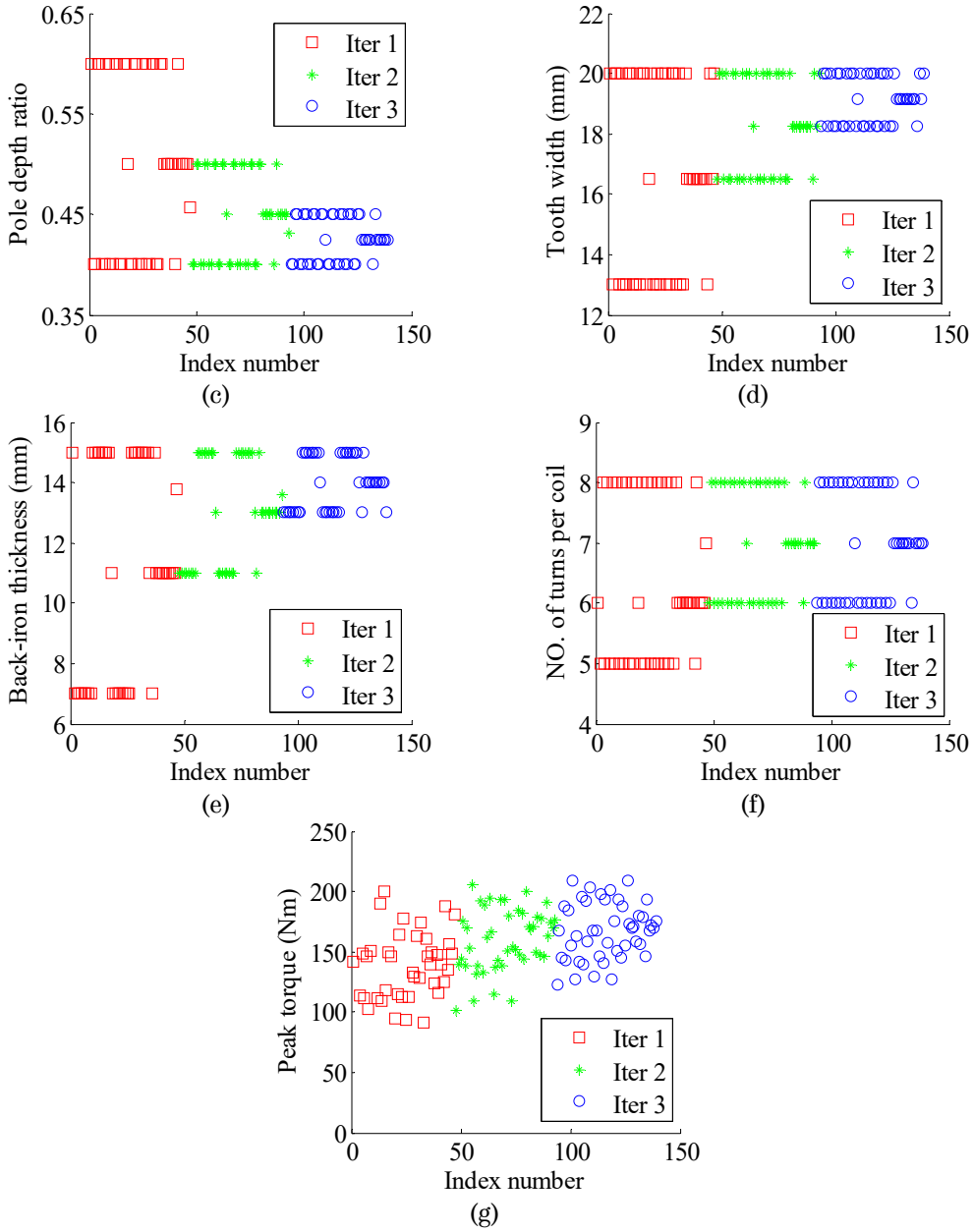

Fig. 6-7. Optimisation trends of variables and objective of 9-phase 18-slot 16-pole machine. (a) Split ratio. (b) Pole arc. (c) Pole depth ratio. (d) Tooth width. (e) Back-iron thickness. (f) NO. of turns per coil. (g) Peak torque.

Fig. 6-8 illustrates the cross-section of the optimised 9-phase 18-slot 16-pole IPM machine with outer diameter of 210mm and active length of 180mm. The optimisation results are listed in Table 6-3.

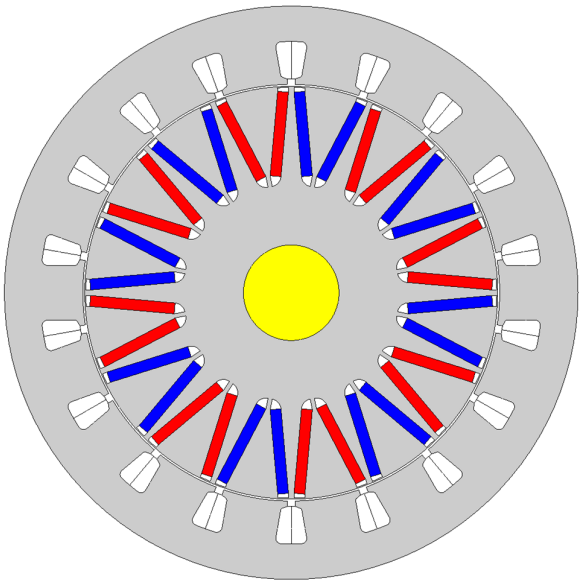

Fig. 6-8. Cross-section of the optimised 9-phase 18-slot 16-pole IPM machine.

Table 6-3. Optimised Parameters of 9-phase 18-slot 16-pole Machine

Quantity	Symbol	Unit	Value
Split ratio	K_s		0.72
Pole arc	β_p	°	167.4
Pole depth ratio	K_p		0.424
Tooth width	T_w	mm	20.0
Back-iron thickness	B_i	mm	13.0
NO. of turns per coil	N_t		7

6.2.2 Mechanical Strength Constraints

In this section, a simplified analytical model to predict the maximum mechanical stress will be presented.

In an IPM machine, flux barriers are usually introduced to reduce the leakage magnetic flux, resulting in the narrow upper and middle bridges as demonstrated in Fig. 6-9. However, the narrow upper and middle bridges will lead to high mechanical stress in the bridges due to the centrifugal force at a high speed. To avoid the fracture of the bridges, the mechanical strength constraints have to be included in the machine global optimisation process, particularly for high-power and high-speed machines. Therefore, an analytical mechanical stress model is proposed in this section.

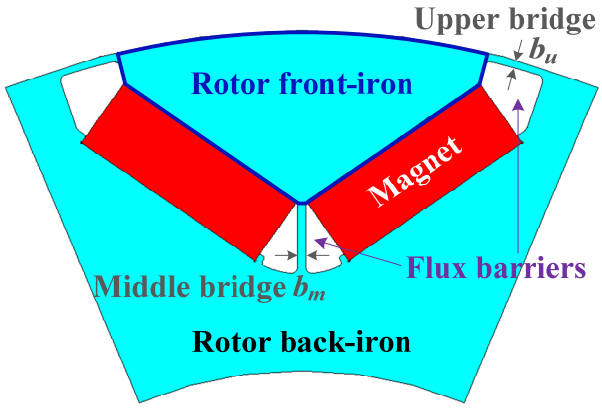

Fig. 6-9. Rotor pole structure of an IPM machine with the single layer "V" shaped magnet layout.

Theoretically, the maximum mechanical stress in upper and middle bridges should be functions of all the rotor parameters to be optimised and also the bridge thicknesses, viz. b_u kand b_m in Fig. 6-9. To simplify the mechanical stress model and meanwhile maintain the model fidelity, the maximum mechanical stresses in the upper and middle bridges, $S_{u\max}$ and $S_{m\max}$, are modeled as functions of bridge thicknesses and the equivalent mass density m_{eqv}, as given in (6.1) and (6.2). The equivalent mass m_{eqv} is defined by (6.3).

$$S_{u\max} = f_u(b_u, m_{eqv}) \tag{6.1}$$

$$S_{m\max} = f_b(b_m, m_{eqv}) \tag{6.2}$$

$$m_{eqv} = \rho_i A_{fi} + \rho_m A_m \tag{6.3}$$

where, ρ_i and ρ_m represent the rotor iron density and magnet density, and A_{fi} and A_m denote the rotor front-iron area and magnet area in one pole as shown in Fig. 6-9.

By calculating the maximum mechanical stress at different upper and middle bridge thicknesses using FEA, as shown in Fig. 6-10, the quadratic polynomial function models in (6.4) and (6.5) are employed to model the nonlinearity between the maximum stress and the bridge thickness at 1.5 times of the maximum speed. Contact elements are employed along the

boundary of two different components to consider the non-linear contact effect in FEA.

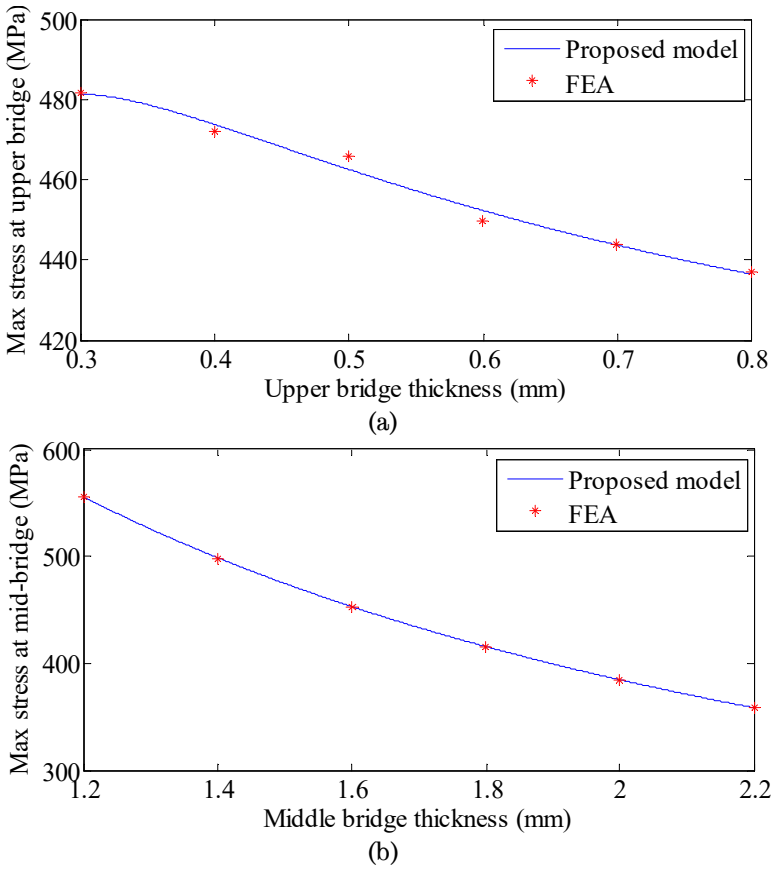

Fig. 6-10. Comparison between the proposed maximum mechanical stress model and the original FEA results of 9-phase 18-slot 16-pole machine. (a) Upper bridge. (b) Middle bridge.

$$S_{u\max} = m_{eqv}\left[C_{u0} + C_{u1}\frac{1}{b_u} + C_{u2}\left(\frac{1}{b_u}\right)^2\right] \tag{6.4}$$

$$S_{m\max} = m_{eqv}\left[C_{m0} + C_{m1}\frac{1}{b_m} + C_{m2}\left(\frac{1}{b_m}\right)^2\right] \tag{6.5}$$

where, C_{u0}, C_{u1}, C_{u2}, C_{m0}, C_{m1} and C_{m2} are the polynomial coefficients for the mechanical stress models of upper and middle bridges. These coefficients are obtained by curve-fitting the original FE data in Fig. 6-10 and listed in Table 6-4. From Fig. 6-10, it can be seen that the proposed mechanical stress models can fit well with the FE results. The material properties of rotor iron and magnets are shown in Table 6-5.

Table 6-4. Polynomial Coefficients for Mechanical Stress Models of 9-phase 18-slot 16-pole Machine

Item	Value
C_{u0}	41.3
C_{u1}	10.9
C_{u2}	-0.984
C_{m0}	37.4
C_{m1}	17.7
C_{m2}	-0.037

Table 6-5. Material Properties of Rotor Iron and Magnets of 9-phase 18-slot 16-pole Machine

Item	Unit	M235-35A	Ferrite NMF-12F
Young modulus	GPa	192	160
Poisson's ratio		0.28	0.24
Density	kg/m^3	7600	5000

To justify the accuracy of the proposed mechanical stress model, three rotors are designed with various parameters as listed in Table 6-6. The mechanical stress models are established using design I while design II and III represent new designs considering all the rotor parameter variations in the optimisation. Compared to design I, design II has -15.7%, 5.2% and -32.4% variations in the split ratio K_s, pole arc β_p and pole depth ratio K_p respectively. This results in 48.1% reduction in the equivalent mass m_{eqv}. The upper and middle bridge thicknesses are kept unchanged in design II in order to separate the influence of rotor parameters on the maximum mechanical stress from that of the bridge thicknesses. In contrast, design III employs the same rotor parameters, i.e. K_s, β_p and K_p, as design II, whereas the upper and middle bridge thicknesses in design III are 40% and 37.5% smaller than those of both designs I and II.

The von Mises stress contours of rotor irons in these three designs are illustrated in Fig. 6-11. Then, the comparison of maximum mechanical stress in FEA and the proposed model for designs I, II and III are shown in Table 6-7, Table 6-8 and Table 6-9 respectively.

Table 6-6. Geometrical Parameters of Design I, Design II and Design III

Item	Design I	Design II	Design II variation ratio	Design III	Design III variation ratio
K_s	0.746	0.629	-15.7%	0.629	-15.7%
β_p (°)	155	163	5.2%	163	5.2%
K_p	0.444	0.3	-32.4%	0.3	-32.4%
m_{eqv} (kg/m)	4.03	2.09	-48.1%	2.09	-48.1%
b_u (mm)	0.5	0.5	0%	0.3	-40.0%
b_m (mm)	1.5	1.5	0%	1.0	-37.5%

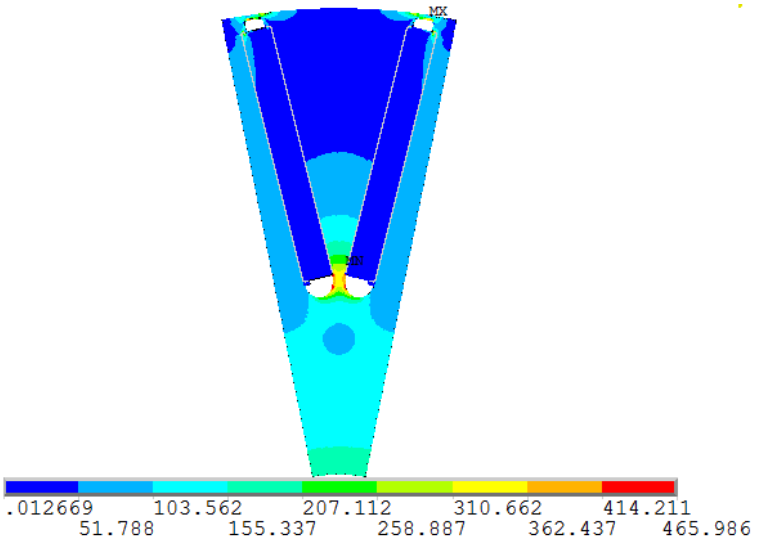

(a)

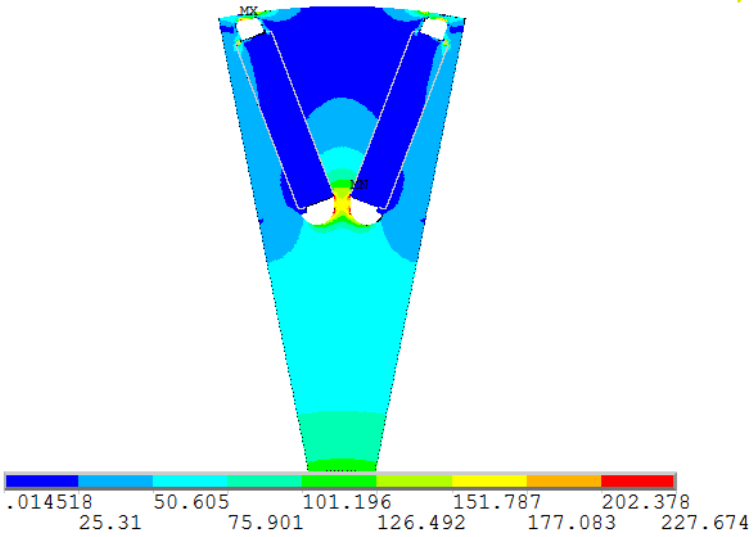

(b)

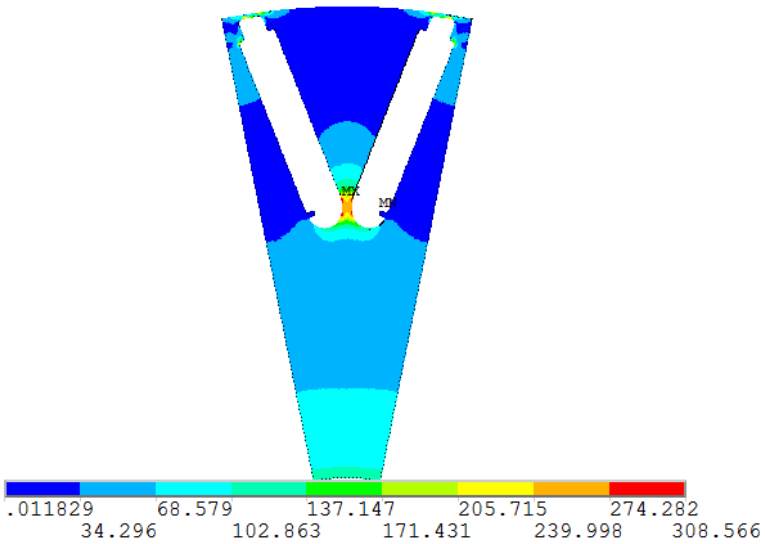

(c)

Fig. 6-11. von Mises contour of rotor iron of 9-phase 18-slot 16-pole machine at 16950r/min. (a) design I. (b) design II. (c) design III.

Table 6-7. Comparison of Maximum Mechanical Stress in FEA and the Proposed Model for Design I

Item	FEA	Proposed model	Error
$S_{u\max}$ (MPa)	466.0	462.5	-0.8%
$S_{m\max}$ (MPa)	453.0	452.9	0.0%

Table 6-8. Comparison of Maximum Mechanical Stress in FEA and the Proposed Model for Design II

Item	FEA	Proposed model	Error
$S_{u\max}$ (MPa)	227.7	240.0	5.4%
$S_{m\max}$ (MPa)	221.2	235.0	6.2%

Table 6-9. Comparison of Maximum Mechanical Stress in FEA and the Proposed Model for Design III

Item	FEA	Proposed model	Error
$S_{u\max}$ (MPa)	263.8	249.7	-5.4%
$S_{m\max}$ (MPa)	308.6	325.2	5.4%

It can be observed that in design I the maximum mechanical stresses at upper and middle bridges, i.e. $S_{u\max}$ and $S_{m\max}$, are 466.0MPa and 453MPa respectively in FEA. These stresses predicted by the proposed model are 462.5MPa and 452.9MPa. These errors are negligible. This is because the proposed model is established based on design I. However, in design II where m_{eqv} is 48.1% lower than that of design I, the errors of the proposed model on $S_{u\max}$ and $S_{m\max}$ become 5.4% and 6.2% respectively. These errors are

attributed to the influence of individual rotor parameters on the maximum mechanical stress. In other words, the proposed model neglects individual rotor parameters whereas employs an equivalent mass as shown in (6.1) and (6.2). In design III, these errors are -5.4% and 5.4%, due to both the neglect of the influence of individual rotor parameters and the non-linearity in the relationship between maximum mechanical stress and bridge thicknesses. It should be noted that although the proposed model shows approximately ±6% errors in design II and III, it allows us to take the mechanical strength constraints into account in the machine global optimisation process. Thus, more unnecessary deigns whose mechanical strength cannot meet requirement can be avoided by using this mechanical stress model. Moreover, the optimisation trends are also affected and the final design will be closer to the true optimum compared to the optimisation without considering mechanical strength constraints.

The mechanical stresses on magnets are not shown since they are not the limiting factors. This mechanical stress model needs to be modified before applying to other rotor interior magnet configurations, such as rotors with double layer V-shaped magnet and spoke type magnet. However, the principle using equivalent mass supported by bridges to build the polynomial functions of the mechanical stress model is generic.

The model accuracy can be improved by considering the influence of all individual rotor parameters on the maximum mechanical stresses on upper and middle bridges. However, this needs a much more complex model and can be done in the future work.

6.2.3 Performance Evaluation

This section evaluates the performances of the optimised 9-phase 18-slot 16-pole rare-earth free IPM shown in Fig. 6-8 and Table 6-3, including the mechanical stress analysis in Section 6.2.3.1 and the electromagnetic performance evaluation in Section 6.2.3.2.

6.2.3.1 Mechanical Stress Analysis

Given that the proposed mechanical stress model in Section 6.2.2 is not as accurate as FEA, the mechanical stress analysis of the optimised machine is performed before the electromagnetic performance evaluation. Fig. 6-12 shows the von Mises contour at 1.5 times of the maximum speed, i.e. 16950r/min. It can be seen that the maximum stress occurs at the middle bridge, being 454.0MPa which is lower than the yield strength 460MPa. Therefore, the mechanical strength constraint is satisfied.

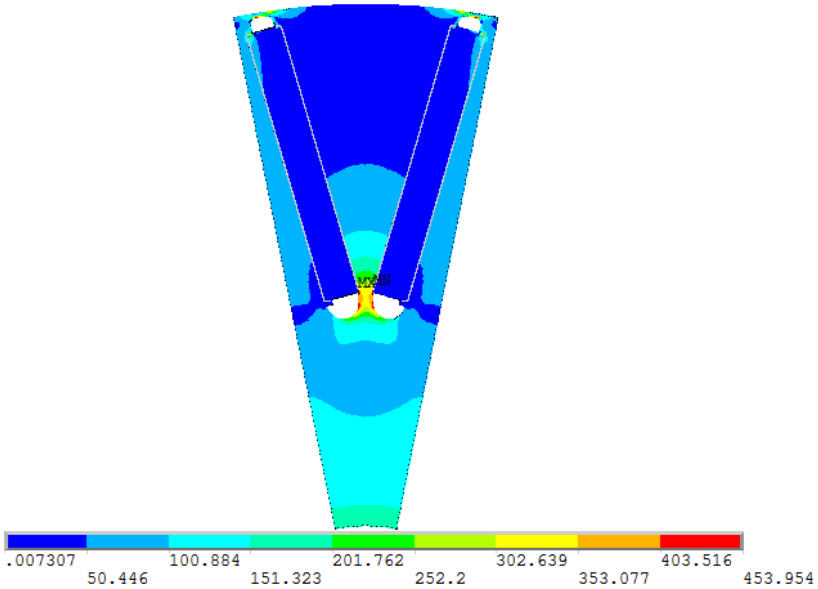

Fig. 6-12. von Mises contour of 9-phase 18-slot 16-pole machine at 16950r/min.

6.2.3.2 Electromagnetic Performance Evaluation

The phase back-EMF waveforms and spectrum at the maximum speed 11300r/min are illustrated in Fig. 6-13. It can be seen that the phase shift angle between phase *D* and phase *A* is 20° with the winding configuration shown in Fig. 6-2. Due to absence of constraints on back-EMF harmonics during the global optimisation, the phase back-EMF contains a large 5th order harmonic component shown in Fig. 6-2. However, this is the optimal design against torque density, as shown in Section 6.2.1. Therefore, no further fine tuning on rotor geometry is performed to make the phase back-EMF more sinusoidal.

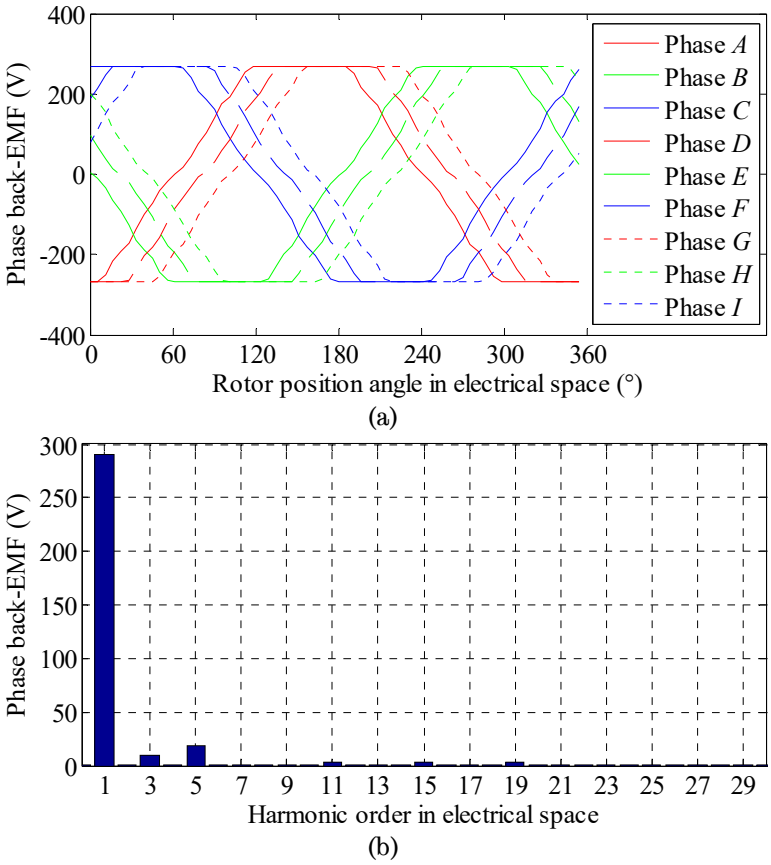

Fig. 6-13. FE-predicted phase back-EMF waveforms and spectrum of 9-phase 18-slot 16-pole machine at maximum speed 11300r/min. (a) Waveforms. (b) Spectrum.

Fig. 6-14 depicts the line-to-line back-EMF waveform and spectrum. It shows that the fundamental line-to-line back-EMF at maximum speed 11300r/min is 504.5V. Therefore, the maximum back-EMF constraint (≤520V), is satisfied.

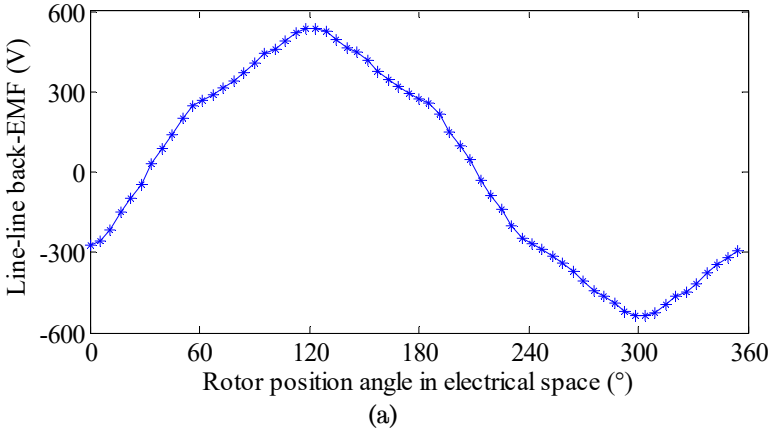

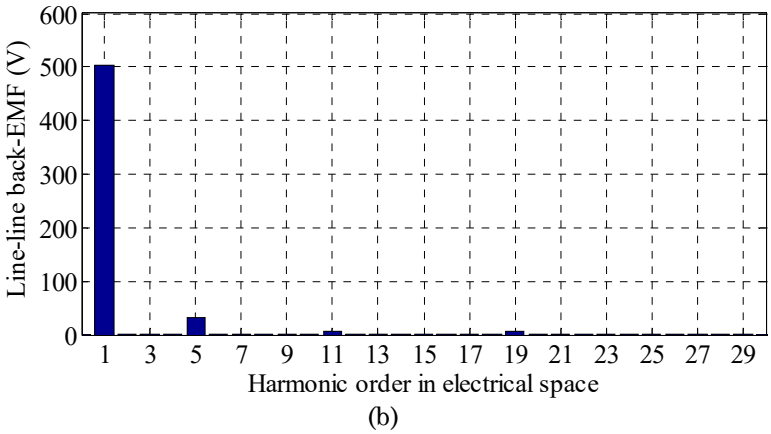

Fig. 6-14. FE-predicted line-to-line back-EMF waveform and spectrum of 9-phase 18-slot 16-pole machine at maximum speed 11300r/min. (a) Waveform. (b) Spectrum.

With phase currents shown in Fig. 6-15, the FE-predicted peak torque waveform is illustrated in Fig. 6-16 (a). The average torque is 180.7Nm which is higher than the required peak torque 150Nm. The torque ripple is only 0.7% and its dominant harmonic is 18th order, which can be observed in Fig. 6-16 (b). This 6th order torque ripple harmonic does not exist although back-EMF has 5th order harmonic as shown in Fig. 6-13 (b). This is because the torque harmonic components produced by the three 3-phase winding sets forms a balanced 3-phase system at 6th, 12th, 24th, 30th ··· orders. The fundamental reason can be found in Section 4.7.2, Chapter 4.

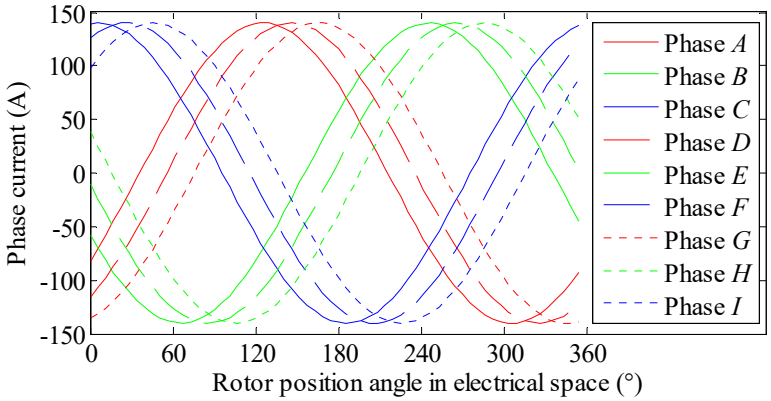

Fig. 6-15. Phase current waveforms at peak torque of 9-phase 18-slot 16-pole machine.

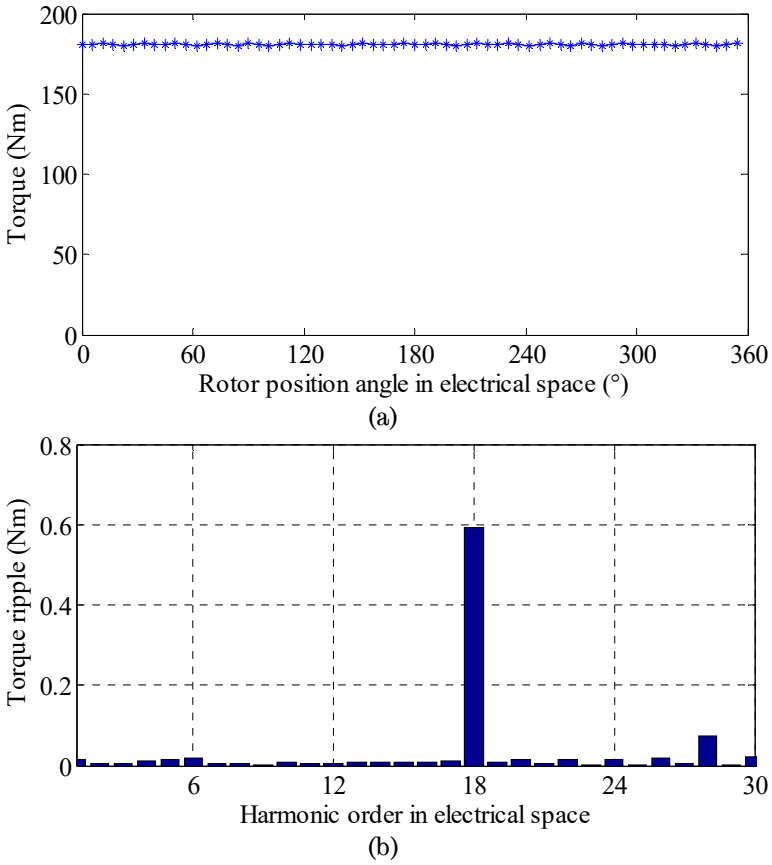

Fig. 6-16. Peak torque waveform and its ripple spectrum of 9-phase 18-slot 16-pole machine. (a) Waveform. (b) Ripple spectrum.

FE-predicted *d*- and *q*-axis inductance waveforms at peak torque are shown in Fig. 6-17. These inductances are calculated using the conventional method neglecting the influence of *d*-axis current on permanent-magnet field, as described in Chapter 3. It can be seen that both *d*- and *q*-axis inductances rarely have ripples. This also confirms that the torque ripple of this 9-phase 18-slot 16-pole machine is negligible.

Table 6-10 lists detailed design information and also the machine performances at both peak and rated operations. The slot fill factor is also known as "copper packing factor", which is calculated by the pure copper area divided by the total slot area excluding the slot-opening area. Due to the segmented tooth technique used in this concentrated winding configuration, a slot fill factor of 0.6 can be achieved. Thus, the copper loss is reduced by approximately 20% compared to the conventional winding technique. The

rated efficiency is 96.5%. It should be noted that this efficiency can be improved if the optimisation objective is chosen to maximise rated efficiency.

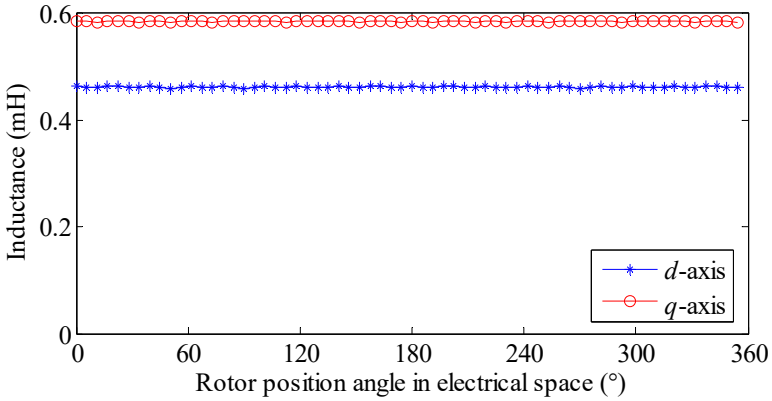

Fig. 6-17. FE-predicted *d*- and *q*-axis inductance waveforms at peak torque of 9-phase 18-slot 16-pole machine.

Table 6-10. Performances of the Optimised 9-phase 18-slot 16-pole Machine

Description	Item	Unit	Value
Dimension	Active length	mm	180
	Stator outer diameter	mm	210
	Stator inner diameter	mm	151.2
Design parameters	PM mass	kg	3.58
	Slot fill factor		0.6
	Phase resistance @ 120°C	Ohm	0.027
	d-axis inductance @ rated torque	mH	0.527
	q-axis inductance @ rated torque	mH	0.694
Performance @ peak torque	Torque	Nm	180.7
	Current	A	140
	Current density (RMS)	A/mm^2	18.0
	Line-to-line voltage @3000r/min	V	334.0
	Torque ripple	%	0.7%
Performance @ rated torque	Torque	Nm	91.0
	Current	A	74.3
	Current density (RMS)	A/mm^2	9.6
	Copper loss	W	669.0
	Stator iron loss	W	523.1
	Rotor iron loss	W	258.7
	Efficiency	%	96.5%
No-load	Line-to-line back-EMF @11300r/min	V	504.5

6.3 48-slot 8-pole IPM Machine Design and Optimisation Incorporating Mechanical Strength Constraints

This section presents the other rare-earth free IPM machine design and optimisation also incorporating mechanical strength constraints, for EV traction application. Given that the reluctance torque capability of distributed winding configuration is higher than that of fractional-slot one, 48-slot 8-pole is chosen as the slot-pole combination for this application. A comparative study of two 48-slot 8-pole IPMs with different rotor topologies, i.e. spoke type and double layer V shape, are performed after both machines are globally optimised with the same objective and constraints. The schematics of these two candidate machines are shown in Fig. 6-18. The machine with better overall performance is selected before demagnetisation analysis is carried out.

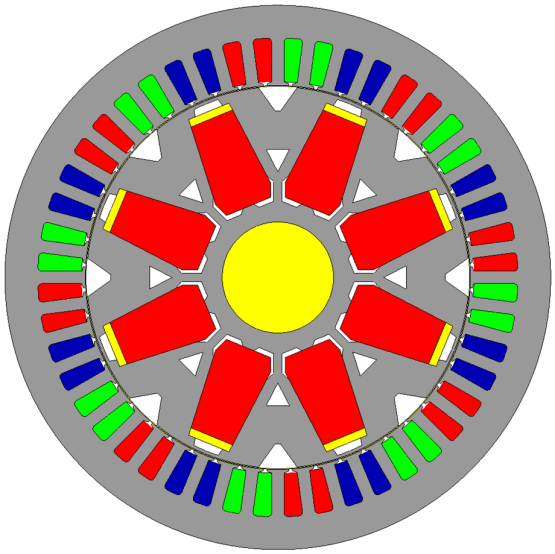

(a)

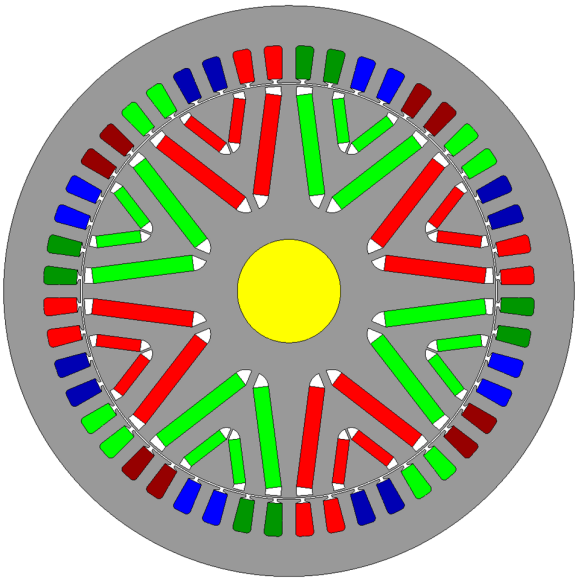

(b)

Fig. 6-18. Schematics of candidate machine topologies. (a) 48-slot 8-pole machine with spoke type rotor. (b) 48-slot 8-pole machine with double layer V shape rotor.

6.3.1 Machine Design and Global Optimisation

The electrical machine to be designed shall fulfil the following torque-speed profiles for both the peak and continuous power operations illustrated in Fig. 6-19. The detailed specification, power rating and design constraints can be found in Table 6-11 and Table 6-12.

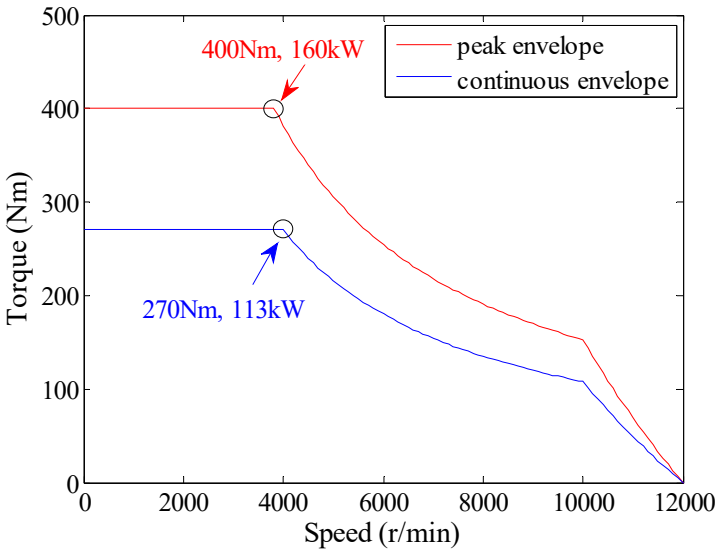

Fig. 6-19. Peak and continuous torque-speed envelopes of 48-slot 8-pole machines.

Table 6-11. Specification and VA Rating of 48-slot 8-pole Machines

Parameters	Units	Values
Stator outer diameter	mm	280
Active length	mm	170
DC link voltage	V	630
Max current (RMS)	A	400

Table 6-12. Design Constrains of 48-slot 8-pole Machines

Parameters	Units	Values
Peak torque	Nm	400
Max current density	A/mm^2	20
Max line-to-line voltage	V	630
Max current (RMS)	A	400
Max back-EMF (RMS)	V	778
Max mechanical stress	MPa	450
Max temperature at continuous power operation	°C	120
No demagnetisation at -20°C	N/A	N/A

As shown in Fig. 6-19, the required peak power is 160kW and the maximum speed is 12,000r/min, resulting in the potential risk on the mechanical failure of the rotor due to the high centrifugal force. Therefore, the rotor mechanical stress analysis has to be considered in the following machine design and optimisation process.

6.3.2 48-slot 8-pole Machine with Spoke Type Rotor

The spoke type rotor structure is initially designed, as shown in Fig. 6-20. The non-magnetic material (stainless steel 304) part is employed for both the magnet tensile stress reduction and demagnetisation protection purposes. The notch features are introduced to improve the rotor saliency ratio and also reduce the torque ripple.

Neglecting mechanical stress variation with temperature, the no-load condition at the maximum speed, viz. 12000r/min, is considered as the worst case scenario.

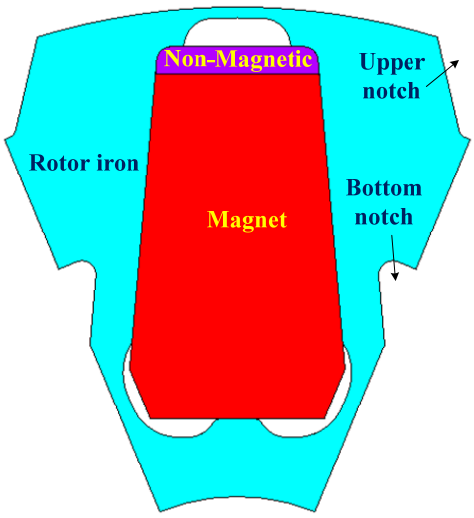

Fig. 6-20. Spoke type rotor structure of 48-slot 8-pole machine.

By varying the bridge thickness, the relationship of the maximum stress with respect to the bridge thicknesses can be obtained using the same approach presented in Section 6.2.2. However, the equivalent mass m_{eqv} is expressed by (6.6).

$$m_{eqv} = \rho_i A_{fi} + \rho_m A_m + \rho_{nm} A_{nm} \tag{6.6}$$

where, ρ_i, ρ_m, A_{fi}, A_m denote the same variables as they are in (6.3), while ρ_{nm} and A_{nm} represent the density and area of non-magnetic part in Fig. 6-21.

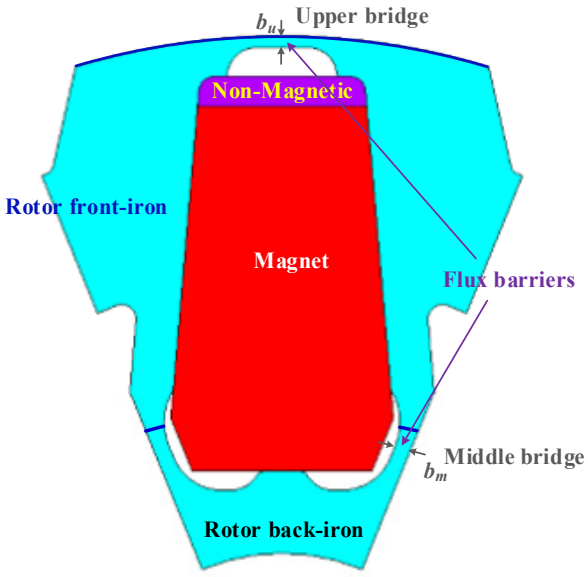

Fig. 6-21. Illustration of parameters for mechanical stress model of spoke type rotor structure of 48-slot 8-pole machine.

The parameters to be optimised in 48-slot 8-pole machine with spoke type rotor include split ratio, pole depth ratio, tooth width, back-iron thickness, and NO. of turns per coil, which are illustrated in Fig. 6-22 and Table 6-13. The definition of the split ratio K_s and pole depth ratio K_p are the same as those in Section 6.2.1. Ferrite magnets with remanence B_r=0.395 and relative recoil permeability μ_r=1.14 are employed for this machine.

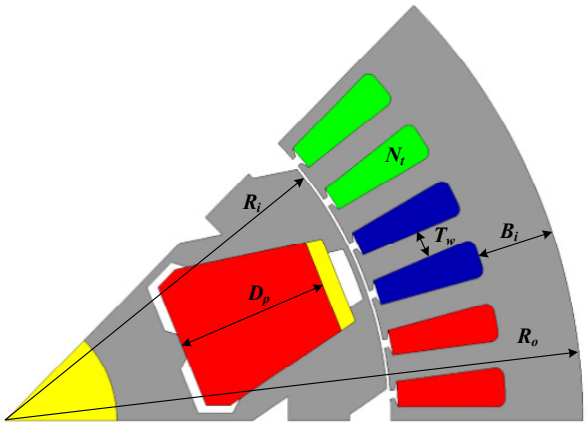

Fig. 6-22. Illustration of the parameters to be optimised for 48-slot 8-pole machine with spoke type rotor.

Table 6-13. Parameter Ranges for the Optimisation of 48-slot 8-pole Machine with Spoke Type Rotor

Parameter	Description	Unit	Range
K_s	Split ratio		0.65~0.75
K_p	Pole depth ratio		0.3~0.5
T_w	Stator tooth width	mm	4~9
B_i	Stator back-iron thickness	mm	10~24
N_t	NO. of turns per coil		2,3,4

The optimisation objective and constraints are listed in Table 6-14. Based on the optimisation method described in Fig. 6-5, 3 iterations are needed whilst each iteration contains 27 samples. The optimisation trends of the design parameters are shown in Fig. 6-23 (a)~(e), and that of the optimisation objective, viz. the rated efficiency, is shown in Fig. 6-23 (f). The optimisation results are shown in Fig. 6-24 and Table 6-15.

Table 6-14. Optimisation Objective and Constraints of 48-slot 8-pole Machines

Description	Item
Objective	Rated efficiency
Constraints	Peak current ≤ 400A (RMS)
	Line-to-line voltage ≤ 630V
	Back-EMF at maximum speed ≤ 1100V
	Current density at peak torque ≤ 20A/mm^2 (RMS)
	Mechanical stress at maximum speed ≤ 450MPa

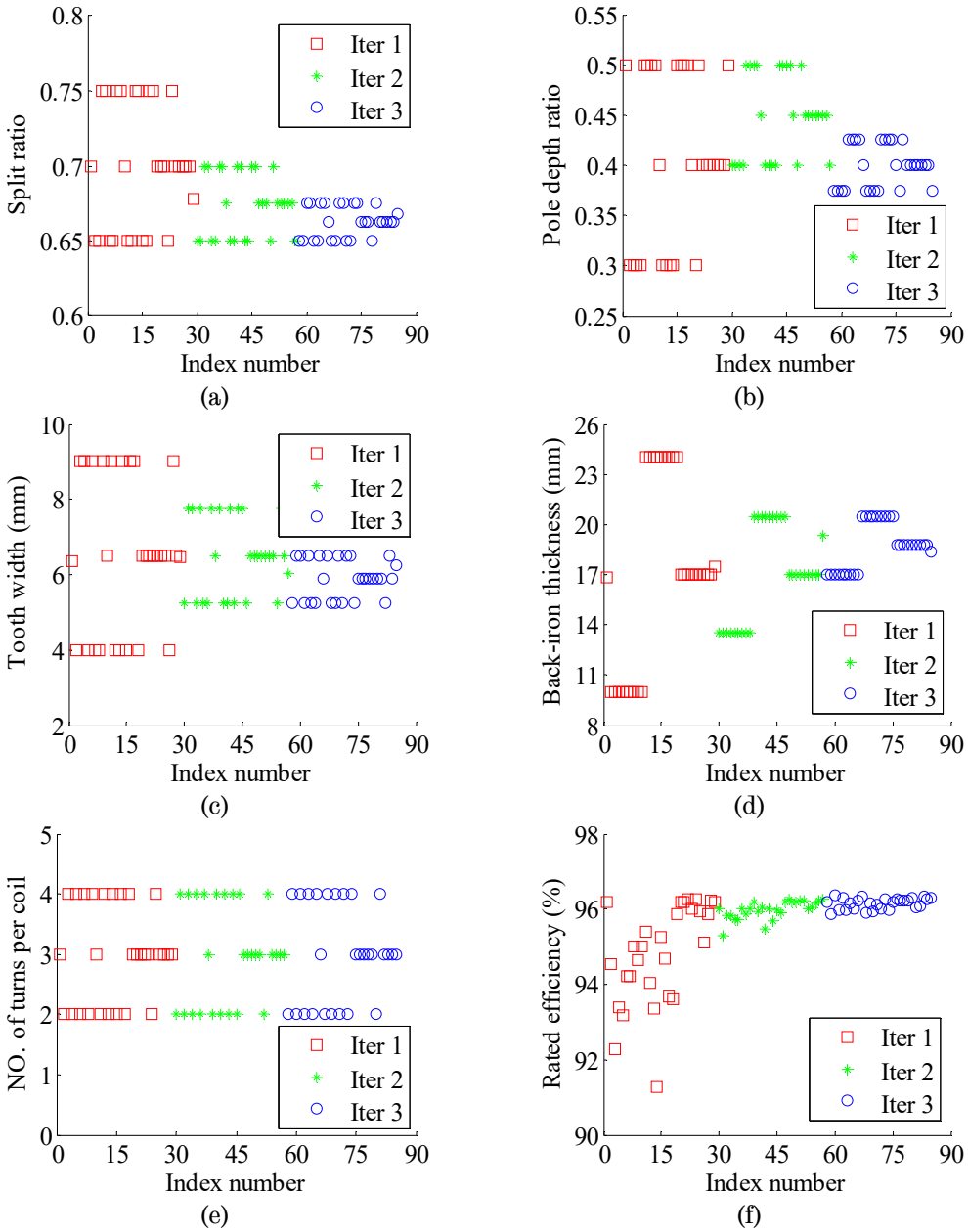

Fig. 6-23. Optimisation trends for 48-slot 8-pole machine with spoke type rotor. (a) Split ratio. (b) Pole depth ratio. (c) Tooth width. (d) Back-iron thickness. (e) NO. of turns per coil. (f) Rated efficiency.

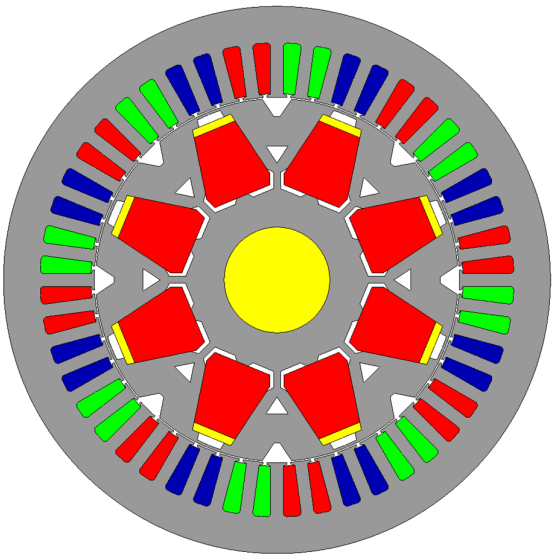

Fig. 6-24. Optimised geometry of 48-slot 8-pole machine with spoke type rotor.

Table 6-15. Optimised Parameters of 48-slot 8-pole Machine with Spoke Type Rotor

Parameter	Description	Unit	Value
K_s	Split ratio		0.6625
K_p	Pole depth ratio		0.4
T_w	Stator tooth width	mm	6.5
B_i	Stator back-iron thickness	mm	18.76
N_t	NO. of turns per coil		3

The mechanical stress analysis in FEA is performed before the electromagnetic performance evaluation of the optimised design. Material properties are listed in Table 6-16. Fig. 6-25 illustrates the von Mises stress contour of the optimised 48-slot 8-pole machine with spoke type rotor. It can be seen that the maximum stress, occurring at the bridge parts, reaches 427MPa, smaller than the M270-35A yield strength 450MPa.

Subsequently, the electromagnetic performances of the optimised design are evaluated via FEA, as listed in Table 6-17.

Table 6-16. Material Properties of Rotor Iron, Magnets and Stainless Steel 304 in 48-slot 8-pole Machines

Parameters	M270-35	Ferrite NMF-12F	Stainless steel 304
Young's modulus (GPa)	192	160	200
Poisson's ratio	0.28	0.24	0.26
Density (kg/m^3)	7,600	5,000	7900

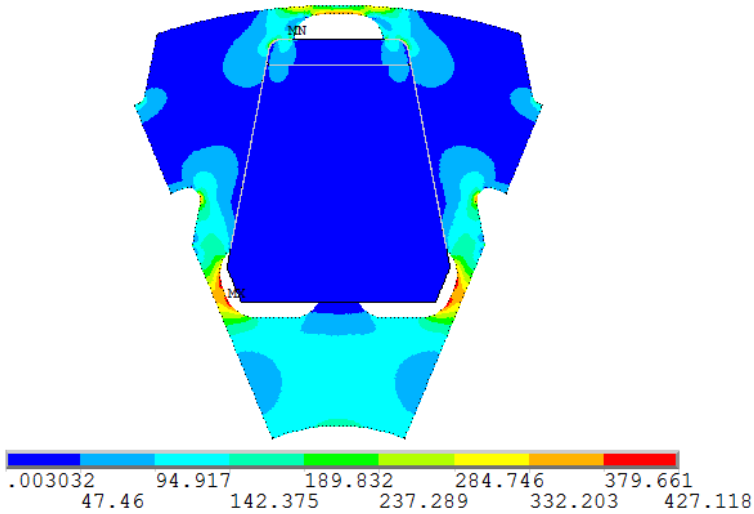

Fig. 6-25. von Mises stress contour of the optimised 48-slot 8-pole machine with spoke type rotor.

Table 6-17. Performance of the Optimised 48-slot 8-pole Machine with Spoke Type Rotor

Description	Item	Unit	Value
Dimension	Active length	mm	170
	Stator outer diameter	mm	280
	Stator inner diameter	mm	185.5
Design parameters	PM mass	kg	7.43
	Slot fill factor		0.45
	Phase resistance @ 120°C	Ohm	0.01
	d-axis inductance @ rated torque	mH	0.264
	q-axis inductance @ rated torque	mH	0.689
Performance @ peak torque	Torque	Nm	400.3
	Current (RMS)	A	393.9
	Current density (RMS)	A/mm^2	13.1
	Line-to-line voltage @3820r/min	V	589.8
	Power factor		0.57
	Reluctance torque contribution	%	72.9%
	Torque ripple	%	26.9%
	Copper loss	W	4676
	Stator iron loss	W	1211
	Rotor iron loss	W	208
	Efficiency	%	96.3%
Performance @ rated torque	Torque	Nm	269.8
	Current (RMS)	A	270.1
	Current density (RMS)	A/mm^2	8.96
	Power factor		0.59
	Reluctance torque contribution	%	68.2%
	Torque ripple	%	12.2%
	Copper loss	W	2199
	Stator iron loss	W	1094
	Rotor iron loss	W	181
	Efficiency	%	97.0%
No-load	Line-to-line back-EMF @12,000r/min	V	366

It can be noticed that all the optimisation constraints shown in Table 6-14 are satisfied. However, when drawing the peak power envelope on the torque-speed plane, it is found that the peak power at the maximum operating speed can only reach 136kW rather than the required 160kW, as shown in Fig. 6-26 (a). This is because the voltage limit at the maximum operating speed confines the current vector within the ellipse shown in Fig. 6-26 (b). However, the required torque profile, viz. 153Nm curve in Fig. 6-26 (b), has no intersections with the voltage ellipse. In other words, there are no common solutions of the *d*- and *q*-axis currents which can satisfy both voltage limit and torque requirements. The fundamental reason is the low torque production capability of the spoke type rotor topology, which will be further explained later.

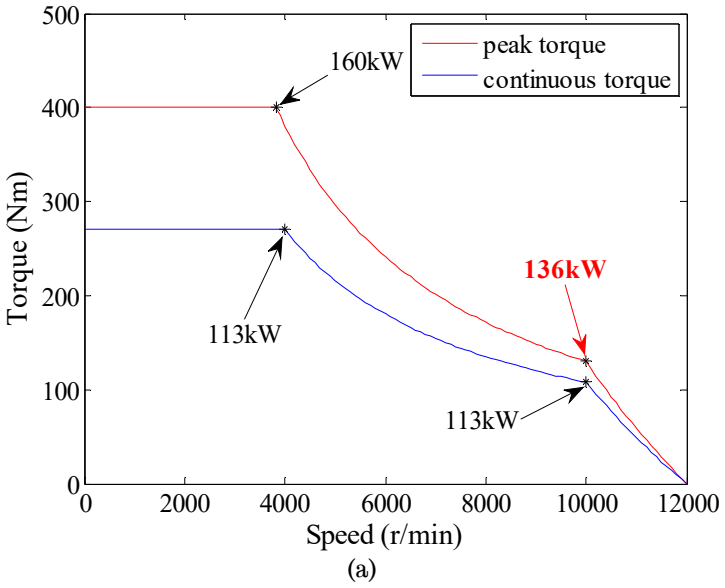

(a)

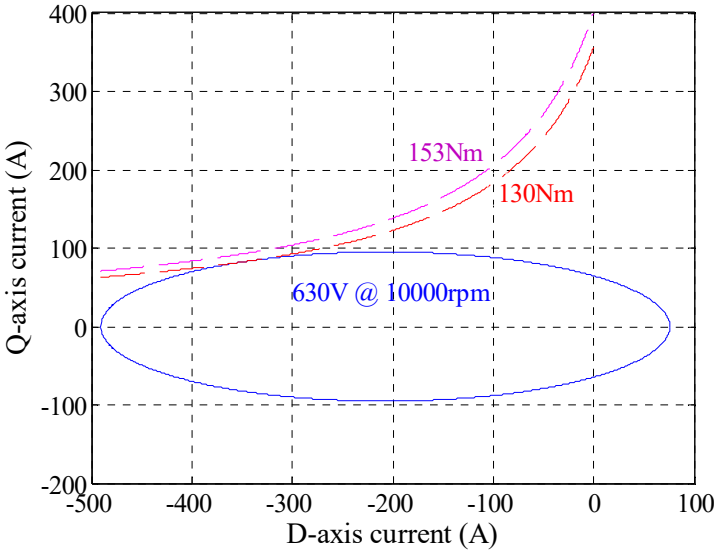

Fig. 6-26. Torque and power production in full speed range of 48-slot 8-pole machine with spoke type rotor. (a) Peak and continuous envelope on torque-speed plane. (b) Torque profile and voltage ellipse on *d*- and *q*-axis currents plane.

6.3.3 48-slot 8-pole Machine with Double Layer V Shape Rotor

The double layer V shape magnet topology is introduced to enhance the flux focusing effect, in order to improve the alignment torque contributed by the interaction of PM magnetic field with the armature current.

The design and optimisation flow of the 48-slot 8-pole machine with double layer V shape rotor is similar to the 48-slot 8-pole machine with spoke type rotor counterpart. Therefore, only the process pertinent to the 48-slot 8-pole machine design is described in this section.

The mechanical stress model of each layer of this V shape rotor topology shown in Fig. 6-18 (b) can be expressed by (6.4) and (6.5). The only difference is that the equivalent mass in the bottom layer should include both the upper layer and also the bottom layer irons and magnets.

The parameters to be optimised in 48-slot 8-pole machine with V shape rotor include split ratio, pole arc, pole depth ratio, magnet thickness, tooth

width, back-iron thickness, and NO. of turns per coil, which are illustrated in Fig. 6-27 and Table 6-18.

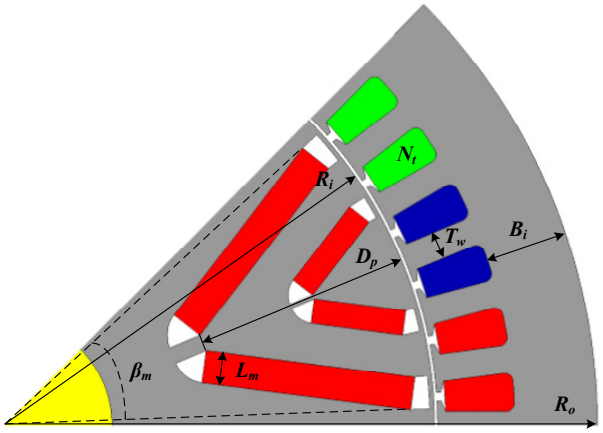

Fig. 6-27. Illustration of the parameters to be optimised for 48-slot 8-pole machine with V shape rotor.

Table 6-18. Parameter Ranges for the Optimisation of 48-slot 8-pole Machine with V shape Rotor

Parameter	Description	Unit	Range
K_s	Split ratio		0.65~0.75
K_p	Pole depth ratio		0.35~0.55
β_p	Pole arc in electrical degree	°	140°~170°
L_m	Magnet thickness	mm	4~9
T_w	Stator tooth width	mm	5~8
B_i	Stator back-iron thickness	mm	12~22
N_t	NO. of turns per coil		2,3,4

The optimisation objective and constraints are the same as the machine with spoke type rotor, as listed in Table 6-14. The optimisation trends of the design parameters are shown in Fig. 6-28 (a)~(g), and that of the optimisation objective, viz. the rated efficiency, is shown in Fig. 6-28 (h).

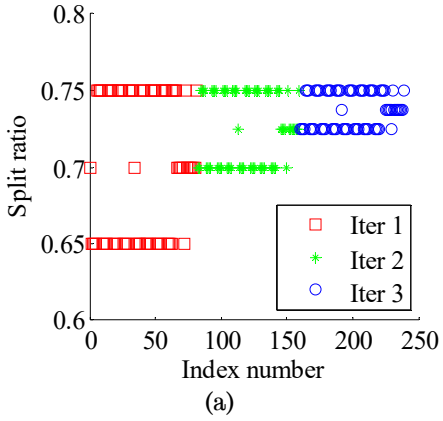

(a)

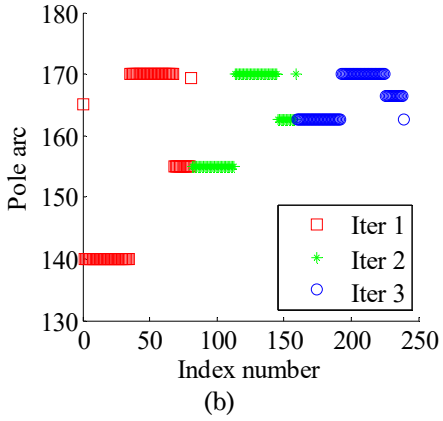

(b)

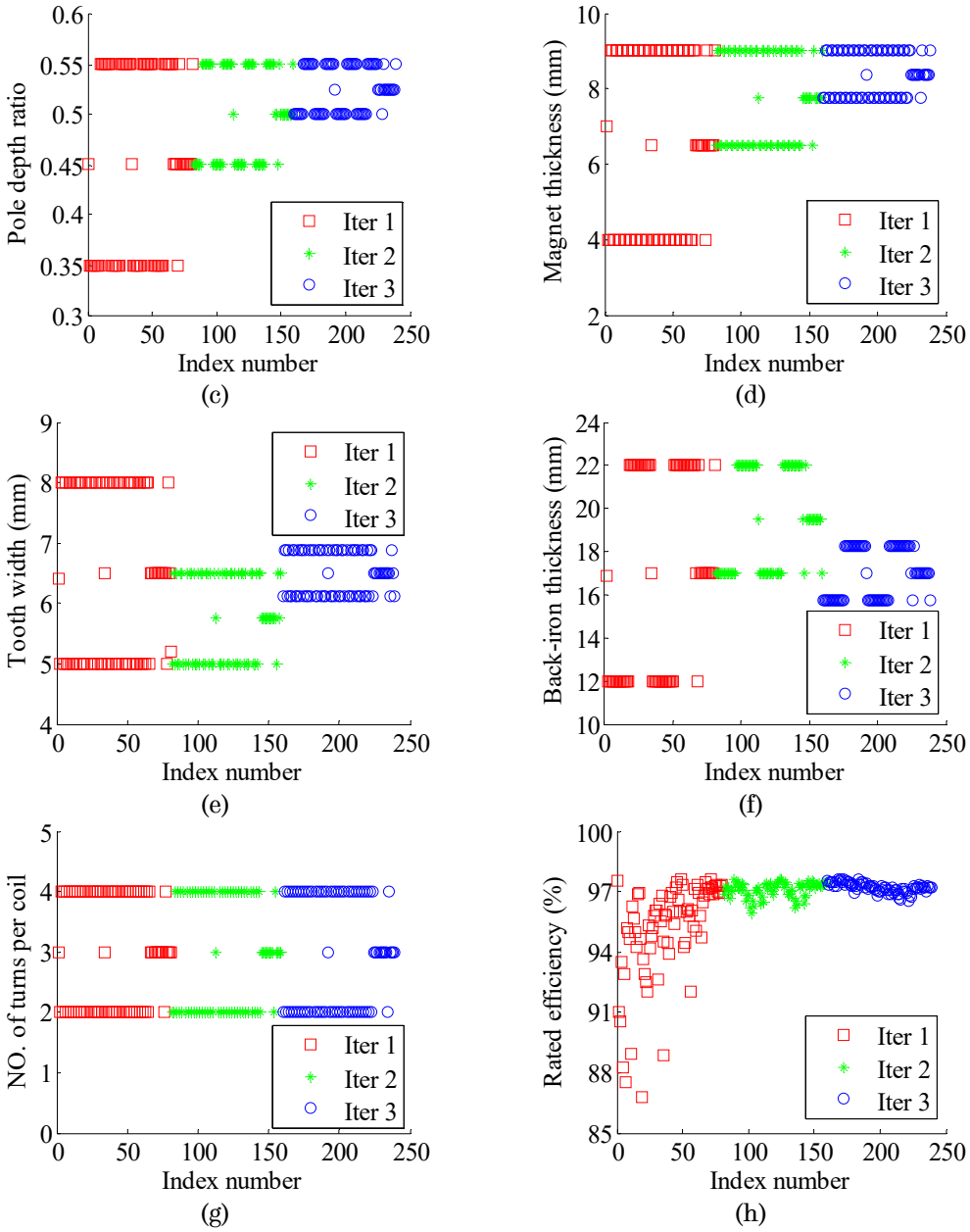

Fig. 6-28. Optimisation trends for 48-slot 8-pole machine with V shape rotor. (a) Split ratio. (b) Pole arc. (c) Pole depth ratio. (d) Magnet thickness. (e) Tooth width. (f) Back-iron thickness. (g) NO. of turns per coil. (h) Rated efficiency.

Due to the high torque production of this machine topology, many samples in Fig. 6-28 can satisfy all of the constraints and meanwhile exhibit similarly good efficiency. Thereby, one sample with the lowest peak current is selected as the optimisation result to cater for the reduction in inverter cost. The optimisation result is shown in Fig. 6-29 and Table 6-19.

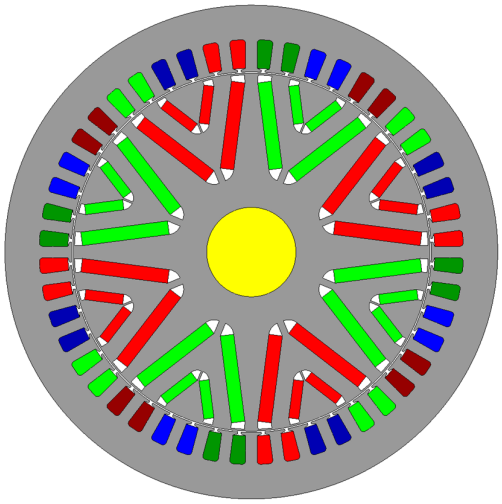

Fig. 6-29. Optimised geometry of 48-slot 8-pole machine with V shape rotor.

Table 6-19. Optimised Parameters of 48-slot 8-pole Machine with V Shape Rotor

Parameter	Description	Unit	Value
K_s	Split ratio		0.725
K_p	Pole depth ratio		0.5
β_p	Pole arc in electrical degree	°	162.6°
L_m	Magnet thickness	mm	7.75
T_w	Stator tooth width	mm	6.5
B_i	Stator back-iron thickness	mm	19.5
N_t	NO. of turns per coil		3

The mechanical stress analysis in FEA is performed before the electromagnetic performance evaluation of the optimised design. Fig. 6-30 illustrates the von Mises stress contour of the optimised 48-slot 8-pole machine with double layer V shape rotor. It can be seen that the maximum stress, occurring at the middle bridge of the bottom layer, reaches 450.7MPa, slight higher than the M270-35A yield strength 450MPa.

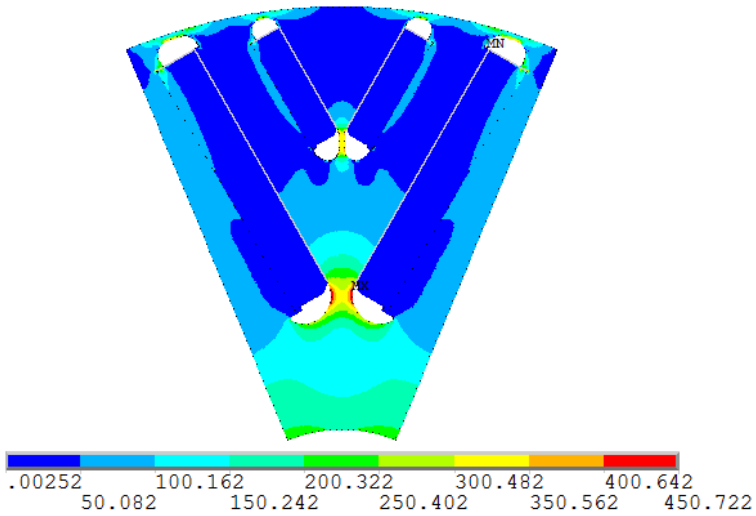

Fig. 6-30. von Mises stress contours of the optimised 48-slot 8-pole machine with V shape rotor.

Subsequently, the electromagnetic performances are evaluated via FEA, as listed in Table 6-20. The torque and power production capability in full speed range can be found in Fig. 6-31.

It can be noticed that all the optimisation constraints shown in Table 6-14 are satisfied, and the peak power at maximum operating speed can reach the required 160kW. It is evident that the V shape topology exhibits better field weakening capability than the spoke type counterpart. This is because that the characteristic current (PM flux-linkage divided by *d*-axis inductance) of the V shape topology is increased as a result of the increase in the PM flux-linkage and becomes close to the peak *d*-axis current. In other words, the V shape topology machine can have a wider constant-power region compared to the spoke type one.

Therefore, the double layer V shape configuration is selected as the rotor topology for this application. The demagnetisation analysis in the following sections is performed only for the 48-slot 8-pole machine with double layer V shape rotor.

Table 6-20. Performance of the Optimised 48-slot 8-pole Machine with V Shape Rotor

Description	Item	Unit	Value
Dimension	Active length	mm	170
	Stator outer diameter	mm	280
	Stator inner diameter	mm	204.5
Design parameters	PM mass	kg	6.96
	Slot fill factor		0.45
	Phase resistance @ 120°C	Ohm	0.016
	d-axis inductance @ rated torque	mH	0.304
	q-axis inductance @ rated torque	mH	1.002
Performance @ peak torque	Torque	Nm	401.7
	Current (RMS)	A	291.8
	Current density (RMS)	A/mm^2	14.3
	Line-to-line voltage @3820r/min	V	665.1
	Power factor		0.78
	Reluctance torque contribution	%	68.7%
	Torque ripple	%	37.1%
	Copper loss	W	4053
	Stator iron loss	W	925
	Rotor iron loss	W	313
	Efficiency	%	96.8%
Performance @ rated torque	Torque	Nm	271.1
	Current (RMS)	A	202.4
	Current density (RMS)	A/mm^2	9.9
	Power factor		0.82
	Reluctance torque contribution	%	63.0%
	Torque ripple	%	23.1%
	Copper loss	W	1948
	Stator iron loss	W	813
	Rotor iron loss	W	277
	Efficiency	%	97.4%
No-load	Line-to-line back-EMF @12,000r/min	V	753

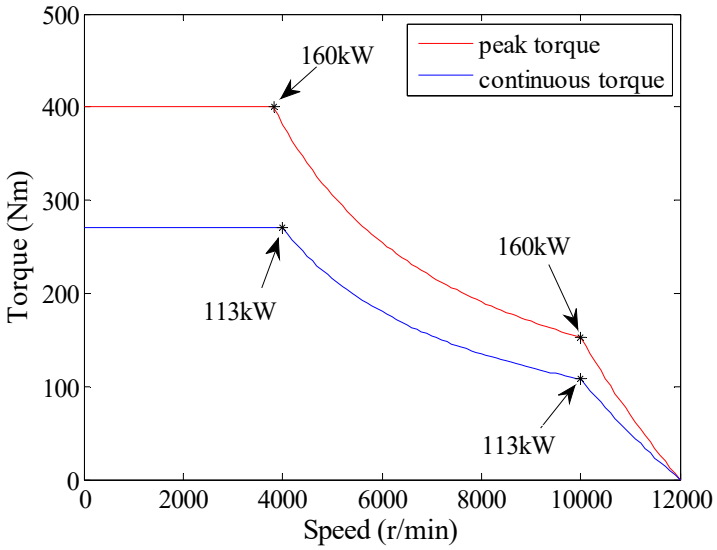

Fig. 6-31. Peak and continuous envelopes on torque-speed plane of 48-slot 8-pole machine with V shape rotor.

6.3.4 Demagnetisation Analysis

The demagnetisation curve of the ferrite NMF-12F used in these two machines is shown in Fig. 6-32. The knee points at 100°C and -20°C are approximately -0.12T and 0.1T respectively.

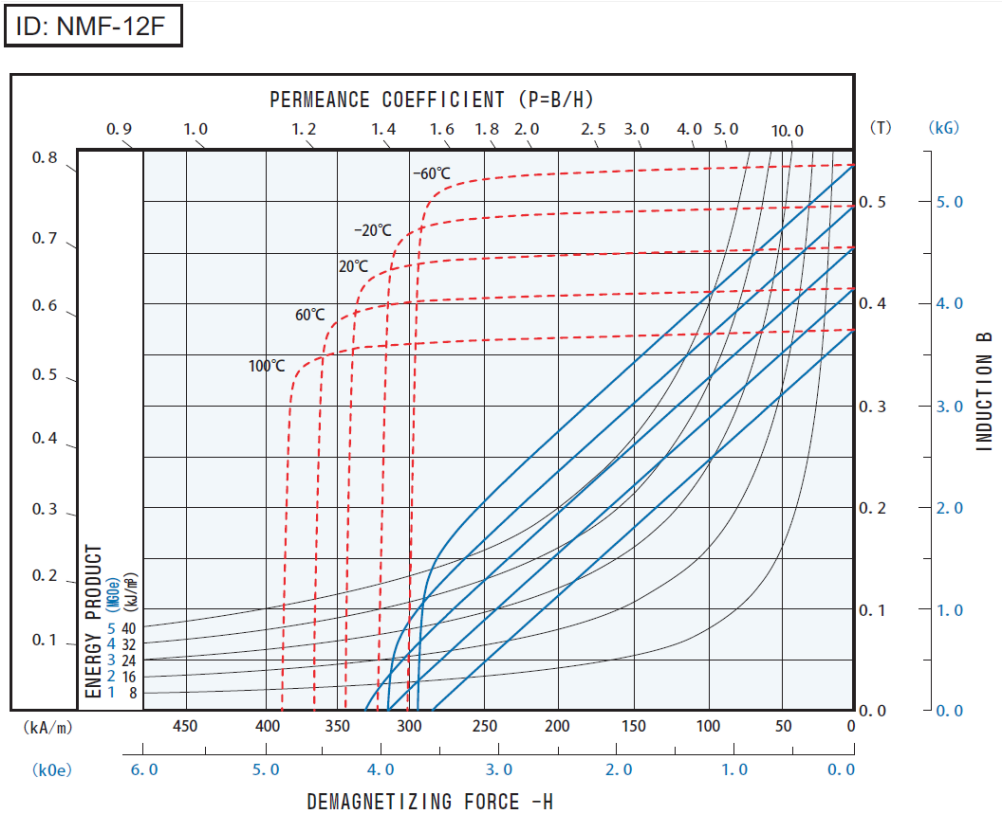

Fig. 6-32. Demagnetisation curve of the ferrite NMF-12F.

The current trajectory of the peak power envelope on the *d*- and *q*-axis current plane for the 48-slot 8-pole design with the V shape rotor is shown in Fig. 6-33. It can be seen that the worst case scenario for the demagnetisation is the peak torque and base speed working point where the *d*-axis current reaches its peak.

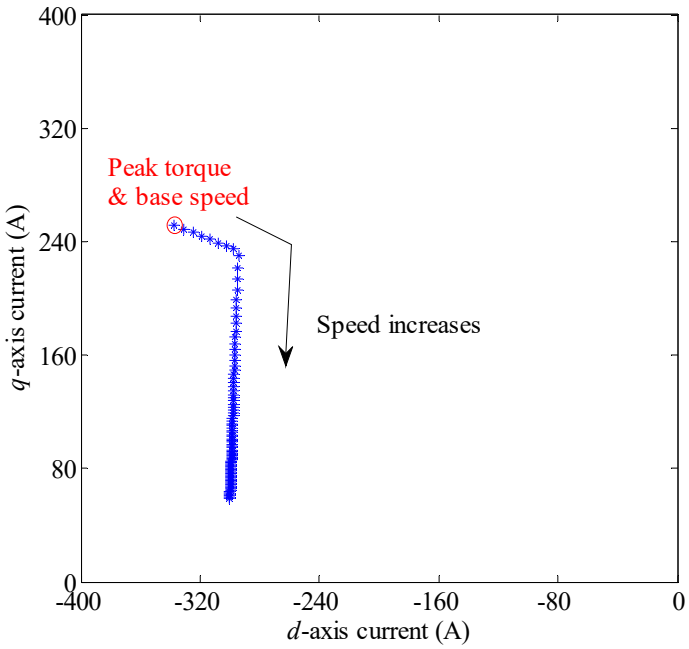

Fig. 6-33. Peak power envelope current trajectory of 48-slot 8-pole machine with V shape rotor.

Therefore, the demagnetisation analysis is performed at the peak torque and base speed working point for both 100°C and -20°C operation conditions. The instantaneous flux density waveforms in magnetisation direction for magnet corners at 100°C are shown in Fig. 6-34 (a). There are 4 magnets in one pole and 4 corners are checked for each magnet. Thereby, 16 curves are presented, in which the lowest flux density point represents the worst case for demagnetisation. Subsequently, the flux density contour in magnet magnetisation direction at the worst case rotor position is shown in Fig. 6-34 (b). It can be seen that no magnet area has the flux density lower than the knee point -0.12T. Therefore, no demagnetisation occurs at 100°C.

Similarly, the demagnetisation analysis results at -20°C are shown in Fig. 6-35. The magnet area where the flux density is lower than the knee point 0.1T (at -20°C) is approximately 0.25% of the total magnet areas. Therefore, the demagnetisation at -20°C is negligible.

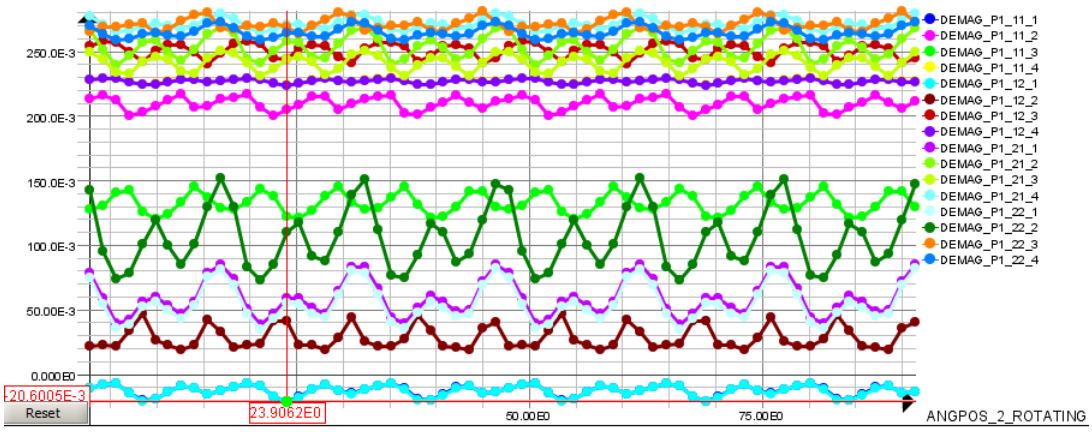

(a)

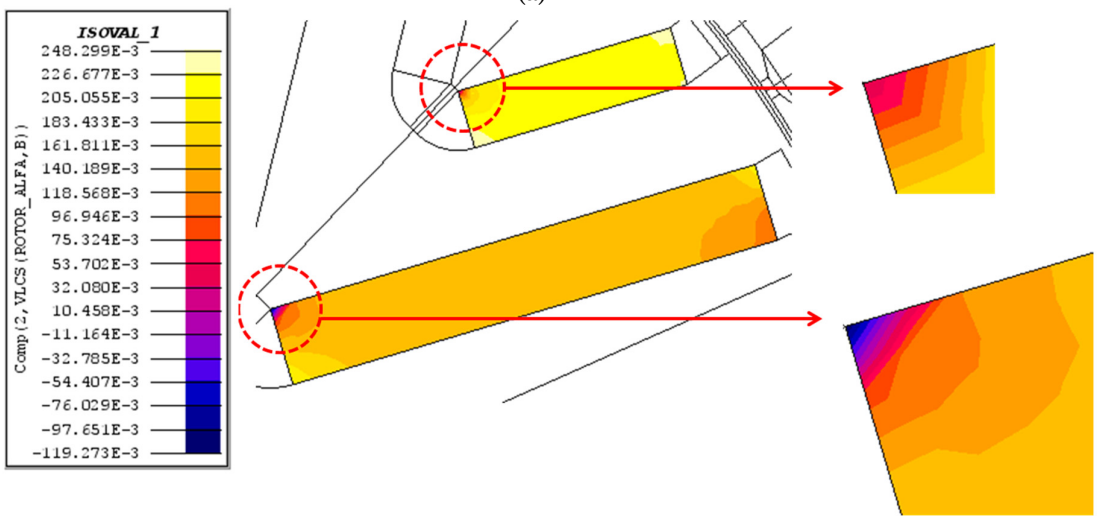

(b)

Fig. 6-34. Demagnetisation analysis results of 48-slot 8-pole machine with V shape rotor at 100°C. (a) Instantaneous flux density waveforms in magnetisation direction for magnet corners. (b) Flux density contour in magnetisation direction at worst case rotor position.

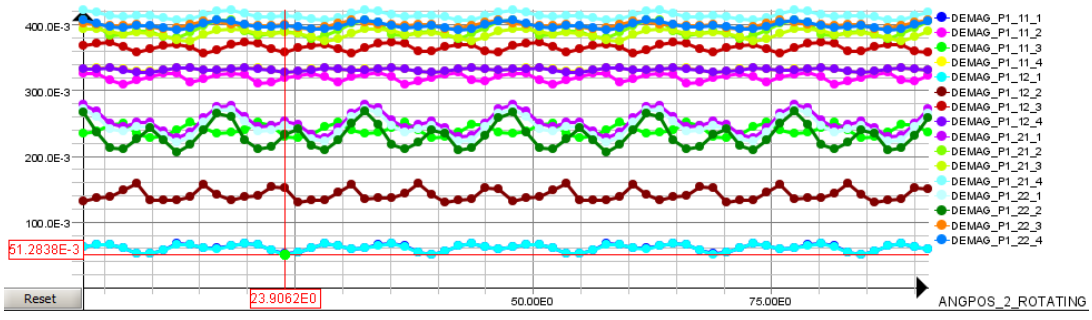

(a)

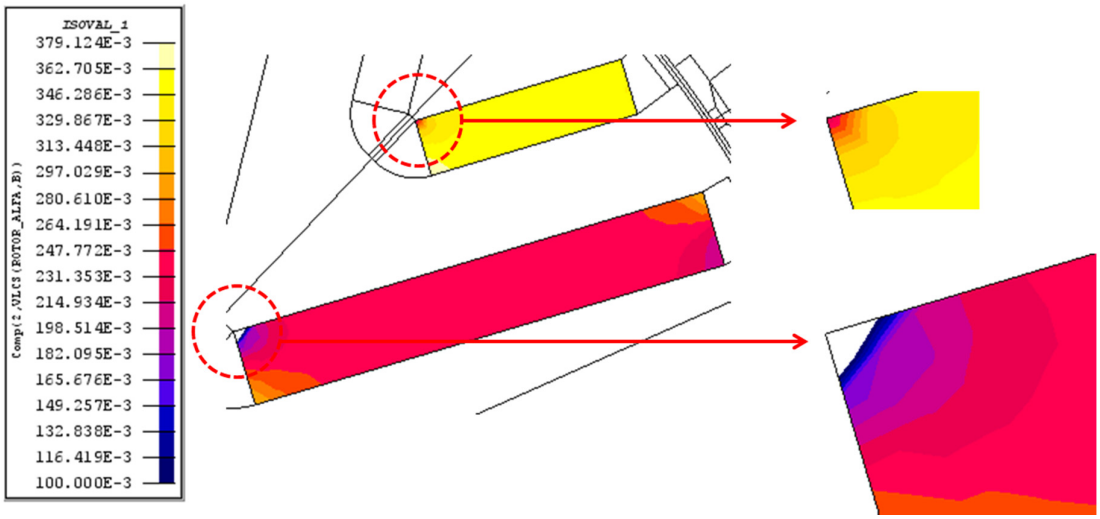

(b)

Fig. 6-35. Demagnetisation analysis results of 48-slot 8-pole machine with V shape rotor at -20°C. (a) Instantaneous flux density waveforms in magnetisation direction for magnet corners. (b) Flux density contour at worst case rotor position.

6.4 Conclusion

To take the mechanical strength constraint into account in the machine global optimisation process, an analytical mechanical stress model is proposed by defining the equivalent mass which has to be supported by rotor bridges. Subsequently, a global optimisation incorporating mechanical strength constraints can be achieved. Thus, unfeasible designs whose mechanical strength cannot meet requirement can be avoided. Moreover, the final design will be closer to the true optimum compared to the optimisation without considering mechanical strength constraints, since the optimisation trends are affected by mechanical strength constraints.

This mechanical stress model needs to be modified before applying to other interior magnet rotor topologies. However, the principle using the equivalent mass supported by the bridges to build the polynomial functions of the mechanical stress model is generic.

The 48-slot 8-pole machine with double layer V shape rotor exhibits better field weakening capability than that with spoke type. This is because in the machine with V shape rotor has a flux focusing effect, and consequently, the PM flux-linkage is increased. The resultant characteristic current of the

machine is also increased, being closer to the peak *d*-axis current. Therefore, the machine with the V shape topology machine in this design has a wider constant-power region compared to the spoke type one. It should be noted that this conclusion may be specific to the machine under consideration. However, it can be concluded that a better field weakening capability can be achieved when the total *d*-axis flux-linkage under peak operating conditions at high speeds is closer to zero.

CHAPTER 7 Conclusion

7.1 Conclusions

This thesis investigates several aspects of modelling and design of PM machines for EV traction applications, including the influence of vehicle dynamics on machine design, PMA-SynRM with fractional-slot winding configurations, reluctance torque evaluation based on frozen permeability concept, generic approach to MMF harmonics reduction using multiple 3-phase concentrated winding configurations, high-fidelity and computationally efficient machine model and also electro-thermally coupled model, and machine global optimisation incorporating mechanical strength constraints.

Regarding the influence of vehicle dynamics on machine design, it is concluded that the tyre slip leads to power loss and thus the size of electrical machine needs to be increased by up to 10% compared to conventional machine sizing process neglecting tyre slip effects. Compared to the concentrated powertrain topology with a single machine drive, the distributed counterpart can reduce the extra power loss incurred in the tyre slip, and thereby save the power consumption and also improve the efficiency of the whole system. In a distributed powertrain topology, the torque split ratio between the front and rear wheels can affect both the machine size and the system efficiency because the tyre slip is dependent on the traction torque of each wheel. An optimum torque split ratio exists to minimise the total size of electrical machines. This optimum torque split ratio is subject to both the location of the vehicle centre of gravity and the vehicle acceleration, and the relationship between them is approximately linear when the influence of the motor efficiency is not considered. The optimum control for the torque split ratio can be realised with a real-time calculation according to the vehicle acceleration. For the powertrain topology with one motor in the front and two in the rear, overtaking at a high speed would be the most dangerous operation if one of the rear motors

fails suddenly. Among the distributed powertrain topologies, the 4-wheel drive option with each motor contributing 25% of the total torque can leave more reaction time for the driver than that of 3-motor powertrain topology and 2-rear motor powertrain topology when the failure occurs suddenly at one motor drive system. For the 4-wheel distributed power train, the failure at the front motor will result in a more serious consequence than that at the rear when the toque split ratio for the front and rear motors is 50%:50%.

Concerning PMA-SynRM with fractional-slot winding configurations, it is found that PMA-SynRM with fractional-slot concentrated non-overlapping winding (12-slot 10-pole) has advantages such as short end-winding, high copper packing factor, low manufacturing cost and the low torque ripple. However, it exhibits relatively high iron loss, low reluctance torque ratio and the low efficiency over NEDC. Therefore, this winding configuration is more suited for in-wheel motor application where the maximum speed is low and the disadvantage of high iron loss is less significant. PMA-SynRM with conventional fractional-slot non-overlapping winding (12-slot 8-pole) is of competitive energy efficiency, short end-winding, high copper packing factor, low manufacturing cost and the good field weakening capability. However, excessive torque ripple is a major issue of concern for EV traction applications. This problem needs to be addressed in future. PMA-SynRM with fractional-slot overlapping winding (18-slot 8-pole) has slightly longer end-winding and higher manufacturing cost compared with the other two candidate fractional-slot PMA-SynRM machines. However, it possesses high efficiency over a very wide operating region, low torque ripple, high reluctance torque ratio and the good field weakening capability, and thereby it is attractive for high speed and low torque ripple EV applications.

In terms of the reluctance evaluation, it shows that the classic models which assume that the PM flux-linkage is independent with *d*-axis current, can only match the average total torque but not the instantaneous torque waveform. However, the proposed model based on frozen permeability

concept can match both average and instantaneous torque very well with the direct FEA results. Therefore, a more accurate model which allows for separation of torque components via FP process for IPM machines is presented. The proposed model can reproduce the instantaneous torque waveform at any load condition, and hence provides a more accurate evaluation of reluctance torque compared to the conventional methods.

Regarding MMF harmonics reduction in PM machines, a generic approach using multiple 3-phase concentrated windings has been proposed. The MMF harmonic cancellation is achieved by employing multiple 3-phase windings and selecting appropriate phase shifts in both space and time. The proposed winding configuration cancels out all the MMF sub-harmonics and some high order MMF harmonics. The reduction in MMF harmonics leads to a number of benefits. Firstly it reduces both stator and rotor iron losses, particularly at high speeds, and hence, prevents excessive rotor temperature. Furthermore it improves reluctance torque capability of IPM machines with concentrated windings, and machine efficiency. In addition, the technique also reduces torque ripple since the torque ripples associated with a specific set of harmonics may be cancelled in a multiple 3-phase machine.

A 9-phase 18-slot 14-pole machine is devised based on the proposed generic MMF harmonic reduction technique. To drive this machine, a 9-phase inverter needs to be employed. This 9-phase inverter should be configured as three 3-phase inverters with standard modules, and each 3-phase inverter may be controlled based on conventional field oriented control technique. It should be noted that although the need for multiple 3-phase inverters for the proposed winding configuration might be seen as a disadvantage, the total inverter VA rating is the same as that of a 3-phase machine since the current rating of one 3-phase inverter is proportionally reduced. The use of three 3-phase inverters with low current rating spreads the inverter loss and is conducive to cooling and integration of the inverter into the machine. It also contributes to a degree of fault tolerance in that the

machine can continue to operate even if one set of 3-phase winding/drive fails. This is valuable and significant for machines in EV traction application where the safety requirement of the powertrain system is relatively high. Moreover, the torque ripple can be dramatically reduced without skew techniques in that certain torque ripple harmonics can be completely cancelled out. Therefore, it is worthwhile and advantageous to develop multiple 3-phase winding configurations for electrical machines in EV traction applications.

Compared to the MMF harmonic reduction techniques in literature, the proposed machine topology in this thesis retains the advantages of the concentrated windings and exhibits a high winding factor, low torque ripple, low manufacture cost, high torque density and the high efficiency over wide torque and speed ranges. The proposed MMF harmonics reduction technique is also applicable to other slot-pole combinations with concentrated windings except for those with slot number being equal to 1.5 times the pole number.

A high-fidelity, computationally efficient model for IPM machines has been proposed in this thesis. The model captures all significant effects associated with the electromagnetic behaviour of the machines, including magnetic saturation, spatial harmonics, iron loss effect and temperature effects, and has been validated by both FEA and experiments. The proposed model provides an accurate means of assessing the drive performance of an IPM machine. It has been shown that torque ripple may increase significantly in the field weakening region due to current waveform distortions resulting from the inverter voltage limit. It is important to capture these adverse effects in drive system simulations in order to develop a robust control for high efficiency operations in both constant-torque and field weakening regions.

By taking into account of the temperature effects on both the *d*- and *q*-axis flux-linkages and the torque, the proposed machine model allows for

accurate prediction of the electromagnetic behaviour at any feasible given temperature. This model is conducive to developing correct MTPA control strategy for IPMs when temperature varies. A high-fidelity, computationally efficient electro-thermally coupled model has been subsequently established by integrating the proposed temperature-dependent, high-fidelity electromagnetic model with a state-space lumped parameter thermal model. The proposed electro-thermally coupled model provides a useful platform to assess the temperature effect on electromagnetic behaviour of IPMs during design and over driving cycles. It has been shown through simulation studies at the rated torque and over Artemis urban driving cycle operations that by neglecting temperature effects, the winding and magnet temperatures can be under-estimated by approximately 20°C. Even if the temperature effect on the winding resistance is considered, the predicted temperatures can still be under-estimated by approximately 10°C. Under-estimate of temperatures in magnets and windings pose a serious risk of irreversible demagnetisation and reduction of machine lifetime. It has also been shown that, in field weakening region, neglect of temperature effect on magnets leads to less significant under-estimate of magnet and winding temperatures since the increase in q-axis current and decrease in d-axis current when PM field is reduced at high temperature tends to have some cancellation effect.

To take the mechanical strength constraint into account in the machine global optimisation process, an analytical mechanical stress model has been proposed by defining the equivalent mass supported by rotor bridges. Subsequently, a global optimisation incorporating mechanical strength constraints is achieved. Thus, unfeasible designs whose mechanical strength cannot meet the requirement can be avoided. Moreover, the final design will be closer to the true optimum compared to the optimisation without considering mechanical strength constraints, since the optimisation trends are affected by mechanical strength constraints.

7.2 Future work

PMA-SynRM with conventional fractional-slot non-overlapping winding (12-slot 8-pole) exhibits high reluctance torque production and thus high efficiency, retaining all the advantages of concentrated windings. However, its significant torque ripple is a major issue of concern for EV traction applications. Therefore, if the torque ripple problem can be addressed without comprising machine performance, this machine topology will be more preferable for EV traction applications.

Although the proposed MMF harmonic reduction technique in this thesis can eliminate all the sub-harmonics and some of high order harmonics of the MMF of a fractional-slot concentrated winding configuration, the backward MMF harmonic whose order is very close to the order of working harmonic cannot be reduced by the proposed technique. To further reduce rotor iron loss and improve reluctance torque production, the future work on the MMF harmonic reduction aspect is to reduce this backward MMF harmonic without comprising advantages of concentrated windings.

Due to the lack of a 9-phase inverter, the 9-phase 18-slot 14-pole IPM machine prototype is only tested in generating mode. When the 9-phase inverter is available in future, the machine performance in driving mode should be tested. Moreover, its efficiency map should also be measured. Furthermore, the future work on testing may include the single 3-phase or two 3-phase operations which indicate the fault tolerant capability of this machine.

To simplify the mechanical stress model and meanwhile maintain the model fidelity, the maximum mechanical stresses are modelled as functions of bridge thicknesses and the equivalent mass density in this thesis. In other words, the proposed mechanical stress model neglects the influence of individual rotor parameters on the maximum mechanical stress. This results in an additional error in the maximum mechanical stress prediction. To

reduce this error, a much more complex model needs to be developed by considering the influence of all individual rotor parameters on the maximum mechanical stress. This should be subject to future work.

REFERENCES

[1] C. C. Chan, "The State of the Art of Electric, Hybrid, and Fuel Cell Vehicles," *Proceedings of the IEEE,* vol. 95, pp. 704-718, 2007.

[2] Z. Q. Zhu and D. Howe, "Electrical Machines and Drives for Electric, Hybrid, and Fuel Cell Vehicles," *Proceedings of the IEEE,* vol. 95, pp. 746-765, 2007.

[3] K. T. Chau, C. C. Chan, and L. Chunhua, "Overview of Permanent-Magnet Brushless Drives for Electric and Hybrid Electric Vehicles," *Industrial Electronics, IEEE Transactions on,* vol. 55, pp. 2246-2257, 2008.

[4] X. Wei, Z. Jianguo, G. Youguang, W. Shuhong, W. Yi, and S. Zhanghai, "Survey on electrical machines in electrical vehicles," in *Applied Superconductivity and Electromagnetic Devices, 2009. ASEMD 2009. International Conference on*, 2009, pp. 167-170.

[5] T. J. Woolmer and M. D. McCulloch, "Axial flux permanent magnet machines: A new topology for high performance applications," in *Hybrid Vehicle Conference, IET The Institution of Engineering and Technology, 2006*, 2006, pp. 27-42.

[6] YASA-Motors. (2015). *YASA Motors axial flux machines*. Available: http://www.yasamotors.com/products

[7] M. U. Lamperth, A. Beaudet, and M. Jaensch, "Disc Motors for Automotive Applications," in *Hybrid and Eco-Friendly Vehicle Conference, 2008. IET HEVC 2008*, 2008, pp. 1-5.

[8] GKN-EVO. (2015). *GKN-EVO axial flux machines* Available: http://www.evo-electric.com

[9] S. Lie and C. Di Pietro, "Copper die-cast rotor efficiency improvement and economic consideration," *Energy Conversion, IEEE Transactions on,* vol. 10, pp. 419-424, 1995.

[10] J. Malinowski, J. McCormick, and K. Dunn, "Advances in construction techniques of AC induction motors: preparation for super-premium efficiency levels," *Industry Applications, IEEE Transactions on,* vol. 40, pp. 1665-1670, 2004.

[11] A. Boglietti, A. Cavagnino, L. Feraris, and M. Lazzari, "Energy-efficient motors," *Industrial Electronics Magazine, IEEE,* vol. 2, pp. 32-37, 2008.

[12] R. E. Araujo, G. Ribeiro, R. P. de Castro, and H. S. Oliveira, "Experimental evaluation of a loss-minimization control of induction motors used in EV," in *Industrial Electronics, 2008. IECON 2008. 34th Annual Conference of IEEE*, 2008, pp. 1194-1199.

[13] A. Haddoun, M. E. H. Benbouzid, D. Diallo, R. Abdessemed, J. Ghouili, and K. Srairi, "A Loss-Minimization DTC Scheme for EV Induction Motors," *Vehicular Technology, IEEE Transactions on,* vol. 56, pp. 81-88, 2007.

[14] A. Haddoun, M. E. H. Benbouzid, D. Diallo, R. Abdessemed, J. Ghouili, and K. Srairi, "Comparative Analysis of Control Techniques for Efficiency Improvement in Electric

Vehicles," in *Vehicle Power and Propulsion Conference, 2007. VPPC 2007. IEEE*, 2007, pp. 629-634.

[15] E. Hussein and P. Mutschler, "Improving the efficiency for speed sensorless indirect field oriented control induction motor," in *Power Electronics and Motion Control Conference (EPE/PEMC), 2010 14th International*, 2010, pp. T5-136-T5-141.

[16] E. S. Sergaki, "Motor flux minimization controller based on fuzzy logic control for DTC AC drives," in *Electrical Machines (ICEM), 2010 XIX International Conference on*, 2010, pp. 1-6.

[17] A. Scarmin, C. L. Gnoatto, E. L. Aguiar, H. T. Camara, and E. G. Carati, "Hybrid Adaptive Efficiency Control technique for energy optimization in induction motor drives," in *Industry Applications (INDUSCON), 2010 9th IEEE/IAS International Conference on*, 2010, pp. 1-6.

[18] E. J. Ryan and C. K. Narayan, "Efficiency Improvements from an Electric Vehicle Induction Motor Drive, with Augmentations to a PI Control," in *Electrical and Computer Engineering, 2006. CCECE '06. Canadian Conference on*, 2006, pp. 1228-1231.

[19] A. Chiba, Y. Takano, M. Takeno, T. Imakawa, N. Hoshi, M. Takemoto*, et al.*, "Torque Density and Efficiency Improvements of a Switched Reluctance Motor Without Rare-Earth Material for Hybrid Vehicles," *Industry Applications, IEEE Transactions on,* vol. 47, pp. 1240-1246, 2011.

[20] A. Chiba, K. Kiyota, N. Hoshi, M. Takemoto, and S. Ogasawara, "Development of a Rare-Earth-Free SR Motor With High Torque Density for Hybrid Vehicles," *Energy Conversion, IEEE Transactions on,* vol. 30, pp. 175-182, 2015.

[21] A. Chiba and K. Kiyota, "Review of research and development of switched reluctance motor for hybrid electrical vehicle," in *Electrical Machines Design, Control and Diagnosis (WEMDCD), 2015 IEEE Workshop on*, 2015, pp. 127-131.

[22] Y. Ozoglu, M. Garip, and E. Mese, "New pole tip shapes mitigating torque ripple in short pitched and fully pitched switched reluctance motors," in *Industry Applications Conference, 2002. 37th IAS Annual Meeting. Conference Record of the*, 2002, pp. 43-50 vol.1.

[23] T. Higuchi, T. Ueda, and T. Abe, "Torque ripple reduction control of a novel segment type SRM with 2-steps slide rotor," in *Power Electronics Conference (IPEC), 2010 International*, 2010, pp. 2175-2180.

[24] F. Sahin, H. B. Ertan, and K. Leblebicioglu, "Optimum geometry for torque ripple minimization of switched reluctance motors," *Energy Conversion, IEEE Transactions on,* vol. 15, pp. 30-39, 2000.

[25] M. Divandari and A. Dadpour, "Radial force and torque ripple optimization for acoustic noise reduction of SRM drives via fuzzy logic control," in *Industry*

Applications (INDUSCON), 2010 9th IEEE/IAS International Conference on, 2010, pp. 1-6.

[26] Z. Zhang, C. Cai, and W. Liu, "Study on reduction of running noise from a switched reluctance motor," in *Computer Science and Education (ICCSE), 2010 5th International Conference on*, 2010, pp. 1204-1027.

[27] H. Ishikawa, D. Wang, and H. Naitoh, "A new switched reluctance motor drive circuit for torque ripple reduction," in *Power Conversion Conference, 2002. PCC Osaka 2002. Proceedings of the*, 2002, pp. 683-688 vol.2.

[28] A. Hofmann, M. Harries, E. Weißenborn, and R. W. De Doncker, "Making the acoustic case for hysteresis control in switched reluctance machines," in *Power Electronics, Machines and Drives (PEMD 2014), 7th IET International Conference on*, 2014, pp. 1-6.

[29] A. Hofmann, F. Qi, and R. W. De Doncker, "Developing the concept for an automotive high-speed SRM drive with focus on acoustics," in *Power Electronics, Machines and Drives (PEMD 2014), 7th IET International Conference on*, 2014, pp. 1-5.

[30] G. Brown, "Developing Synchronous Reluctance Motors For Variable Speed Operation," in *Power Electronics, Machines and Drives (PEMD 2012), IET International Conference on*, 2012.

[31] A. Fratta, G. P. Troglia, A. Vagati, and F. Villata, "Evaluation of torque ripple in high performance synchronous reluctance machines," in *Industry Applications Society Annual Meeting, 1993., Conference Record of the 1993 IEEE*, 1993, pp. 163-170 vol.1.

[32] A. Vagati, "Synchronous reluctance electrical motor having a low torque-ripple design," US Patent US5818140 A, 1998.

[33] A. Vagati, M. Pastorelli, G. Francheschini, and S. C. Petrache, "Design of low-torque-ripple synchronous reluctance motors," *Industry Applications, IEEE Transactions on,* vol. 34, pp. 758-765, 1998.

[34] M. Sanada, K. Hiramoto, S. Morimoto, and Y. Takeda, "Torque ripple improvement for synchronous reluctance motor using an asymmetric flux barrier arrangement," *Industry Applications, IEEE Transactions on,* vol. 40, pp. 1076-1082, 2004.

[35] N. Bianchi, S. Bolognani, D. Bon, and M. Dai Pre, "Torque Harmonic Compensation in a Synchronous Reluctance Motor," *Energy Conversion, IEEE Transactions on,* vol. 23, pp. 466-473, 2008.

[36] N. Bianchi, S. Bolognani, D. Bon, and M. Dai Pre, "Rotor Flux-Barrier Design for Torque Ripple Reduction in Synchronous Reluctance and PM-Assisted Synchronous Reluctance Motors," *Industry Applications, IEEE Transactions on,* vol. 45, pp. 921-928, 2009.

[37] T. Lange, B. Kerdsup, C. Weiss, and R. W. De Doncker, "Torque ripple reduction in Reluctance Synchronous Machines using an asymmetric rotor structure," in *Power*

Electronics, Machines and Drives (PEMD 2014), 7th IET International Conference on, 2014, pp. 1-5.

[38] T. A. Lipo, "Synchronous reluctance machines-a viable alternative for ac drives?," *Electric Machines and Power Systems,* vol. 19, pp. 659-671, 1991.

[39] R. R. Moghaddam, F. Magnussen, and C. Sadarangani, "Theoretical and Experimental Reevaluation of Synchronous Reluctance Machine," *Industrial Electronics, IEEE Transactions on,* vol. 57, pp. 6-13, 2010.

[40] T. Matsuo and T. A. Lipo, "Rotor design optimization of synchronous reluctance machine," *Energy Conversion, IEEE Transactions on,* vol. 9, pp. 359-365, 1994.

[41] F. Magnussen, P. Thelin, and C. Sadarangani, "Performance evaluation of permanent magnet synchronous machines with concentrated and distributed windings including the effect of field-weakening," in *Power Electronics, Machines and Drives, 2004. (PEMD 2004). Second International Conference on (Conf. Publ. No. 498)*, 2004, pp. 679-685 Vol.2.

[42] A. M. El-Refaie and T. M. Jahns, "Optimal flux weakening in surface PM machines using fractional-slot concentrated windings," *Industry Applications, IEEE Transactions on,* vol. 41, pp. 790-800, 2005.

[43] A. M. El-Refaie and T. M. Jahns, "Scalability of surface PM Machines with concentrated windings designed to achieve wide speed ranges of constant-power operation," *Energy Conversion, IEEE Transactions on,* vol. 21, pp. 362-369, 2006.

[44] J. Cros and P. Viarouge, "Synthesis of high performance PM motors with concentrated windings," *Energy Conversion, IEEE Transactions on,* vol. 17, pp. 248-253, 2002.

[45] N. Bianchi and E. Fornasiero, "Impact of MMF Space Harmonic on Rotor Losses in Fractional-Slot Permanent-Magnet Machines," *Energy Conversion, IEEE Transactions on,* vol. 24, pp. 323-328, 2009.

[46] K. Atallah, D. Howe, P. H. Mellor, and D. A. Stone, "Rotor loss in permanent-magnet brushless AC machines," *Industry Applications, IEEE Transactions on,* vol. 36, pp. 1612-1618, 2000.

[47] W. Jiabin, K. Atallah, R. Chin, W. M. Arshad, and H. Lendenmann, "Rotor Eddy-Current Loss in Permanent-Magnet Brushless AC Machines," *Magnetics, IEEE Transactions on,* vol. 46, pp. 2701-2707, 2010.

[48] K. Yamazaki and Y. Fukushima, "Effect of Eddy-Current Loss Reduction by Magnet Segmentation in Synchronous Motors With Concentrated Windings," *Industry Applications, IEEE Transactions on,* vol. 47, pp. 779-788, 2011.

[49] J. D. Ede, K. Atallah, G. W. Jewell, J. B. Wang, and D. Howe, "Effect of Axial Segmentation of Permanent Magnets on Rotor Loss in Modular Permanent-Magnet

Brushless Machines," *Industry Applications, IEEE Transactions on,* vol. 43, pp. 1207-1213, 2007.

[50] G. Dajaku and D. Gerling, "A Novel 24-Slots/10-Poles Winding Topology for Electric Machines," in *Electric Machines & Drives Conference (IEMDC), 2011 IEEE International*, 2011, pp. 65-70.

[51] W. Jiabin, V. I. Patel, and W. Weiya, "Fractional-Slot Permanent Magnet Brushless Machines with Low Space Harmonic Contents," *Magnetics, IEEE Transactions on,* vol. 50, pp. 1-9, 2014.

[52] T. M. Jahns, G. B. Kliman, and T. W. Neumann, "Interior Permanent-Magnet Synchronous Motors for Adjustable-Speed Drives," *Industry Applications, IEEE Transactions on,* vol. IA-22, pp. 738-747, 1986.

[53] A. Vagati, G. Pellegrino, and P. Guglielmi, "Comparison between SPM and IPM motor drives for EV application," in *Electrical Machines (ICEM), 2010 XIX International Conference on*, 2010, pp. 1-6.

[54] T. Finken, M. Hombitzer, and K. Hameyer, "Study and comparison of several permanent-magnet excited rotor types regarding their applicability in electric vehicles," in *Emobility - Electrical Power Train, 2010*, 2010, pp. 1-7.

[55] Z. Q. Zhu, Y. S. Chen, and D. Howe, "Iron loss in permanent-magnet brushless AC machines under maximum torque per ampere and flux weakening control," *Magnetics, IEEE Transactions on,* vol. 38, pp. 3285-3287, 2002.

[56] L. Chong, R. Dutta, N. Q. Dai, M. F. Rahman, and H. Lovatt, "Comparison of concentrated and distributed windings in an IPM machine for field weakening applications," in *Universities Power Engineering Conference (AUPEC), 2010 20th Australasian*, 2010, pp. 1-5.

[57] J. K. Tangudu and T. M. Jahns, "Comparison of interior PM machines with concentrated and distributed stator windings for traction applications," in *Vehicle Power and Propulsion Conference (VPPC), 2011 IEEE*, 2011, pp. 1-8.

[58] J. K. Tangudu, T. M. Jahns, and A. El-Refaie, "Core loss prediction using magnetic circuit model for fractional-slot concentrated-winding interior permanent magnet machines," in *Energy Conversion Congress and Exposition (ECCE), 2010 IEEE*, 2010, pp. 1004-1011.

[59] P. H. Mellor, R. Wrobel, and D. Holliday, "A computationally efficient iron loss model for brushless AC machines that caters for rated flux and field weakened operation," in *Electric Machines and Drives Conference, 2009. IEMDC '09. IEEE International*, 2009, pp. 490-494.

[60] M. Barcaro, N. Bianchi, and F. Magnussen, "Rotor Flux-Barrier Geometry Design to Reduce Stator Iron Losses in Synchronous IPM Motors Under FW Operations," *Industry Applications, IEEE Transactions on,* vol. 46, pp. 1950-1958, 2010.

[61] K. Yamazaki and H. Ishigami, "Rotor-Shape Optimization of Interior-Permanent-Magnet Motors to Reduce Harmonic Iron Losses," *Industrial Electronics, IEEE Transactions on,* vol. 57, pp. 61-69, 2010.

[62] V. Zivotic-Kukolj, W. L. Soong, and N. Ertugrul, "Iron Loss Reduction in an Interior PM Automotive Alternator," *Industry Applications, IEEE Transactions on,* vol. 42, pp. 1478-1486, 2006.

[63] H. Seok-Hee, W. L. Soong, and T. M. Jahns, "An Analytical Design Approach for Reducing Stator Iron Losses in Interior PM Synchronous Machines During Flux-Weakening Operation," in *Industry Applications Conference, 2007. 42nd IAS Annual Meeting. Conference Record of the 2007 IEEE*, 2007, pp. 103-110.

[64] H. Seok-Hee, W. L. Soong, T. M. Jahns, M. K. Guven, and M. S. Illindala, "Reducing Harmonic Eddy-Current Losses in the Stator Teeth of Interior Permanent Magnet Synchronous Machines During Flux Weakening," *Energy Conversion, IEEE Transactions on,* vol. 25, pp. 441-449, 2010.

[65] H. Seok-Hee, T. M. Jahns, and Z. Q. Zhu, "Design Tradeoffs Between Stator Core Loss and Torque Ripple in IPM Machines," *Industry Applications, IEEE Transactions on,* vol. 46, pp. 187-195, 2010.

[66] G. Pellegrino, P. Guglielmi, A. Vagati, and F. Villata, "Core Losses and Torque Ripple in IPM Machines: Dedicated Modeling and Design Tradeoff," *Industry Applications, IEEE Transactions on,* vol. 46, pp. 2381-2391, 2010.

[67] S. Morimoto, M. Sanada, and Y. Takeda, "Performance of PM-assisted synchronous reluctance motor for high-efficiency and wide constant-power operation," *Industry Applications, IEEE Transactions on,* vol. 37, pp. 1234-1240, 2001.

[68] H. Murakami, Y. Honda, Y. Sadanaga, Y. Ikkai, S. Morimoto, and Y. Takeda, "Optimum design of highly efficient magnet assisted reluctance motor," in *Industry Applications Conference, 2001. Thirty-Sixth IAS Annual Meeting. Conference Record of the 2001 IEEE*, 2001, pp. 2296-2301 vol.4.

[69] S. Ooi, S. Morimoto, M. Sanada, and Y. Inoue, "Performance Evaluation of a High-Power-Density PMASynRM With Ferrite Magnets," *Industry Applications, IEEE Transactions on,* vol. 49, pp. 1308-1315, 2013.

[70] T. Tokuda, M. Sanada, and S. Morimoto, "Influence of rotor structure on performance of permanent magnet assisted synchronous reluctance motor," in *Electrical Machines and Systems, 2009. ICEMS 2009. International Conference on*, 2009, pp. 1-6.

[71] M. Paradkar and J. Boecker, "Design of a high performance ferrite magnet-assisted synchronous reluctance motor for an electric vehicle," in *IECON 2012 - 38th Annual Conference on IEEE Industrial Electronics Society*, 2012, pp. 4099-4103.

[72] A. Vagati, B. Boazzo, P. Guglielmi, and G. Pellegrino, "Design of Ferrite-Assisted Synchronous Reluctance Machines Robust Toward Demagnetization," *Industry Applications, IEEE Transactions on,* vol. 50, pp. 1768-1779, 2014.

[73] Z. Fengge, B. Haijun, H. P. Gruenberger, and E. Nolle, "Comparative Study on Claw Pole Electrical Machine with Different Structure," in *Industrial Electronics and Applications, 2007. ICIEA 2007. 2nd IEEE Conference on*, 2007, pp. 636-640.

[74] I. Ramesohl, G. Henneberger, S. Kuppers, and W. Hadrys, "Three dimensional calculation of magnetic forces and displacements of a claw-pole generator," *Magnetics, IEEE Transactions on,* vol. 32, pp. 1685-1688, 1996.

[75] G. YouGuang, Z. Jian Guo, P. A. Watterson, and W. Wei, "Comparative study of 3-D flux electrical machines with soft magnetic composite cores," *Industry Applications, IEEE Transactions on,* vol. 39, pp. 1696-1703, 2003.

[76] G. YouGuang, Z. Jian Guo, Z. Jin Jiang, and W. Wei, "Core losses in claw pole permanent magnet machines with soft magnetic composite stators," *Magnetics, IEEE Transactions on,* vol. 39, pp. 3199-3201, 2003.

[77] G. YouGuang, Z. Jian Guo, L. Zhi Wei, and Z. Jin Jiang, "Measurement and modeling of core losses of soft magnetic composites under 3-D magnetic excitations in rotating motors," *Magnetics, IEEE Transactions on,* vol. 41, pp. 3925-3927, 2005.

[78] G. YouGuang, Z. Jian Guo, and W. Wu, "Thermal analysis of soft magnetic composite motors using a hybrid model with distributed heat sources," *Magnetics, IEEE Transactions on,* vol. 41, pp. 2124-2128, 2005.

[79] G. You Guang, Z. Jian Guo, and L. Hai Yan, "Effects of Armature Reaction on the Performance of a Claw Pole Motor With Soft Magnetic Composite Stator by Finite-Element Analysis," *Magnetics, IEEE Transactions on,* vol. 43, pp. 1072-1077, 2007.

[80] Z. Fengge, L. Yu, and B. Haijun, "Study and design of 3-D flux permanent magnet claw-pole motor with SMC stator," in *Applied Superconductivity and Electromagnetic Devices, 2009. ASEMD 2009. International Conference on*, 2009, pp. 316-319.

[81] S. Schulte, C. Kaehler, C. Schlensok, and G. Henneberger, "Combined analytical and numerical computation approach for design and optimisation of six-phase claw-pole alternators," *Science, Measurement and Technology, IEE Proceedings -,* vol. 151, pp. 496-498, 2004.

[82] Y. G. Guo, J. G. Zhu, and H. Y. Lu, "Accurate determination of parameters of a claw-pole motor with SMC stator core by finite-element magnetic-field analysis," *Electric Power Applications, IEE Proceedings -,* vol. 153, pp. 568-574, 2006.

[83] G. Youguang, Z. Jianguo, C. Jiaxin, S. Su, L. Haiyan, and J. Jianxun, "Performance analysis of a claw pole PM motor using improved FEA-based phase variable model," in *Power Engineering Conference, 2008. AUPEC '08. Australasian Universities*, 2008, pp. 1-5.

[84] J. A. Tapia, F. Leonardi, and T. A. Lipo, "Consequent pole permanent magnet machine with field weakening capability," in *Electric Machines and Drives Conference, 2001. IEMDC 2001. IEEE International*, 2001, pp. 126-131.

[85] J. A. Tapia, F. Leonardi, and T. A. Lipo, "Consequent-pole permanent-magnet machine with extended field-weakening capability," *Industry Applications, IEEE Transactions on,* vol. 39, pp. 1704-1709, 2003.

[86] W. Hua, Z. Q. Zhu, M. Cheng, Y. Pang, and D. Howe, "Comparison of flux-switching and doubly-salient permanent magnet brushless machines," in *Electrical Machines and Systems, 2005. ICEMS 2005. Proceedings of the Eighth International Conference on*, 2005, pp. 165-170 Vol. 1.

[87] M. Cheng, K. T. Chau, and C. C. Chan, "Design and analysis of a new doubly salient permanent magnet motor," *Magnetics, IEEE Transactions on,* vol. 37, pp. 3012-3020, 2001.

[88] G. Yu, K. T. Chau, J. Z. Jiang, Y. Chuang, and L. Wenlong, "Design of Doubly Salient Permanent Magnet Motors With Minimum Torque Ripple," *Magnetics, IEEE Transactions on,* vol. 45, pp. 4704-4707, 2009.

[89] C. Ming, H. Wei, Z. Jianzhong, and Z. Wenxiang, "Overview of Stator-Permanent Magnet Brushless Machines," *Industrial Electronics, IEEE Transactions on,* vol. 58, pp. 5087-5101, 2011.

[90] R. P. Deodhar, S. Andersson, I. Boldea, and T. J. E. Miller, "The flux-reversal machine: a new brushless doubly-salient permanent-magnet machine," *Industry Applications, IEEE Transactions on,* vol. 33, pp. 925-934, 1997.

[91] C. Wang, S. A. Nasar, and I. Boldea, "Three-phase flux reversal machine (FRM)," *Electric Power Applications, IEE Proceedings -,* vol. 146, pp. 139-146, 1999.

[92] K. Tae Heoung and L. Ju, "A study of the design for the flux reversal machine," *Magnetics, IEEE Transactions on,* vol. 40, pp. 2053-2055, 2004.

[93] X. Wei, Z. Jianguo, Z. Yongchang, W. Yi, L. Yongjian, and H. Jiefeng, "Flux-switching permanent magnet machine drive system for plug-in hybrid electrical vehicle," in *Universities Power Engineering Conference (AUPEC), 2010 20th Australasian*, 2010, pp. 1-6.

[94] F. Weizhong, P. C. K. Luk, S. Jian Xin, X. Bin, and W. Yu, "Permanent-Magnet Flux-Switching Integrated Starter Generator With Different Rotor Configurations for Cogging Torque and Torque Ripple Mitigations," *Industry Applications, IEEE Transactions on,* vol. 47, pp. 1247-1256, 2011.

[95] X. Wei, Z. Jianguo, Z. Yongchang, and W. Tianshi, "Electromagnetic design and performance evaluation on 75 kW axially laminated flux switching permanent magnet machine," in *Electrical Machines and Systems (ICEMS), 2011 International Conference on*, 2011, pp. 1-6.

[96] C. Yu, K. T. Chau, X. Liu, and J. Z. Jiang, "A flux-mnemonic permanent magnet brushless motor for electric vehicles," *Journal of Applied Physics,* vol. 103, pp. 07F103-07F103-3, 2008.

[97] Y. Chuang, Z. Xiaodong, G. Shuang, and W. Diyun, "Comparison of permanent magnet brushless motors for electric vehicles," in *Vehicle Power and Propulsion Conference (VPPC), 2010 IEEE*, 2010, pp. 1-5.

[98] Y. Chuang and G. Yu, "Performance analysis of new fault-tolerant flux-mnemonic doubly-salient permanent-magnet motor drive," in *Power Electronics and Drive Systems, 2009. PEDS 2009. International Conference on*, 2009, pp. 500-505.

[99] M. Zeraoulia, M. E. H. Benbouzid, and D. Diallo, "Electric Motor Drive Selection Issues for HEV Propulsion Systems: A Comparative Study," *Vehicular Technology, IEEE Transactions on,* vol. 55, pp. 1756-1764, 2006.

[100] N. Hashemnia and B. Asaei, "Comparative study of using different electric motors in the electric vehicles," in *Electrical Machines, 2008. ICEM 2008. 18th International Conference on*, 2008, pp. 1-5.

[101] T. Gnann, M. Haag, P. Plotz, and M. Wietschel, "Market potential for electric vehicles in the German commercial passenger transport sector," in *Electric Vehicle Symposium and Exhibition (EVS27), 2013 World*, 2013, pp. 1-10.

[102] B. Frieske, M. Kloetzke, and F. Mauser, "Trends in vehicle concept and key technology development for hybrid and battery electric vehicles," in *Electric Vehicle Symposium and Exhibition (EVS27), 2013 World*, 2013, pp. 1-12.

[103] S. Kahourzade, A. Mahmoudi, N. A. Rahim, and P. Hew Wooi, "Sizing equation and Finite Element Analysis optimum design of axial-flux permanent-magnet motor for electric vehicle direct drive," in *Power Engineering and Optimization Conference (PEDCO) Melaka, Malaysia, 2012 Ieee International*, 2012, pp. 1-6.

[104] J. M. da Fonte Terras, A. Neves, D. M. Sousa, and A. Roque, "Modelling and simulation of a commercial electric vehicle," in *Intelligent Transportation Systems (ITSC), 2010 13th International IEEE Conference on*, 2010, pp. 1588-1593.

[105] J. M. Terras, D. M. Sousa, A. Roque, and A. Neves, "Simulation of a commercial electric vehicle: Dynamic aspects and performance," in *Power Electronics and Applications (EPE 2011), Proceedings of the 2011-14th European Conference on*, 2011, pp. 1-10.

[106] H. B. Pacejka, *Tyre and Vehicle Dynamics*: Butterworth-Heinemann, 2006.

[107] N. Mutoh, Y. Miyamoto, T. Horigome, and K. Takita, "Driving characteristics of an electric vehicle system with independently driven front and rear wheels," in *Industrial Electronics Society, 2003. IECON '03. The 29th Annual Conference of the IEEE*, 2003, pp. 931-938 vol.1.

[108] O. Tur, H. Ucarol, E. Ozsu, M. Demirci, Y. Solak, E. Elcik*, et al.*, "Sizing, Design and Prototyping of an Electric Drive System for a Split Drive Hybrid Electric Vehicle," in *Electric Machines & Drives Conference, 2007. IEMDC '07. IEEE International*, 2007, pp. 1745-1750.

[109] N. Mutoh and Y. Nakano, "Dynamic characteristic analyses of the front-and rear-wheel independent-drive-type electric vehicle (FRID EV) when the drive system failed during running under various road conditions," in *Vehicle Power and Propulsion Conference, 2009. VPPC '09. IEEE*, 2009, pp. 1162-1169.

[110] N. Mutoh, "Driving and Braking Torque Distribution Methods for Front- and Rear-Wheel-Independent Drive-Type Electric Vehicles on Roads With Low Friction Coefficient," *Industrial Electronics, IEEE Transactions on,* vol. 59, pp. 3919-3933, 2012.

[111] N. Mutoh and Y. Takahashi, "Front-and-rear-wheel-independent-drive type electric vehicle (FRID EV) with the outstanding driving performance suitable for next-generation adavanced EVs," in *Vehicle Power and Propulsion Conference, 2009. VPPC '09. IEEE*, 2009, pp. 1064-1070.

[112] N. Mutoh, Y. Takahashi, and Y. Tomita, "Failsafe Drive Performance of FRID Electric Vehicles With the Structure Driven by the Front and Rear Wheels Independently," *Industrial Electronics, IEEE Transactions on,* vol. 55, pp. 2306-2315, 2008.

[113] N. Mutoh and Y. Nakano, "Dynamics of Front-and-Rear-Wheel-Independent-Drive-Type Electric Vehicles at the Time of Failure," *Industrial Electronics, IEEE Transactions on,* vol. 59, pp. 1488-1499, 2012.

[114] A. Porcel, P. Laurence, M. Basset, and G. L. Gissinger, "Tyre model for vehicle simulation: overview and real time solution for critical situations," in *Control Applications, 2001. (CCA '01). Proceedings of the 2001 IEEE International Conference on*, 2001, pp. 817-822.

[115] H. B. Pacejka and I. J. M. Besselink, "Magic Formula Tyre Model with Transient Properties," *Vehicle System Dynamics,* vol. 27, pp. 234-249, 1997/01/01 1997.

[116] Mathworks. (2010). *MATLAB*. Available: http://uk.mathworks.com/products/matlab/

[117] A. Georgi, M. Zimmermann, T. Lich, L. Blank, N. Kickler, and R. Marchthaler, "New approach of accident benefit analysis for rear end collision avoidance and mitigation systems," in *21st International Technical Conference on the Enhanced Safety of Vehicles*, 2009.

[118] G. Meyer, *Advanced Microsystems for Automotive Applications 2012: Smart Systems for Safe, Sustainable and Networked Vehicles*: Springer Berlin Heidelberg, 2012.

[119] M. Barcaro and N. Bianchi, "Interior PM machines using Ferrite to substitute rare-earth surface PM machines," in *Electrical Machines (ICEM), 2012 XXth International Conference on*, 2012, pp. 1339-1345.

[120] A. Vagati, B. Boazzo, P. Guglielmi, and G. Pellegrino, "Ferrite assisted synchronous reluctance machines: A general approach," in *Electrical Machines (ICEM), 2012 XXth International Conference on*, 2012, pp. 1315-1321.

[121] J. H. Lee, J. C. Kim, and D. S. Hyun, "Effect analysis of magnet on Ld and Lq inductance of permanent magnet assisted synchronous reluctance motor using finite element method," *Magnetics, IEEE Transactions on,* vol. 35, pp. 1199-1202, 1999.

[122] J.-H. Lee, Y.-J. Jang, and J.-P. Hong, "Characteristic analysis of permanent magnet-assisted synchronous reluctance motor for high power application," *Journal of Applied Physics,* vol. 97, pp. 10Q503-10Q503-3, 2005.

[123] P. Niazi, H. A. Toliyat, and A. Goodarzi, "Robust Maximum Torque per Ampere (MTPA) Control of PM-Assisted SynRM for Traction Applications," *Vehicular Technology, IEEE Transactions on,* vol. 56, pp. 1538-1545, 2007.

[124] P. Guglielmi, B. Boazzo, E. Armando, G. Pellegrino, and A. Vagati, "Permanent-Magnet Minimization in PM-Assisted Synchronous Reluctance Motors for Wide Speed Range," *Industry Applications, IEEE Transactions on,* vol. 49, pp. 31-41, 2013.

[125] P. Niazi, H. A. Toliyat, C. Dal-Ho, and K. Jung-Chul, "A Low-Cost and Efficient Permanent-Magnet-Assisted Synchronous Reluctance Motor Drive," *Industry Applications, IEEE Transactions on,* vol. 43, pp. 542-550, 2007.

[126] K. Won-Ho, K. Kwang-Soo, K. Seung-Joo, K. Dong-Woo, G. Sung-Chul, C. Yon-Do*, et al.*, "Optimal PM Design of PMA-SynRM for Wide Constant-Power Operation and Torque Ripple Reduction," *Magnetics, IEEE Transactions on,* vol. 45, pp. 4660-4663, 2009.

[127] I. Boldea, L. Tutelea, and C. I. Pitic, "PM-assisted reluctance synchronous motor/generator (PM-RSM) for mild hybrid vehicles: electromagnetic design," *Industry Applications, IEEE Transactions on,* vol. 40, pp. 492-498, 2004.

[128] T. Hosoi, K. Shima, and T. Fukami, "Magnetic Circuit Analysis of Permanent-Magnet-Assisted Salient-Pole Synchronous Machines Under Steady States," *Industry Applications, IEEE Transactions on,* vol. 48, pp. 895-902, 2012.

[129] J. Wang, "An Electric Machine," UK Patent 1221635.4, 2012.

[130] P. Lazari, J. Wang, and L. Chen, "A computationally efficient design technique for electric vehicle traction machines," in *Electrical Machines (ICEM), 2012 XXth International Conference on*, 2012, pp. 2596-2602.

[131] CEDRAT. (2013). *Flux v11.1.2 user manual.* Available: http://www.cedrat.com/en/software/flux.html

[132] CEDRAT. (2013). *GOT-It v2.0.1 user manual.* Available: http://www.cedrat.com/en/software/got-it.html

[133] L. Chen, J. Wang, P. Lombard, P. Lazari, and V. Leconte, "Design optimisation of permanent magnet assisted synchronous reluctance machines for electric vehicle applications," in *Electrical Machines (ICEM), 2012 XXth International Conference on*, 2012, pp. 2647-2653.

[134] G. Qi, J. T. Chen, Z. Q. Zhu, D. Howe, L. B. Zhou, and C. L. Gu, "Influence of Skew and Cross-Coupling on Flux-Weakening Performance of Permanent-Magnet Brushless AC Machines," *Magnetics, IEEE Transactions on,* vol. 45, pp. 2110-2117, 2009.

[135] N. Bianchi and S. Bolognani, "Magnetic models of saturated interior permanent magnet motors based on finite element analysis," in *Industry Applications Conference, 1998. Thirty-Third IAS Annual Meeting. The 1998 IEEE*, 1998, pp. 27-34 vol.1.

[136] J. K. Tangudu, T. M. Jahns, A. M. El-Refaie, and Z. Q. Zhu, "Segregation of torque components in fractional-slot concentrated-winding interior PM machines using frozen permeability," in *Energy Conversion Congress and Exposition, 2009. ECCE 2009. IEEE*, 2009, pp. 3814-3821.

[137] J. A. Walker, D. G. Dorrell, and C. Cossar, "Flux-linkage calculation in permanent-magnet motors using the frozen permeabilities method," *Magnetics, IEEE Transactions on,* vol. 41, pp. 3946-3948, 2005.

[138] K. Sang-Yeop, K. Jae-Kwang, and J. Hyun-Kyo, "Characteristic Analysis of Multilayer-Buried Magnet Synchronous Motor Using Fixed Permeability Method," *Energy Conversion, IEEE Transactions on,* vol. 20, pp. 549-555, 2005.

[139] W. Q. Chu and Z. Q. Zhu, "Average Torque Separation in Permanent Magnet Synchronous Machines Using Frozen Permeability," *Magnetics, IEEE Transactions on,* vol. 49, pp. 1202-1210, 2013.

[140] N. Bianchi and L. Alberti, "MMF Harmonics Effect on the Embedded FE Analytical Computation of PM Motors," *Industry Applications, IEEE Transactions on,* vol. 46, pp. 812-820, 2010.

[141] M. W. Brainard, "Synchronous Machines with Rotating Permanent-Magnet Fields; Part I. Characteristics and Mechanical Construction [includes discussion]," *Power*

Apparatus and Systems, Part III. Transactions of the American Institute of Electrical Engineers, vol. 71, 1952.

[142] J. Wang, X. Yuan, and K. Atallah, "Design Optimization of a Surface-Mounted Permanent-Magnet Motor With Concentrated Windings for Electric Vehicle Applications," *Vehicular Technology, IEEE Transactions on,* vol. 62, pp. 1053-1064, 2013.

[143] I. Boldea, L. N. Tutelea, L. Parsa, and D. Dorrell, "Automotive Electric Propulsion Systems With Reduced or No Permanent Magnets: An Overview," *Industrial Electronics, IEEE Transactions on,* vol. 61, pp. 5696-5711, 2014.

[144] X. Chen, J. Wang, P. Lazari, and L. Chen, "Permanent Magnet Assisted Synchronous Reluctance Machine with fractional-slot winding configurations," in *Electric Machines & Drives Conference (IEMDC), 2013 IEEE International*, 2013, pp. 374-381.

[145] P. B. Reddy, A. M. El-Refaie, H. Kum-Kang, J. K. Tangudu, and T. M. Jahns, "Comparison of Interior and Surface PM Machines Equipped With Fractional-Slot Concentrated Windings for Hybrid Traction Applications," *Energy Conversion, IEEE Transactions on,* vol. 27, pp. 593-602, 2012.

[146] R. Dutta and M. F. Rahman, "Design and Analysis of an Interior Permanent Magnet (IPM) Machine With Very Wide Constant Power Operation Range," *Energy Conversion, IEEE Transactions on,* vol. 23, pp. 25-33, 2008.

[147] G. Pellegrino, A. Vagati, P. Guglielmi, and B. Boazzo, "Performance Comparison Between Surface-Mounted and Interior PM Motor Drives for Electric Vehicle Application," *Industrial Electronics, IEEE Transactions on,* vol. 59, pp. 803-811, 2012.

[148] H. Cai, B. Guan, and L. Xu, "Low-Cost Ferrite PM-Assisted Synchronous Reluctance Machine for Electric Vehicles," *Industrial Electronics, IEEE Transactions on,* vol. 61, pp. 5741-5748, 2014.

[149] R. Dutta, L. Chong, and M. F. Rahman, "Design and Experimental Verification of an 18-Slot/14-pole Fractional-Slot Concentrated Winding Interior Permanent Magnet Machine," *Energy Conversion, IEEE Transactions on,* vol. 28, pp. 181-190, 2013.

[150] A. M. El-Refaie, "Fractional-Slot Concentrated-Windings Synchronous Permanent Magnet Machines: Opportunities and Challenges," *Industrial Electronics, IEEE Transactions on,* vol. 57, pp. 107-121, 2010.

[151] J. Wang, K. Atallah, R. Chin, W. M. Arshad, and H. Lendenmann, "Rotor Eddy-Current Loss in Permanent-Magnet Brushless AC Machines," *Magnetics, IEEE Transactions on,* vol. 46, pp. 2701-2707, 2010.

[152] P. B. Reddy, H. Kum-Kang, and A. M. El-Refaie, "Generalized Approach of Stator Shifting in Interior Permanent-Magnet Machines Equipped With Fractional-Slot

Concentrated Windings," *Industrial Electronics, IEEE Transactions on,* vol. 61, pp. 5035-5046, 2014.

[153] G. Dajaku, "Elektrische machine," Germany Patent DE 102 008 057 349, Jul. 15, 2010.

[154] G. Dajaku and D. Gerling, "A novel tooth concentrated winding with low space harmonic contents," in *Electric Machines & Drives Conference (IEMDC), 2013 IEEE International*, 2013, pp. 755-760.

[155] G. Dajaku, W. Xie, and D. Gerling, "Reduction of Low Space Harmonics for the Fractional Slot Concentrated Windings Using a Novel Stator Design," *Magnetics, IEEE Transactions on,* vol. 50, pp. 1-12, 2014.

[156] J. Wang, V. I. Patel, and W. Wang, "Fractional-Slot Permanent Magnet Brushless Machines with Low Space Harmonic Contents," *Magnetics, IEEE Transactions on,* vol. 50, pp. 1-9, 2014.

[157] V. I. Patel, J. Wang, W. Wang, and X. Chen, "Six-Phase Fractional-Slot-per-Pole-per-Phase Permanent-Magnet Machines With Low Space Harmonics for Electric Vehicle Application," *Industry Applications, IEEE Transactions on,* vol. 50, pp. 2554-2563, 2014.

[158] N. Bianchi, S. Bolognani, Pre, x, and M. D., "Magnetic Loading of Fractional-Slot Three-Phase PM Motors With Nonoverlapped Coils," *Industry Applications, IEEE Transactions on,* vol. 44, pp. 1513-1521, 2008.

[159] P. Lazari, J. Wang, and L. Chen, "A Computationally Efficient Design Technique for Electric-Vehicle Traction Machines," *Industry Applications, IEEE Transactions on,* vol. 50, pp. 3203-3213, 2014.

[160] P. Mellor, R. Wrobel, and N. Simpson, "AC losses in high frequency electrical machine windings formed from large section conductors," in *Energy Conversion Congress and Exposition (ECCE), 2014 IEEE*, 2014, pp. 5563-5570.

[161] H. Hamalainen, J. Pyrhonen, and J. Nerg, "AC Resistance Factor in One-Layer Form-Wound Winding Used in Rotating Electrical Machines," *Magnetics, IEEE Transactions on,* vol. 49, pp. 2967-2973, 2013.

[162] M. Popescu and D. G. Dorrell, "Proximity Losses in the Windings of High Speed Brushless Permanent Magnet AC Motors With Single Tooth Windings and Parallel Paths," *Magnetics, IEEE Transactions on,* vol. 49, pp. 3913-3916, 2013.

[163] MotorDesignLimited. (2015). *Motor-CAD v8.3.8 user manual.* Available: http://www.motor-design.com/motorcad.php

[164] ANSYS. (2009). *ANSYS Mechanical v12.1 user manual.* Available: http://www.ansys.com/Products/Simulation+Technology/Structural+Analysis/ANSYS+Mechanical

[165] D. Dorrell, L. Parsa, and I. Boldea, "Automotive Electric Motors, Generators, and Actuator Drive Systems With Reduced or No Permanent Magnets and Innovative Design Concepts," *Industrial Electronics, IEEE Transactions on,* vol. 61, pp. 5693-5695, 2014.

[166] J. Linni, K. T. Chau, and J. Z. Jiang, "A Magnetic-Geared Outer-Rotor Permanent-Magnet Brushless Machine for Wind Power Generation," *Industry Applications, IEEE Transactions on,* vol. 45, pp. 954-962, 2009.

[167] K. Sung-Il, K. Young-Kyoun, L. Geun-Ho, and H. Jung-Pyo, "A Novel Rotor Configuration and Experimental Verification of Interior PM Synchronous Motor for High-Speed Applications," *Magnetics, IEEE Transactions on,* vol. 48, pp. 843-846, 2012.

[168] S. Morimoto, O. Shohei, Y. Inoue, and M. Sanada, "Experimental Evaluation of a Rare-Earth-Free PMASynRM With Ferrite Magnets for Automotive Applications," *Industrial Electronics, IEEE Transactions on,* vol. 61, pp. 5749-5756, 2014.

[169] L. Parsa and H. Lei, "Interior Permanent Magnet Motors With Reduced Torque Pulsation," *Industrial Electronics, IEEE Transactions on,* vol. 55, pp. 602-609, 2008.

[170] L. Di Leonardo, F. Parasiliti, M. Tursini, and M. Villani, "Transient analysis of PM synchronous motor drives by finite element model co-simulation," in *Industrial Electronics Society, IECON 2013 - 39th Annual Conference of the IEEE*, 2013, pp. 6834-6840.

[171] F. Parasiliti, M. Villani, and A. Tassi, "Dynamic Analysis of Synchronous Reluctance Motor Drives Based on SimulinkÂ® and Finite Element Model," in *IEEE Industrial Electronics, IECON 2006 - 32nd Annual Conference on*, 2006, pp. 1516-1520.

[172] W. Liang, J. Wang, T. Lu, and W. Fang, "A New Method for Multiple Finite-Element Models in Cosimulation With Electrical Circuit Using Machine Multiloop Modeling Scheme," *Industrial Electronics, IEEE Transactions on,* vol. 61, pp. 6583-6590, 2014.

[173] Y. Kano, K. Watanabe, T. Kosaka, and N. Matsui, "A Novel Approach for Circuit-Field-Coupled Time-Stepping Electromagnetic Analysis of Saturated Interior PM Motors," *Industry Applications, IEEE Transactions on,* vol. 45, pp. 1325-1333, 2009.

[174] O. Wallmark and J. Galic, "Prediction of dc-link current harmonics from PM-motor drives in railway applications," in *Electrical Systems for Aircraft, Railway and Ship Propulsion (ESARS), 2012*, 2012, pp. 1-8.

[175] M. Boesing, M. Niessen, T. Lange, and R. De Doncker, "Modeling spatial harmonics and switching frequencies in PM synchronous machines and their electromagnetic forces," in *Electrical Machines (ICEM), 2012 XXth International Conference on*, 2012, pp. 3001-3007.

[176] G. Weidenholzer, S. Silber, G. Jungmayr, G. Bramerdorfer, H. Grabner, and W. Amrhein, "A flux-based PMSM motor model using RBF interpolation for time-

stepping simulations," in *Electric Machines & Drives Conference (IEMDC), 2013 IEEE International*, 2013, pp. 1418-1423.

[177] T. Sebastian, "Temperature effects on torque production and efficiency of PM motors using NdFeB magnets," *Industry Applications, IEEE Transactions on,* vol. 31, pp. 353-357, 1995.

[178] R. Bojoi, A. Cavagnino, M. Cossale, and S. Vaschetta, "Methodology for the IPM motor magnetic model computation based on finite element analysis," in *Industrial Electronics Society, IECON 2014 - 40th Annual Conference of the IEEE*, 2014, pp. 722-728.

[179] S. Ruoho, J. Kolehmainen, J. Ikaheimo, and A. Arkkio, "Interdependence of Demagnetization, Loading, and Temperature Rise in a Permanent-Magnet Synchronous Motor," *Magnetics, IEEE Transactions on,* vol. 46, pp. 949-953, 2010.

[180] J. Wang, W. Wang, K. Atallah, and D. Howe, "Demagnetization Assessment for Three-Phase Tubular Brushless Permanent-Magnet Machines," *Magnetics, IEEE Transactions on,* vol. 44, pp. 2195-2203, 2008.

[181] J. Daesuk, C. Ju-Hee, W. Kyungil, K. Byung-Taek, and K. Dae-kyong, "Electromagnetic Field and Thermal Linked Analysis of Interior Permanent-Magnet Synchronous Motor for Agricultural Electric Vehicle," *Magnetics, IEEE Transactions on,* vol. 47, pp. 4242-4245, 2011.

[182] W. Jiang and T. M. Jahns, "Development of efficient electromagnetic-thermal coupled model of electric machines based on finite element analysis," in *Electric Machines & Drives Conference (IEMDC), 2013 IEEE International*, 2013, pp. 816-823.

[183] X. Zhang, W. Li, B. Kou, J. Cao, H. Cao, C. Gerada*, et al.*, "Electrothermal Combined Optimization on Notch in Air-Cooled High-Speed Permanent-Magnet Generator," *Magnetics, IEEE Transactions on,* vol. 51, pp. 1-10, 2015.

[184] X. Sun, M. Cheng, S. Zhu, and J. Zhang, "Coupled Electromagnetic-Thermal-Mechanical Analysis for Accurate Prediction of Dual-Mechanical-Port Machine Performance," *Industry Applications, IEEE Transactions on,* vol. 48, pp. 2240-2248, 2012.

[185] F. A. Potra and S. J. Wright, "Interior-point methods," *Journal of Computational and Applied Mathematics,* vol. 124, pp. 281-302, 2000.

[186] J. Goss, P. H. Mellor, R. Wrobel, D. A. Staton, and M. Popescu, "The design of AC permanent magnet motors for electric vehicles: A computationally efficient model of the operational envelope," in *Power Electronics, Machines and Drives (PEMD 2012), 6th IET International Conference on*, 2012, pp. 1-6.

[187] W. Zhao, D. Chen, T. Lipo, and B. Kwon, "Performance Improvement of Ferrite-Assisted Synchronous Reluctance Machines Using Asymmetrical Rotor Configurations," *Magnetics, IEEE Transactions on,* vol. PP, pp. 1-1, 2015.

[188] W. Fei and P. C. K. Luk, "Design and performance analysis of a high-speed air-cored axial-flux permanent-magnet generator with circular magnets and coils," in *Electric Machines and Drives Conference, 2009. IEMDC '09. IEEE International*, 2009, pp. 1617-1624.

[189] W. Fei, P. C. K. Luk, and K. Jinupun, "Design and analysis of high-speed coreless axial flux permanent magnet generator with circular magnets and coils," *Electric Power Applications, IET,* vol. 4, pp. 739-747, 2010.

[190] J. Jae-Woo, L. Byeong-Hwa, K. Do-Jin, H. Jung-Pyo, K. Jae-Young, J. Seong-Min*, et al.*, "Mechanical Stress Reduction of Rotor Core of Interior Permanent Magnet Synchronous Motor," *Magnetics, IEEE Transactions on,* vol. 48, pp. 911-914, 2012.

[191] M. Caprio, V. Lelos, J. Herbst, and J. Upshaw, "Advanced Induction Motor Endring Design Features for High Speed Applications," in *Electric Machines and Drives, 2005 IEEE International Conference on*, 2005, pp. 993-998.

TABLE OF FIGURES

LIST OF TABLES

APPENDIX A Harmonic Distributions of Iron Loss Associated with Eddy Current Component

To investigate the influence of MMF harmonics on iron loss associated with eddy current component, the iron loss is calculated by flux densities of stator and rotor iron nodes from FEA. The flow chart of this calculation is illustrated in Fig. A-1.

Firstly, perform FEA over one mechanical period at given load condition before extracting flux density B information of all the nodes on stator and rotor irons at each time step. Subsequently, extract the mesh information which contains relationships between elements and nodes of stator and rotor irons from FEA. Then, calculate average flux density B and also area of each element. Next, at each element, calculate the flux density amplitude $B_{\max}$ over one mechanical/electrical period for both stator and rotor irons, get x and y components of flux density (B_x, B_y) on stator iron, and calculate radial and circumferential components of flux density (B_r, B_t) on rotor iron. After this, obtain the spectra of B_x, B_y, B_r and B_t of each element via FFT, and then calculate the flux density magnitude with square roots of B_x, B_y on stator iron and B_r, B_t on rotor iron. Subsequently, the hysteresis loss density, eddy current loss density and excessive loss density of each element on stator and rotor iron are obtained by (A.1), (A.2) and (A.3) respectively. Finally, these three loss components are calculated by the integral of their loss densities over the stator and rotor volumes. The PYTHON script to extract nodal flux density from FEA and the MATLAB script to calculate the iron loss components based on the nodal flux density are attached at the end of this section.

It should be noted that the above calculation has to be performed over one mechanical period rather than one electrical period. Otherwise, the

fractional harmonic component will be missed. To ensure the calculation accuracy, the mesh density needs to be reasonably high.

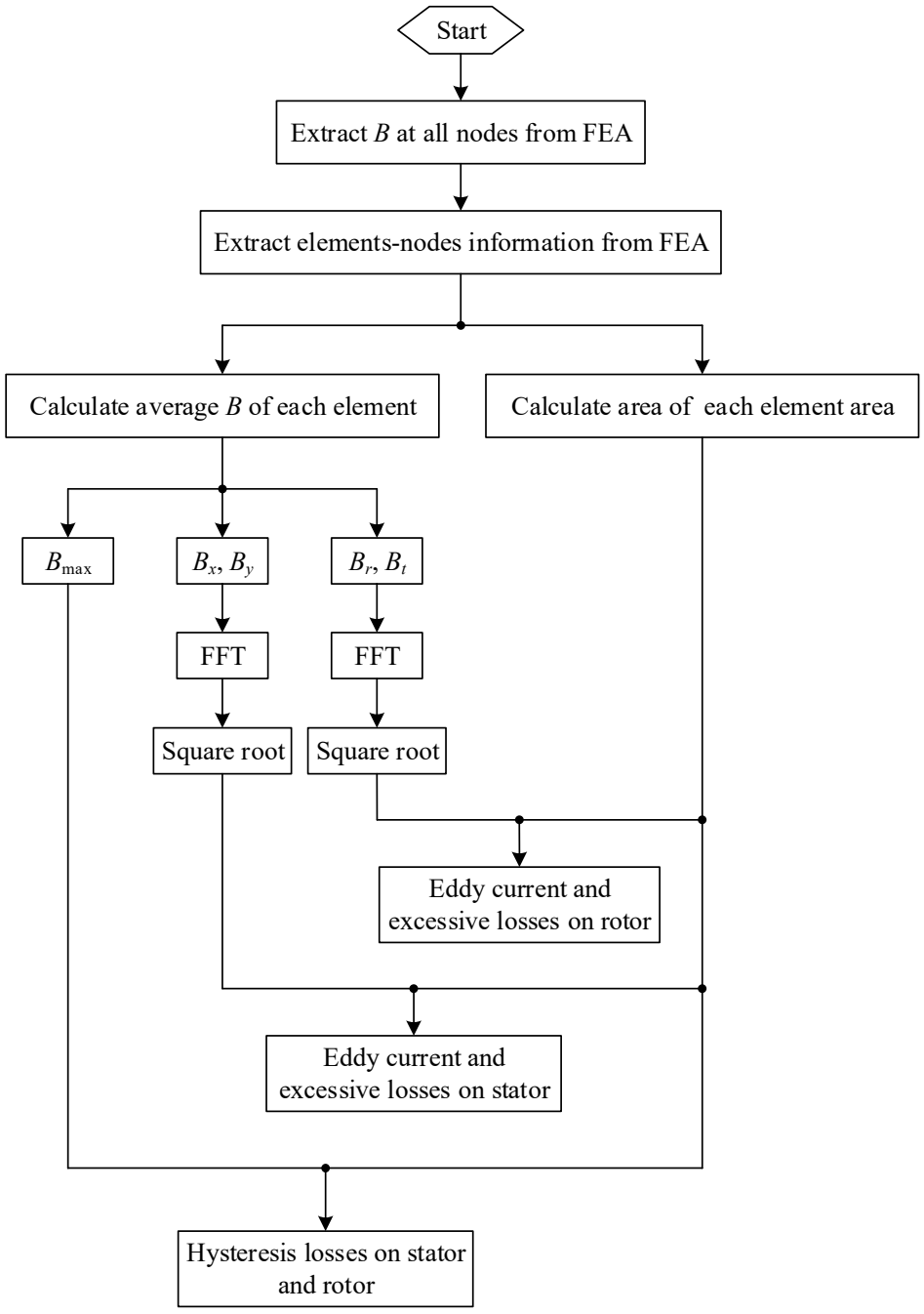

Fig. A-1. Flow chart of iron loss calculation based on nodal flux density from FEA.

$$dP_{hys} = K_s K_h B_{\max}{}^2 f_e \tag{A.1}$$

where K_s is the lamination stacking factor, K_h is the hysteresis loss coefficient, and f_e is the electrical frequency.

$$dP_{eddy} = \frac{K_s}{T}\int_0^T \sigma \frac{d_l}{12}\left(\frac{dB}{dt}\right)^2 dt \tag{A.2}$$

where T is the mechanical period, t is time, σ is the lamination conductivity, and d_l is the lamination thickness.

$$dP_{exc} = \frac{K_s}{T}\int_0^T K_{exc}\left(\frac{dB}{dt}\right)^{1.5} dt \tag{A.3}$$

where K_{exc} is the excessive loss coefficient.

$$p_{Fe} = \iiint_v \left(dP_{hys} + dP_{eddy} + dP_{exc}\right)dv \tag{A.4}$$

where v is the iron volume.

```
#*******  PYTHON script to extract flux density of each node at each time step from FEA  ******
#****************************************  Header information  ****************************************
#! Preflu2D 11.1

#*************************************  Angular step information  *************************************
Ang_step=360.0/256.0;

#**********************  Extract B of stator and rotor irons at each time step  **********************
for i in range(256):
        Ang=0.0+Ang_step*(i+2);
        selectCurrentStep(activeScenario=Scenario['SCENARIO_MECH'],
parameterValue=['ANGPOS_2_ROTATING='+str(Ang)]);
        result =
ExportDataRegionFace(exportDataFile=exportDexFluxFile(fileName='B_extract_9ph/Peak_B_S
_'+str(i+1)),
                mechanicalSetPosition=CurrentPosition(),
                formula='B',
                regionFace=RegionFace['STATOR'],
```

```
                lengthUnit=LengthUnit['MILLIMETER'],
                coordSys=CoordSys['XY1']);
        result = ExportDataRegionFace(exportDataFile=exportDexFluxFile(fileName='B_extract_9ph/Peak_B_R_'+str(i+1)),
                mechanicalSetPosition=CurrentPosition(),
                formula='B',
                regionFace=RegionFace['ROTOR'],
                lengthUnit=LengthUnit['MILLIMETER'],
                coordSys=CoordSys['XY1']);

%********  MATLAB script to calculate iron loss based on nodal flux density from FEA  *********
%************************************  Parameter definition  ****************************************
Speed=1350.0;                   %Speed at which FEA runs
p=7;                            %NO. of pole pair
f=Speed/60*p;                   %Electrical frequency
kh=130.246;                     %Hysteresis loss coefficient
sigema=1923077;                 %Conductivity of stator and rotor laminations
ke=0.357;                       %Excessive loss coefficient
d=3.5e-4;                       %Lamination sheet thickness
kf=0.97;                        %Lamination stacking factor
La=66.4;                        %Stack length
periodicity=2;                  %FE model periodicity
n=256;                          %NO. of time steps (rotor angle steps) in FEA

%************  Import mesh information of both stator and rotor regions from FEA  **************
load('C:\PMOB_18s14p_bonded_neo\B_extract_9ph\Element_table_stator_origin.txt');
load('C:\PMOB_18s14p_bonded_neo\B_extract_9ph\Element_table_rotor_origin.txt');

%*****************************  Import B data PYTHON script generated  ***************************
for i=1:n

B_s_origin=importdata(['C:\PMOB_18s14p_bonded_neo\B_extract_9ph\PEAK_B_S_',num2str(i),'.DEX']);
   B_s_x(:,i)=B_s_origin.data(:,4);
   B_s_y(:,i)=B_s_origin.data(:,5);

B_r_origin=importdata(['C:\PMOB_18s14p_bonded_neo\B_extract_9ph\PEAK_B_R_',num2str(i),'.DEX']);
   B_r_x(:,i)=B_r_origin.data(:,4);
   B_r_y(:,i)=B_r_origin.data(:,5);
```

```
    Coor_ori_r_x(:,i)=B_r_origin.data(:,1);
    Coor_ori_r_y(:,i)=B_r_origin.data(:,2);
end

%********  Data process to obtain radial and circumferential components of nodal flux density (Br, Bt)  ********
Coor_ori_s_x=B_s_origin.data(:,1);
Coor_ori_s_y=B_s_origin.data(:,2);

B_r_r=B_r_x.*Coor_ori_r_x./sqrt(Coor_ori_r_x.^2+Coor_ori_r_y.^2)+B_r_y.*Coor_ori_r_y./sqrt(Coor_ori_r_x.^2+Coor_ori_r_y.^2);
B_r_t=B_r_y.*Coor_ori_r_x./sqrt(Coor_ori_r_x.^2+Coor_ori_r_y.^2)-B_r_x.*Coor_ori_r_y./sqrt(Coor_ori_r_x.^2+Coor_ori_r_y.^2);

%********************  Data process to obtain element information of stator iron  ********************
[n_s,n_nodes]=size(Element_table_stator_origin);
Element_table_stator=zeros(n_s/2,n_nodes);
for i=1:n_s/2
    Element_table_stator(i,:)=Element_table_stator_origin(i*2,:);
end
n_s=n_s/2;

%*************  Calculate element flux density of stator iron based on nodal ones  **************
B_ele_s_x=zeros(n_s,n);
B_ele_s_y=zeros(n_s,n);
Coor_ele_s_x=zeros(n_s,1);
Coor_ele_s_y=zeros(n_s,1);
for i=1:n_s

B_ele_s_x(i,:)=(B_s_x(Element_table_stator(i,1),:)+B_s_x(Element_table_stator(i,2),:)+B_s_x(Element_table_stator(i,3),:)+B_s_x(Element_table_stator(i,4),:)+B_s_x(Element_table_stator(i,5),:)+B_s_x(Element_table_stator(i,6),:))/6;

B_ele_s_y(i,:)=(B_s_y(Element_table_stator(i,1),:)+B_s_y(Element_table_stator(i,2),:)+B_s_y(Element_table_stator(i,3),:)+B_s_y(Element_table_stator(i,4),:)+B_s_y(Element_table_stator(i,5),:)+B_s_y(Element_table_stator(i,6),:))/6;

Coor_ele_s_x(i)=(Coor_ori_s_x(Element_table_stator(i,1))+Coor_ori_s_x(Element_table_stator(i,2))+Coor_ori_s_x(Element_table_stator(i,3))+Coor_ori_s_x(Element_table_stator(i,4))+Coor_ori_s_x(Element_table_stator(i,5))+Coor_ori_s_x(Element_table_stator(i,6)))/6;

Coor_ele_s_y(i)=(Coor_ori_s_y(Element_table_stator(i,1))+Coor_ori_s_y(Element_table_stator(
```

```
i,2))+Coor_ori_s_y(Element_table_stator(i,3))+Coor_ori_s_y(Element_table_stator(i,4))+Coor_o
ri_s_y(Element_table_stator(i,5))+Coor_ori_s_y(Element_table_stator(i,6)))/6;
end

%******************  Data process to obtain element information of rotor iron  ******************
[n_r,n_nodes]=size(Element_table_rotor_origin);
Element_table_rotor=zeros(n_s/2,n_nodes);
for i=1:n_r/2
   Element_table_rotor(i,:)=Element_table_rotor_origin(i*2,:);
end
n_r=n_r/2;

%*************  Calculate element flux density of rotor iron based on nodal ones  ***************
B_ele_r_x=zeros(n_r,n);
B_ele_r_y=zeros(n_r,n);
Coor_ele_r_x=zeros(n_r,n);
Coor_ele_r_y=zeros(n_r,n);
for i=1:n_r

B_ele_r_x(i,:)=(B_r_x(Element_table_rotor(i,1),:)+B_r_x(Element_table_rotor(i,2),:)+B_r_x(Elem
ent_table_rotor(i,3),:)+B_r_x(Element_table_rotor(i,4),:)+B_r_x(Element_table_rotor(i,5),:)+B_r_
x(Element_table_rotor(i,6),:))/6;

B_ele_r_y(i,:)=(B_r_y(Element_table_rotor(i,1),:)+B_r_y(Element_table_rotor(i,2),:)+B_r_y(Elem
ent_table_rotor(i,3),:)+B_r_y(Element_table_rotor(i,4),:)+B_r_y(Element_table_rotor(i,5),:)+B_r_
y(Element_table_rotor(i,6),:))/6;

Coor_ele_r_x(i,:)=(Coor_ori_r_x(Element_table_rotor(i,1),:)+Coor_ori_r_x(Element_table_rotor(i
,2),:)+Coor_ori_r_x(Element_table_rotor(i,3),:)+Coor_ori_r_x(Element_table_rotor(i,4),:)+Coor_
ori_r_x(Element_table_rotor(i,5),:)+Coor_ori_r_x(Element_table_rotor(i,6),:))/6;

Coor_ele_r_y(i,:)=(Coor_ori_r_y(Element_table_rotor(i,1),:)+Coor_ori_r_y(Element_table_rotor(i
,2),:)+Coor_ori_r_y(Element_table_rotor(i,3),:)+Coor_ori_r_y(Element_table_rotor(i,4),:)+Coor_
ori_r_y(Element_table_rotor(i,5),:)+Coor_ori_r_y(Element_table_rotor(i,6),:))/6;
end

B_ele_r_r=zeros(n_r,n);
B_ele_r_t=zeros(n_r,n);
for i=1:n_r

B_ele_r_r(i,:)=(B_r_r(Element_table_rotor(i,1),:)+B_r_r(Element_table_rotor(i,2),:)+B_r_r(Eleme
nt_table_rotor(i,3),:)+B_r_r(Element_table_rotor(i,4),:)+B_r_r(Element_table_rotor(i,5),:)+B_r_r(
Element_table_rotor(i,6),:))/6;

B_ele_r_t(i,:)=(B_r_t(Element_table_rotor(i,1),:)+B_r_t(Element_table_rotor(i,2),:)+B_r_t(Eleme
```

```
nt_table_rotor(i,3),:)+B_r_t(Element_table_rotor(i,4),:)+B_r_t(Element_table_rotor(i,5),:)+B_r_t(
Element_table_rotor(i,6),:))/6;
end

%************************************  Calculate element areas  ************************************
Coor_s_x=zeros(n_s,6);
Coor_s_y=zeros(n_s,6);
Coor_r_x=zeros(n_r,6);
Coor_r_y=zeros(n_r,6);

for j=1:6
   Coor_s_x(:,j)=B_s_origin.data(Element_table_stator(:,j),1);
   Coor_s_y(:,j)=B_s_origin.data(Element_table_stator(:,j),2);
   Coor_r_x(:,j)=B_r_origin.data(Element_table_rotor(:,j),1);
   Coor_r_y(:,j)=B_r_origin.data(Element_table_rotor(:,j),2);
end

Aera_s=0.5*(Coor_s_x(:,1).*Coor_s_y(:,2)-Coor_s_x(:,1).*Coor_s_y(:,3)-
Coor_s_x(:,2).*Coor_s_y(:,1)+Coor_s_x(:,3).*Coor_s_y(:,1)+Coor_s_x(:,2).*Coor_s_y(:,3)-
Coor_s_x(:,3).*Coor_s_y(:,2));
Aera_r=0.5*(Coor_r_x(:,1).*Coor_r_y(:,2)-Coor_r_x(:,1).*Coor_r_y(:,3)-
Coor_r_x(:,2).*Coor_r_y(:,1)+Coor_r_x(:,3).*Coor_r_y(:,1)+Coor_r_x(:,2).*Coor_r_y(:,3)-
Coor_r_x(:,3).*Coor_r_y(:,2));

%*****************************  Calculate hysteresis loss components  *****************************
B_ele_s=sqrt(B_ele_s_x.^2+B_ele_s_y.^2);
B_ele_r=sqrt(B_ele_r_x.^2+B_ele_r_y.^2);
B_ele_r_rt=sqrt(B_ele_r_r.^2+B_ele_r_t.^2);

Bm_ele_s=max(B_ele_s');
Bm_ele_r=max(B_ele_r');

pFe_hys_ele_s_18s14p=periodicity*kf*kh*f*sum((Bm_ele_s').^2.*Aera_s)*La*1e-9;
pFe_hys_ele_r_18s14p=periodicity*kf*kh*f*sum((Bm_ele_r').^2.*Aera_r)*La*1e-9;

%**********  FFT of (Bx, By) on stator iron elements and (Br, Bt) on rotor iron elements  *********
B_ele_s_x_fft=fft(B_ele_s_x');
B_ele_s_x_ang=angle(B_ele_s_x_fft);
B_ele_s_x_h=abs(B_ele_s_x_fft)*2/n;
B_ele_s_x_h(1,:)=abs(B_ele_s_x_fft(1,:))/n;
```

```
B_ele_s_y_fft=fft(B_ele_s_y');
B_ele_s_y_ang=angle(B_ele_s_y_fft);
B_ele_s_y_h=abs(B_ele_s_y_fft)*2/n;
B_ele_s_y_h(1,:)=abs(B_ele_s_y_fft(1,:))/n;

B_ele_r_r_fft=fft(B_ele_r_r');
B_ele_r_r_ang=angle(B_ele_r_r_fft);
B_ele_r_r_h=abs(B_ele_r_r_fft)*2/n;
B_ele_r_r_h(1,:)=abs(B_ele_r_r_fft(1,:))/n;

B_ele_r_t_fft=fft(B_ele_r_t');
B_ele_r_t_ang=angle(B_ele_r_t_fft);
B_ele_r_t_h=abs(B_ele_r_t_fft)*2/n;
B_ele_r_t_h(1,:)=abs(B_ele_r_t_fft(1,:))/n;

B_ele_s_h=sqrt(B_ele_s_x_h(1:round(n/2),:).^2+B_ele_s_y_h(1:round(n/2),:).^2);
B_ele_r_rt_h=sqrt(B_ele_r_r_h(1:round(n/2),:).^2+B_ele_r_t_h(1:round(n/2),:).^2);

%**********  Calculate eddy current and excessive loss components of each element  **********
for k=1:round(n/2)
   pFe_eddy_ele_s_18s14p(k)=periodicity*kf*sigema*d^2/12*(2*pi*f/p)^2*(k-
1)^2*sum((B_ele_s_h(k,:).^2)'.*Aera_s)*La*(1e-9)*0.5;
   pFe_eddy_ele_r_18s14p_rt(k)=periodicity*kf*sigema*d^2/12*(2*pi*f/p)^2*(k-
1)^2*sum((B_ele_r_rt_h(k,:).^2)'.*Aera_r)*La*(1e-9)*0.5;

   pFe_exc_ele_s_18s14p(k)=periodicity*kf*ke*(2*pi*f/p)^1.5*(k-
1)^1.5*sum((B_ele_s_h(k,:).^1.5)'.*Aera_s)*La*(1e-9)*0.39344;
   pFe_exc_ele_r_18s14p_rt(k)=periodicity*kf*ke*(2*pi*f/p)^1.5*(k-
1)^1.5*sum((B_ele_r_rt_h(k,:).^1.5)'.*Aera_r)*La*(1e-9)*0.39344;
end

%**********  Calculate eddy current and excessive loss components of stator and rotor iron by
sum of element results  **********
pFe_eddy_ele_s_18s14p_total=sum(pFe_eddy_ele_s_18s14p);
pFe_eddy_ele_r_18s14p_rt_total=sum(pFe_eddy_ele_r_18s14p_rt);

pFe_exc_ele_s_18s14p_total=sum(pFe_exc_ele_s_18s14p);
pFe_exc_ele_r_18s14p_rt_total=sum(pFe_exc_ele_r_18s14p_rt);
```

APPENDIX B Reluctance Torque Evaluation Using Frozen Permeability Method

The flow chart of torque separation process using frozen permeability method has been shown in Fig. 3-16 and described in Section 3.5.2.2 in Chapter 3. The PYTHON script used to perform this process is attached as follows. The green texts are comments while red ones are important procedures users need to pay attention to. The red texts include two aspects:

(1) To avoid large errors in frozen permeability process, first order elements are recommended in mesh.

(2) To update the material properties at each time step using the permeability frozen at the condition with combined excitations (both magnets and currents), the scenario needs to be made only 2 steps initially and then continuously add new time steps onto it.

```
#************************************  Header information  ************************************
#! Preflu2D 11.1
import math;

#************************************  Define parameters  ************************************
p=3.0;                                  #Pole pair number
N_sample=64.0;                          #Time step number over one electrical period
N_points=int(N_sample)+2;
Ang_step=360.0/p/N_sample;              #Rotor angular position step

Project_name='PMOB/IPM_36s6p_v11_rated_fine_mesh_1st_order_rotorang_skew1';

#*****************************  Run scenario at given load condition  *****************************
saveProjectAs(Project_name+'.FLU');
generateFirstOrderElements();           #Generate first order mesh
Scenario['SCENARIO_PFE'].solve(projectName=getProjectName());
```

```
#*****************  Extract relative permeability of each node at each time step  ******************
for i in range(N_points):
        selectCurrentStep(activeScenario=Scenario['SCENARIO_PFE'],parameterValue=['ANG
POS_2_ROTATING='+str(Ang_step*i)]);
        ConstantTabulatedSpatialQuantityByValueStorageContinuous(spatialParameterName='
ur_rotor_'+str(i),
                                        formula='Mur',
                                        unit=Unit['Zero_dimension'],
                                        regionFace=[RegionFace['ROTOR']]);
        ConstantTabulatedSpatialQuantityByValueStorageContinuous(spatialParameterName='
ur_stator_'+str(i),
                                        formula='Mur',
                                        unit=Unit['Zero_dimension'],
                                        regionFace=[RegionFace['STATOR']]);
DeleteAllResults(deletePostprocessingResults='YES');
saveProjectAs(Project_name+'_frozen.FLU');

#************  Define new materials for laminations using the extracted permeability  *************
for i in range(N_points):
        lastInstance = Material(name='LAMINATION_R_'+str(i),
    propertyBH=PropertyBhLinearSpatial(mur='UR_ROTOR_'+str(i)));
        lastInstance = Material(name='LAMINATION_S_'+str(i),
    propertyBH=PropertyBhLinearSpatial(mur='UR_STATOR_'+str(i)));

#********  Update material properties with the new ones created above at 1st time step  *********
startMacroTransaction();
RegionFace['STATOR'].magneticTransient2D=MagneticTransient2DFaceMagnetic(material=Ma
terial['LAMINATION_S_1']);
RegionFace['ROTOR'].magneticTransient2D=MagneticTransient2DFaceMagnetic(material=Mat
erial['LAMINATION_R_1']);
endMacroTransaction();
try:
        Scenario['SCENARIO_FROZEN_TRANSIENT'].delete();
except:
        pass;
Scenario(name='SCENARIO_FROZEN_TRANSIENT');
startMacroTransaction();
Scenario['SCENARIO_FROZEN_TRANSIENT'].addPilot(pilot=MultiValues(parameter=Variation
Parameter['ANGPOS_2_ROTATING'],intervals=[IntervalStepValue(minValue=0.0,maxValue=An
g_step,stepValue=Ang_step)]));
```

```
endMacroTransaction();
saveProject();


#********  Remove magnet excitation and then re-run the scenario with the permeability at original load condition  *********
closeProject();
loadProject(Project_name+'_frozen.FLU');
saveProjectAs(Project_name+'_frozen_0M.FLU');
Material['SINTERED_N35EH'].propertyBH=PropertyBhLinear(mur='1.1');     #Remove magnet
Scenario['SCENARIO_FROZEN_TRANSIENT'].solve(projectName=getProjectName());
for i in range(int(N_sample)):
        startMacroTransaction();
        Scenario['SCENARIO_FROZEN_TRANSIENT'].pilots['ANGPOS_2_ROTATING'].addInterval(Interval=IntervalStepValue(minValue=Ang_step*(i+1.0),maxValue=Ang_step*(i+2.0),stepValue=Ang_step));                    #Continuously add the new time step into the scenario
        endMacroTransaction();
        RegionFace['ROTOR'].changeMater(material=Material['LAMINATION_R_'+str(i+2)]);
        RegionFace['STATOR'].changeMater(material=Material['LAMINATION_S_'+str(i+2)]);
        Scenario['SCENARIO_FROZEN_TRANSIENT'].continueToSolve(projectName=getProjectName(),option='IterateOnNonConvergentSteps');
saveProject();


#********  Set iq=0 and then re-run the scenario with the permeability at original load condition *********


closeProject();
loadProject(Project_name+'_frozen.FLU');
saveProjectAs(Project_name+'_frozen_0Iq.FLU');
I0=VariationParameter['ACS'].referenceValue;
Gamma0=VariationParameter['GAMMA'].referenceValue;
I1=I0*math.sin(Gamma0/180.0*math.pi);
Gamma1=90.0;
VariationParameter['ACS'].referenceValue=I1;
VariationParameter['GAMMA'].referenceValue=Gamma1;
Scenario['SCENARIO_FROZEN_TRANSIENT'].solve(projectName=getProjectName());
for i in range(int(N_sample)):
        startMacroTransaction();
        Scenario['SCENARIO_FROZEN_TRANSIENT'].pilots['ANGPOS_2_ROTATING'].addInterval(Interval=IntervalStepValue(minValue=Ang_step*(i+1.0),maxValue=Ang_step*(i+2.0),stepValue=Ang_step));
        endMacroTransaction();
```

```
        RegionFace['ROTOR'].changeMater(material=Material['LAMINATION_R_'+str(i+2)]);
        RegionFace['STATOR'].changeMater(material=Material['LAMINATION_S_'+str(i+2)]);
        Scenario['SCENARIO_FROZEN_TRANSIENT'].continueToSolve(projectName=getProj
ectName(),option='IterateOnNonConvergentSteps');
saveProject();

#********  Set id=0 and then re-run the scenario with the permeability at original load condition
*********
closeProject();
loadProject(Project_name+'_frozen.FLU');
saveProjectAs(Project_name+'_frozen_0Id.FLU');
I0=VariationParameter['ACS'].referenceValue;
Gamma0=VariationParameter['GAMMA'].referenceValue;
I1=I0*math.cos(Gamma0/180.0*math.pi);
Gamma1=0.0;
VariationParameter['ACS'].referenceValue=I1;
VariationParameter['GAMMA'].referenceValue=Gamma1;
Scenario['SCENARIO_FROZEN_TRANSIENT'].solve(projectName=getProjectName());
for i in range(int(N_sample)):
        startMacroTransaction();
        Scenario['SCENARIO_FROZEN_TRANSIENT'].pilots['ANGPOS_2_ROTATING'].addInt
erval(Interval=IntervalStepValue(minValue=Ang_step*(i+1.0),maxValue=Ang_step*(i+2.0),stepV
alue=Ang_step));
        endMacroTransaction();
        RegionFace['ROTOR'].changeMater(material=Material['LAMINATION_R_'+str(i+2)]);
        RegionFace['STATOR'].changeMater(material=Material['LAMINATION_S_'+str(i+2)]);
        Scenario['SCENARIO_FROZEN_TRANSIENT'].continueToSolve(projectName=getProj
ectName(),option='IterateOnNonConvergentSteps');
saveProject();

#********  Remove magnet excitation and also set iq=0 and then re-run the scenario with the
permeability at original load condition  *********
closeProject();
loadProject(Project_name+'_frozen.FLU');
saveProjectAs(Project_name+'_frozen_only_id.FLU');
Material['SINTERED_N35EH'].propertyBH=PropertyBhLinear(mur='1.1');
I0=VariationParameter['ACS'].referenceValue;
Gamma0=VariationParameter['GAMMA'].referenceValue;
I1=I0*math.sin(Gamma0/180.0*math.pi);
Gamma1=90.0;
VariationParameter['ACS'].referenceValue=I1;
```

```
VariationParameter['GAMMA'].referenceValue=Gamma1;
Scenario['SCENARIO_FROZEN_TRANSIENT'].solve(projectName=getProjectName());
for i in range(int(N_sample)):
	startMacroTransaction();
	Scenario['SCENARIO_FROZEN_TRANSIENT'].pilots['ANGPOS_2_ROTATING'].addInterval(Interval=IntervalStepValue(minValue=Ang_step*(i+1.0),maxValue=Ang_step*(i+2.0),stepValue=Ang_step));
	endMacroTransaction();
	RegionFace['ROTOR'].changeMater(material=Material['LAMINATION_R_'+str(i+2)]);
	RegionFace['STATOR'].changeMater(material=Material['LAMINATION_S_'+str(i+2)]);
	Scenario['SCENARIO_FROZEN_TRANSIENT'].continueToSolve(projectName=getProjectName(),option='IterateOnNonConvergentSteps');
saveProject();

#********  Remove magnet excitation and also set id=0 and then re-run the scenario with the permeability at original load condition  *********
closeProject();
loadProject(Project_name+'_frozen.FLU');
saveProjectAs(Project_name+'_frozen_only_iq.FLU');
Material['SINTERED_N35EH'].propertyBH=PropertyBhLinear(mur='1.1');
I0=VariationParameter['ACS'].referenceValue;
Gamma0=VariationParameter['GAMMA'].referenceValue;
I1=I0*math.cos(Gamma0/180.0*math.pi);
Gamma1=0.0;
VariationParameter['ACS'].referenceValue=I1;
VariationParameter['GAMMA'].referenceValue=Gamma1;
Scenario['SCENARIO_FROZEN_TRANSIENT'].solve(projectName=getProjectName());
for i in range(int(N_sample)):
	startMacroTransaction();
	Scenario['SCENARIO_FROZEN_TRANSIENT'].pilots['ANGPOS_2_ROTATING'].addInterval(Interval=IntervalStepValue(minValue=Ang_step*(i+1.0),maxValue=Ang_step*(i+2.0),stepValue=Ang_step));
	endMacroTransaction();
	RegionFace['ROTOR'].changeMater(material=Material['LAMINATION_R_'+str(i+2)]);
	RegionFace['STATOR'].changeMater(material=Material['LAMINATION_S_'+str(i+2)]);
	Scenario['SCENARIO_FROZEN_TRANSIENT'].continueToSolve(projectName=getProjectName(),option='IterateOnNonConvergentSteps');
saveProject();

#********  Set id=0, iq=0 and then re-run the scenario with the permeability at original load condition  *********
```

```
closeProject();
loadProject(Project_name+'_frozen.FLU');
saveProjectAs(Project_name+'_frozen_only_mag.FLU');
VariationParameter['ACS'].referenceValue=0.0;
VariationParameter['GAMMA'].referenceValue=0.0;
Scenario['SCENARIO_FROZEN_TRANSIENT'].solve(projectName=getProjectName());
for i in range(int(N_sample)):
        startMacroTransaction();
        Scenario['SCENARIO_FROZEN_TRANSIENT'].pilots['ANGPOS_2_ROTATING'].addInterval(Interval=IntervalStepValue(minValue=Ang_step*(i+1.0),maxValue=Ang_step*(i+2.0),stepValue=Ang_step));
        endMacroTransaction();
        RegionFace['ROTOR'].changeMater(material=Material['LAMINATION_R_'+str(i+2)]);
        RegionFace['STATOR'].changeMater(material=Material['LAMINATION_S_'+str(i+2)]);

        Scenario['SCENARIO_FROZEN_TRANSIENT'].continueToSolve(projectName=getProjectName(),option='IterateOnNonConvergentSteps');
saveProject();
```

APPENDIX C MMF Harmonic Calculation for a Given Winding Configuration

For a given winding configuration, its MMF spectra due to current excitation is calculated using the following MATLAB script. Taking 9-phase 18-slot 14-pole winding configuration as an example, firstly, current array for each phase is created according to the winding configuration arrangement. Each current array contains 18 elements corresponding to 18-slots. As shown in the script below, "1" element means 1 coil conductor with positive current at the corresponding slot position. On the contrary, "-1" element represents 1 coil conductor with negative current at the corresponding slot position. "0" element means no coil conductor at that corresponding slot position.

Subsequently, the MMF waveform of each phase is produced based on the current array contents. According to sampling and FFT theories, MMF waveform containing 18 elements (samples) can only predict up to 9 order harmonics. To obtain more harmonic orders via FFT, the number of samples of MMF has to be increased. Therefore, the mechanical space is split into very fine angular elements (4096 elements in this example). Thus, much finer MMF waveform of each phase can be generated. After that, the total MMF is calculated by the sum of phase MMFs. Finally, the MMF harmonics of this winding configuration are obtained by performing FFT of the total MMF.

```
%****************************************  Parameter definition  ****************************************
p=7;              %Pole pair number
ns=18;            %Slot number
N=1;              %Number of turns per coil

%*****************  9-phase 18-slot 14-pole winding configuration arrangement  ******************
%****************  Current array contains 18 elements corresponding to 18 slots  *****************
```

```
%************************  "1" means 1 coil conductor with positive current  ************************
%************************  "-1" means 1 coil conductor with negative current  ************************
%*****************************  "0" means no coil conductor in that slot  *****************************
Ia_18s14p_9phase=[1,-1,0,0,0,0,0,0,0,-1,1,0,0,0,0,0,0,0,0];
Ib_18s14p_9phase=cosd(-120)*[0,0,0,0,0,0,0,1,-1,0,0,0,0,0,0,0,0,-1,1,0];
Ic_18s14p_9phase=cosd(-240)*[0,0,0,-1,1,0,0,0,0,0,0,0,0,1,-1,0,0,0,0];
Id_18s14p_9phase=cosd(-20)*[0,0,0,0,-1,1,0,0,0,0,0,0,0,0,1,-1,0,0,0];
Ie_18s14p_9phase=cosd(-120-20)*[0,1,-1,0,0,0,0,0,0,0,-1,1,0,0,0,0,0,0,0];
If_18s14p_9phase=cosd(-240-20)*[0,0,0,0,0,0,0,0,1,-1,0,0,0,0,0,0,0,0,-1,1];
Ig_18s14p_9phase=cosd(-40)*[1,0,0,0,0,0,0,0,0,1,-1,0,0,0,0,0,0,0,0,-1];
Ih_18s14p_9phase=cosd(-120-40)*[0,0,0,0,0,0,-1,1,0,0,0,0,0,0,0,0,1,-1,0,0];
Ii_18s14p_9phase=cosd(-240-40)*[0,0,1,-1,0,0,0,0,0,0,0,0,-1,1,0,0,0,0,0,0];

%*******************  Split mechanical space into very fine angular elements  *******************
N_sample=4096;          %Number of samples
Slots=1:ns;
SSlots=ns/N_sample:ns/N_sample:ns;
SSlots_ang=0:360/N_sample:(360-360/N_sample);

%********  Produce MMF waveform for each phase according to winding arrangement  *********
Fa_18s14p_9phase(1)=N*Ia_18s14p_9phase(1);
for i=2:length(Ia_18s14p_9phase)
   Fa_18s14p_9phase(i)=Fa_18s14p_9phase(i-1)+N*Ia_18s14p_9phase(i);
end

Fb_18s14p_9phase(1)=N*Ib_18s14p_9phase(1);
for i=2:length(Ib_18s14p_9phase)
   Fb_18s14p_9phase(i)=Fb_18s14p_9phase(i-1)+N*Ib_18s14p_9phase(i);
end

Fc_18s14p_9phase(1)=N*Ic_18s14p_9phase(1);
for i=2:length(Ic_18s14p_9phase)
   Fc_18s14p_9phase(i)=Fc_18s14p_9phase(i-1)+N*Ic_18s14p_9phase(i);
end

Fd_18s14p_9phase(1)=N*Id_18s14p_9phase(1);
for i=2:length(Id_18s14p_9phase)
   Fd_18s14p_9phase(i)=Fd_18s14p_9phase(i-1)+N*Id_18s14p_9phase(i);
end
```

```
Fe_18s14p_9phase(1)=N*Ie_18s14p_9phase(1);
for i=2:length(Ie_18s14p_9phase)
   Fe_18s14p_9phase(i)=Fe_18s14p_9phase(i-1)+N*Ie_18s14p_9phase(i);
end

Ff_18s14p_9phase(1)=N*If_18s14p_9phase(1);
for i=2:length(If_18s14p_9phase)
   Ff_18s14p_9phase(i)=Ff_18s14p_9phase(i-1)+N*If_18s14p_9phase(i);
end

Fg_18s14p_9phase(1)=N*Ig_18s14p_9phase(1);
for i=2:length(Ig_18s14p_9phase)
   Fg_18s14p_9phase(i)=Fg_18s14p_9phase(i-1)+N*Ig_18s14p_9phase(i);
end

Fh_18s14p_9phase(1)=N*Ih_18s14p_9phase(1);
for i=2:length(Ih_18s14p_9phase)
   Fh_18s14p_9phase(i)=Fh_18s14p_9phase(i-1)+N*Ih_18s14p_9phase(i);
end

Fi_18s14p_9phase(1)=N*Ii_18s14p_9phase(1);
for i=2:length(Ii_18s14p_9phase)
   Fi_18s14p_9phase(i)=Fi_18s14p_9phase(i-1)+N*Ii_18s14p_9phase(i);
end

%*****************************  Generate much finer MMF waveforms  ****************************
 for i=1:ns-1
   Index(i)=find(SSlots>=i,1,'first');
   Index(i+1)=find(SSlots>=i+1,1,'first');
   FFa_18s14p_9phase(Index(i):Index(i+1))=Fa_18s14p_9phase(i);
   FFb_18s14p_9phase(Index(i):Index(i+1))=Fb_18s14p_9phase(i);
   FFc_18s14p_9phase(Index(i):Index(i+1))=Fc_18s14p_9phase(i);
   FFd_18s14p_9phase(Index(i):Index(i+1))=Fd_18s14p_9phase(i);
   FFe_18s14p_9phase(Index(i):Index(i+1))=Fe_18s14p_9phase(i);
   FFf_18s14p_9phase(Index(i):Index(i+1))=Ff_18s14p_9phase(i);
   FFg_18s14p_9phase(Index(i):Index(i+1))=Fg_18s14p_9phase(i);
   FFh_18s14p_9phase(Index(i):Index(i+1))=Fh_18s14p_9phase(i);
   FFi_18s14p_9phase(Index(i):Index(i+1))=Fi_18s14p_9phase(i);
```

```
end

FFa_18s14p_9phase(1:Index(1))=Fa_18s14p_9phase(ns);
FFa_18s14p_9phase_mean=mean(FFa_18s14p_9phase);
FFa_18s14p_9phase=FFa_18s14p_9phase-FFa_18s14p_9phase_mean;

FFb_18s14p_9phase(1:Index(1))=Fb_18s14p_9phase(ns);
FFb_18s14p_9phase_mean=mean(FFb_18s14p_9phase);
FFb_18s14p_9phase=FFb_18s14p_9phase-FFb_18s14p_9phase_mean;

FFc_18s14p_9phase(1:Index(1))=Fc_18s14p_9phase(ns);
FFc_18s14p_9phase_mean=mean(FFc_18s14p_9phase);
FFc_18s14p_9phase=FFc_18s14p_9phase-FFc_18s14p_9phase_mean;

FFd_18s14p_9phase(1:Index(1))=Fd_18s14p_9phase(ns);
FFd_18s14p_9phase_mean=mean(FFd_18s14p_9phase);
FFd_18s14p_9phase=FFd_18s14p_9phase-FFd_18s14p_9phase_mean;

FFe_18s14p_9phase(1:Index(1))=Fe_18s14p_9phase(ns);
FFe_18s14p_9phase_mean=mean(FFe_18s14p_9phase);
FFe_18s14p_9phase=FFe_18s14p_9phase-FFe_18s14p_9phase_mean;

FFf_18s14p_9phase(1:Index(1))=Ff_18s14p_9phase(ns);
FFf_18s14p_9phase_mean=mean(FFf_18s14p_9phase);
FFf_18s14p_9phase=FFf_18s14p_9phase-FFf_18s14p_9phase_mean;

FFg_18s14p_9phase(1:Index(1))=Fg_18s14p_9phase(ns);
FFg_18s14p_9phase_mean=mean(FFg_18s14p_9phase);
FFg_18s14p_9phase=FFg_18s14p_9phase-FFg_18s14p_9phase_mean;

FFh_18s14p_9phase(1:Index(1))=Fh_18s14p_9phase(ns);
FFh_18s14p_9phase_mean=mean(FFh_18s14p_9phase);
FFh_18s14p_9phase=FFh_18s14p_9phase-FFh_18s14p_9phase_mean;

FFi_18s14p_9phase(1:Index(1))=Fi_18s14p_9phase(ns);
FFi_18s14p_9phase_mean=mean(FFi_18s14p_9phase);
FFi_18s14p_9phase=FFi_18s14p_9phase-FFi_18s14p_9phase_mean;

%**********  Calculate the total MMF with sum of MMF from each phase  **********
```

```
FF_18s14p_9phase=FFa_18s14p_9phase+FFb_18s14p_9phase+FFc_18s14p_9phase+FFd_1
8s14p_9phase+FFe_18s14p_9phase+FFf_18s14p_9phase+FFg_18s14p_9phase+FFh_18s14
p_9phase+FFi_18s14p_9phase;


%************************************  FFT of the total MMF  ************************************
FF_18s14p_9phase_fft=fft(FF_18s14p_9phase);
FF_18s14p_9phase_ang=angle(FF_18s14p_9phase_fft);
FF_18s14p_9phase_h=abs(FF_18s14p_9phase_fft)*2/N_sample;
FF_18s14p_9phase_h(1)=abs(FF_18s14p_9phase_fft(1))/N_sample;
```

APPENDIX D Inverse Solution of Currents versus Flux-linkages

To build the computationally efficient and high-fidelity IPM machine model shown in Chapter 5, the key is to obtain $i_d(\Psi_d,\Psi_q,\theta)$ and $i_q(\Psi_d,\Psi_q,\theta)$ based on $\Psi_d(i_d,i_q,\theta)$ and $\Psi_q(i_d,i_q,\theta)$ extracted from FEA. This section describes the detailed procedures of both the extraction of $\Psi_d(i_d,i_q,\theta)$ and $\Psi_q(i_d,i_q,\theta)$ and also the calculation of $i_d(\Psi_d,\Psi_q,\theta)$ and $i_q(\Psi_d,\Psi_q,\theta)$.

Fig. D-1 shows the flow chart of $\Psi_d(i_d,i_q,\theta)$, $\Psi_q(i_d,i_q,\theta)$ and also $T_{em}(i_d,i_q,\theta)$ extraction from FEA. This process is performed in FLUX2D by the PYTHON script attached below. Firstly, define parameters, such as i_d, i_q and θ ranges, the alignment angle between d-axis and phase A to perform the d-q transformation, and also NO. of time steps. Then, initialise FLUX I/O parameters, such as the operation speed and also the parameters corresponding to definition of currents (using d-q components i_d,i_q or magnitude and current angle I_m,γ). Subsequently, initialise output file including its name and column indications. Finally, solve the scenario at various load conditions and output $\Psi_d(i_d,i_q,\theta)$, $\Psi_q(i_d,i_q,\theta)$ and $T_{em}(i_d,i_q,\theta)$. The various load conditions cover all the i_d, i_q samples defined in the first step.

It should be noted that if stepped skew technique is employed in the machine, the above process should be performed for each machine stack. Then the flux-linkages and table tables of all stacks need to be averaged to generate the final $\Psi_d(i_d,i_q,\theta)$, $\Psi_q(i_d,i_q,\theta)$ and $T_{em}(i_d,i_q,\theta)$.

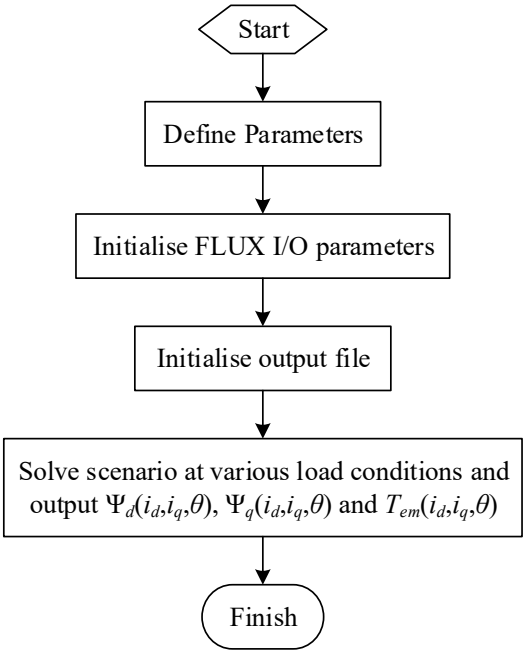

Fig. D-1. Flow chart of d- and q-axis flux-linkages and torque tables extraction from FEA.

Fig. D-2 shows the flow chart of inverse solution of $\Psi_d(i_d,i_q,\theta)$ and $\Psi_q(i_d,i_q,\theta)$ to obtain $i_d(\Psi_d,\Psi_q,\theta)$ and $i_q(\Psi_d,\Psi_q,\theta)$. A MATLAB script is programed to achieve this. The script contains 1 main function and 3 sub-functions shown below. Firstly, import $\Psi_d(i_d,i_q,\theta)$, $\Psi_q(i_d,i_q,\theta)$ and $T_{em}(i_d,i_q,\theta)$. Then, define parameters including global variables used in the main and sub-functions, i_d, i_q and θ ranges, and also time steps. Next, it is the data process for the preparation of inverse solution, including changing the data dimensions from 36375×1 to 97×25×15 for call convenience in future and also generating mesh grids of i_d, i_q and Ψ_d, Ψ_q for interpolation convenience in future. Subsequently, it is the inverse solution of $\Psi_d(i_d,i_q,\theta)$, $\Psi_q(i_d,i_q,\theta)$ to obtain $i_d(\Psi_d,\Psi_q,\theta)$, $i_q(\Psi_d,\Psi_q,\theta)$. The principle and algorithm have been described in Section 5.3.2, Chapter 5. After that, it is the first round error analysis by calculating the errors of Ψ_d, Ψ_q by substituting i_d, i_q obtained from $i_d(\Psi_d,\Psi_q,\theta)$, $i_q(\Psi_d,\Psi_q,\theta)$ into original $\Psi_d(i_d,i_q,\theta)$, $\Psi_q(i_d,i_q,\theta)$. If the error at certain load condition exceeds the predefined limit, replace i_d, i_q with interpolated i_d, i_q according to q-axis data at other load conditions. This process is named by "first round correction of $i_d(\Psi_d,\Psi_q,\theta)$ and $i_q(\Psi_d,\Psi_q,\theta)$". After that, perform

second round error analysis using the corrected $i_d(\Psi_d,\Psi_q,\theta)$ and $i_q(\Psi_d,\Psi_q,\theta)$. Then, carry out the second round correction of $i_d(\Psi_d,\Psi_q,\theta)$ and $i_q(\Psi_d,\Psi_q,\theta)$ by interpolating i_d, i_q according to d-axis data at other load conditions when the error at certain load condition exceeds the predefined limit. Subsequently, it is the third round error analysis. Finally, output the final $i_d(\Psi_d,\Psi_q,\theta)$, $i_q(\Psi_d,\Psi_q,\theta)$ and also $T_{em}(i_d,i_q,\theta)$ to MAT files which can be called by SIMULINK model.

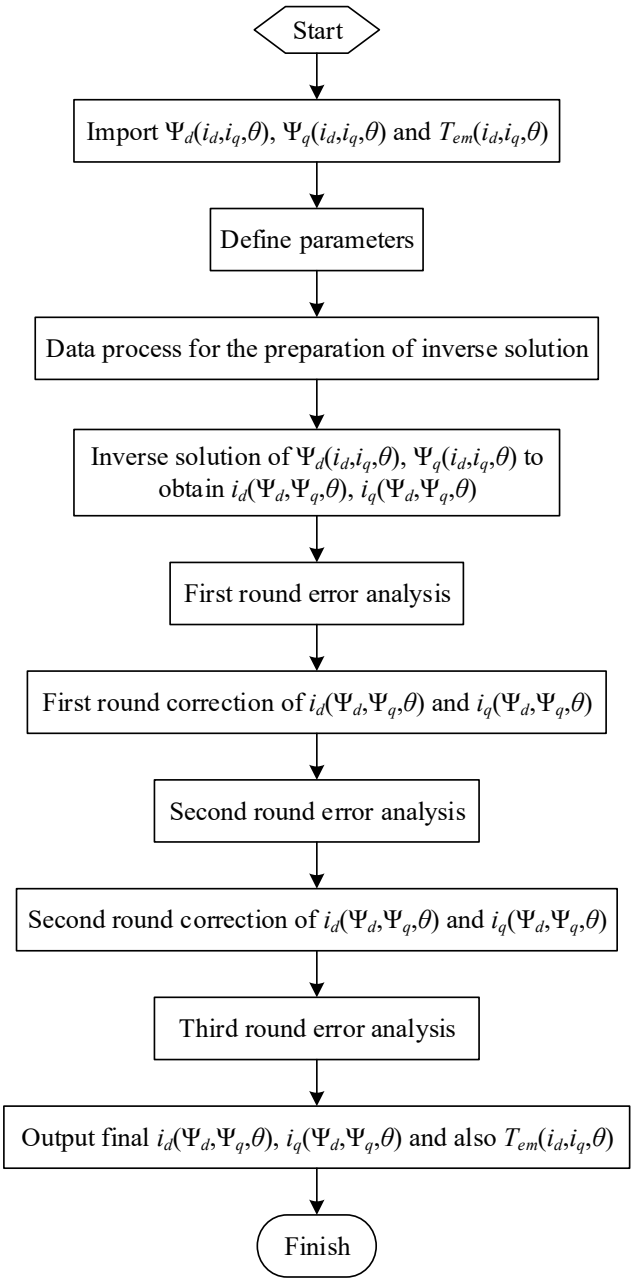

Fig. D-2. Flow chart of inverse solution of $\Psi_d(i_d,i_q,\theta)$ and $\Psi_q(i_d,i_q,\theta)$ to obtain $i_d(\Psi_d,\Psi_q,\theta)$ and $i_q(\Psi_d,\Psi_q,\theta)$.

It should be noted that the predefined error limits for both Ψ_d and Ψ_q are 0.1% which is defined by the ratio of flux-linkage error and the maximum flux-linkage variation range. Most of Ψ_d and Ψ_q errors at the first round error analysis are within 0.1% and only a few i_d, i_q need to be corrected. This is also the fundamental of using interpolation to correct errors. After two round error corrections, almost all of Ψ_d and Ψ_q errors are within 0.1%. The difference between the first and second round error corrections of $i_d(\Psi_d,\Psi_q,\theta)$ and $i_q(\Psi_d,\Psi_q,\theta)$ is that the former utilises q-axis data to do the interpolation while the later one uses d-axis data.

```
#*****************  PYTHON script to obtain Ψd(id,iq,θ), Ψq(id,iq,θ) and Tem(id,iq,θ)  ******************
#*****************************************  Header information  *****************************************
#! Preflu2D 11.1
import math;
import copy;

#*************************************  Define parameters  *************************************
B_speed=1350.0;         #Base speed
P_r=3.0;                #Pole pair number
Ns_r=int(96);           #Number of steps
Gamma_D_=240.0;         #phase angle for phase A d-axis current source expression (not d-axis angle away from middle line angle)
ANG_mech=10.0;          #Rotor should be rotated by 10 mech degree in advance

Id_min0=-140.0;         #min in Id scanning;
Id_max0=140.0;          #max in Id scanning;
Iq_min0=-240.0;         #min in Iq scanning;
Iq_max0=240.0;          #max in Iq scanning;

N_Id=15;                #sample number in Id scanning;
N_Iq=25;                #sample number in Iq scanning;
Id_step=(Id_max0-Id_min0)/(N_Id-1);
```

```
Iq_step=(Iq_max0-Iq_min0)/(N_Iq-1);
PeriodPart=6.0;            #FE Model periodicity;

min_pfe_r=360.0/P_r/Ns_r*2.0;
max_pfe_r=360.0/P_r/Ns_r*(Ns_r+2.0);

min_fe_r1=60.0/B_speed/P_r/Ns_r*2.0;
max_fe_r1=60.0/B_speed/P_r/Ns_r*(Ns_r+2.0);
alpha_=Gamma_D_-90.0;

#**********************************  Initialise FLUX I/O parameters  **********************************
VariationParameter['AMP_TRUE'].referenceValue=0.0;
VariationParameter['IDCS_TRUE'].referenceValue=1.0;
VariationParameter['IQCS_TRUE'].referenceValue=1.0;
VariationParameter['Speed'].referenceValue=B_speed;

#**************************************  Initialise output file  **************************************
my_file=open("PMOB_IPM_36s6p_simulink_data_integer_rotorang_new2_neg_iq_T120_skew
1.txt","a");
my_file.write("ia"+"\t"+"ib"+"\t"+"ic"+"\t"+"id"+"\t"+"iq"+"\t"+"theta"+"\t"+"psi_a"+"\t"+"psi_b"+"\t"+"
psi_c"+"\t"+"psi_d"+"\t"+"psi_q"+"\t"+"Torque"+"\t");
my_file.write("\n");
my_file.close();

#*************  Solve scenario at various load conditions and output Ψd(id,iq,θ), Ψq(id,iq,θ) and
Tem(id,iq,θ)  *************
for i in range(N_Id):
        VariationParameter['IDCS'].referenceValue=Id_min0+i*Id_step;
        for j in range(N_Iq):
                VariationParameter['IQCS'].referenceValue=Iq_min0+j*Iq_step;
                Scenario['SCENARIO_SIMULINK'].solve(projectName=getProjectName());
                EvolutiveCurve2D(name='Torque',evolutivePath=EvolutivePath(parameterSet=[
SetParameterXVariable(paramEvol=VariationParameter['ANGPOS_2_ROTATING'],limi
tMin=min_pfe_r,limitMax=max_pfe_r)]),formula=['TorqueElecMag(2_ROTATING)']);
                Torque1=CurveVariation2D['Torque'].y[0].values;
                theta1=CurveVariation2D['Torque'].xAxis.x;
                EvolutiveCurve2D(name='psi',evolutivePath=EvolutivePath(parameterSet=[Set
ParameterXVariable(paramEvol=VariationParameter['ANGPOS_2_ROTATING'],limitMi
n=min_pfe_r,limitMax=max_pfe_r)]),formula=['PSI_A1','PSI_B1','PSI_C2']);
                Psi_A1=CurveVariation2D['psi'].y[0].values;
                Psi_B1=CurveVariation2D['psi'].y[1].values;
```

```
        Psi_C1=CurveVariation2D['psi'].y[2].values;
        EvolutiveCurve2D(name='I',evolutivePath=EvolutivePath(parameterSet=[SetPa
rameterXVariable(paramEvol=VariationParameter['ANGPOS_2_ROTATING'],limitMin=
min_pfe_r,limitMax=max_pfe_r)]),formula=['I(A1)','I(B1)','I(C2)']);
        I_A1=CurveVariation2D['I'].y[0].values;
        I_B1=CurveVariation2D['I'].y[1].values;
        I_C1=CurveVariation2D['I'].y[2].values;
        Scenario['SCENARIO_SIMULINK'].deleteAllResults();
        my_file=open("PMOB_IPM_36s6p_simulink_data_integer_rotorang_new2_neg
_iq_T120_skew1.txt","a");
        for k in range(Ns_r+1):
            I_d1=2.0/3.0*(I_A1[k]*math.cos((theta1[k]*P_r+alpha_)*math.pi/180.0)+
I_B1[k]*math.cos((theta1[k]*P_r+alpha_-
120.0)*math.pi/180.0)+I_C1[k]*math.cos((theta1[k]*P_r+alpha_+120.0)*math.pi/
180.0));
            I_q1=-
2.0/3.0*(I_A1[k]*math.sin((theta1[k]*P_r+alpha_)*math.pi/180.0)+I_B1[k]*math.s
in((theta1[k]*P_r+alpha_-
120.0)*math.pi/180.0)+I_C1[k]*math.sin((theta1[k]*P_r+alpha_+120.0)*math.pi/
180.0));
            Psi_d1=2.0/3.0*(Psi_A1[k]*math.cos((theta1[k]*P_r+alpha_)*math.pi/18
0.0)+Psi_B1[k]*math.cos((theta1[k]*P_r+alpha_-
120.0)*math.pi/180.0)+Psi_C1[k]*math.cos((theta1[k]*P_r+alpha_+120.0)*math.
pi/180.0));
            Psi_q1=-
2.0/3.0*(Psi_A1[k]*math.sin((theta1[k]*P_r+alpha_)*math.pi/180.0)+Psi_B1[k]*
math.sin((theta1[k]*P_r+alpha_-
120.0)*math.pi/180.0)+Psi_C1[k]*math.sin((theta1[k]*P_r+alpha_+120.0)*math.
pi/180.0));
            my_file.write(str(I_A1[k])+"\t"+str(I_B1[k])+"\t"+str(I_C1[k])+"\t"+str(I_d1)
+"\t"+str(I_q1)+"\t"+str(theta1[k])+"\t"+str(Psi_A1[k])+"\t"+str(Psi_B1[k])+"\t"+str(
Psi_C1[k])+"\t"+str(Psi_d1)+"\t"+str(Psi_q1)+"\t"+str(Torque1[k])+"\t");
            my_file.write("\n");
        my_file.close();
```

```
%*********************  MATLAB script to obtain id(Ψd,Ψq,θ) and iq(Ψd,Ψq,θ)  ***********************
%*****************************************  Main function  *****************************************
%*************************************  Header information  *************************************
clear;
clc;

%****************************  Import Ψd(id,iq,θ), Ψq(id,iq,θ) and Tem(id,iq,θ)  ***************************
load('psi_table_after_skew_rotorang_neg_iq_new2_T120.mat');
```

```
%************************************** Define parameters ***************************************
global ID_0 IQ_0 PSI_D_0 PSI_Q_0 INDEX_THETA PSI_D_REF PSI_Q_REF
PSI_EQ_RANGE

INDEX_THETA=1;
PSI_D_REF=0;
PSI_Q_REF=0;
Tolerance_ref=0.001;
N_theta=97;
N_theta_steps=N_theta-1;
N_Id=15;
N_Iq=25;
p=3;
Id_min=-140;
Id_max=140;
Iq_min=-240;
Iq_max=240;
id_0_v=Id_min:20:Id_max;
iq_0_v=Iq_min:20:Iq_max;
theta_0_v=360/p/N_theta_steps*2:360/p/N_theta_steps:360/p/N_theta_steps*(N_theta+1);

%********************** Data process for the preparation of inverse solution **********************
psi_d_00=reshape(psi_table(:,4),N_theta,N_Iq,N_Id);
psi_q_00=reshape(psi_table(:,5),N_theta,N_Iq,N_Id);
Torque_00=reshape(psi_table(:,6),N_theta,N_Iq,N_Id);
id_00=reshape(psi_table(:,1),N_theta,N_Iq,N_Id);
iq_00=reshape(psi_table(:,2),N_theta,N_Iq,N_Id);

[m,n,k]=size(psi_d_00);
for i=1:m
   PSI_D_0{1,i}=reshape(psi_d_00(i,:,:),n,k);
   PSI_Q_0{1,i}=reshape(psi_q_00(i,:,:),n,k);
   TORQUE_0{1,i}=reshape(Torque_00(i,:,:),n,k);
end

[ID_0,IQ_0]=meshgrid(id_0_v,iq_0_v);

for i=1:m
   psi_d_min_buf(i)=max(min(PSI_D_0{1,i}'));
```

```
    psi_d_max_buf(i)=min(max(PSI_D_0{1,i}'));
    psi_q_min_buf(i)=max(min(PSI_Q_0{1,i}));
    psi_q_max_buf(i)=min(max(PSI_Q_0{1,i}));
end

psi_d_min=max(psi_d_min_buf);
psi_d_max=min(psi_d_max_buf);
psi_q_min=max(psi_q_min_buf);
psi_q_max=min(psi_q_max_buf);

PSI_EQ_RANGE=(psi_d_max-psi_d_min)+(psi_q_max-psi_q_min);

psi_d_v=linspace(psi_d_min,psi_d_max,16);
psi_q_v=linspace(psi_q_min,psi_q_max,16);
[psi_d,psi_q]=meshgrid(psi_d_v,psi_q_v);

n_err=0;

%***************  Inverse solution of Ψd(id,iq,θ), Ψq(id,iq,θ) to obtain id(Ψd,Ψq,θ) and iq(Ψd,Ψq,θ)
****************
for i=1:m
    for j=1:length(psi_q_v)
        for k=1:length(psi_d_v)

[flag_err{1,i}(j,k),tolerance_psi{1,i}(j,k),id{1,i}(j,k),iq{1,i}(j,k)]=f_id_iq_tool(psi_d_v(k),psi_q_v(j),i,I
d_min,Id_max,Iq_min,Iq_max);
            [psi_d_verify{1,i}(j,k),psi_q_verify{1,i}(j,k)]=f_psi_d_q(id{1,i}(j,k),iq{1,i}(j,k));
            % First round error analysis
            psi_d_err{1,i}(j,k)=(psi_d_verify{1,i}(j,k)-psi_d_v(k))/(psi_d_max-psi_d_min);
            psi_q_err{1,i}(j,k)=(psi_q_verify{1,i}(j,k)-psi_q_v(j))/(psi_q_max-psi_q_min);
        end
    end
end

%**********************  First round correction of id(Ψd,Ψq,θ) and iq(Ψd,Ψq,θ)  **********************
for i=1:m
    for k=1:length(psi_d_v)
        ind_q_q=0;
        ind_q_d=0;
        for j=1:length(psi_q_v)
```

```
        if abs(psi_q_err{1,i}(j,k))<=Tolerance_ref || j==1 || j==length(psi_q_v)   %scan q
            ind_q_q=ind_q_q+1;
            iq_buf_q{1,i}(ind_q_q,k)=iq{1,i}(j,k);
            psi_q_buf_q{1,i}(ind_q_q,k)=psi_q_v(j);
        end
        if abs(psi_d_err{1,i}(j,k))<=Tolerance_ref || j==1 || j==length(psi_q_v)   %scan q
            ind_q_d=ind_q_d+1;
            id_buf_q{1,i}(ind_q_d,k)=id{1,i}(j,k);
            psi_q_buf_d{1,i}(ind_q_d,k)=psi_q_v(j);
        end
    end
    if ind_q_q==length(psi_q_v)
        iq_final_1{1,i}(:,k)=iq_buf_q{1,i}(:,k);
    else

iq_final_1{1,i}(:,k)=interp1(psi_q_buf_q{1,i}(1:ind_q_q,k),iq_buf_q{1,i}(1:ind_q_q,k),psi_q_v','spli
ne');
    end
    if ind_q_d==length(psi_q_v)
        id_final_1{1,i}(:,k)=id_buf_q{1,i}(:,k);
    else

id_final_1{1,i}(:,k)=interp1(psi_q_buf_d{1,i}(1:ind_q_d,k),id_buf_q{1,i}(1:ind_q_d,k),psi_q_v','spli
ne');
    end
  end
end

%**********************************  Second round error analysis  **********************************
id_revise_2=id_final_1;
iq_revise_2=iq_final_1;
for i=1:m
  INDEX_THETA=i;
  for j=1:length(psi_q_v)
    for k=1:length(psi_d_v)

[psi_d_verify_2{1,i}(j,k),psi_q_verify_2{1,i}(j,k)]=f_psi_d_q(id_final_1{1,i}(j,k),iq_final_1{1,i}(j,k));
        psi_d_err_2{1,i}(j,k)=(psi_d_verify_2{1,i}(j,k)-psi_d_v(k))/(psi_d_max-psi_d_min);
        psi_q_err_2{1,i}(j,k)=(psi_q_verify_2{1,i}(j,k)-psi_q_v(j))/(psi_q_max-psi_q_min);
    end
```

```
    end
end

%********************  Second round correction of id(Ψd,Ψq,θ) and iq(Ψd,Ψq,θ)  **********************
for i=1:m
    for j=1:length(psi_q_v)
        ind_d_d=0;
        ind_d_q=0;
        for k=1:length(psi_d_v)
            if abs(psi_d_err_2{1,i}(j,k))<=Tolerance_ref || k==1 || k==length(psi_d_v)  %scan d
                ind_d_d=ind_d_d+1;
                id_buf_d{1,i}(j,ind_d_d)=id_final_1{1,i}(j,k);
                psi_d_buf_d{1,i}(j,ind_d_d)=psi_d_v(k);
            end
            if abs(psi_q_err_2{1,i}(j,k))<=Tolerance_ref || k==1 || k==length(psi_d_v)  %scan d
                ind_d_q=ind_d_q+1;
                iq_buf_d{1,i}(j,ind_d_q)=iq_final_1{1,i}(j,k);
                psi_d_buf_q{1,i}(j,ind_d_q)=psi_d_v(k);
            end
        end
        if ind_d_d==length(psi_d_v)
            id_final_2{1,i}(j,:)=id_buf_d{1,i}(j,:);
        else

id_final_2{1,i}(j,:)=interp1(psi_d_buf_d{1,i}(j,1:ind_d_d),id_buf_d{1,i}(j,1:ind_d_d),psi_d_v,'spline
');
        end
        if ind_d_q==length(psi_d_v)
            iq_final_2{1,i}(j,:)=iq_buf_d{1,i}(j,:);
        else

iq_final_2{1,i}(j,:)=interp1(psi_d_buf_q{1,i}(j,1:ind_d_q),iq_buf_d{1,i}(j,1:ind_d_q),psi_d_v,'spline
');
        end
    end
end

%**********************************  Third round error analysis  **********************************
id_revise_3=id_final_2;
iq_revise_3=iq_final_2;
```

```
for i=1:m
   INDEX_THETA=i;
   for j=1:length(psi_q_v)
      for k=1:length(psi_d_v)

[psi_d_verify_3{1,i}(j,k),psi_q_verify_3{1,i}(j,k)]=f_psi_d_q(id_final_2{1,i}(j,k),iq_final_2{1,i}(j,k));
         psi_d_err_3{1,i}(j,k)=(psi_d_verify_3{1,i}(j,k)-psi_d_v(k))/(psi_d_max-psi_d_min);
         psi_q_err_3{1,i}(j,k)=(psi_q_verify_3{1,i}(j,k)-psi_q_v(j))/(psi_q_max-psi_q_min);
      end
   end
end

psi_d_err_max=0;
psi_q_err_max=0;
for i=1:N_theta
   psi_d_err_buf(i)=max(max(abs(psi_d_err_3{1,i})));
   if abs(psi_d_err_buf(i))>psi_d_err_max
      psi_d_err_max=abs(psi_d_err_buf(i));
   end
   psi_q_err_buf(i)=max(max(abs(psi_q_err_3{1,i})));
   if abs(psi_q_err_buf(i))>psi_q_err_max
      psi_q_err_max=abs(psi_q_err_buf(i));
   end
end

%********************  Output final id(Ψd,Ψq,θ), iq(Ψd,Ψq,θ) and also Tem(id,iq,θ)  *********************
torque_table=Torque_00;
theta_v_table=0:360/p/N_theta_steps:360/p;
id_v_table=id_0_v;
iq_v_table=iq_0_v;

id_table=zeros(N_theta,16,16);
iq_table=zeros(N_theta,16,16);
for i=1:m
   id_table(i,:,:)=id_final_2{1,i};
   iq_table(i,:,:)=iq_final_2{1,i};
end
psi_d_v_table=psi_d_v;
psi_q_v_table=psi_q_v;
```

```
%***********************************  Sub-function f_id_iq_tool  ************************************
function [Err,Tole,Id,Iq]=f_id_iq_tool(psi_d,psi_q,theta_index,Id_min,Id_max,Iq_min,Iq_max)
    global INDEX_THETA PSI_D_REF PSI_Q_REF PSI_EQ_RANGE
    INDEX_THETA=theta_index;
    PSI_D_REF=psi_d;
    PSI_Q_REF=psi_q;
    x0=[(Id_min+Id_max)/2,(Iq_min+Iq_max)/2];
    lb=[Id_min,Iq_min];
    ub=[Id_max,Iq_max];
    options=optimset('Algorithm','interior-point');
    [x,fval,exitFlag]=fmincon(@f_psi_eq,x0,[],[],[],[],lb,ub,[],options);
    Id=x(1);
    Iq=x(2);
    Tole=fval/PSI_EQ_RANGE;
    Err=exitFlag;

%************************************  Sub-function f_psi_eq  *************************************
function [feq]=f_psi_eq(x)
    global PSI_D_REF PSI_Q_REF ID_0 IQ_0 PSI_D_0 PSI_Q_0 INDEX_THETA
    psi_d=interp2(ID_0,IQ_0,PSI_D_0{1,INDEX_THETA},x(1),x(2),'linear');
    psi_q=interp2(ID_0,IQ_0,PSI_Q_0{1,INDEX_THETA},x(1),x(2),'linear');
    feq=abs(psi_d-PSI_D_REF)+abs(psi_q-PSI_Q_REF);

%************************************  Sub-function f_psi_d_q  *************************************
function [psi_d,psi_q]=f_psi_d_q(id,iq)
    global ID_0 IQ_0 PSI_D_0 PSI_Q_0 INDEX_THETA
    psi_d=interp2(ID_0,IQ_0,PSI_D_0{1,INDEX_THETA},id,iq,'linear');
    psi_q=interp2(ID_0,IQ_0,PSI_Q_0{1,INDEX_THETA},id,iq,'linear');
```

APPENDIX E Mechanical Stress Analysis

To efficiently build the mechanical stress model shown in Chapter 6, a parameterised rotor model is established in mechanical stress FEA. Fig. E-1 shows the flow chart of mechanical stress analysis for electrical machines via FEA. Firstly, define parameters which determine rotor geometry. This can also be found in the attached ANSYS script at the end of this section. Then, all the key-point coordinates are represented by mathematical equations with rotor parameters. Subsequently, build rotor geometry including key-points, lines and areas for both rotor iron and magnets. Only 1 pole is needed due to the periodicity of mechanical stress. After that, choose element type for the following FEA. Element type PLANE183 (2^{nd} order element with 8 nodes) is recommended to use in 2-D FEA of mechanical stress. Next, define material properties for both rotor iron and magnets, including density, Young's modulus and Poisson's ratio. Then, define overall mesh density and also improve mesh quality for specific lines particularly at the bridge parts where the maximum mechanical stress occurs. After that, mesh all areas using selected elements, i.e. PLANE183. Subsequently, create non-linear contact pairs between magnets and rotor iron. Element types TARGE169 and CONTA172 are recommended to use in the target and contact lines. Subsequently, define symmetry boundary conditions on both longitude lines of this 1-pole geometry. Define the rotating speed as the load condition. Solve the scenario using static analysis with large-deflection (large rotation) effects which can be done by setting NLGEOM to be 1. Moreover, 20 sub-steps are recommended to be taken in solution process. Finally, plot mechanical stress contour after the solution.

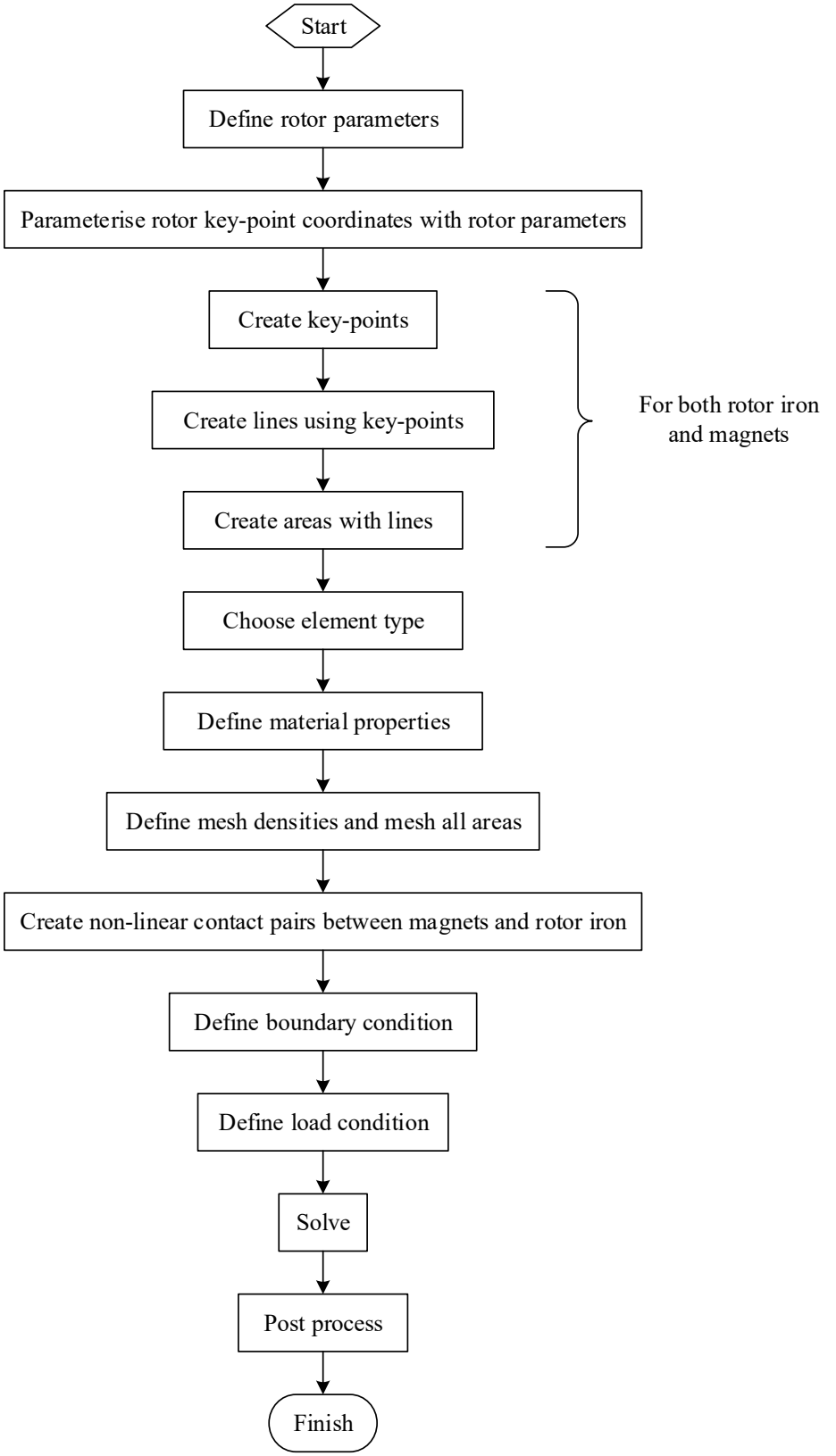

Fig. E-1. Flow chart of mechanical stress analysis for electrical machines via FEA.

Users need to pay attention to the following aspects:

(1) To ensure the mechanical stress calculation accuracy in FEA, a higher mesh density is recommended in the allowable computation time, particularly at the bridge parts where the maximum mechanical stress occurs. In principle, at least 2 layer meshes are needed to have a good accuracy in the narrowest geometry when using PLANE183. However, 5 layer meshes are recommended.

(2) To avoid rigid body motion, such as one or more magnets flying out of rotor iron, proper contact settings have to be performed. Firstly, the contact areas belonging to rotor iron are recommended to be chosen as “target” while those belonging to magnets are recommended to be chosen as “contact”. Secondly, the mesh sizes on both sides of the contact should be similar. Thirdly, initial penetration and initial contact closure also matter. Use default settings first. If rigid body motion happens, try to change KEYOPT,,9,0 to KEYOPT,,9,4 and also change R,,,,1.0,0.1,0 to R,,,,1.0,0.1,0.9. It should be noted that this does not mean the physical contact condition has been changed but means a different initial computation condition in ANSYS. As long as the solution is converged, its results are trustable.

```
!*********************************** Header information ***********************************
/prep7

!*********************************** Parameter definition ***********************************
Rad1=75.6
BetaM=167.4
R_MR=0.424
Bridge=0.4
MiddleBridge=1.55
LM=4
```

```
Poles=16
RadSh=17.5
Barrier_h=0.8
Boss_top=0.7
Boss_bot_w=0.5
Boss_bot_h=0.8
Fillet_radius_m=0.3

!**********************************  Parameterised rotor geometry  **********************************
PI=3.1415926535898
RHQ=Rad1-R_MR*Rad1
ba4=90-BetaM/Poles*0.5
Xa4=2*(Rad1-Bridge-Barrier_h)*sin(BetaM/Poles*0.5/180*PI)
Ya4=Rad1-Bridge-Barrier_h-RHQ
Alfa3=atan(Xa4*sin(ba4/180*PI)/(Ya4-Xa4*cos(ba4/180*PI)))*180/PI
Barrier_h2=Barrier_h+LM*cos((90-Alfa3+BetaM/Poles)/180*PI)
X1=cos(BetaM/Poles/180*PI)*(Rad1-Bridge-Barrier_h2)
X12=X1-RHQ
Y1=-sin(BetaM/Poles/180*PI)*(Rad1-Bridge-Barrier_h2)
Y12=-Y1-MiddleBridge*0.5
L12=sqrt(X12**2+Y12**2)
Alfa2=(atan(Y12/X12)-asin(LM/L12))*180/PI
theta=90-Alfa2
Xm1=(Rad1-Bridge-Barrier_h2)*sin(BetaM/Poles/180*PI)
Ym1=(Rad1-Bridge-Barrier_h2)*cos(BetaM/Poles/180*PI)
Xt1=Xm1-Boss_top*sin(theta/180*PI)
Yt1=Ym1+Boss_top*cos(theta/180*PI)
Xt2=Xm1-(LM-Boss_top)*sin(theta/180*PI)
Yt2=Ym1+(LM-Boss_top)*cos(theta/180*PI)
Xm2=Xm1-LM*sin(theta/180*PI)
Ym2=Ym1+LM*cos(theta/180*PI)
a_xb1=1+tan(theta/180*PI)**2
b_xb1=2*(Yt1-Xt1*tan(theta/180*PI))*tan(theta/180*PI)
c_xb1=(Yt1-Xt1*tan(theta/180*PI))**2-(Rad1-Bridge)**2
Xb1=(-b_xb1+sqrt(b_xb1**2-4*a_xb1*c_xb1))/2/a_xb1
Yb1=Yt1+(Xb1-Xt1)*tan(theta/180*PI)
a_xb2=1+tan(theta/180*PI)**2
b_xb2=2*(Yt2-Xt2*tan(theta/180*PI))*tan(theta/180*PI)
c_xb2=(Yt2-Xt2*tan(theta/180*PI))**2-(Rad1-Bridge)**2
```

```
Xb2=(-b_xb2+sqrt(b_xb2**2-4*a_xb2*c_xb2))/2/a_xb2
Yb2=Yt2+(Xb2-Xt2)*tan(theta/180*PI)
Xm3=MiddleBridge/2
Ym3=RHQ
Xm3f=Xm3+Fillet_radius_m*cos(theta/180*PI)
Ym3f=Ym3+Fillet_radius_m*sin(theta/180*PI)
Xm3f2=Xm3+Fillet_radius_m*sin(theta/180*PI)
Ym3f2=Ym3-Fillet_radius_m*cos(theta/180*PI)
Xm4=Xm3+LM*sin(theta/180*PI)
Ym4=Ym3-LM*cos(theta/180*PI)
Xt4_1=Xm4-Boss_bot_h*sin(theta/180*PI)
Yt4_1=Ym4+Boss_bot_h*cos(theta/180*PI)
Xt4_2=Xt4_1-Boss_bot_w*cos(theta/180*PI)
Yt4_2=Yt4_1-Boss_bot_w*sin(theta/180*PI)
a_xt4_3=1+tan((theta+90)/180*PI)**2
b_xt4_3=2*(Yt4_2-Ym3-Xt4_2*tan((theta+90)/180*PI))*tan((theta+90)/180*PI)-2*Xm3
c_xt4_3=Xm3**2+(Yt4_2-Ym3-Xt4_2*tan((theta+90)/180*PI))**2-LM**2
Xt4_3=(-b_xt4_3+sqrt(b_xt4_3**2-4*a_xt4_3*c_xt4_3))/2/a_xt4_3
Yt4_3=Yt4_2+(Xt4_3-Xt4_2)*tan((theta+90)/180*PI)

!*****************************************  Build rotor geometry  *****************************************
!*****************************************  Define coordinates  *****************************************
LOCAL,11,0,0,0,0, , , ,1,1
LOCAL,12,1,0,0,0, , , ,1,1
CSYS,11
!*****************************************  Define key-points  *****************************************
K,1,Xm1,Ym1
K,2,Xt1,Yt1
K,3,Xb1,Yb1
K,4,Xb2,Yb2
K,5,Xt2,Yt2
K,6,Xm2,Ym2
K,7,Xm3f,Ym3f
K,8,Xm3,Ym3
K,9,Xm3,Ym3-LM
K,10,Xt4_3,Yt4_3
K,11,Xt4_2,Yt4_2
K,12,Xt4_1,Yt4_1
K,13,Xm4,Ym4
```

```
!************************************  Create lines using key-points  *********************************
L,1,2
L,2,3
LARC,3,4,5,Rad1-Bridge
*DO,I,4,8
  L,I,I+1
*ENDDO
LARC,9,10,8,LM
*DO,I,10,12
  L,I,I+1
*ENDDO
L,13,1
!************************************  Create lines using key-points  *********************************
LFILLT,13,1,Fillet_radius_m
LFILLT,1,2,0.2
LFILLT,2,3,0.8
LFILLT,3,4,0.8
LFILLT,4,5,0.2
LFILLT,5,6,Fillet_radius_m
LFILLT,7,8,1.5
LFILLT,8,9,1.8
LFILLT,9,10,0.2
LFILLT,10,11,0.15
LFILLT,11,12,0.15
LFILLT,12,13,Fillet_radius_m
!************************************  Create areas using lines  **********************************
AL,ALL
ARSYM,X,1, , , ,0,0
PCIRC,RadSh,Rad1,90-360/Poles/2,90+360/Poles/2
ASBA,3,1
ASBA,4,2
numcmp,all
!***********************************  Create geometry of magnets  **********************************
LGEN,2,1,,,0,0,0,100
LGEN,2,5,6,1,0,0,0,100
LGEN,2,12,14,1,0,0,0,100
LGEN,2,19,,,0,0,0,100
LGEN,2,25,,,0,0,0,100
K,108,Xm3f2,Ym3f2
```

```
L,116,123
LARC,107,108,1,Fillet_radius_m
L,108,135
LSLA,U
AL,ALL
ALLSEL,ALL
LGEN,2,26,,,0,0,0,100
LGEN,2,34,36,1,0,0,0,100
LGEN,2,47,50,1,0,0,0,100
K,150,-Xm3f2,Ym3f2
L,146,139
L,159,150
LARC,150,149,38,Fillet_radius_m
LSLA,U
AL,ALL
ALLSEL,ALL
L,49,7
L,52,28
FLST,3,2,4,ORDE,2
FITEM,3,77
FITEM,3,-78
ASBL,1,P51X

!*********************************************  Element type  ***************************************
ET,1,PLANE183

!*********************************************  Material property  ***************************************
MP,EX,1,1.92e5
MP,PRXY,1,0.28
MP,DENS,1,7.6e-9
MP,EX,2,1.6e5
MP,PRXY,2,0.24
MP,DENS,2,5e-9

!*********************************************  Mesh  ***************************************************
LESIZE,ALL,0.2
LESIZE,77,0.03
LESIZE,78,0.03
LESIZE,7,0.01
```

```
LESIZE,37,0.01
LESIZE,38,0.005
LESIZE,20,0.005
LESIZE,39,0.01
LESIZE,8,0.01
LESIZE,40,0.02
LESIZE,21,0.02
LESIZE,51,0.1
LESIZE,16,0.01
LESIZE,3,0.01
LESIZE,17,0.01
LESIZE,31,0.01
LESIZE,30,0.01
LESIZE,29,0.01
LESIZE,2,0.01
LESIZE,4,0.1
LESIZE,32,0.1
LESIZE,28,0.1
LESIZE,34,0.025
LESIZE,67,0.025
LESIZE,35,0.075
LESIZE,68,0.075
LESIZE,33,0.05
LESIZE,26,0.025
LESIZE,66,0.025
LESIZE,50,0.075
LESIZE,73,0.075
LESIZE,27,0.05
LESIZE,5,0.025
LESIZE,56,0.025
LESIZE,19,0.075
LESIZE,61,0.075
LESIZE,18,0.05
LESIZE,1,0.025
LESIZE,55,0.025
LESIZE,14,0.075
LESIZE,60,0.075
LESIZE,15,0.05
LESIZE,63,0.1
```

```
LESIZE,74,0.1

TYPE,1
MAT,1
MSHAPE,0,2D
MSHKEY,2
AMESH,4,5,1
TYPE,1
MAT,2
MSHAPE,0,2D
MSHKEY,2
AMESH,2,3,1

!*********************  Non-linear contact between magnets and rotor iron  *********************
!*******************************************  Contact pair 1  *******************************************
/COM, CONTACT PAIR CREATION - START
CM,_NODECM,NODE
CM,_ELEMCM,ELEM
CM,_KPCM,KP
CM,_LINECM,LINE
CM,_AREACM,AREA
CM,_VOLUCM,VOLU
/GSAV,cwz,gsav,,temp
MP,MU,1,0.2
MAT,1
MP,EMIS,1,7.88860905221e-031
R,3
REAL,3
ET,2,169
ET,3,172
R,3,,,1.0,0.1,,
RMORE,,,1.0E20,0.0,1.0,
RMORE,0.0,0,1.0,,1.0,0.5
RMORE,0,1.0,1.0,0.0,,1.0
KEYOPT,3,3,0
KEYOPT,3,4,0
KEYOPT,3,5,0
KEYOPT,3,7,0
KEYOPT,3,8,0
```

```
KEYOPT,3,9,0
KEYOPT,3,10,2
KEYOPT,3,11,0
KEYOPT,3,12,0
KEYOPT,3,2,0
! Generate the target surface
LSEL,S,,,5
LSEL,A,,,6
LSEL,A,,,19
CM,_TARGET,LINE
TYPE,2
NSLL,S,1
ESLN,S,0
ESURF
CMSEL,S,_ELEMCM
! Generate the contact surface
LSEL,S,,,56
LSEL,A,,,57
LSEL,A,,,61
CM,_CONTACT,LINE
TYPE,3
NSLL,S,1
ESLN,S,0
ESURF
ALLSEL
ESEL,ALL
ESEL,S,TYPE,,2
ESEL,A,TYPE,,3
ESEL,R,REAL,,3
/PSYMB,ESYS,1
/PNUM,TYPE,1
/NUM,1
EPLOT
ESEL,ALL
ESEL,S,TYPE,,2
ESEL,A,TYPE,,3
ESEL,R,REAL,,3
CMSEL,A,_NODECM
CMDEL,_NODECM
```

```
CMSEL,A,_ELEMCM
CMDEL,_ELEMCM
CMSEL,S,_KPCM
CMDEL,_KPCM
CMSEL,S,_LINECM
CMDEL,_LINECM
CMSEL,S,_AREACM
CMDEL,_AREACM
CMSEL,S,_VOLUCM
CMDEL,_VOLUCM
/GRES,cwz,gsav
CMDEL,_TARGET
CMDEL,_CONTACT
/COM, CONTACT PAIR CREATION - END

!*********** Contact pair 2 ***********
/COM, CONTACT PAIR CREATION - START
CM,_NODECM,NODE
CM,_ELEMCM,ELEM
CM,_KPCM,KP
CM,_LINECM,LINE
CM,_AREACM,AREA
CM,_VOLUCM,VOLU
/GSAV,cwz,gsav,,temp
MP,MU,1,0.2
MAT,1
MP,EMIS,1,7.88860905221e-031
R,4
REAL,4
ET,4,169
ET,5,172
R,4,,,1.0,0.1,,
RMORE,,,1.0E20,0.0,1.0,
RMORE,0.0,0,1.0,,1.0,0.5
RMORE,0,1.0,1.0,0.0,,1.0
KEYOPT,5,3,0
KEYOPT,5,4,0
KEYOPT,5,5,0
KEYOPT,5,7,0
```

```
KEYOPT,5,8,0
KEYOPT,5,9,0
KEYOPT,5,10,2
KEYOPT,5,11,0
KEYOPT,5,12,0
KEYOPT,5,2,0
! Generate the target surface
LSEL,S,,,34
LSEL,A,,,35
LSEL,A,,,36
CM,_TARGET,LINE
TYPE,4
NSLL,S,1
ESLN,S,0
ESURF
CMSEL,S,_ELEMCM
! Generate the contact surface
LSEL,S,,,67
LSEL,A,,,68
LSEL,A,,,69
CM,_CONTACT,LINE
TYPE,5
NSLL,S,1
ESLN,S,0
ESURF
ALLSEL
ESEL,ALL
ESEL,S,TYPE,,4
ESEL,A,TYPE,,5
ESEL,R,REAL,,4
/PSYMB,ESYS,1
/PNUM,TYPE,1
/NUM,1
EPLOT
ESEL,ALL
ESEL,S,TYPE,,4
ESEL,A,TYPE,,5
ESEL,R,REAL,,4
CMSEL,A,_NODECM
```

```
CMDEL,_NODECM
CMSEL,A,_ELEMCM
CMDEL,_ELEMCM
CMSEL,S,_KPCM
CMDEL,_KPCM
CMSEL,S,_LINECM
CMDEL,_LINECM
CMSEL,S,_AREACM
CMDEL,_AREACM
CMSEL,S,_VOLUCM
CMDEL,_VOLUCM
/GRES,cwz,gsav
CMDEL,_TARGET
CMDEL,_CONTACT
/COM, CONTACT PAIR CREATION - END

!*****************************************  Contact pair 3  *****************************************
/COM, CONTACT PAIR CREATION - START
CM,_NODECM,NODE
CM,_ELEMCM,ELEM
CM,_KPCM,KP
CM,_LINECM,LINE
CM,_AREACM,AREA
CM,_VOLUCM,VOLU
/GSAV,cwz,gsav,,temp
MP,MU,1,0.2
MAT,1
MP,EMIS,1,7.88860905221e-031
R,5
REAL,5
ET,6,169
ET,7,172
R,5,,,1.0,0.1,,
RMORE,,,1.0E20,0.0,1.0,
RMORE,0.0,0,1.0,,1.0,0.5
RMORE,0,1.0,1.0,0.0,,1.0
KEYOPT,7,3,0
KEYOPT,7,4,0
KEYOPT,7,5,0
```

```
KEYOPT,7,7,0
KEYOPT,7,8,0
KEYOPT,7,9,0
KEYOPT,7,10,2
KEYOPT,7,11,0
KEYOPT,7,12,0
KEYOPT,7,2,0
! Generate the target surface
LSEL,S,,,1
LSEL,A,,,12
LSEL,A,,,13
LSEL,A,,,14
LSEL,A,,,25
CM,_TARGET,LINE
TYPE,6
NSLL,S,1
ESLN,S,0
ESURF
CMSEL,S,_ELEMCM
! Generate the contact surface
LSEL,S,,,55
LSEL,A,,,58
LSEL,A,,,59
LSEL,A,,,60
LSEL,A,,,62
CM,_CONTACT,LINE
TYPE,7
NSLL,S,1
ESLN,S,0
ESURF
ALLSEL
ESEL,ALL
ESEL,S,TYPE,,6
ESEL,A,TYPE,,7
ESEL,R,REAL,,5
/PSYMB,ESYS,1
/PNUM,TYPE,1
/NUM,1
EPLOT
```

```
ESEL,ALL
ESEL,S,TYPE,,6
ESEL,A,TYPE,,7
ESEL,R,REAL,,5
CMSEL,A,_NODECM
CMDEL,_NODECM
CMSEL,A,_ELEMCM
CMDEL,_ELEMCM
CMSEL,S,_KPCM
CMDEL,_KPCM
CMSEL,S,_LINECM
CMDEL,_LINECM
CMSEL,S,_AREACM
CMDEL,_AREACM
CMSEL,S,_VOLUCM
CMDEL,_VOLUCM
/GRES,cwz,gsav
CMDEL,_TARGET
CMDEL,_CONTACT
/COM, CONTACT PAIR CREATION - END

!*****************************************  Contact pair 4  *****************************************
/COM, CONTACT PAIR CREATION - START
CM,_NODECM,NODE
CM,_ELEMCM,ELEM
CM,_KPCM,KP
CM,_LINECM,LINE
CM,_AREACM,AREA
CM,_VOLUCM,VOLU
/GSAV,cwz,gsav,,temp
MP,MU,1,0.2
MAT,1
MP,EMIS,1,7.88860905221e-031
R,6
REAL,6
ET,8,169
ET,9,172
R,6,,,1.0,0.1,,
RMORE,,,1.0E20,0.0,1.0,
```

```
RMORE,0.0,0,1.0,,1.0,0.5
RMORE,0,1.0,1.0,0.0,,1.0
KEYOPT,9,3,0
KEYOPT,9,4,0
KEYOPT,9,5,0
KEYOPT,9,7,0
KEYOPT,9,8,0
KEYOPT,9,9,0
KEYOPT,9,10,2
KEYOPT,9,11,0
KEYOPT,9,12,0
KEYOPT,9,2,0
! Generate the target surface
LSEL,S,,,26
LSEL,A,,,47
LSEL,A,,,48
LSEL,A,,,49
LSEL,A,,,50
CM,_TARGET,LINE
TYPE,8
NSLL,S,1
ESLN,S,0
ESURF
CMSEL,S,_ELEMCM
! Generate the contact surface
LSEL,S,,,66
LSEL,A,,,70
LSEL,A,,,71
LSEL,A,,,72
LSEL,A,,,73
CM,_CONTACT,LINE
TYPE,9
NSLL,S,1
ESLN,S,0
ESURF
ALLSEL
ESEL,ALL
ESEL,S,TYPE,,8
ESEL,A,TYPE,,9
```

```
ESEL,R,REAL,,6
/PSYMB,ESYS,1
/PNUM,TYPE,1
/NUM,1
EPLOT
ESEL,ALL
ESEL,S,TYPE,,8
ESEL,A,TYPE,,9
ESEL,R,REAL,,6
CMSEL,A,_NODECM
CMDEL,_NODECM
CMSEL,A,_ELEMCM
CMDEL,_ELEMCM
CMSEL,S,_KPCM
CMDEL,_KPCM
CMSEL,S,_LINECM
CMDEL,_LINECM
CMSEL,S,_AREACM
CMDEL,_AREACM
CMSEL,S,_VOLUCM
CMDEL,_VOLUCM
/GRES,cwz,gsav
CMDEL,_TARGET
CMDEL,_CONTACT
/COM, CONTACT PAIR CREATION - END
/MREP,EPLOT

EPLOT

!*********** Boundary condition ***********
DL,52,,SYMM
DL,54,,SYMM

!*********** Load condition ***********
OMEGA,0,0,1.5*11300/60*2*3.1415926,0
FINISH

!*********** Solve ***********
/SOL
```

```
ANTYPE,STATIC
NLGEOM,1
NSUBST,20,0,0
SOLVE
FINISH

!*********************************************  Post-process  *********************************************
/POST1
/DSCALE,ALL,1.0
/EFACET,1
PLNSOL, S,EQV, 0,1.0
```

APPENDIX F Rotor-dynamics Analysis

To perform the rotor-dynamics analysis shown in Chapter 4, a FE model of rotor-bearing system model needs to be established. This section describes the detailed procedures to build the rotor-bearing system FE model and also shows the processes of rotor-dynamics analysis. Given that the rotor-dynamics behaviour of a rotor-bearing system is insensitive to localised geometry variation, the rotor-bearing system model is simplified by combining rotor iron, magnets and rotor end-plates into one equivalent solid cylinder.

Fig. F-1 shows the flow chart of rotor-dynamics analysis for electrical machines via FEA. Firstly, Define speed samples for the sweep range of CAMPBELL diagram. In the ANSYS script example shown below, the defined speed samples are from 0 to 90000r/min with the step of 10000r/min. Then, define material properties including density, Young's modulus and Poisson's ratio. After that, choose element types for rotor and bearings. 3-D 2-node beam elements (BEAM188) are employed to model the rotor whilst spring-damper elements (COMBIN14) are utilised to represent the bearings. Next, set the bearing stiffness according to the radial load of bearings. This procedure has been described in Section 4.7.5, Chapter 4. Subsequently, define rotor section properties, i.e. rotor radius at different sections in axial direction. Then, create nodes based on the axial positions of different sections and also the number of elements for each rotor section. After that, create elements based on the nodes. Next, define boundary conditions including no degree of freedom (DOF) for either movement at axial direction or torsion around axial direction, no DOF for the bearing outer ring nodes at all directions. Subsequently, set solution options, such as choosing modal analysis, turning on Coriolis effect and selecting QR algorithm for a damped system as the modal analysis algorithm. Then, solve the scenario with the

defined speed samples in the first step. Finally, draw the CAMPBELL diagram in the post-process.

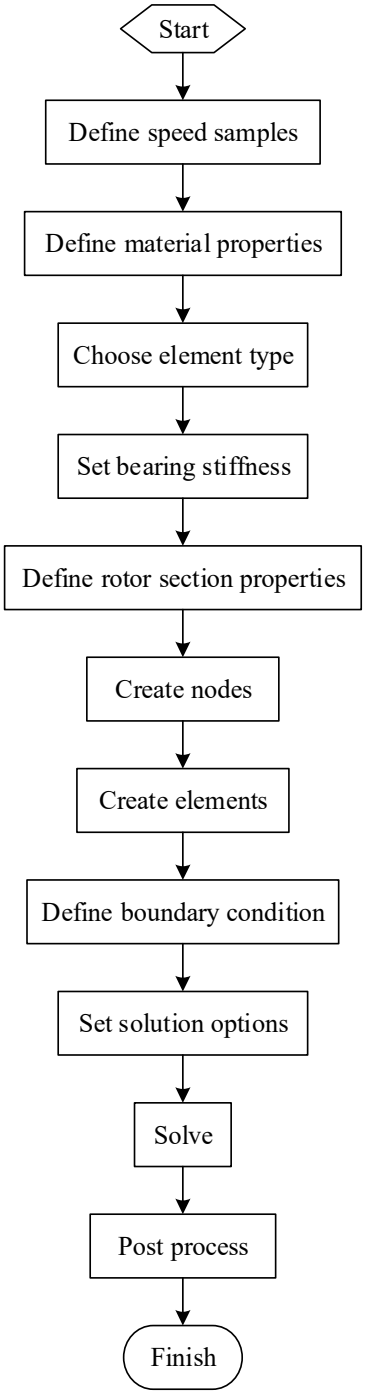

Fig. F-1. Flow chart of rotor-dynamic analysis for electrical machines via FEA.

It should be noted that no key-points or lines are needed for mesh, due to the feature of BEAM188 and also the simple rotor structure. The meshes are directly made based on the nodes created according to axial positions of different rotor sections and also the number of elements for each rotor section.

```
!*********************************** Header information ***********************************
/PREP7

!*********************************** Speed sample definition ***********************************
*DIM,SPIN,,10
SPIN(1) = 0.
SPIN(2) = 10000.
SPIN(3) = 20000.
SPIN(4) = 30000.
SPIN(5) = 40000.
SPIN(6) = 50000.
SPIN(7) = 60000.
SPIN(8) = 70000.
SPIN(9) = 80000.
SPIN(10) = 90000.

!*********************************** Material property ***********************************
RO = 7850
PEX = 2.09E+11
PV = 0.269
MP,EX,1,PEX
MP,PRXY,1,PV
MP,DENS,1,RO

!*********************************** Element type ***********************************
ET,1,BEAM188,,,2                    ! Element type #1 : Rotor
ET,3,COMBIN14                       ! Element type #3 : Bearings
KEYOPT,3,2,2                        ! Y direction
```

```
ET,4,COMBIN14
KEYOPT,4,2,3                    ! Z direction

!*****************************************  Bearing stiffness  *****************************************
R,300,5.15E7

!*************************************  Rotor section properties  *************************************
NBRADI = 106
*DIM,RADIUS,ARRAY,NBRADI
RADIUS(1)=0.004
RADIUS(2)=0.004
RADIUS(3)=0.004
RADIUS(4)=0.004
RADIUS(5)=0.004
RADIUS(6)=0.004
RADIUS(7)=0.0125
RADIUS(8)=0.0125
RADIUS(9)=0.0125
RADIUS(10)=0.0125
RADIUS(11)=0.0125
RADIUS(12)=0.0125
RADIUS(13)=0.015
RADIUS(14)=0.015
RADIUS(15)=0.015
RADIUS(16)=0.015
RADIUS(17)=0.022
RADIUS(18)=0.022
RADIUS(19)=0.022
RADIUS(20)=0.022
RADIUS(21)=0.07
RADIUS(22)=0.07
RADIUS(23)=0.07
RADIUS(24)=0.07
RADIUS(25)=0.07
RADIUS(26)=0.07
RADIUS(27)=0.07
RADIUS(28)=0.07
RADIUS(29)=0.07
RADIUS(30)=0.07
```

RADIUS(31)=0.07
RADIUS(32)=0.07
RADIUS(33)=0.07
RADIUS(34)=0.07
RADIUS(35)=0.07
RADIUS(36)=0.07
RADIUS(37)=0.07
RADIUS(38)=0.07
RADIUS(39)=0.07
RADIUS(40)=0.07
RADIUS(41)=0.07
RADIUS(42)=0.07
RADIUS(43)=0.07
RADIUS(44)=0.07
RADIUS(45)=0.07
RADIUS(46)=0.07
RADIUS(47)=0.07
RADIUS(48)=0.07
RADIUS(49)=0.07
RADIUS(50)=0.07
RADIUS(51)=0.07
RADIUS(52)=0.07
RADIUS(53)=0.015
RADIUS(54)=0.015
RADIUS(55)=0.015
RADIUS(56)=0.015
RADIUS(57)=0.015
RADIUS(58)=0.015
RADIUS(59)=0.015
RADIUS(60)=0.015
RADIUS(61)=0.0125
RADIUS(62)=0.0125
RADIUS(63)=0.0125
RADIUS(64)=0.0125
RADIUS(65)=0.0125
RADIUS(66)=0.0125
RADIUS(67)=0.012
RADIUS(68)=0.012
RADIUS(69)=0.012

```
RADIUS(70)=0.012
RADIUS(71)=0.012
RADIUS(72)=0.012
RADIUS(73)=0.012
RADIUS(74)=0.012
RADIUS(75)=0.012
RADIUS(76)=0.012
RADIUS(77)=0.012
RADIUS(78)=0.012
RADIUS(79)=0.012
RADIUS(80)=0.012
RADIUS(81)=0.012
RADIUS(82)=0.012
RADIUS(83)=0.012
RADIUS(84)=0.012
RADIUS(85)=0.012
RADIUS(86)=0.012
RADIUS(87)=0.012
RADIUS(88)=0.012
RADIUS(89)=0.012
RADIUS(90)=0.012
RADIUS(91)=0.012
RADIUS(92)=0.012
RADIUS(93)=0.012
RADIUS(94)=0.012
RADIUS(95)=0.012
RADIUS(96)=0.012
RADIUS(97)=0.012
RADIUS(98)=0.012
RADIUS(99)=0.012
RADIUS(100)=0.012
RADIUS(101)=0.012
RADIUS(102)=0.012
RADIUS(103)=0.012
RADIUS(104)=0.012
RADIUS(105)=0.012
RADIUS(106)=0.012
*DO,I,1,NBRADI
  SECTYPE,I,BEAM,CSOLID
```

```
   SECDATA,RADIUS(I),32,8
*ENDDO

!*****************************************  Create nodes  *****************************************
N,1,0
N,2,0.0025833
N,3,0.0051667
N,4,0.00775
N,5,0.010333
N,6,0.012917
N,7,0.0155
N,8,0.01825
N,9,0.021
N,10,0.02325
N,11,0.0255
N,12,0.02775
N,13,0.03
N,14,0.033
N,15,0.036
N,16,0.039
N,17,0.042
N,18,0.0444
N,19,0.0468
N,20,0.0492
N,21,0.0516
N,22,0.054238
N,23,0.056875
N,24,0.059513
N,25,0.06215
N,26,0.064787
N,27,0.067425
N,28,0.070063
N,29,0.0727
N,30,0.075338
N,31,0.077975
N,32,0.080613
N,33,0.08325
N,34,0.085888
N,35,0.088525
```

N,36,0.091163
N,37,0.0938
N,38,0.096438
N,39,0.099075
N,40,0.10171
N,41,0.10435
N,42,0.10699
N,43,0.10963
N,44,0.11226
N,45,0.1149
N,46,0.11754
N,47,0.12018
N,48,0.12281
N,49,0.12545
N,50,0.12809
N,51,0.13072
N,52,0.13336
N,53,0.136
N,54,0.1385
N,55,0.141
N,56,0.1435
N,57,0.146
N,58,0.1485
N,59,0.151
N,60,0.1535
N,61,0.156
N,62,0.15825
N,63,0.1605
N,64,0.16275
N,65,0.165
N,66,0.16775
N,67,0.1705
N,68,0.17326
N,69,0.17602
N,70,0.17879
N,71,0.18155
N,72,0.18431
N,73,0.18707
N,74,0.18984

```
N,75,0.1926
N,76,0.19536
N,77,0.19813
N,78,0.20089
N,79,0.20365
N,80,0.20641
N,81,0.20918
N,82,0.21194
N,83,0.2147
N,84,0.21746
N,85,0.22023
N,86,0.22299
N,87,0.22575
N,88,0.22851
N,89,0.23128
N,90,0.23404
N,91,0.2368
N,92,0.23956
N,93,0.24233
N,94,0.24509
N,95,0.24785
N,96,0.25061
N,97,0.25338
N,98,0.25614
N,99,0.2589
N,100,0.26166
N,101,0.26443
N,102,0.26719
N,103,0.26995
N,104,0.27271
N,105,0.27548
N,106,0.27824
N,107,0.281

BRG = 0.03                    ! Bearing “length” for visualisation
N,1001,0.0255,BRG
N,1002,0.0255,,BRG
N,1003,0.1605,BRG
N,1004,0.1605,,BRG
```

```
!*********************************************  Create elements  *********************************************
TYPE,1                                  ! Create rotor elements
MAT,1
*DO,I,1,NBRADI
  SECNUM,I
  E,I,I+1
*ENDDO
TYPE,3                                  ! Create bearing elements
REAL,300
E,11,1001
E,63,1003
TYPE,4                                  ! Create bearing elements
REAL,300
E,11,1002
E,63,1004
EPLOT
/ESHAPE,1.0
EPLOT
FINISH

!*********************************************  Solution settings  *********************************************
!*********************************************  Boundary condition  *********************************************
/SOLU
D,ALL,UX                                ! No traction or torsion
D,ALL,ROTX
D,1001,ALL
D,1002,ALL
D,1003,ALL
D,1004,ALL

!*********************************************  Solution option  *********************************************
RATIO = 4*ATAN(1)/30
ANTYPE,MODAL
CORIOLIS,ON,,,ON                        ! Coriolis ON in a stationary reference frame
NBF = 40
MODOPT,QRDAMP,NBF,,,ON
/OUT,SCRATCH
```

```
!*********************************************** Solve ***********************************************
*DO,I,1,10
  OMEGA,SPIN(I)*RATIO
  MXPAND,NBF,,,1
  SOLVE
*ENDDO
FINISH

!******************************************** Post-process ********************************************
/POST1
PRCAMP,,1.,RPM                    ! Print CAMPBELL values for slope=1, unit=rpm
PLCAMP,,1.,RPM
```